Confronting Plate Models with the Deep Mantle

Thomas Christopher New

A thesis submitted in fulfilment of the requirements
for the degree of Doctor of Philosophy

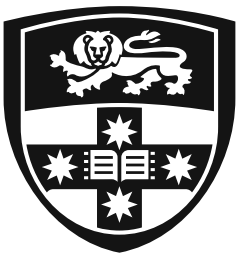

THE UNIVERSITY OF
SYDNEY

School of Geosciences
Faculty of Science

The University of Sydney
NSW, 2006, Australia

2026

Declaration

I declare that this thesis is less than 80 000 words in length, and that the work contained in this thesis has not been submitted for a higher degree at any other university or institution.

During the preparation of the thesis I used GPT-3.5, the GPT-4.X family of models, the o1 family of models, and the GPT-5.X family of models, for the purposes of minor text-editing (e.g., paraphrasing, sentence structure) and generation/modification of code snippets for analysing and plotting data. I confirm that where text and code was modified by generative AI, the content was reviewed for possible errors, inaccuracies, and bias. I take full responsibility for the submitted thesis, and confirm the work is my own and used generative AI within the parameters of use (refer to the University of Sydney generative AI guide for researchers).

Tom New, 12th June 2026

Acknowledgements

If you helped, I'm thankful. I couldn't have done it without you. Special thanks to my supervisors, Maria, Dietmar, and Ben, and to our collaborators in the capital, Sia and Rhodri. I especially couldn't have done it without you. And to my family overseas—8 to 9 time zones away, yet somehow still close enough to be there when it mattered—thank you for the love, patience, and unwavering support (despite the logistical comedy of trying to talk across sleep schedules).

I also acknowledge support from the Postgraduate Research Scholarship in Plate–Plume Interactions, funded by an ARC Discovery Project and the School of Geosciences.

Abstract

The coupled plate–mantle system is fundamental to understanding Earth's surface evolution, geodynamics, and geochemistry. A common approach to studying this system is to generate predictions of present-day mantle structure using mantle circulation models—numerical models of whole-mantle convection forced by tectonic reconstructions as a kinematic boundary condition. Such models have been used to infer slab sinking rates, mantle viscosity, and mantle mineralogy, and—the focus of this thesis—to evaluate tectonic reconstructions. However, many studies compare modelled temperature fields directly with seismic velocity anomalies from tomography, overlooking nonlinearity in the temperature–velocity relationship and the strongly heterogeneous spatial resolution of seismic imaging. In addition, commonly used misfit metrics can saturate when anomalies do not overlap pointwise. Together, these issues motivate the need for a robust, physically consistent approach to using tomography to evaluate, and discriminate between, competing tectonic reconstructions.

Meeting this need is the central aim of this thesis. Robustly evaluating a tectonic reconstruction against tomography, however, depends on two prerequisites: a physically consistent way to compare a model with the imaged mantle, and confidence that the chosen circulation model behaves sensibly in subducting regimes. I therefore first develop a comparison methodology that is transferable across mantle circulation modelling approaches (demonstrated here using models run with the G-ADOPT geoscientific finite-element modelling library). This comprises: (i) a physically consistent framework for converting predicted temperature structure into seismic velocity perturbations; (ii) the incorporation of tomographic resolution operators to filter these converted structures prior to comparison; and (iii) new to this application, use of the Wasserstein metric to quantify misfit in a way that remains informative even when predicted and imaged anomalies do not overlap. I then evaluate the strengths and limitations of current G-ADOPT circulation models across a suite of well-studied subduction regimes. With these foundations in place, I apply them to a case study: the collision of the Ontong–Java plateau with the Melanesian arc subduction system, where collision timing remains uncertain (∼25 versus ∼12 Ma), to provide an independent line of evidence for the timing of collision.

I show that physically consistent post-processing can flip qualitative inferences of slab morphology (i.e., continuous to discontinuous or vice versa). Tomographic filtering may render discontinuous slabs apparently continuous, continuous slabs apparently segmented, and fine-scale structure present in the model suppressed below tomography's resolving power—showing that without such filtering, model–tomography comparisons can yield false negatives when predicted features are simply below tomographic resolution. Filtering also shifts inferred slab basal depths by tens of kilometres in either direction, changing inferred mean sinking rates by up to $1.2\,\mathrm{mm\,yr^{-1}}$ (and by $4.6\,\mathrm{mm\,yr^{-1}}$ where filtering artificially merges separate anomalies), and laterally displaces slab-like anomalies by up to 639 km—offsets that exceed the accompanying depth changes and bear directly on slab-unfolding estimates of subducted lithosphere length. Across the benchmark subduction regimes, I find that mantle circulation modelling in G-ADOPT reproduces upper mantle and transition-zone structure well where slab rollback dominates and the kinematics are relatively straightforward. In contrast, where there is significant trench advance in the mantle frame, G-ADOPT systematically predicts the incorrect dip polarity. This arises because slab dip arises dynamically from the imposed plate kinematics rather than being prescribed, making model predictions sensitive to kinematic regimes in which slab dip is tightly coupled to boundary-condition choices.

Results from the case study strongly support an older collision scenario. Only the ∼25 Ma model reproduces slab material in the upper mantle and transition zone beneath the Melanesian arc region, and it achieves substantially lower misfit (10–28 % across all metrics) compared to the ∼12 Ma

model. These findings support the hypothesis that Ontong–Java collision played an important role in a regional plate reorganisation event at ∼25 Ma in the southwest Pacific. However, because a relatively small modification (∼2000 km) to the regional tectonic boundaries at this time is sufficient to reproduce present-day mantle structure, its role in any contemporaneous global reorganisation event remains unclear, as such events are typically associated with much larger changes to the global plate circuit.

Collectively, these studies highlight the importance of publishing seismic tomography models alongside resolution operators, as tomographic filtering substantially improves the validity of using seismic imaging to ground-truth geodynamic predictions. The workflows developed here are broadly applicable to mantle circulation models beyond G-ADOPT. Within the G-ADOPT ecosystem, they provide essential infrastructure for future adjoint and data-assimilation experiments, allowing optimisation toward the imaged mantle in observation space rather than fitting to the spatial heterogeneity inherent to tomographic models.

Authorship Attribution

This thesis is based on the following three articles:

Article 1: New, T., Ghelichkhan, S., Davies, D. R., Seton, M., Mather, B., & Müller, R. D. (2025a). Calibrating plate reconstructions with global mantle convection models. *Manuscript in revision, Geochemistry, Geophysics, Geosystems.*

I designed this study in collaboration with D.R.D. and S.G., ran early versions of the numerical model, contributed to refining the model's parameter space, performed all data analysis including updating/writing tomographic filtering code, produced all figures and tables, and wrote drafts of the manuscript. All authors contributed feedback on drafts of the manuscript.

Article 2: New, T., Seton, M., Müller, R. D., Davies, D. R., Ghelichkhan, S., & Mather, B. (2025c). Testing plate reconstructions with emergent slab geometry. *Prepared for submission to the Journal of Geodynamics.*

I designed this study in collaboration with M.S., R.D.M., and B.M., performed all data analysis, produced all figures and tables, and wrote drafts of the manuscript. M.S. and R.D.M. contributed feedback on drafts of the manuscript. Methods follow Article 1 (co-developed with D.R.D. and S.G.).

Article 3: New, T., Seton, M., Mather, B., Müller, R. D., Ghelichkhan, S., & Davies, D. R. (2025b). Coupled plate–mantle models support a 25 Ma Ontong–Java collision. *Prepared for submission to Earth and Planetary Science Letters.*

I designed this study in collaboration with M.S., B.M., and R.D.M., derived the alternative plate model, performed all data analysis, produced all figures and tables, and wrote drafts of the manuscript. M.S. and R.D.M. contributed feedback on drafts of the manuscript. Methods follow Article 1 (co-developed with D.R.D. and S.G.).

Articles 2 and 3 apply the numerical modelling framework, tomographic filtering workflow, and analysis approach developed for Article 1. Because D.R.D. and S.G. co-developed key components of this methodology and provided ongoing methodological input, they are co-authors on Articles 2 and 3 in addition to Article 1.

Tom New, 12th June 2026

As principal supervisor for this candidature, I confirm that the above authorship attribution statements are accurate and faithfully reflect the contributions to each publication and to the relevant sections of this dissertation.

Maria Seton, 12th June 2026

Contents

1 | Introduction

1 Background

The interplay between and evolution of plate tectonics and mantle convection (the plate–mantle system) over geologic time has played a critical role in shaping both past and present features of the Earth, from the surface to the core. At the deepest levels, this system plays important roles in the conditions that sustain Earth's magnetic field (Biggin et al., 2012), protecting the surface from deadly cosmic radiation, and in the formation of large, low-shear-velocity provinces just above the core–mantle boundary, which drive certain volcanic hot-spots at the Earth's surface (Maruyama et al., 2007; Torsvik et al., 2014). Near the surface, on the other hand, this system is key to understanding the drivers of plate motions (McKenzie, 1969; Gurnis, 1988; Bercovici, 2003), which in turn plays a role in the sinking of oceanic lithosphere into the deep mantle, and its recirculation and convection together with mantle material. Changes in mantle convection and plate interactions have also been important factors determining the assembly and dispersal of supercontinents (Müller et al., 2022b), palaeotopography (Faccenna et al., 2019), sea level (Miller et al., 2005; Cao et al., 2019; Young et al., 2022), palaeoclimate (Raymo & Ruddiman, 1992; Flament et al., 2013; Scotese et al., 2021), cryosphere (Austermann et al., 2015), and the distribution of mineral and energy resources (Groves & Bierlein, 2007; Cawood & Hawkesworth, 2014; Müller et al., 2022b).

One framework for studying the plate–mantle system is to model, using finite element numerical methods, whole-mantle flow through deep time as being driven by plate tectonics at the surface (imposed as a zero-slip kinematic boundary condition), a so-called *mantle circulation model* (MCM; Bunge et al., 2002). Such an approach has been used to estimate slab sinking rates and mantle viscosity (e.g., Butterworth et al., 2014; Peng & Liu, 2022), place constraints on mantle mineralogy (e.g., Schuberth et al., 2009; Styles et al., 2011; Davies et al., 2012; Su et al., 2023; Dannberg et al., 2024; Roy et al., 2025), and—the focus of this thesis—to evaluate tectonic reconstructions (e.g., Bunge et al., 2002; Liu & Stegman, 2011; Shephard et al., 2012; Flament et al., 2015; Seton et al., 2015; Nerlich et al., 2016; Zahirovic et al., 2016; Harrington et al., 2017; Hu et al., 2018a, 2018b; Peng et al., 2021a, 2021b; Lin et al., 2022; Li et al., 2023). The primary way to validate the temperature structure predicted by these models is with comparison to *seismic tomography models*—3D images of present-day mantle seismic-velocity structure derived from joint inversion of travel-time and waveform data from hundreds to thousands of earthquakes—from which mantle temperature anomalies can be inferred (Fichtner et al., 2025).

As the sophistication of numerical methods, computational power, and our understanding of mantle physics and mineralogy has increased over the last three decades, so too has the resolving power and accuracy of both mantle circulation models and seismic tomography. Together with increasingly detailed plate tectonic reconstructions, this now provides an opportunity to treat reconstructions, mantle flow models, and seismic images as complementary constraints on the evolving plate–mantle system. However, bringing these tools into a single, consistent workflow

raises a set of practical and conceptual challenges that this thesis will address.

Plate tectonic history

The motion of a tectonic plate can be described either relative to another plate, or relative to a fixed external frame—a so-called absolute plate motion (Torsvik et al., 2008). Either way, motions are encoded as finite rotations about an Euler pole (McKenzie & Parker, 1967; Morgan, 1968), exploiting the fact that the displacement of a point on a sphere is fully described by a single rotation. A complete reconstruction is therefore a hierarchy of such rotations tying every plate, through a chain of relative motions, to a chosen absolute reference frame. The data and assumptions reviewed below feed into different parts of this hierarchy.

For Mesozoic–Cenozoic history, if oceanic crust is preserved on both flanks of a mid-ocean ridge, tectonic history of the continents and oceans can be reliably determined from marine magnetic anomalies and fracture zone traces. If only one flank is preserved, history can still be inferred by assuming symmetric spreading of the lost flank, or introducing a degree of asymmetry based on other constraints. If a large portion of oceanic crust has been consumed by subduction (as is the case for pre-Mesozoic time), plate boundaries have to be deduced from the onshore geologic record (such as ophiolites, accretionary prisms, or magmatic arcs). Spreading rates and direction must be extrapolated from the remaining oceanic crust. Valid kinematic interpretations—given such a lack of constraints—are often non-unique, and subject to significant uncertainty.

For pre-Mesozoic times, continental positions are anchored primarily by palaeomagnetism. On timescales of 10^5–10^6 yr the geomagnetic field approximates a geocentric axial dipole, so a rock's remanent magnetisation records its palaeolatitude and azimuthal orientation at the time of formation (Torsvik et al., 2012). However, the axial symmetry of the field leaves palaeolongitude unconstrained, which is the principal obstacle to reconstructing absolute positions in deep time. The two dominant absolute frames address this differently: the *palaeomagnetic reference frame* ties plates to the spin axis and is preferred for palaeoclimate and palaeobiology, whereas *mantle reference frames*—hotspot-based or tomographic—reconstruct plates relative to deep-Earth structure (Torsvik et al., 2008, 2014). The two drift apart through true polar wander, and mantle frames extend reliably back only ∼130 Myr (hotspots) to ∼300 Myr (slabs); deeper than that, palaeolongitude must be estimated by, for example, reconstructing large igneous provinces to the margins of the large low shear velocity provinces under the assumption that the latter are fixed (Torsvik et al., 2014) or using an optimised reference frame (Müller et al., 2022a).

Beyond magnetic anomalies and palaeomagnetism, a heterogeneous set of geological and geophysical observations constrains reconstructions, particularly where ocean crust has been lost. Age-progressive seamount chains record absolute plate motion over long-lived mantle plumes (Tuzo Wilson, 1963; Morgan, 1971); suture zones, accretionary complexes and arc geochemistry mark former convergent margins; and passive-margin and syn-rift sequences record past divergence. Increasingly, seismic tomography contributes directly: fast anomalies interpreted as subducted slabs constrain the location of palaeotrenches otherwise inaccessible from the surface record (Sigloch & Mihalynuk, 2013; van der Meer et al., 2018). The volume, fidelity and spatial coverage of all these constraints generally decrease with increasing age, so that deeper-time reconstructions rest on progressively sparser data and correspondingly stronger assumptions.

Reconstructions were first idealised as assemblages of rigid plates, with deformation confined to discrete boundaries. This is a first-order approximation, given that roughly 14 % of the present surface deforms diffusely (Kreemer et al., 2014; Hasterok et al., 2022). Within this idealisation, four classes of model can be distinguished by the processes they capture (Seton et al., 2023). Continental-

drift models track isolated crustal blocks without an enclosing network of plate boundaries. Plate-focused models add such a network through continuously closing plate topologies (Gurnis et al., 2012), so that boundaries evolve self-consistently and plate geometries are defined at every instant. Deforming-plate models further relax the rigidity assumption within defined zones (Gurnis et al., 2018; Müller et al., 2019), while tomotectonic models incorporate slab-derived palaeotrench constraints (Clennett et al., 2020). No single class is universally best; the appropriate choice depends on the research question.

Constructing a model in any of these classes means piecing together the constraints above and interpolating between them. The earliest reconstructions were drawn by hand, region by region, which made consistency between successive time slices difficult to enforce. Bullard et al. (1965) were the first to model tectonic motions rigorously with a computer, and dedicated software—PCME (Schettino, 1998), PaleoMac (Cogné, 2003) and GPlates (first public release 2003; Müller et al., 2018)—made the plate-focused approach practical on a global scale. Modern models built this way provide global coverage at 1 Myr resolution (e.g., Seton et al., 2012; Müller et al., 2016, 2019; Zahirovic et al., 2022).

However, these reconstructions are still limited by the completeness of the geologic record and the assumptions made when interpolating between known constraints. Quantifying the resulting uncertainty is difficult, but reconstructed positions are estimated to be uncertain by 500–1000 km over the last 100–200 Myr, with uncertainty growing into deeper time and varying with plate configuration (Engebretson et al., 1985; Scotese, 2004). They also face challenges due to the sheer complexity of the plate tectonic system through time, which involves tens of thousands of individual finite rotations between thousands of different plates, each made up of multiple hand-drawn polygonal chains over hundreds of time steps. This can result in broken plate boundaries (gaps or overlaps between plates), or incorrectly assigned margin types (e.g., a subduction zone assigned where two plates are diverging), or unrealistically high plate velocities. Though some automatic tools exist to check for internal consistency (e.g., automatically flagging abnormally high plate velocities, fixing cross-overs from one sequence of rotations to another, checking for gaps between plates), such programs cannot guarantee complete coverage and manual fixes are often required.

Mantle circulation models

Over geologic timescales the Earth's mantle convects in response to thermal and compositional density (buoyancy) contrasts. The extent to which this occurs in a *layered* or *whole-mantle* fashion has long been debated, but most modern interpretations favour predominantly whole-mantle convection. In this view, subducted lithosphere sinks from the surface to the core–mantle boundary, linking surface plate motions to flow at depth, while upwelling from the core–mantle boundary helps drive those same plate motions—together forming the dynamically coupled plate–mantle system.

Numerous finite element codes solve the governing fluid-dynamic equations to produce forward predictions of mantle flow from prescribed inputs such as plate kinematics and rheological and thermodynamic parameterisations; examples include CitComS (Moresi & Solomatov, 1995; Zhong et al., 2000; Moresi et al., 2007; Zhong et al., 2008; Bower et al., 2015), TERRA (Baumgardner, 1985; Bunge et al., 1997; Davies & Davies, 2009; Wolstencroft et al., 2009; Davies et al., 2013; Wolstencroft & Davies, 2017), ASPECT (Kronbichler et al., 2012; Heister et al., 2017; Gassmöller et al., 2018, 2020; Clevenger & Heister, 2021), and G-ADOPT (Davies et al., 2022; Ghelichkhan et al., 2024; Gibson et al., 2024). In this forward setting, evaluation is straightforward in principle—integrate the governing equations from chosen initial and boundary conditions and compare the output with

present-day observations—but calibration is not. Earth-like convection is sensitive to both physical parameterisation (e.g., viscosity profile, reference state, thermal expansivity) and numerical design (e.g., discretisation), so even modest changes can yield substantially different convective regimes. Numerical stability and accuracy are also hard to maintain over runtimes of hundreds of millions to billions of years, especially with complex, time-evolving boundary conditions such as plate reconstructions, which may contain kinematically impossible artefacts. Finally, high-resolution 3D spherical models are computationally expensive, requiring high-performance computing facilities.

Beyond forward modelling, MCMs can be cast as inverse problems: adjoint (variational) data assimilation efficiently computes the gradient of a misfit—for example between predicted present-day structure and seismic tomography—with respect to the initial conditions and mantle parameterisation, overcoming the forward model's reliance on an arbitrary initial condition, albeit at greater computational cost. The landmark early application in global 3D spherical modelling is the variational data-assimilation framework implemented in TERRA by Bunge et al. (2003); adjoint inversion has since been added to CitComS (Liu & Gurnis, 2008) and automated within G-ADOPT (Ghelichkhan et al., 2024). Such approaches have already addressed tectonic questions—testing plateau-subduction scenarios for the Laramide orogeny (Liu et al., 2010) and linking Andean–Amazon drainage evolution to dynamic topography (Shephard et al., 2010)—and are likely to become central to future G-ADOPT-based reconstruction studies. Because a good backward model depends on a good forward model, the forward models refined in this thesis will be critical to that adjoint-based future (see Discussion).

A parallel development concerns how the present-day mantle state estimate is constructed in the first place. Rather than comparing model output against seismic velocities directly, recent retrodiction studies convert tomography into the physical fields that drive flow—temperature and density—via thermodynamically self-consistent mineralogical models (e.g., Stixrude & Lithgow-Bertelloni, 2005, 2011, 2024), with an anelasticity correction for the non-linear mapping from shear-wave speed to temperature (e.g., Cammarano et al., 2003; Goes et al., 2004). Ghelichkhan et al. (2021) exemplify this, running eight compressible global retrodictions to 50 Ma that assimilate a plate-motion history as the surface velocity field while probing two tomographic inputs and four radial viscosity profiles. Retrodiction is distinct from—though often implemented via—the adjoint method: it denotes the recovery of past mantle states, achievable through backward advection (Steinberger & O'Connell, 1997), sequential or ensemble assimilation (Bocher et al., 2016), or adjoint optimisation (Ghelichkhan et al., 2024). Incorporating mineralogical models is what makes that state estimate—and therefore the retrodiction itself—physically self-consistent and testable against independent data.

How such trajectories should be tested motivates a second strand of recent work. Because past mantle structure is not directly observable, model trajectories are most usefully validated through their surface expression—principally dynamic topography (Hager et al., 1985)—which can be compared against a range of geological indicators such as river profiles, sediment budgets, hiatus maps, palaeo-sea-level markers and thermochronology. Crucially, this comparison need not rely on point-wise or ℓ^2 measures. Taiwo et al. (2023), for instance, note that gridpoint metrics suffer from the double-penalty problem—a prediction correct in amplitude and shape but slightly displaced is penalised twice—and instead borrow pattern-based metrics from meteorology and oceanography (the Taylor diagram and power ratio, with object-based verification) to assess mantle-flow trajectories, reframing validation in terms of pattern, amplitude and phase rather than node-by-node agreement.

Seismic tomography

Seismic tomography models—images of the mantle derived from perturbations from expected seismic wave travel times—have proved to be one our best methods of understanding present-day mantle structure. Seismic tomography exploits the fact that different seismic waves sense different parts of the Earth. Surface waves propagate horizontally through the crust and upper mantle, with a penetration depth that scales with period—short-period waves are confined to the crust, while long-period waves illuminate the deeper upper mantle (Dahlen et al., 2000; Ritsema et al., 2011)—making them the primary constraint on uppermost-mantle structure. Body waves, by contrast, traverse the deep interior and constrain the lower mantle, but propagate too steeply through the upper mantle to resolve it, and sample the lower mantle unevenly because earthquakes cluster at plate boundaries and most stations sit on land. The resulting sensitivity is therefore strongly depth- and region-dependent, a limitation that propagates directly into the resolution of any resulting model.

Converting these data into an image is an inverse problem: one seeks the three-dimensional velocity structure that best explains the observed travel times (or, more generally, the recorded waveforms). This problem is ill posed, in that infinitely many models fit the data to within their uncertainties, so inversions must be regularized—typically through damping toward a reference model or smoothing between adjacent model parameters—to converge on a single solution (Fichtner, 2010). Regularization is inherently subjective and not informed by the data themselves, and it can blur or displace features in the recovered image; this is one reason a sharp, well-defined structure in a geodynamic model may appear smeared or shifted once imaged tomographically. Methodological choices compound this effect. Older models such as *S40RTS* rely on ray-theoretical travel-time tomography, whereas more recent models such as *REVEAL* and *GLAD-M35* use full-waveform inversion, which simulates the complete seismic wavefield and exploits far more of the information in each seismogram at the cost of substantially greater computational expense (Cui et al., 2024; Thrastarson et al., 2024). Together with the many smaller choices made during model construction (e.g., parameterization, discretization, crustal corrections, the treatment of anisotropy and density), these differences mean that models can diverge by more than their individual uncertainty estimates would suggest (Fichtner et al., 2025).

Since the first global tomographic models were conceived (e.g., Woodhouse & Dziewonski, 1984; Romanowicz, 1991), numerous iterations have been made using ever more sophisticated methods of inverting the seismic data, paired with larger datasets of seismometers and earthquakes and exponentially growing computational power, to produce increasingly refined images of mantle structure, such as *S40RTS* (Ritsema et al., 2011), *GAP_P4* (Obayashi et al., 2013), *LLNL-G3D-JPS* (Simmons et al., 2015), *TX2019slab* (Lu et al., 2019), *REVEAL* (Thrastarson et al., 2024), and *GLAD-M35* (Cui et al., 2024), to name a few. Today, so many tomography models exist it is difficult to choose which ones one should use in any particular study, as there are too many to simultaneously present in a single published article. The free-to-use community tool SubMachine (Hosseini et al., 2018) allows users to quickly produce comparative vertical and cross-sections from a broad suite of modern, global (and some regional) tomography models.

Once a set of tomography models have been chosen for comparison, the question then becomes how to compare them to a mantle model (or each other). Because temperature and seismic speed are strongly related (Gutenberg, 1959, p. 76), a visual comparison between predicted temperature structure and imaged seismic structure is informative and powerful (e.g., whether a cold anomaly in the mantle model corresponds to a fast anomaly in tomography at the same location). However, the temperature–velocity relationship becomes increasingly nonlinear as depth increases due to

the anelastic response of mantle minerals(Karato, 1993), and this response is subject to significant uncertainty (Cammarano et al., 2003; Goes et al., 2004). By making a one-to-one comparison between predicted thermal structure and imaged seismic structure, such effects are implicitly neglected.

The use of seismic tomography as ground truth is also limited by the fact that only a few tomography models have published resolution operators (*S40RTS* and its predecessors and *LLNL-G3D-JPS*, at the time of writing). The resolution operator is an essential tool for comparing mantle models to tomography, as it allows one to image a geodynamic mantle model with the same limitations in spatial resolution as the tomography model itself (Zaroli et al., 2017). This tomographic filtering step is crucial, as mantle models typically have much higher spatial resolution than tomography models, and features that are sharp and well-defined in the mantle model may be blurred out or even disappear entirely when imaged with the limited resolution of tomography. Without this step, one risks over-interpreting differences between mantle models and tomography that may simply be artefacts of differing spatial resolution.

Beyond visual comparison, one common statistical method is to compute the ℓ^2-norm (otherwise known as the root-mean-square error or misfit) between two models over some volume of interest (e.g., Lin et al., 2022), which has the advantage of being easy to understand, and computationally inexpensive, and would typically be used for one-to-one comparisons between a geodynamic mantle model and a tomographic image of the mantle. Another approach is to use a *votemap*, wherein each voxel in a 3D grid is assigned a score based on how many tomography models agree on the presence of an anomaly at that location (e.g., Shephard et al., 2017). Such votemaps are useful for comparing multiple tomography models simultaneously to each other and identifying robust features that are common across many models, but are less useful for comparing a single mantle model to tomography, where tomography is treated as data against which to ground-truth the geodynamic prediction. A common shortfall between both these approaches is that neither are sensitive to the degree of spatial displacement between two features, only to the presence or absence of overlap at a location.

Key challenges in calibrating reconstructions with mantle circulation models

Taken together, tectonic reconstructions, mantle circulation models, and seismic tomography provide a powerful framework for interrogating the plate–mantle system through deep time, but their implementation and comparison is not straightforward. Reconstructions are uncertain and often non-unique, and small kinematic inconsistencies can propagate into strongly different mantle-flow predictions. At the same time, MCM predictions depend sensitively on physical parameterisation and numerical choices, and practical constraints often limit model resolution and ensemble size. Finally, tomography does not provide a direct picture of temperature: the temperature–velocity relationship is nonlinear and tomographic resolution is heterogeneous in space, so structures may reflect imaging limitations rather than true geodynamic features. Finally, misfit metrics based purely on pointwise overlap are not an ideal tool with which to quantify these predictions. In many cases, MCM predictions generated from different candidate reconstructions resemble one another more closely than they resemble tomography; if they have little or no pointwise overlap with a seismic model, then a pointwise misfit saturates and provides little discriminatory power for ranking competing tectonic scenarios.

2 Scope of thesis

This thesis aims to use forced MCMs to evaluate poorly constrained tectonic reconstructions in subducting regimes. Doing this robustly, however, rests on two prerequisites, which form the subject of the first two results chapters. Chapter 2 establishes the post-processing methodology that any meaningful comparison between a model and the mantle requires. Comparing modelled temperature directly with the tomographically imaged mantle is unsound, because the temperature–velocity relationship is nonlinear and because seismic tomography models do not image the mantle with spatially uniform resolution; I therefore present new workflows for converting predicted temperature to seismic velocity and for tomographically filtering the result, and show that neglecting these steps can substantively change the qualitative interpretation of slab morphology. Chapter 3 then establishes that the chosen model is fit for purpose in subducting regimes. In recent generations of G-ADOPT MCMs, slab morphology is not imposed at the surface but arises dynamically from the kinematics of the plate reconstruction used as the surface boundary condition; I assess the strengths and weaknesses of this approach by comparing its predicted slab morphology against tomography across a range of well-studied subduction systems, identifying the regimes in which it performs well (those dominated by rollback, especially arc settings) and those in which it does not (e.g. strong trench advance, or errors in the reconstruction itself). With a defensible post-processing methodology (Chapter 2) and a characterised, trustworthy model (Chapter 3) in hand, Chapter 4 applies these findings to a case study—the collision of the Ontong–Java plateau with the Melanesian arc subduction system—to present a new, robust line of independent evidence resolving the discrepancy in reported collision timing between the two most common tectonic interpretations in the literature. Two generations of G-ADOPT MCMs are used across these chapters: Chapters 3 and 4 use an earlier generation, while Chapter 2 uses the newest, in which the lower mantle viscosity profile has been revised and continental lithosphere implemented (Section 3); the computational expense of these models precluded re-running every analysis as the models evolved (see Discussion).

Chapter 2

This chapter explores two key challenges in comparing the thermal structure of the mantle predicted by MCMs to that imaged by seismic tomography, which are often overlooked in studies that use MCMs to distinguish between competing tectonic reconstructions. First, the relationship between temperature and seismic velocity is nonlinear due to anelastic effects on the seismic response of mantle minerals, but many previous studies have implicitly assumed a linear relation by comparing these quantities directly. Second, seismic tomography models do not image the mantle with uniform spatial resolution—depending on the region, limited numbers of sources and/or receivers can drastically reduce the local resolving power of the model.

I present new workflows for (i) converting predicted mantle temperature to seismic velocity perturbations, and (ii) tomographically filtering this converted seismic structure. Applying these workflows to output from the newest generation of G-ADOPT MCMs (Section 3), I show that this post-processing can substantively change the qualitative interpretation of slab morphology. For example, slab breaks in the temperature structure may become blurred out by tomographic filtering, resulting in continuous slab morphology, or filtering may introduce a slab break where none is present in the temperature structure. I also find that these workflows can change the inferred depth and sinking rate of slabs by tens of kilometres and up to $1.2\,\mathrm{mm\,yr^{-1}}$ in either direction—or considerably more where filtering merges separate anomalies—and can laterally displace slab anomalies by several hundred kilometres, offsets that exceed the accompanying depth changes. These results highlight

the importance of epistemologically consistent post-processing when using MCMs to ground-truth a tectonic reconstruction against seismic tomography.

Chapter 3

In this chapter, I explore the strengths and weaknesses of G-ADOPT MCMs in which slab geometry arises dynamically from the kinematics of the imposed tectonic reconstruction, instead of being imposed at the surface as derived from other data (e.g., dip angle as inferred from tomography). The model assessed here belongs to the generation preceding that used in Chapter 2 (Section 3). I compare the slab morphology it produces to seismic tomography across several well-studied subduction systems: Aegean, Brasilia, Aleutian, Caribbean, Izu–Bonin, Mariana, Sunda, and Tonga–Kermadec–Hikurangi (as named by van der Meer et al., 2018).

I find that, in regimes dominated by rollback, and especially in arc settings, G-ADOPT reproduces tomography relatively well, with close matches to dip angle, depth, and lateral location (although lateral extent is often underestimated as compared to tomography). In cases where the model prediction disagrees with tomography, two categories emerge. The first category is settings where there is significant trench advance in the mantle reference frame. In such cases, predicted slab polarity is consistently reversed compared to what would be expected, given the geological and tomographic evidence. However, this is unsurprising, given that dip angle is not imposed and there is no mineralogical difference between oceanic and continental lithosphere in these models beyond their temperature difference—a limitation since addressed by the implementation of continental lithosphere in the subsequent model generation (Section 3; see also Discussion). The second category is cases where there are errors in the tectonic reconstruction, for example kinematically implausible rollback speeds (leading to underproduction of slab material) or misprescribed margin types (e.g., convergence across a mid-ocean ridge leading to unwanted slab material).

Chapter 4

This chapter applies the findings of the previous two chapters to a case study: the collision of the Ontong–Java plateau (OJP) with the Melanesian arc subduction system (MSS). This event has been interpreted to occur at either ∼25 Ma (e.g., Hall, 2002; Schellart et al., 2006) or ∼12 Ma (e.g., Mann & Taira, 2004), each supported by different lines of geologic and geophysical evidence. Although Chapter 3 identifies subduction regimes in which G-ADOPT models struggle to achieve sensible slab geometries, the OJP–MSS collision occurs in a relatively simple, rollback-dominated, oceanic regime—a setting in which these models perform well, and one in which the absence of continental lithosphere from the model generation used (the same as in Chapter 3; Section 3) is not expected to affect the results. This event therefore provides an ideal test case for applying the methods developed in the previous chapters to discriminate between the two competing interpretations.

Here, I make small corrections to the existing reconstruction of Zahirovic et al. (2022, hereafter *Z22*), which I use as the reconstruction favouring the earlier collision timing. I then derive an alternative reconstruction which instead favours the later collision timing (*Z22M04*), making sure to maintain kinematic consistency (e.g., plate velocities) and geological plausibility with the broader southwest Pacific region. For each reconstruction, I run a tectonically forced MCM implemented in G-ADOPT, convert the present-day temperature field output to seismic velocity, and tomographically filter it, following the methodology introduced in Chapter 2.

I find that the early collision timing (*Z22*) is favoured, as it is the only reconstruction which is able to reproduce a slab material at the correct depth and lateral location under the OJP–MSS region. In order to overcome one of the main limitations of more traditional approaches to

statistically testing the fit between modelled and tomographically imaged slabs (namely, the inability to distinguish between fit quality in the total absence of overlap of slab material), I introduce the *Wasserstein metric*. Familiar from the field of optimal transport theory, the Wasserstein metric provides a measure of the work required to transform one distribution into another, and crucially, linearly increases with the displacement between two anomalies. Here, I apply it to quantify the difference between modelled and tomographically imaged slab distributions, finding that *Z22* has a significantly lower Wasserstein score (i.e., better fit) than the late collision reconstruction (*Z22M04*).

3 Data and methodology

This thesis integrates G-ADOPT MCMs with high-resolution tomography models and novel workflows for model comparison to address long-standing uncertainties in tectonic reconstructions. Detailed references and descriptions of these methods are available in each chapter, but a brief overview is provided here.

Tectonic reconstructions

The plate reconstruction *Z22* used as the kinematic boundary condition for the mantle model in Chapters 2–4 is that of Zahirovic et al. (2022), with minor modifications to fix kinematic consistency (i.e., modifying some topological networks to remove small gaps or overlaps between plates). Surface velocities were then extracted and fed into the MCM using pyGPlates (Mather et al., 2024), an open-source Python library for working plate tectonic reconstructions created in GPlates (Müller et al., 2018). The alternative reconstruction *Z22M04* (presented in Chapter 4) was created by modifying *Z22* in GPlates to delay the OJP–MSS collision to initiate at ∼12 Ma, which involved altering the rotations and topological networks of several plates in the southwest Pacific to maintain kinematic and geologic consistency with existing constraints from the broader region.

Mantle circulation models

The geodynamic mantle circulation models were implemented in G-ADOPT (Davies et al., 2022; Ghelichkhan et al., 2024; Gibson et al., 2024), an open source software library for simulating geodynamical processes. It builds on Firedrake (Rathgeber et al., 2016) to make the modelling geodynamical problems accessible to non-specialists in numerical methods, and has been extensively benchmarked and validated for global mantle flow (Davies et al., 2022). Chapter 2 uses the latest generation of G-ADOPT MCMs, in which the lower mantle viscosity profile has been revised and a special rheology for continental cratons is implemented (reconstructed through time using pyGPlates). Simulations used the G-ADOPT platform (commit `a04f14d`, branch `sghelichkhani/gtrack`) on Firedrake (`main` branch, NCI module `firedrake/main-20260312`, built 2026-03-12, commit `ef4c1bf`) with PETSc v3.24.5, run on Gadi@NCI in April 2026. Owing to the computational expense of these models, Chapters 3 and 4 use a slightly older generation of G-ADOPT MCMs without these continental craton rheologies and with the earlier lower mantle viscosity profile; given that the OJP–MSS collision occurs in an oceanic regime, and that the analyses in both chapters concern recently subducted slabs in the upper mantle and transition zone, this is not expected to have significantly affected the results (see Discussion).

MCM post-processing

Models of mantle mineral physics are crucial to converting mantle temperature to seismic velocity. While the effect of pressure varies predictably with depth, the effect of temperature is more complex,

as it depends on both elastic and anelastic contributions to the seismic response of the mantle mineral ensemble. S.G. used MMA-EoS (Chust et al., 2017) to implement the solution parameters of Stixrude and Lithgow-Bertelloni (2022) for a pyrolitic mantle, assuming that the largest seismic heterogeneities arise from a predominantly thermal origin (Ringwood, 1991; Schuberth et al., 2009; Davies et al., 2012). I then implemented the methodology of Cammarano et al. (2003) to correct for anelastic effects using their Q6 parameterisation. This workflow is available as the open-source library G-DRIFT (https://github.com/g-adopt/g-drift).

To tomographically filter the resulting seismic velocity structure, I developed and tested the original workflows for applying the resolution operators of *S40RTS* (Ritsema et al., 2011) and *LLNL-G3D-JPS* (Simmons et al., 2019), building on the codes published in the respective papers. These workflows, which I implemented and validated, became the basis for the libraries now published as the open-source libraries https://github.com/g-adopt/srts and https://github.com/g-adopt/llnltofi, after refactoring by S.G. to improve portability and user-friendliness. In addition, my fork of convection-to-seismic, available at https://github.com/tom-new/convection-to-seismic, provides a user-friendly workflow and guide for the complete pipeline—seismic velocity conversion, *S40RTS* filtering, and *LLNL-G3D-JPS* filtering—using the G-DRIFT, srts, and llnltofi libraries.

2 | Calibrating Plate Reconstructions with Global Mantle Convection Models

Tom New[1], Siavash Ghelichkhan[2], D. Rhodri Davies[2], Maria Seton[1], Ben Mather[2], and R. Dietmar Müller[1]

[1] *EarthByte Group, School of Geosciences, The University of Sydney, NSW, Australia*
[2] *Research School of Earth Sciences, Australian National University, ACT, Australia*
[3] *School of Geography, Earth and Atmospheric Sciences, The University of Melbourne, VIC, Australia*

Abstract

The coupled plate–mantle system governs Earth's surface evolution, geodynamics, and geochemistry. Coupled plate tectonic–mantle convection models are commonly evaluated by comparing model temperatures to seismic tomography, but this often assumes a direct, linear temperature–velocity mapping and neglects the spatially variable resolution of tomography.

We present a workflow that (i) predicts seismic velocity from model temperature using a mineral–physics relationship which accounts for anelastic (nonlinear) effects, and (ii) applies tomographic resolution operators to the synthetic velocities to match the spatial sensitivity of the *LLNL-G3D-JPS* and *S40RTS* models. Implemented in the open-source libraries G-DRIFT, srts, and llnltofi, this approach shows that upper- to mid-mantle velocity perturbations are strongly damped relative to raw temperature fields, affecting inferences about slab history and behaviour (e.g., stagnation). Tomographic filtering shifts the apparent basal depth of slab-like anomalies by tens of kilometres in either direction, changing inferred whole-mantle sinking rates by up to $1.2\,\mathrm{mm\,yr^{-1}}$ (and by $4.6\,\mathrm{mm\,yr^{-1}}$ where filtering artificially connects separate anomalies), and can displace anomalies laterally by up to 639 km. Crucially, the heterogeneous resolution operators can also alter qualitative interpretations of slab morphology: across our tests, conversion to seismic velocity reduces misfit to tomography by up to 51 %, while filtering changes misfit only modestly yet can artificially connect discontinuous structures—masking slab breaks that are present in the predicted mantle structure.

These results underscore the need for physically consistent post-processing when validating tectonic reconstructions against seismic observations, and they motivate publishing future tomography models alongside corresponding resolution operators.

Plain Language Summary

The movement of Earth's tectonic plates is driven by slow but powerful currents in the mantle, shaping mountains, oceans, and climate over millions of years. To study this connection, scientists

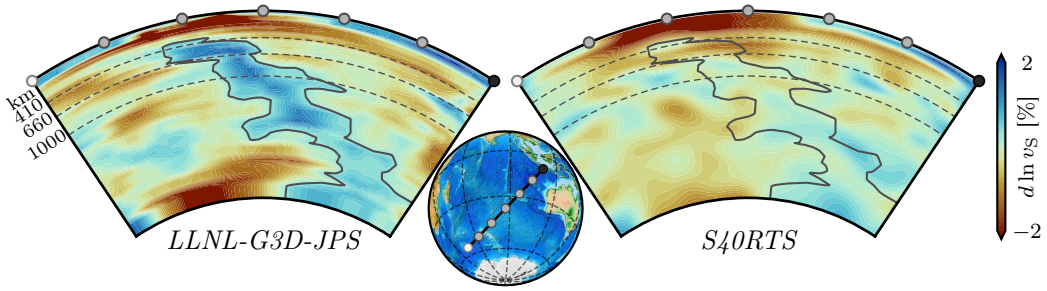

Figure 1

Comparison of resolving power between LLNL-G3D-JPS (Simmons et al., 2015) and S40RTS (Ritsema et al., 2011), as seen in slab structures under the southern Indian Ocean. A continuous slab structure is visible from throughout the mantle in LLNL-G3D-JPS, while S40RTS cannot resolve a continuous structure.

build computer models of mantle temperature and compare them with seismic tomography—images of wave speeds created from earthquakes. But tomography blurs features differently at different geographic locations and at different depths, making direct comparisons misleading. We introduce a method that converts model temperatures into seismic wave speeds and applies the same lens as tomography. This reveals slabs can appear tens of kilometres shallower or deeper than they really are, and shifted sideways by several hundred kilometres. Recognising these effects is essential for building reliable reconstructions of Earth's past and testing ideas about how plate tectonics work.

1 Introduction

The dynamics of the plate–mantle system have played a crucial role in shaping Earth's surface and influenced its geodynamic and geochemical evolution over geologic time. Understanding this system is essential to explaining the drivers of plate motions (e.g., McKenzie, 1969; Gurnis, 1988; Bercovici, 2003), the assembly and dispersal of supercontinents (e.g., Müller et al., 2022a), and the conditions that sustain the geodynamo (e.g., Biggin et al., 2012). Changes in mantle convection and plate interactions have also left strong imprints on sea level (e.g., Miller et al., 2005; Cao et al., 2019; Young et al., 2022), palaeoclimate (e.g., Raymo & Ruddiman, 1992; Flament et al., 2013; Scotese et al., 2021), and the distribution of mineral and energy resources (e.g., Groves & Bierlein, 2007; Cawood & Hawkesworth, 2014; Müller et al., 2022b).

One approach to studying this coupled system is to assimilate information from plate reconstructions into mantle convection models—through so-called mantle circulation models (MCMs)—and then compare synthetic mantle structure to seismic tomography. This strategy has been used to calibrate tectonic reconstructions (e.g., Nerlich et al., 2016), estimate slab sinking rates and mantle viscosity (e.g., Peng & Liu, 2022), and place constraints on mantle mineralogy (e.g., Schuberth et al., 2009; Styles et al., 2011; Davies et al., 2012). A common assumption has been a simple linear relationship between modelled temperature and seismic velocity (e.g., Liu & Stegman, 2011; Flament et al., 2015; Seton et al., 2015; Zahirovic et al., 2016; Harrington et al., 2017; Hu et al., 2018a, 2018b; Peng et al., 2021a, 2021b; Li et al., 2023), despite well-known nonlinearities and uncertainties in how seismic images map to physical structure (e.g., Cammarano et al., 2003; Goes et al., 2004; Cobden et al., 2008). A smaller number of studies have gone further by incorporating mineral physics-based conversions that account for these nonlinearities (e.g., Styles et al., 2011; Davies et al., 2012; Nerlich et al., 2016; Lin et al., 2022; Su et al., 2023), but such approaches

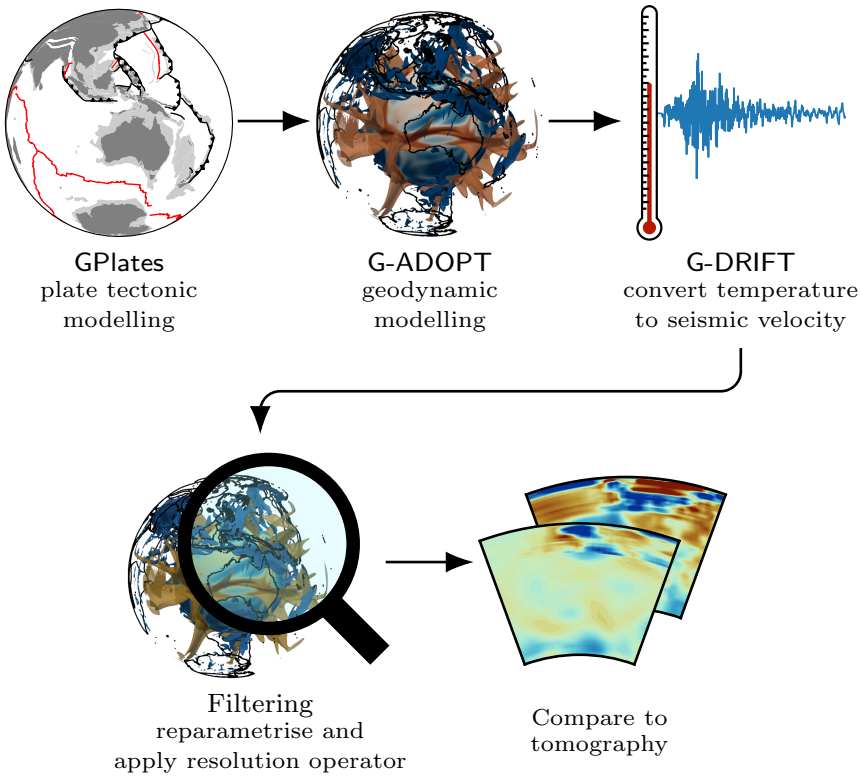

Figure 2

The workflow for converting synthetic models of mantle temperature to seismic velocity and applying tomographic filtering.

remain in the minority.

Two developments are required to make comparisons more robust. The first is to convert temperature and pressure variations in coupled models to seismic velocity using mineral physics. Recent advances in mantle thermodynamics and computational tools make this increasingly tractable (e.g., Stixrude & Lithgow-Bertelloni, 2005, 2011; Chust et al., 2017; Stixrude & Lithgow-Bertelloni, 2022, 2024). The second is to account for the variable spatial resolution of tomography, which blurs features differently with both depth and geographic location. This mismatch complicates comparisons with mantle models, which typically have smoothly varying mesh resolutions, and can alter interpretations of slab continuity and geometry (Mégnin et al., 1997; Zaroli et al., 2017). Resolution operators provide a way to view mantle models through the same lens as tomography—explicitly showing how heterogeneities are smeared, shifted, and modified in amplitude—though few tomographic models have been published with them, reflecting the considerable conceptual and computational effort required for their calculation. As a result, for many years the only widely-used options were *S20RTS* (Ritsema et al., 1999) and its successor *S40RTS* (Ritsema et al., 2011), a pair of shear (S-wave) velocity models. Together, they provided the sole means of applying tomographic filtering to geodynamic models (Ritsema et al., 2007).

Of these, *S40RTS* became the standard reference: despite its relatively coarse nominal resolution of ∼1100 km (Trampert et al., 2013) (spherical harmonics to degree 40 with vertical splines), it was widely adopted for linking geodynamical models and tomography. Studies have used it to evaluate the morphology of subducted slabs, to estimate slab sinking rates and mantle viscosity, and to test hypotheses about large-scale lower-mantle structure such as the presence of post-perovskite (e.g., Schuberth et al., 2009; Davies et al., 2012; Nerlich et al., 2016; Koelemeijer et al., 2018).

Its widespread use established a foundation for comparing mantle flow simulations with seismic structure, and it continues to provide a valuable point of comparison even as higher-resolution models emerge.

The more recent *LLNL-G3D-JPS* model (Simmons et al., 2015, 2019) builds on this foundation by offering substantially finer effective resolution (∼400 km in the upper-mantle, ∼800 km in the lower-mantle), which improves the ability to resolve slab-like features in MCMs when tomographic filtering is applied (Figure 1). Crucially, *LLNL-G3D-JPS* provides a resolution operator for compressional (P-wave) velocity, enabling us to directly filter synthetic models into the space constrained by P-wave data—which reflect different sensitivities to temperature, composition, and anelastic effects. In the last few years, a handful of studies have employed this filtering to interrogate geodynamic models (e.g., Su et al., 2023). However, among studies using MCMs to calibrate tectonic reconstructions, those employing tomographic filtering remain in the vast minority (e.g., Lin et al., 2022). Together, *S40RTS* and *LLNL-G3D-JPS* therefore provide complementary tests: *S40RTS*, which is specific to S-wave velocity, offers a transparent, widely used baseline for filtering, while *LLNL-G3D-JPS* provides a finer-resolution benchmark tied to modern P-wave observations.

Here, we apply the *S40RTS* operator alongside the *LLNL-G3D-JPS* P-wave operator to assess their effects on slab characteristics, including morphology, continuity, and depth. Our workflow converts synthetic mantle temperature fields to P- and S-wave velocities, corrects for anelasticity, linearises the velocity, and applies the appropriate resolution operators. We then quantify how these steps influence comparisons between mantle convection models and seismic observations, with particular emphasis on calibrating tectonic reconstructions and estimating slab sinking rates. This approach underscores the value of physically consistent post-processing in geodynamic studies and provides a framework for future research.

2 Methodology

2.1 Coupled plate tectonic–mantle circulation model

Various finite element modelling codes have been used to develop mantle circulation models, for example CitComS (Zhong et al., 2000; Bower et al., 2015), TERRA (Bunge & Davies, 2001; Davies et al., 2013), ASPECT (Heister et al., 2017) and—more recently—G-ADOPT (Davies et al., 2022; Ghelichkhan et al., 2024). To predict mantle structure implied by plate reconstructions, we couple plate kinematic modelling in pyGPlates with finite-element simulations in G-ADOPT. pyGPlates (Mather et al., 2024) is an open-source Python library for analysing and visualising reconstructions generated with GPlates (Müller et al., 2018). Here, we use the 410 Myr reconstruction of Zahirovic et al. (2022), which is largely based on the reconstruction of Müller et al. (2019). G-ADOPT (Davies et al., 2022; Ghelichkhan et al., 2024) builds on Firedrake, an automated finite-element system (Rathgeber et al., 2016), and has been extensively validated and benchmarked for global mantle flow (Davies et al., 2022).

We solve the Stokes and energy equations under the truncated anelastic liquid approximation in a spherical shell bounded by the core–mantle boundary (CMB) and Earth's surface. Radial reference properties (Figure 3) are derived using the open-source phase-equilibrium solver MMA-EoS (Chust et al., 2017), which minimises Gibbs free energy to determine stable mineral assemblages and thermodynamic parameters for a primitive pyrolitic mantle composition (CFMAS formulation of Workman & Hart, 2005). The adiabat is integrated downward from a surface temperature of 1600 K following $\frac{\partial T}{\partial z} = \frac{\alpha g}{C_p} T$, with the thermal expansion coefficient α, gravity g, and heat capacity C_p extracted from pre-computed MMA-EoS tables (Table A1). Depths are converted to

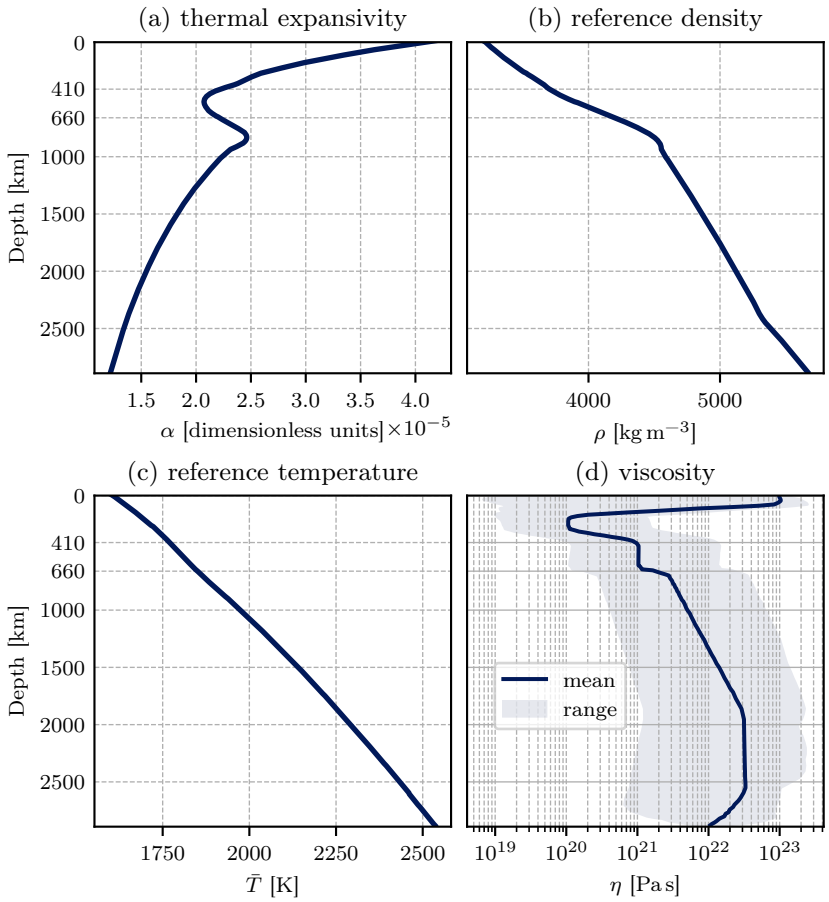

Figure 3

Key material properties of mantle circulation model: (a) thermal expansivity α; (b) reference density $\bar{\rho}$; (c) reference temperature $\bar{T}$; and (d) viscosity η, showing mean (navy line) and range (shaded).

pressure assuming hydrostatic equilibrium, using the PREM density profile, allowing thermodynamic properties (ρ, α, C_v, C_p) to be sampled consistently with mantle conditions.

Viscosity is depth- and temperature-dependent, given by

$$\eta(T, r) = \eta_0(r) \exp[E\,(0.5 - T)]\,, \tag{1}$$

where T is the non-dimensionalised mantle temperature, $\eta_0(r)$ a radially dependent prefactor, and E the non-dimensional activation energy (set to 10^5 in the upper-mantle and 10^4 in the lower-mantle) controlling thermal viscosity contrast. The resulting profile is compatible with independent geodetic and plate torque-balance constraints (e.g., Paulson & Richards, 2009; Iaffaldano & Lambeck, 2014; Stotz et al., 2018).

We employ a cubed sphere mesh with a nominal spacing of 70 km at the surface and 40 km at the CMB, with radial refinement toward both boundaries. For the Stokes system, we use Q2Q1 elements for velocity and pressure, respectively, with the linear system solved using a conjugate-gradient method, preconditioned with a geometric algebraic multigrid. Temperature is discretised with a second-order discontinuous Galerkin scheme, integrated in time using an implicit mid-point rule, and solved with the generalized minimal residual method and successive over-relaxation preconditioning. Higher-order polynomial discretisations for velocity and temperature ensure adequate resolution of

flow and thermal fields.

The model is first spun-up with free-slip, isothermal boundary conditions at the surface (300 K) and CMB (4000 K) until a quasi-steady state is achieved after approximately 500 Myr. Plate velocities from pyGPlates are then assimilated from 410 Ma to the present day. This coupled framework provides the synthetic mantle temperature fields that we subsequently convert to seismic velocities for comparison with tomography.

2.2 Seismic velocity perturbation

Mantle mineral physics models (Stixrude & Lithgow-Bertelloni, 2005; Piazzoni et al., 2007; Stixrude & Lithgow-Bertelloni, 2011, 2024) provide the link between the temperature and pressure fields predicted by mantle circulation models and the seismic heterogeneities imaged by tomography. Pressure effects vary predictably with depth (Cammarano et al., 2005), but the influence of temperature is more complex, involving both elastic and anelastic contributions. Using MMA-EoS (Chust et al., 2017), we implemented the solution parameters of Stixrude and Lithgow-Bertelloni (2024) to generate look-up tables for a homogenous pyrolitic mantle, under the assumption that the largest seismic anomalies have a predominantly thermal origin (Ringwood, 1991; Schuberth et al., 2009; Davies et al., 2012). While chemical heterogeneity undoubtedly contributes to seismic structure (e.g., Wang et al., 2021; Goes et al., 2022; Zhou et al., 2022), this thermal assumption is consistent with our coupled model, which only includes thermal anomalies.

To ensure robust application in geodynamic simulations, we regularised the thermodynamic tables by filtering the temperature–velocity relationship. Sharp, non-physical variations can produce abrupt jumps in seismic velocity that are not consistent with underlying mantle behaviour. We therefore constrained the gradient to the interval $[-1.5, 0.0]$ for S-waves and $[-\infty, 0.0]$ for P-waves, removing excessively steep slopes or gradients. Out-of-range values were replaced via inverse-distance weighted interpolation from neighbouring in-range points. The filtered gradient field was then reintegrated to reconstruct velocity tables anchored to the reference adiabat at each depth. This procedure yields a smooth, monotonic relationship between temperature and seismic velocity which is suitable for geodynamic applications.

We also account for viscoelastic relaxation, which modifies seismic wave speeds at mantle conditions. Following Cammarano et al. (2003), the anelastic response is expressed as

$$Q_{\mathrm{S}}(\hat{r}, z) = B\omega^{a} \exp\left(\frac{agT_{\mathrm{m}}(z)}{T(\hat{r})}\right), \tag{2}$$

where B is a normalisation factor, ω the seismic frequency, a the frequency dependence of attenuation, g a dimensionless scaling factor that reduces the pressure dependence to a dependence on temperature $T(\hat{r})$ at a given location in the model, and $T_{\mathrm{m}}(z)$ the solidus at depth z. Given the uncertainty in attenuation, we adopt the Q6 parameterisation of Cammarano et al. (2003), which represents a moderate anelastic response (Table 1). This correction modestly amplifies seismic velocity perturbations, with a depth- and temperature- effect that is nonlinear (Figure 4).

This workflow—conversion of temperature fields to seismic velocity, gradient regularisation, and anelastic correction—has been encapsulated in G-DRIFT, a companion library to G-ADOPT, available at https://github.com/g-adopt/g-drift.

2.3 Resolution operator

To evaluate how tomographic resolution shapes the appearance of synthetic mantle structure, we apply resolution operators from two widely used global models: *S40RTS* for S-waves and

Table 1

Values for the anelasticity model parameters used in this study (Q6 from Cammarano et al., 2003).

Parameter	Upper-mantle	Lower-mantle
B	0.077	4.95
ω	1	
a	0.2	
g	30	15

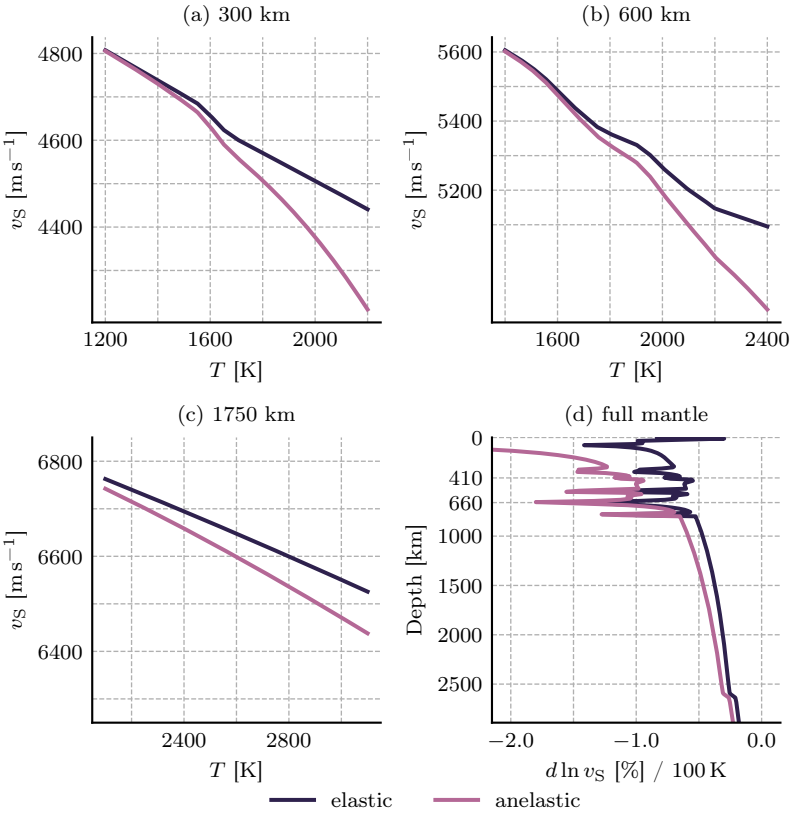

Figure 4

Relationship between temperature T and elastic (navy line) and anelastic (pink line) S-wave speed v_S at depths of (a) 300*, (b)* 600*, and (c)* 1750 km*, with temperature ranges in each spanning those found in our MCM at that depth. Panel (d) shows the effect of correcting for anelasticity throughout the whole mantle, given a change in temperature of* 100 K*, relative to the reference temperature shown in Figure 3c.*

LLNL-G3D-JPS for P-waves. These models provide complementary perspectives, since S- and P-waves differ in their sensitivities to temperature, composition, and anelastic effects.

S40RTS (Ritsema et al., 2011) is a global S-wave velocity model parameterised in spherical harmonics to degree 40 with vertical splines. For over a decade, it was the standard reference for tomographic filtering, largely because its resolution operator was made available (Ritsema et al., 2007). Despite its relatively coarse nominal resolution of ∼1100 km (Trampert et al., 2013), *S40RTS* has been widely used to compare mantle circulation models with tomography, particularly in studies of slab morphology, sinking rates, and deep mantle structure. Its longevity makes it a valuable baseline against which to test newer approaches.

LLNL-G3D-JPS (Simmons et al., 2015) is a more recent global joint P- and S-wave velocity

model built using a multi-resolution regional parameterisation. It achieves substantially finer effective resolution than *S40RTS*: ∼400 km in the upper-mantle and ∼800 km in the lower-mantle (Simmons et al., 2019). Crucially, it is one of the very few P-wave models published with a resolution operator, making it an ideal benchmark for filtering synthetic mantle fields into the space constrained by P-wave data.

Before either resolution operator $\mathcal{R}$ can be applied to a synthetic mantle model m, the model must first be reparameterised into the same basis as the tomography model, which we denote $\tilde{m}$. For *LLNL-G3D-JPS*, this involves downsampling onto the model's native tessellated triangular mesh (about one million nodes). For *S40RTS*, our synthetic seismic velocity structure is expanded into spherical harmonics up to degree 40. In both cases, the filtered model $\tilde{m}'$ is obtained through matrix–vector multiplication:

$$\tilde{m}' = \mathcal{R}\tilde{m}. \tag{3}$$

Programmatically, applying $\mathcal{R}$ is non-trivial. For *LLNL-G3D-JPS*, the operator contains on the order of 10^{12} elements; the llnltofi library (https://github.com/g-adopt/llnltofi), which updates the implementation of Simmons et al. (2019) to Python 3, exploits sparsity and parallelism to make the calculation tractable. For *S40RTS*, a similar library, srts (https://github.com/g-adopt/srts), refactors the originally distributed Fortran code to Python 3. By applying both operators we are able to examine how P- and S-wave resolution differently filter synthetic mantle anomalies, providing complementary insights into slab geometry and dynamics. It is important to note that in principle this stage of post-processing is easy to replace with the resolution operator for any other seismic tomography model.

2.4 Comparison with seismic tomography

We assess the impact of post-processing using two complementary approaches that are common in the literature. First, we present radial cross-sections (basemaps) at multiple depths, along with vertical cross-sections through the Aleutian, Java, Mariana, Neo-Tethys, and Tonga–Kermadec subduction systems. These regions were chosen because of their relatively simple subduction histories, which allows us to more clearly isolate the effects of each post-processing step on the qualitative character of slab-like anomalies, as well as for their wide geographic separation.

Second, we compute the ℓ^2-norm misfit between each of the processed models and the target tomography. For S-wave comparisons we use *S40RTS*, while for P-wave comparisons we use *LLNL-G3D-JPS*. Because raw temperature perturbation differ in magnitude from seismic velocity perturbations, all fields are first normalised such that perturbation strengths lie within $[-1, 1]$. This scaling removes global amplification or damping and focuses the comparison on relative spatial patterns.

The ℓ^2-norm provides a convenient summary metric, but it has limitations as a measure of spatial correlation. Once two anomalies no longer overlap the norm saturates and cannot distinguish between larger separation distances. In other words, it is sensitive to the presence or absence of overlap but less so to the degree of misalignment. For this reason, we interpret the ℓ^2 results alongside the visual cross-sections, which remain essential for assessing the morphology, continuity, and depth extent of slab-like features.

3 Results

3.1 Global effects

To characterise the global behaviour of our mantle circulation model, we reduce the full 3D temperature field to a one-dimensional (1D) description in which lateral variations are aggregated and only the depth dependence is retained. In other words, at each depth we consider the distribution of values across all horizontal positions, so that quantities such as the layer mean refer to the horizontal average at that depth. This 1D framing lets us summarise the radial structure of the flow without reference to any particular location. We present this as histograms showing how temperature, deviation from the layer mean, and percentage deviation change with depth (Figure 5). Figure 5b, the deviation from the layer mean, shows that our model reproduces thermal signatures consistent with the expected behaviour of both slabs and plumes. Slabs are naturally cooler than the surrounding mantle and appear as negative deviations; as they sink their absolute temperature rises no faster than temperature naturally increases with depth, so they retain their cool anomaly and warm only marginally relative to the layer mean. Plumes appear as positive deviations that diminish more rapidly as they rise: they cool faster than the 1D profile, so their temperature converges towards the layer mean. Together these features confirm that the model preserves the distinct thermal character of downwellings and upwellings throughout the mantle.

To assess the impact of the post-processing steps, we plot histograms of S- and P-wave perturbation ($d\ln v_S$ and $d\ln v_P$) and how these distributions change due to reparametrisation and filtering (Figures 6 and 7). The most significant change when temperature is converted to seismic velocity is that the magnitude of perturbation is reduced by about an order of magnitude at all depths (Figures 5c, 6a and 7a). However, this reduction in perturbation strength does not occur uniformly, with less damping in the upper-mantle and TZ as compared to the lower-mantle. Additionally, the conversion to seismic speed introduces an increase in perturbation strength in the TZ which is not present in the temperature distribution.

The spherical harmonic reparametrisation for *S40RTS* leads to a loss in detail at both global and regional scales. Extreme values of $d\ln v_S$ are damped by a factor of $\sim$2 in the TZ and lower mantle, while the bump in perturbation strength in the TZ is flattened for fast (cold) anomalies but not for slow (hot) anomalies (Figure 6b). Tomographic filtering with *S40RTS* (Figure 6c) further narrows the distribution of $d\ln v_S$, particularly for anomalies in the upper-mantle and TZ. The bump in perturbation strength in the TZ in slow anomalies is also removed.

Reparametrisation to the *LLNL-G3D-JPS* native mesh also changes the global character of the model, again with the most notable effects being damping of extreme values across all depths, and a change to the perturbation bump in the TZ. Here, the gradual decrease in $d\ln v_P$ across the bottom of the TZ becomes a step-function at 660 km, for both fast and slow anomalies (Figure 7b). Filtering with *LLNL-G3D-JPS* (Figure 7c) further narrows the distribution of $d\ln v_P$, and at this stage a step-reduction in perturbation strength is also introduced at the top of the TZ.

To further investigate the effect of post-processing on P- and S-wave velocity and compare our results to previous studies, we computed the root-mean-square (RMS) of perturbation strength of wave velocity as a function of depth (Figure 8). As expected, linearisation eliminates abrupt jumps in seismic velocity caused by phase boundaries, but does not affect seismic velocity elsewhere, while the anelasticity correction increases the strength of perturbation by 0.4–0.5 % in the lithosphere and uppermost-mantle and 0.1–0.2 % in the mid- to lower-mantle. Reparametrisation decreases the perturbation strength by 0.1–0.2 % in the mid- to lower-mantle and reduces detail in the profiles of the TZ and lowermost mantle, similar to the effect found by Simmons et al. (2019). Filtering of the

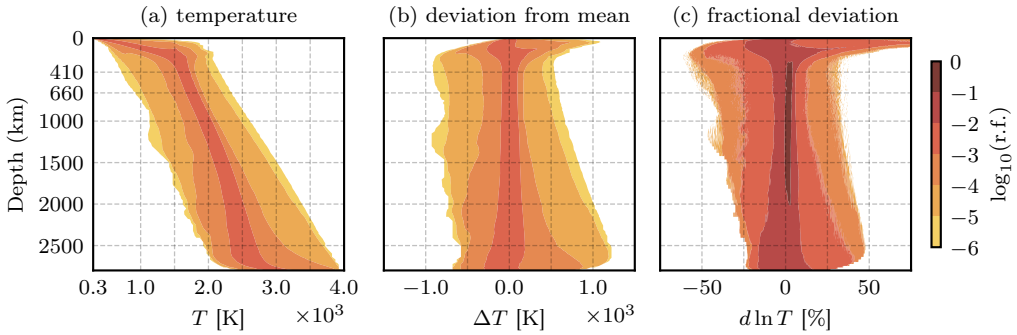

Figure 5

The distribution of temperature in our MCM as depth increases. Contours are the relative frequency (r.f.) of grid points with a particular deviation from the mean value at that depth, with darker colours indicating more points. Subfigures show (a) temperature (T); (b) temperature difference from layer mean (ΔT); and (c) percentage temperature perturbation from layer mean ($d \ln T$).

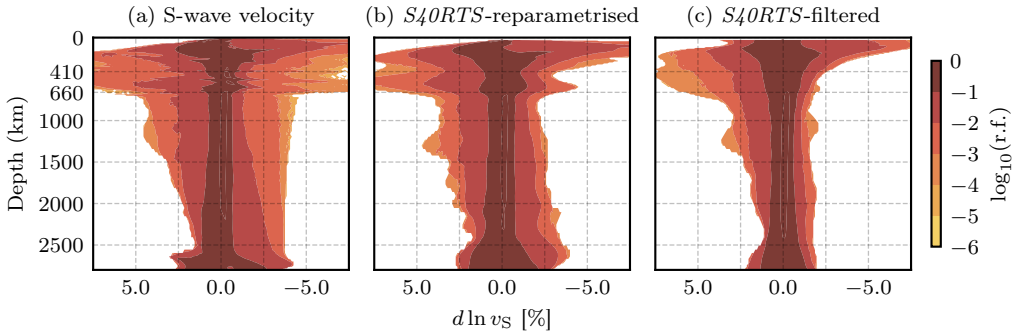

Figure 6

The distribution of S-wave velocity perturbation from layer mean ($d \ln v_S$) as depth increases. Contours are the relative frequency (r.f.) of grid points with a particular deviation from the mean value at that depth, with darker colours indicating more points. Subfigures show (a) $d \ln v_S$ in our MCM's native mesh; (b) spherical harmonic reparametrisation up to degree 40; and (c) filtering by S40RTS.

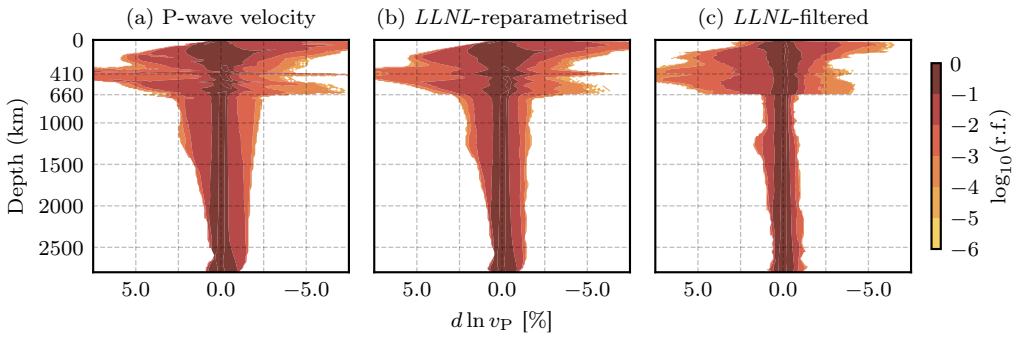

Figure 7

The distribution of P-wave velocity perturbation from layer mean ($d \ln v_P$) as depth increases. Contours are the relative frequency (r.f.) of grid points with a particular deviation from the mean value at that depth, with darker colours indicating more points. Subfigures show (a) $d \ln v_P$ in our MCM's native mesh; (b) reparametrisation to the LLNL-G3D-JPS native mesh; and (c) filtering by LLNL-G3D-JPS.

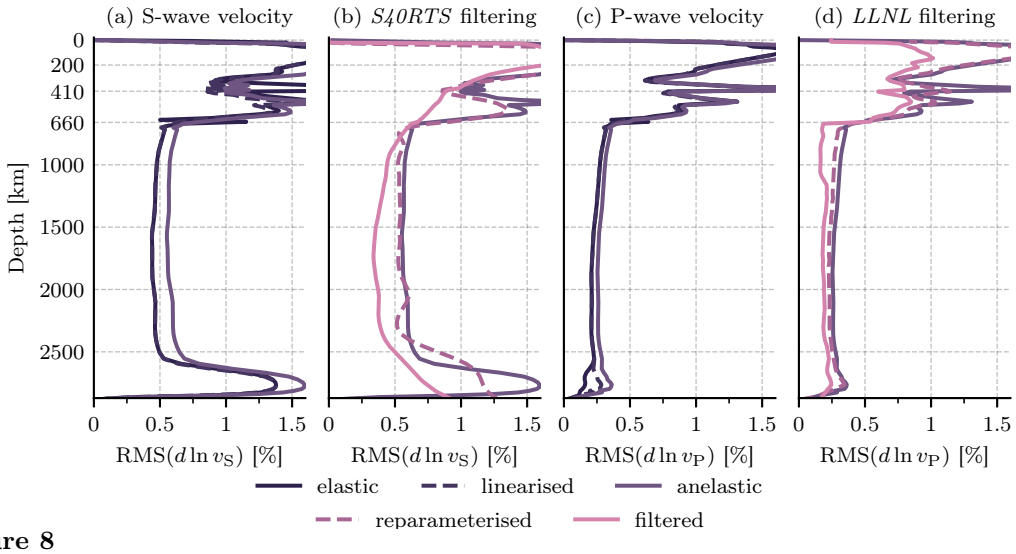

Figure 8

Effect of each post-processing stage on the root-mean-square (RMS) of S-wave velocity perturbation strength by depth. (a) G-DRIFT conversion to S-wave velocity, linearisation, and anelasticity correction; (b) S-wave velocities reparameterised for spherical harmonic degree 40; (c) S-wave velocities filtered by S40RTS; and (d) P-wave velocities.

model by applying the resolution operator significantly changes both the strength of perturbation and the shape of the distribution. There is a large reduction in perturbation strength of 1.0–1.5 % in the lithosphere and uppermost mantle, and sharp drops of 0.4–0.5 % at the 410 km and 660 km discontinuities, which are not present in the reparameterised seismic velocity perturbation. From the mid-mantle to the CMB, filtering reduces perturbation strength by 0.1–0.3 %.

3.2 Horizontal and vertical cross-sections

To demonstrate the effect of post-processing on the shape of particular anomalies that one may identify with features observed in seismic tomography models, we show how horizontal (Figures 9–11) and vertical (Figures 12–14 and 16) cross-sections change after each step in our workflow. For the vertical cross-sections, we chose slices through the Aleutian, Java, Mariana, Neo-Tethys, and Tonga–Kermadec subduction systems (following those chosen by van der Meer et al., 2018), as these regions have relatively straightforward tectonic histories, allowing us to better isolate the effect of the post-processing on physical interpretations that one may make from a coupled model.

In the upper mantle and TZ, converting the temperature to seismic velocity does not significantly change the visible intensity of perturbation when the colour map is normalised to cover most of the range of perturbation strength (Figures 9a and 9b, 150–600 km), while correcting for anelastic effects noticeably increases perturbation strength (Figure 9c, 150–600 km). In the lower mantle, perturbation strength is dampened after conversion to seismic velocity, relative to the strength of the most prominent anomalies at shallower depths (Figures 9a and 9b, 1000–2750 km), while correcting for anelasticity in the lower mantle has almost no effect on perturbation strength (Figure 9c, 1000–2750 km), consistent with the temperature–velocity curves shown in Figure 4.

In horizontal cross-section, we see that reparametrisation for *S40RTS* causes many fine details become blurry. For instance, the deep slab under South America at 1000 km depth has discernable structure in Figure 10a becomes a featureless blur in Figure 10b. On the other hand, there is much less loss in fidelity when considering reparametrisation for *LLNL-G3D-JPS*, even in the lower

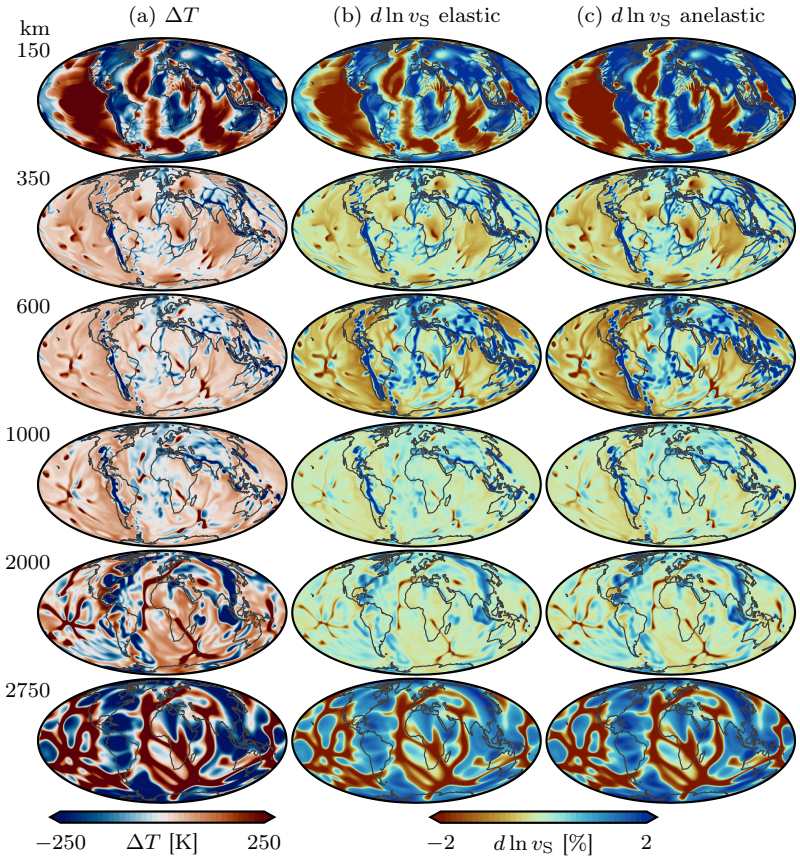

Figure 9

Horizontal cross-sections at various depths of: (a) temperature perturbation (ΔT) from layer mean in the G-ADOPT synthetic mantle model; (b) model is converted to S-wave velocity percentage perturbation ($d\ln v_S$); (c) S-wave velocity is linearised to remove unphysical jumps; and (d) S-wave velocity is corrected to account for anelasticity.

mantle where the mesh resolution is halved compared to the upper mantle and TZ. Consider again the structure under South America, the shape of which is preserved between Figures 11a and 11b with only slight blurring.

While the reparametrisation step does not change the qualitative interpretation of either horizontal or vertical cross-sections, the effect of applying the resolution operator is significant. At all depths in horizontal cross-sections—but especially in the uppermost mantle—the size of most anomalies (fast and slow) is reduced (Figure 11). In the vertical cross-section through the Aleutian arc (Figure 12), the perturbation strength of the high-velocity anomaly is significantly reduced by up to ∼0.6 % between the 410 and 660 km discontinuities.

Tomographic filtering can also meaningfully change the qualitative interpretation in vertical cross-section. In the Neo-Tethys cross-section, the slab-like anomaly (in the centre of the cross-section between the uppermost mantle and TZ) is a continuous body of material both in the raw temperature field and after conversion to seismic velocity (Figures 15a and 15b). However, after tomographic filtering with *S40RTS* the anomaly becomes discontinuous (Figure 15d), while filtering with *LLNL-G3D-JPS* retains a continuous slab (Figure 15h), however in both tomography models, the slab is continuous (Figures 15e and 15i). On the other hand, in the Aleutian cross-section, the opposite occurs. An initially discontinuous body of slab-like material (Figure 12a) becomes continuous after the model has been fully post-processed with both *S40RTS* and *LLNL-G3D-JPS* filtering (Figures 12d and 12h). In this case, the match to tomography is improved, since both

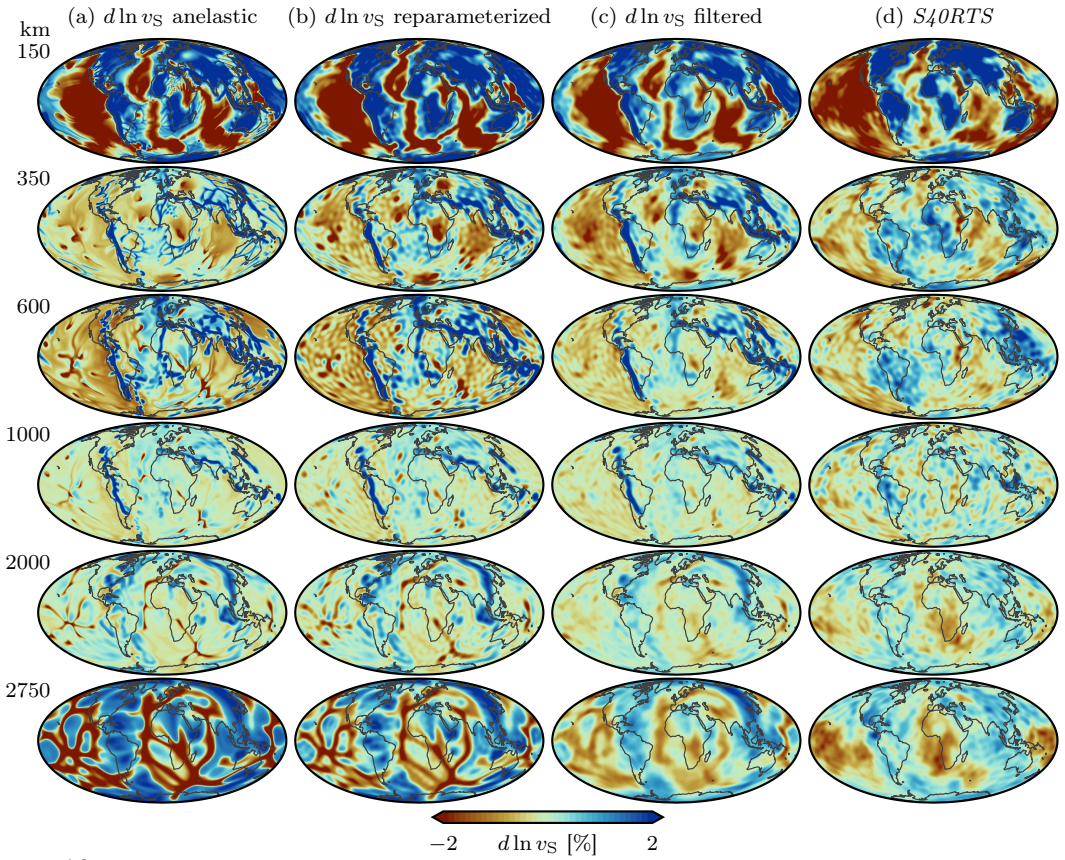

Figure 10

Horizontal cross-sections at increasing depths of: (a) elastic and anelastic S-wave velocity; (b) reparameterised to spherical harmonic degree 40; (c) tomographically filtered by S40RTS; and (d) the S40RTS tomography model.

tomographic models image a continuous slab (Figures 12e and 12i).

Meanwhile, the quantitative misfit (ℓ^2-norm) shows the largest change at the temperature to velocity conversion stage of post-processing with reductions in misfit relative to tomography of up to 35 % and 51 % for *S40RTS* and *LLNL-G3D-JPS*, respectively (Figures 12–14 and 16). Reparametrisation and filtering generally have a much more modest effect on misfit, with changes of only 1–2 % in either direction (though typically increasing misfit).

The combined effects of converting temperature to seismic velocity and subsequently applying the resolution operator are shown in Figures 17–21, where we plot equivalent contours in temperature and seismic velocity perturbation, chosen to represent the base of the subducting slab, on top of tomography. To achieve this, we normalised the cross-sections such that values of ΔT and $d\ln v_{S,P}$ between the 5th and 95th percentile fall in the range $[-1, 1]$, using the same contour level for each variable (though different contour levels for each location). Using the ages for each slab from van der Meer et al. (2018) combined with these estimated basal depths, we compute the inferred slab sinking rates (Table 2).

For the Aleutian slab, tomographic filtering with *LLNL-G3D-JPS* increases the basal depth from 455 to 676 km, which correspond to sinking rates of 9.5 and 14.1 mm yr^{-1} respectively, or an increase in sinking rate of 4.6 mm yr^{-1}. This is by far the largest change found across the five subduction systems surveyed, and probably anomalous due to filtering connecting the slab to a fast anomaly that originates from lithospheric drip. We find smaller changes for the Java

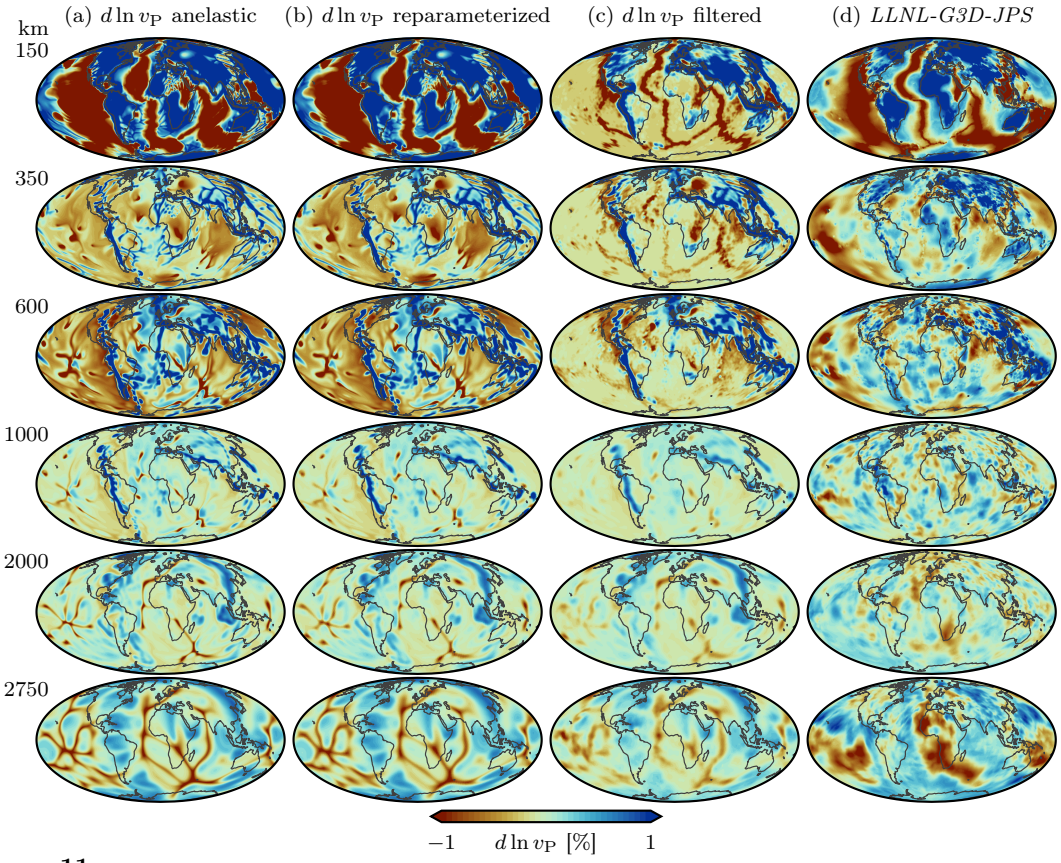

Figure 11

Horizontal cross-sections at increasing depths of: (a) elastic and anelastic P-wave velocity; (b) reparameterised to the LLNL-G3D-JPS native grid points; (c) tomographically filtered by LLNL-G3D-JPS; and (d) the LLNL-G3D-JPS tomography model.

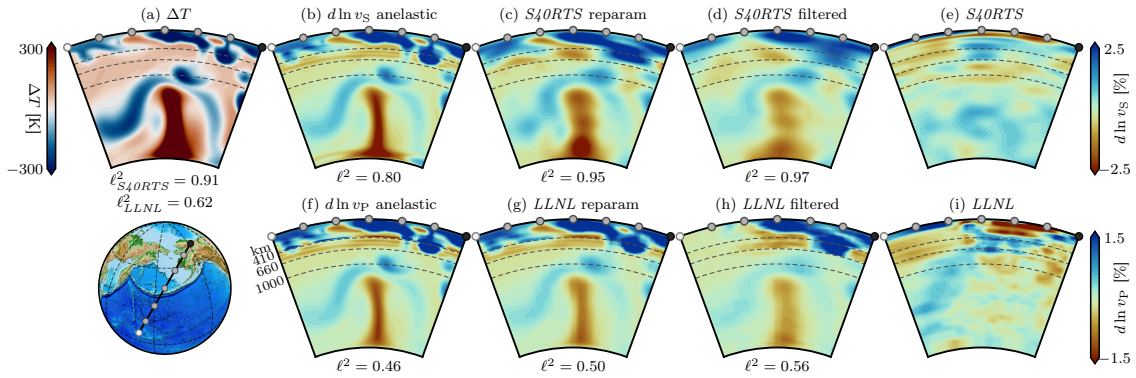

Figure 12

Vertical cross-sections in the Aleutian subduction system, showing: (a) temperature perturbation (ΔT) from layer mean in the G-ADOPT synthetic mantle model; (b) anelastic S-wave velocity perturbation ($d\ln v_S$) from the G-ADOPT synthetic mantle model; (c) $d\ln v_S$ reparameterised to spherical harmonic degree 40; (d) $d\ln v_S$ tomographically filtered by S40RTS; (e) $d\ln v_S$ in the S40RTS tomography model; (f) anelastic P-wave velocity perturbation ($d\ln v_P$) from the G-ADOPT synthetic mantle model; (g) $d\ln v_P$ reparameterised to the LLNL-G3D-JPS native grid points; (h) $d\ln v_P$ tomographically filtered by LLNL-G3D-JPS; and (i) $d\ln v_P$ in the LLNL-G3D-JPS tomography model. The ℓ^2 misfit is also reported for each stage of post-processing, relative to the corresponding tomography model.

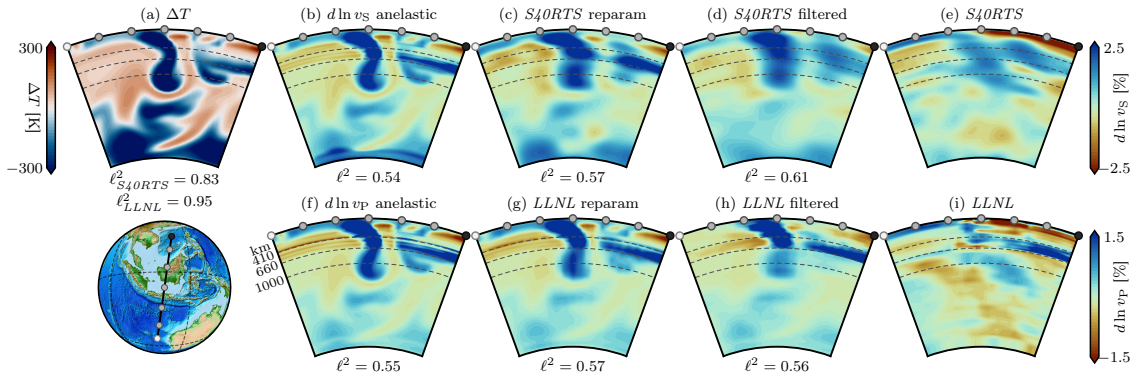

Figure 13

As in Figure 12, but for the Java subduction system.

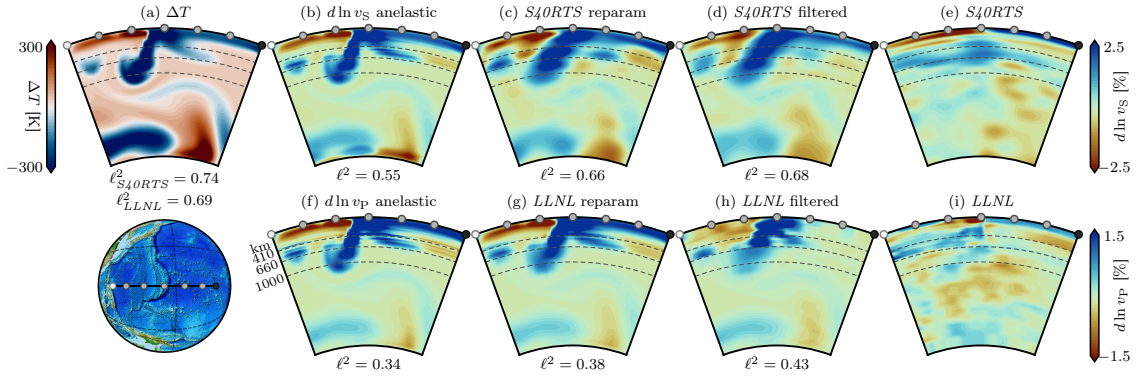

Figure 14

As in Figure 12, but for the Mariana subduction system.

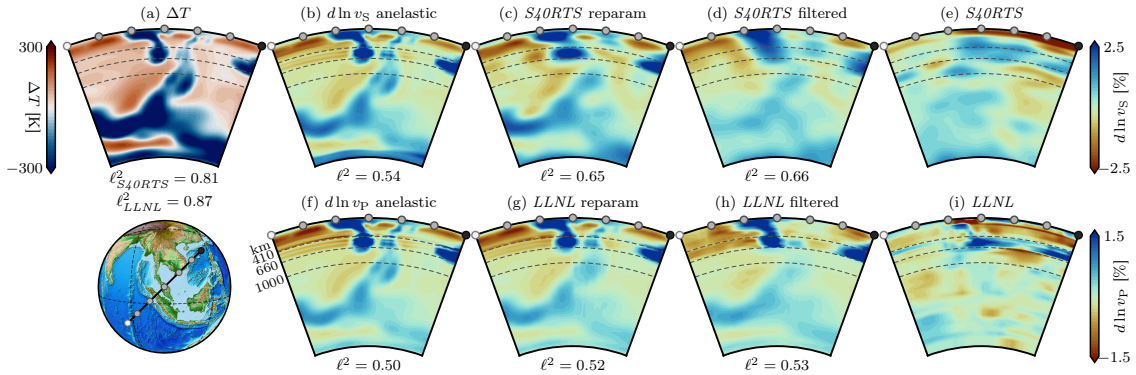

Figure 15

As in Figure 12, but for the Neo-Tethys subduction system.

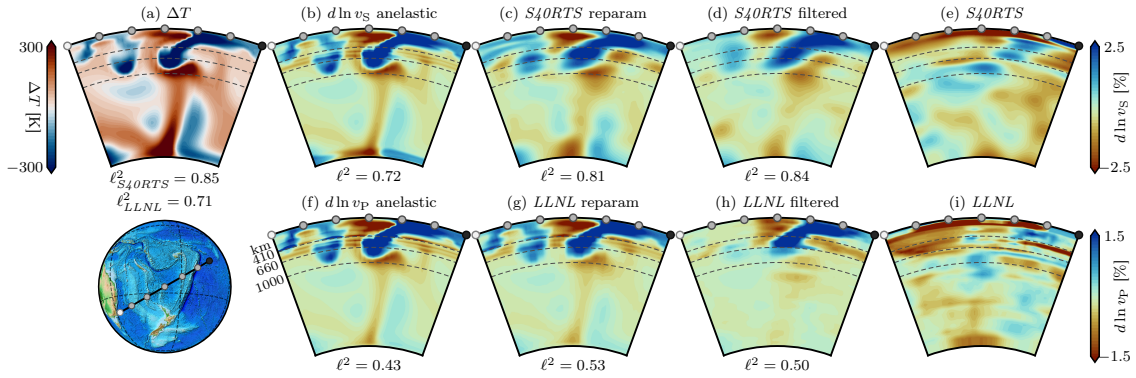

Figure 16

As in Figure 12, but for the Tonga–Kermadec subduction system.

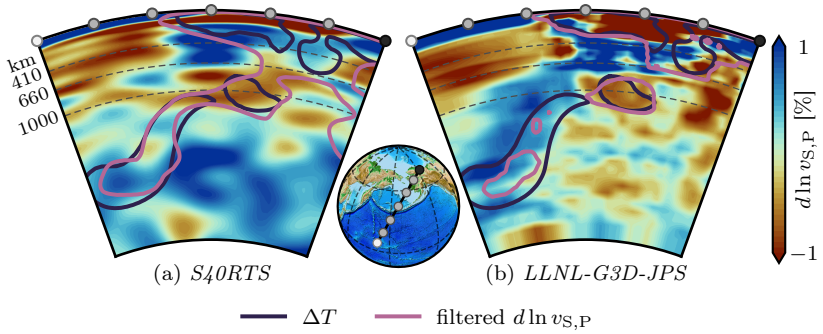

Figure 17

Comparison in the Aleutian subduction system between the equivalent contour levels in temperature perturbation (ΔT) and tomographically filtered seismic velocity perturbation ($d\ln v_{S,P}$), overlain on the respective tomography model: (a) S40RTS; and (b) LLNL-G3D-JPS.

(1401 to 1363 km and 29.6 to 28.8 mm yr^{-1}), Mariana (1257 to 1319 km and 24.4 to 25.6 mm yr^{-1}), Neo-Tethys (804 to 790 km and 17.0 to 16.7 mm yr^{-1}), and Tonga–Kermadec slabs (909 to 932 km and 20.5 to 21.0 mm yr^{-1}). In most cases, filtering with *S40RTS* has a similar effect on these systems (also reported in Table 2).

The largest changes due to filtering are found in the lateral offsets between the temperature field and the filtered output, which can reach several hundred kilometres even where basal depths and sinking rates are only modestly affected. The largest measurable offsets are 639 km for the Neo-Tethys slab filtered with *LLNL-G3D-JPS* and 579 km for the Aleutian slab filtered with *S40RTS*. In two cases (Neo-Tethys and Aleutian filtered with *S40RTS*), no values are reported because filtering connects multiple small anomalies into larger ones, rendering a numerical comparison of slab boundaries misleading. For the remaining systems, filtering with *S40RTS* generally produces larger offsets than *LLNL-G3D-JPS*: 250 and 42 km respectively for Java and 218 and 93 km for Mariana, with Tonga–Kermadec the exception (304 and 398 km). These offsets demonstrate that, even when filtering preserves the apparent depth of a slab's base, it can displace the anomaly laterally by distances comparable to or exceeding the changes in basal depth (Table 2).

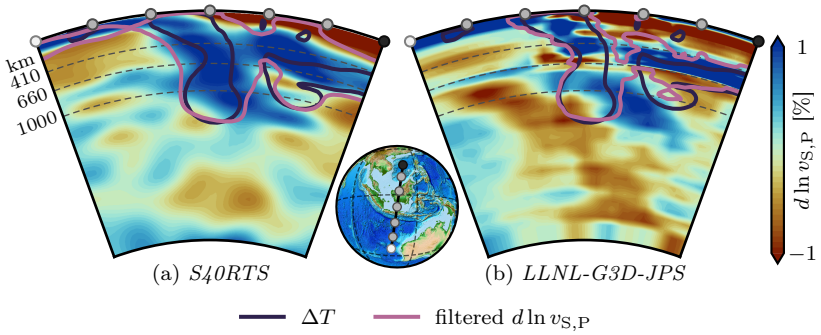

Figure 18

As in Figure 17, but for the Java subduction system.

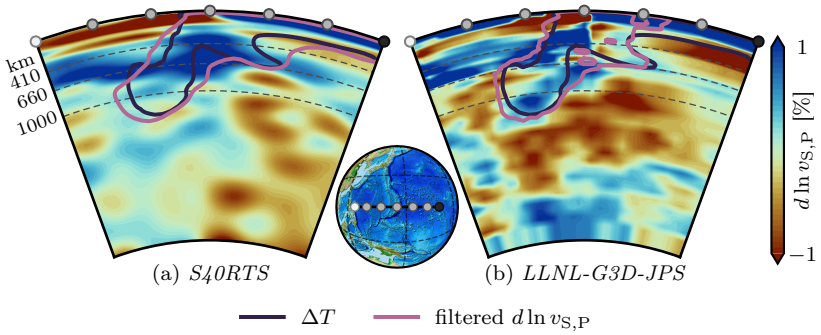

Figure 19

As in Figure 17, but for the Mariana subduction system.

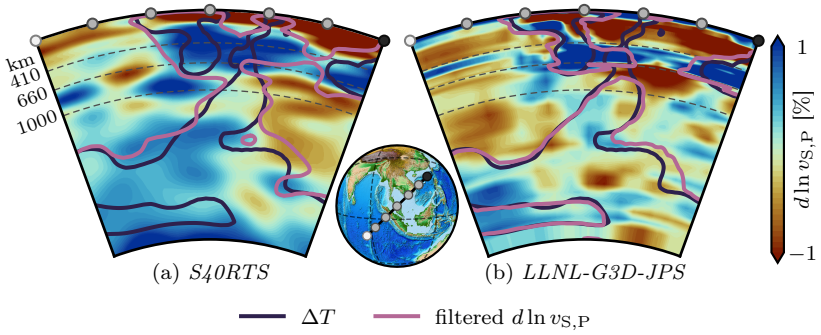

Figure 20

As in Figure 17, but for the Neo-Tethys subduction system.

4 Discussion

4.1 Effects of velocity conversion and tomographic filtering

Converting temperature to seismic velocity enables a more epistemologically satisfying comparison between the synthetic mantle and seismic tomography by allowing comparison of the same physical property and revealing meaningful differences. Beyond enabling this comparison, however, the conversion also reshapes the anomalies themselves—in both magnitude and spatial distribution—as a first step towards the observation space in which tomographic models are ultimately interpreted.

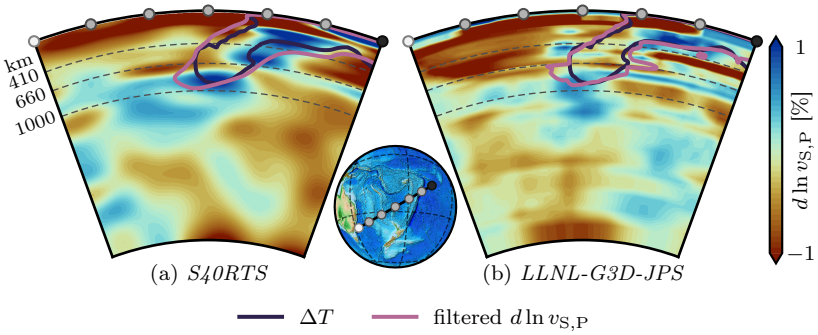

Figure 21

As in Figure 17, but for the Tonga–Kermadec subduction system.

Table 2

The depths of the bases of the slab-like anomalies in Figures 17–19 and 21 and corresponding mean sinking rates given base ages from van der Meer et al. (2018). Also shown are the maximum lateral offsets, assuming vertical sinking, between temperature and filtered output. Uncertainties in sinking rates are estimated from uncertainties in depth (for tomography) and age (for all systems). Sinking rates for Java and Neo-Tethys are compared to the slab named Sunda in van der Meer et al. (2018); all three are the same subduction system at different locations.

Subduction system	Normalised contour level	Age [Ma]		Depth [km]	Mean sinking rate [mm yr^{-1}]	Lateral offset [km]
Aleutian	0.2	50–46	ΔT	455	9.5 ± 0.4	
			S40RTS-filtered	—	—	579
			LLNL-filtered	676	14.1 ± 0.6	278
			v.d.M. et al.	750 ± 100	16 ± 2	
Java	0.25	50–45	ΔT	1401	29.6 ± 1.6	
			S40RTS-filtered	1382	29.2 ± 1.5	250
			LLNL-filtered	1363	28.8 ± 1.5	42
			v.d.M. et al.	1100 ± 100	23 ± 2	
Mariana	0.2	52–51	ΔT	1257	24.4 ± 0.2	
			S40RTS-filtered	1323	25.7 ± 0.3	218
			LLNL-filtered	1319	25.6 ± 0.3	93
			v.d.M. et al.	1250 ± 100	17 ± 3	
Neo-Tethys	0.125	50–45	ΔT	804	17.0 ± 0.9	
			S40RTS-filtered	—	—	—
			LLNL-filtered	790	16.7 ± 0.9	639
			v.d.M. et al.	1100 ± 100	23 ± 2	
Tonga–Kermadec	0.175	85–30	ΔT	909	20.5 ± 9.8	
			S40RTS-filtered	969	21.8 ± 10.5	304
			LLNL-filtered	932	21.0 ± 10.0	398
			v.d.M. et al.	1600 ± 100	28 ± 13	

Globally, the strength of perturbation was reduced by an order of magnitude, but this reduction was inhomogeneous. In the TZ, we observe a decrease in both S- and P-wave perturbation amplitude across the 660 km discontinuity (Figures 6a and 7a) which is not present in temperature (Figure 5b). This matters for interpreting geodynamic models, because slabs can stagnate within the TZ. For instance, a slab that is actually sinking just below the TZ in an MCM could, after conversion to velocity, appear instead to be trapped at its base—potentially yielding a better match to tomography.

The application of the resolution operator has an even more profound effect on the coupled

model. It should be no surprise that the reduction in perturbation strength is inhomogeneous; after all, the purpose of the resolution operator is to view a synthetic mantle model through the spatially variable lens of the associated tomography model. Nevertheless, the extent of the effect of this inhomogeneity is noteworthy. Anomalies may be:

- *Initially continuous, but broken into separate bodies.* See, for example, the Neo-Tethys cross-section; continuous in temperature and seismic speed (Figures 15a and 15f), but broken into two separate bodies after *LLNL*-filtering (Figure 15h). This apparent segmentation emerges where the local resolution length increases and the anomaly's peak amplitude is pushed below the colour scale or noise floor, leaving gaps. Because the resolution operator is spatially variable and often anisotropic, the same feature can remain coherent in one region and fragment in another. Interpreted naïvely, this pattern could mimic slab tearing or along-strike offsets that are not present in the synthetic model.

- *Initially discontinuous, but connected into a single body.* See, for example, the Aleutian cross-section; discontinuous in temperature and seismic speed (Figures 12a and 12b), but connected into a single body after *S40RTS*-filtering (Figure 12e). Here, poor local resolution causes amplitude to leak into low-signal regions, creating an artificial bridge. The effect is strongest where adjacent anomalies are closer than the local resolution length, and can be misread as mechanical continuity (e.g., an uninterrupted slab segment or channelised upwelling).

- *Increased in size but damped.* See, for example, the fast anomaly between the 3rd and 4th pips in the Neo-Tethys cross-section; ∼300 km wide in temperature and seismic speed (Figures 15a and 15b), but ∼600 km wide yet heavily damped after *S40RTS*-filtering (Figure 15e). Convolution with the operator's point–spread function broadens narrow features (vertical and/or lateral smearing) while reducing peak amplitude. The net effect is an apparently more voluminous but intrinsically weaker anomaly, reflecting wavelength-dependent damping: short-wavelength structure is preferentially broadened and attenuated.

- *Reduced in size or eliminated.* See, for example, the small shallow anomaly under the 5th pip in the Java cross-section; present in temperature and seismic velocity (Figures 13a and 13f), but essentially eliminated after *LLNL*-filtering (Figure 13i). Where anomaly wavelengths fall below the local resolution, or where neighbouring signals interfere destructively, the operator suppresses the feature to below detectability, yielding false negatives for genuine but fine-scale structure.

In summary, temperature-to-velocity conversion changes both the magnitude and distribution of anomalies—especially across the TZ—so structures that truly sink below 660 km can instead appear to stagnate at the base of the TZ, potentially giving a genuinely improved match to tomography. Tomographic filtering can then further reshape the synthetic mantle in strongly inhomogeneous ways: continuous anomalies can fragment into separate bodies (mimicking slab tearing or offsets), discontinuous anomalies can be artificially connected (mimicking mechanical continuity or channelised flow), narrow features can be broadened while their peaks are damped (creating apparently larger but weaker bodies), and genuine fine-scale structure can be suppressed entirely (false negatives). Filtering can also displace anomalies laterally by several hundred kilometres—distances comparable to or exceeding the accompanying changes in basal depth—making lateral position arguably the least robust property recovered from tomographic images. Without explicitly considering these effects, apparent slab geometry, continuity, thickness, depth

extent, and location inferred from model–tomography comparisons may reflect the observation filter more than the underlying geodynamics.

The misfit metrics highlight the relative importance of each step in the model–tomography comparison workflow. Conversion from temperature to seismic velocity produces by far the largest reduction in misfit (exceeding 50 % in some cases), most likely because a direct comparison between temperature and seismic tomography rests on unstated assumptions—e.g., a simple linear mapping between thermal and velocity anomalies—that the explicit conversion removes. Tomographic filtering, by contrast, generally *increases* misfit (though only by 1–2 %). This should not be interpreted as a deficiency of the filtering step: by degrading the model prediction in the same way that limited data coverage and regularisation degrade the tomographic image, filtering enables an honest, like-for-like comparison in observation space, rather than an artificially favourable one in model space.

4.2 Implication for plate tectonic reconstructions

MCMs are widely used to evaluate and refine plate tectonic reconstructions (Flament et al., 2015; Seton et al., 2015; Zahirovic et al., 2016; Li et al., 2023). Typically, the temperature field from such models are tested against tomographic images of putative past subduction, where anomalies with high seismic velocities are interpreted as fossil slabs. A principled comparison, however, must recognise that tomography does not image the mantle directly; it images the mantle after spatially variable damping and smearing by the inverse problem and its data coverage.

If these filtering effects are ignored, the comparison between predicted slabs and seismic anomalies is biased. Apparent mismatches can be overstated (or understated) by resolution-driven artefacts such as fragmentation of continuous bodies, artificial connections across gaps, broadening with amplitude loss, or wholesale suppression of fine-scale features. Naïvely penalising (or preferring) a reconstruction for such effects risks drawing incorrect conclusions about palaeotrench locations, subduction continuity (and the interpretation of tectonic features which break this continuity), or slab stagnation/penetration.

A robust strategy is therefore to compare in *observation space*. We converted model temperature anomalies to seismic-velocity perturbations and then applied the appropriate resolution operator for each tomographic model (*S40RTS* and *LLNL-G3D-JPS*), yielding a filtered prediction $d\ln v'_{\mathrm{S,P}} = \mathcal{R}\cdot d\ln v_{\mathrm{S,P}}$. The filtered field $d\ln v'_{\mathrm{S,P}}$ could then be compared directly with the observed tomography at matching length scales. This approach reduces false negatives/positives introduced by resolution inhomogeneity, and provides a physically motivated detectability threshold. In turn, reconstructions can be judged more fairly: the largest, longest-lived, and most coherent subduction systems are likely to be preserved, whereas short, weak, or spatially complex segments may be invisible and should not unduly penalise a candidate reconstruction. (The same logic applies to plume-related, low-velocity anomalies, although plumes are not our focus here.)

This shift to observation-space comparisons also influences quantitative inferences drawn from present-day images, including slab thicknesses, basal depths, and time–depth relations used to estimate sinking rates. Resolution-dependent broadening and amplitude loss will bias the interpreted base of slab-like anomalies if not accounted for, although we find that the resulting changes in inferred sinking rate are modest and system-dependent in sign: filtering with *LLNL-G3D-JPS* changes rates by 0.3–1.2 $\mathrm{mm\,yr^{-1}}$ across the Java, Mariana, Neo-Tethys, and Tonga–Kermadec systems, with decreases for Java and Neo-Tethys but increases for Mariana and Tonga–Kermadec, while the much larger Aleutian increase of 4.6 $\mathrm{mm\,yr^{-1}}$ reflects filtering artificially connecting the slab to an unrelated fast anomaly rather than a resolvable change in slab geometry. These biases

are small relative to the 4–6 mm yr^{-1} by which sinking rates from coupled models (e.g., this study, Butterworth et al., 2014) have often exceeded estimates from tomography (e.g., van der Meer et al., 2018), but because they can take either sign and reach up to a quarter of that discrepancy, they must be quantified on a per-system basis before the model–tomography gap can be attributed to geodynamic parameters such as effective mantle viscosity or slab strength.

A larger and less widely appreciated consequence of limited tomographic resolution is the lateral displacement of slab-like anomalies, which here reaches several hundred kilometres (up to 639 km for the Neo-Tethys slab) even where basal depths and sinking rates are only modestly affected. Such offsets have direct implications for methods that unfold slab anomalies in tomographic models to recover the length of subducted lithosphere and, by extension, plate convergence histories and reconstruction constraints (e.g., Wu et al., 2016): a lateral displacement comparable to or exceeding the change in basal depth implies that the apparent dip, curvature, and along-strike continuity of an imaged slab may differ substantially from those of the underlying structure, so that unfolded slab lengths inherit errors of similar magnitude. Because these displacements vary with both the tomographic model and the subduction system, and can merge discrete anomalies into apparently continuous features, estimates of slab length and segmentation derived from unfolding should be regarded as resolution-dependent quantities, best interpreted after passing candidate geodynamic or kinematic scenarios through the same tomographic filter as the observations.

Practically, this leads to a clearer and more defensible workflow for reconstruction validation:

1. Generate coupled-model predictions of thermal structure at present-day for each reconstruction.
2. Convert ΔT to $d \ln v_{\mathrm{S,P}}$ using a consistent mineral physics framework.
3. Apply the resolution operator $\mathcal{R}$ of the chosen tomographic model to obtain $d \ln v'_{\mathrm{S,P}}$.
4. Compute comparisons and misfits in observation space (e.g., spatial overlap, coherence/continuity metrics, depth–extent statistics).

By filtering model output to tomographic resolution we strengthen the logical link between reconstructions, geodynamic predictions, and present-day images. This reduces interpretation bias, clarifies which palaeo-subduction zones should be visible, and yields more reliable estimates of slab geometry and sinking rates. In short, the post-processing advocated here makes coupled models a sharper tool for inferring slab history and behaviour, thereby advancing both geodynamics and plate-tectonic modelling.

5 Conclusions

We have presented a new workflow for analysing the output of coupled plate tectonic–mantle convection models, and for using these coupled models to validate plate tectonic reconstructions against tomography. This workflow involves converting modelled mantle temperature to seismic velocity, and then applying the resolution operator of a seismic tomography model to enhance the validity of comparisons made between tomography and the synthetic model. While neither the concept of using a mantle mineralogy model to convert a synthetic mantle temperature field to seismic velocity nor that of applying the resolution operator of a seismic tomography model are new, most studies aiming to validate a tectonic reconstruction with a coupled model have not taken advantage of them to support their conclusions. Applying this workflow to five well-studied subduction systems, we find that tomographic filtering can alter the qualitative interpretation of

predicted slab structure (e.g., continuous to discontinuous or vice versa), while conversion to seismic velocity alone reduces misfit to tomography by up to 51 %. We also show that filtering changes inferred sinking rates by up to 1.2 mm yr^{-1} in either direction—and by considerably more where it artificially merges anomalies—and displaces slab-like anomalies laterally by several hundred kilometres, with direct consequences for slab-unfolding estimates of subducted lithosphere length.

Despite the importance of seismic velocity conversion and the tomographic filtering being noted for many years, the vast majority of authors do not publish one for their tomography models. While we recognise that calculating the resolution operator is challenging, we believe that with this paper we have demonstrated the importance of expending the effort to produce the resolution operator for global tomography models. We have also provided the workflows necessary to convert MCMs from temperature to seismic velocity (a critical step prior to applying a resolution operator) and tomographically filter them with existing resolution operators. Existing and future resolution operators will enable far more robust comparisons between them and geodynamic models and will thus serve a community of users spanning seismology, geodynamics and tectonics.

Open Research Section

The tectonic reconstruction used in this study, Zahirovic et al. (2022) is freely available from https://www.earthbyte.org/category/resources/data-models/. The software library pyGPlates, used to couple the reconstruction to the mantle convection model, is freely available from https://github.com/gplates under the GPL-2.0 licence. The software libraries G-ADOPT and G-DRIFT, used to construct the mantle convection model and convert it to seismic velocity, respectively, are freely available from https://github.com/g-adopt/ under the MIT licence. The software library llnltofi, used to filter the converted mantle convection model with the *LLNL-G3D-JPS* resolution operator, is freely available from https://github.com/g-adopt/llnltofi under the GPL-3.0 licence. The software library srts, used to filter the converted mantle convection model with the *S40RTS* resolution operator, is freely available from https://github.com/g-adopt/srts. The Python 3 scripts used to generate the figures in this study are archived online at https://doi.org/10.5281/zenodo.15234463.

Due to size constraints, the full output data from the mantle convection model will be published on the National Computing Infrastructure (NCI Australia) data portal shortly after submission. In the interim, model data for the present-day is made available upon request.

Acknowledgments

Development of GPlates and pyGPlates is funded by the AuScope National Collaborative Research Infrastructure System (NCRIS) program. The development of G-ADOPT is currently supported by AuScope through the CoastRI program, and previously by the Australian Research Data Commons. This research was undertaken with the assistance of resources provided by NCI Australia, an NCRIS-enabled capability supported by the Australian Government. S.G. acknowledges support from the Australian Research Council through a Discovery Early Career Researcher Award DE250100663. S.G., D.R.D., and R.D.M. acknowledge funding from an Australian Research Council Discovery Project DP210101215. T.N. and M.S. acknowledge funding from the Australian Research Council Discovery Project DP200100966.

References

Bercovici, D. (2003). The generation of plate tectonics from mantle convection. *Earth and Planetary Science Letters*, *205*(3-4), 107–121. https://doi.org/10.1016/S0012-821X(02)01009-9

Biggin, A. J., Steinberger, B., Aubert, J., Suttie, N., Holme, R., Torsvik, T. H., van der Meer, D. G., & van Hinsbergen, D. J. J. (2012). Possible links between long-term geomagnetic variations and whole-mantle convection processes. *Nature Geoscience*, *5*(8), 526–533. https://doi.org/10.1038/ngeo1521

Bower, D. J., Gurnis, M., & Flament, N. (2015). Assimilating lithosphere and slab history in 4-D Earth models. *Physics of the Earth and Planetary Interiors*, *238*, 8–22. https://doi.org/10.1016/j.pepi.2014.10.013

Bunge, H.-P., & Davies, J. H. (2001). Tomographic images of a mantle circulation model. *Geophysical Research Letters*, *28*(1), 77–80. https://doi.org/10.1029/2000GL011804

Butterworth, N. P., Talsma, A. S., Müller, R. D., Seton, M., Bunge, H.-P., Schuberth, B. S. A., Shephard, G. E., & Heine, C. (2014). Geological, tomographic, kinematic and geodynamic constraints on the dynamics of sinking slabs. *Journal of Geodynamics*, *73*, 1–13. https://doi.org/10.1016/j.jog.2013.10.006

Cammarano, F., Goes, S., Deuss, A., & Giardini, D. (2005). Is a pyrolitic adiabatic mantle compatible with seismic data? *Earth and Planetary Science Letters*, *232*(3), 227–243. https://doi.org/10.1016/j.epsl.2005.01.031

Cammarano, F., Goes, S., Vacher, P., & Giardini, D. (2003). Inferring upper-mantle temperatures from seismic velocities. *Physics of the Earth and Planetary Interiors*, *138*(3), 197–222. https://doi.org/10.1016/S0031-9201(03)00156-0

Cao, W., Flament, N., Zahirovic, S., Williams, S., & Müller, R. D. (2019). The interplay of dynamic topography and eustasy on continental flooding in the late Paleozoic. *Tectonophysics*, *761*, 108–121. https://doi.org/10.1016/j.tecto.2019.04.018

Cawood, P. A., & Hawkesworth, C. J. (2014). Earth's middle age. *Geology*, *42*(6), 503–506. https://doi.org/10.1130/G35402.1

Chust, T. C., Steinle-Neumann, G., Dolejš, D., Schuberth, B. S. A., & Bunge, H.-P. (2017). MMA-EoS: A computational framework for mineralogical thermodynamics. *Journal of Geophysical Research: Solid Earth*, *122*(12), 9881–9920. https://doi.org/10.1002/2017JB014501

Cobden, L., Goes, S., Cammarano, F., & Connolly, J. A. D. (2008). Thermochemical interpretation of one-dimensional seismic reference models for the upper mantle: Evidence for bias due to heterogeneity. *Geophysical Journal International*, *175*(2), 627–648. https://doi.org/10.1111/j.1365-246X.2008.03903.x

Davies, D. R., Davies, J. H., Bollada, P. C., Hassan, O., Morgan, K., & Nithiarasu, P. (2013). A hierarchical mesh refinement technique for global 3-D spherical mantle convection modelling. *Geoscientific Model Development*, *6*(4), 1095–1107. https://doi.org/10.5194/gmd-6-1095-2013

Davies, D. R., Goes, S., Davies, J. H., Schuberth, B. S. A., Bunge, H.-P., & Ritsema, J. (2012). Reconciling dynamic and seismic models of Earth's lower mantle: The dominant role of thermal heterogeneity. *Earth and Planetary Science Letters*, *353–354*, 253–269. https://doi.org/10.1016/j.epsl.2012.08.016

Davies, D. R., Kramer, S. C., Ghelichkhan, S., & Gibson, A. (2022). Towards automatic finite-element methods for geodynamics via Firedrake. *Geoscientific Model Development*, *15*(13), 5127–5166. https://doi.org/10.5194/gmd-15-5127-2022

Flament, N., Gurnis, M., & Müller, R. D. (2013). A review of observations and models of dynamic topography. *Lithosphere*, *5*(2), 189–210. https://doi.org/10.1130/L245.1

Flament, N., Gurnis, M., Müller, R. D., Bower, D. J., & Husson, L. (2015). Influence of subduction history on South American topography. *Earth and Planetary Science Letters*, *430*, 9–18. https://doi.org/10.1016/j.epsl.2015.08.006

Ghelichkhan, S., Gibson, A., Davies, D. R., Kramer, S. C., & Ham, D. A. (2024). Automatic adjoint-based inversion schemes for geodynamics: Reconstructing the evolution of Earth's mantle in space and time. *Geoscientific Model Development*, *17*(13), 5057–5086. https://doi.org/10.5194/gmd-17-5057-2024

Goes, S., Cammarano, F., & Hansen, U. (2004). Synthetic seismic signature of thermal mantle plumes. *Earth and Planetary Science Letters*, *218*(3), 403–419. https://doi.org/10.1016/S0012-821X(03)00680-0

Goes, S., Yu, C., Ballmer, M. D., Yan, J., & van der Hilst, R. D. (2022). Compositional heterogeneity in the mantle transition zone. *Nature Reviews Earth & Environment*, *3*(8), 533–550. https://doi.org/10.1038/s43017-022-00312-w

Groves, D. I., & Bierlein, F. P. (2007). Geodynamic settings of mineral deposit systems. *Journal of the Geological Society*, *164*(1), 19–30. https://doi.org/10.1144/0016-76492006-065

Gurnis, M. (1988). Large-scale mantle convection and the aggregation and dispersal of supercontinents. *Nature*, *332*(6166), 695–699.

Harrington, L., Zahirovic, S., Flament, N., & Müller, R. D. (2017). The role of deep Earth dynamics in driving the flooding and emergence of New Guinea since the Jurassic. *Earth and Planetary Science Letters*, *479*, 273–283. https://doi.org/10.1016/j.epsl.2017.09.039

Heister, T., Dannberg, J., Gassmöller, R., & Bangerth, W. (2017). High accuracy mantle convection simulation through modern numerical methods — II: Realistic models and problems. *Geophysical Journal International*, *210*(2), 833–851. https://doi.org/10.1093/gji/ggx195

Hu, J., Liu, L., Faccenda, M., Zhou, Q., Fischer, K. M., Marshak, S., & Lundstrom, C. (2018a). Modification of the Western Gondwana craton by plume–lithosphere interaction. *Nature Geoscience*, *11*(3), 203–210. https://doi.org/10.1038/s41561-018-0064-1

Hu, J., Liu, L., & Zhou, Q. (2018b). Reproducing past subduction and mantle flow using high-resolution global convection models. *Earth and Planetary Physics*, *2*(3), 189–207. https://doi.org/10.26464/epp2018019

Iaffaldano, G., & Lambeck, K. (2014). Pacific plate-motion change at the time of the Hawaiian–Emperor bend constrains the viscosity of Earth's asthenosphere. *Geophysical Research Letters*, *41*(10), 3398–3406. https://doi.org/10.1002/2014GL059763

Koelemeijer, P., Schuberth, B. S. A., Davies, D. R., Deuss, A., & Ritsema, J. (2018). Constraints on the presence of post-perovskite in Earth's lowermost mantle from tomographic-geodynamic model comparisons. *Earth and Planetary Science Letters*, *494*, 226–238. https://doi.org/10.1016/j.epsl.2018.04.056

Li, Y., Liu, L., Peng, D., Dong, H., & Li, S. (2023). Evaluating tomotectonic plate reconstructions using geodynamic models with data assimilation, the case for North America. *Earth-Science Reviews*, *244*, 104518. https://doi.org/10.1016/j.earscirev.2023.104518

Lin, Y.-A., Colli, L., & Wu, J. (2022). NW Pacific-Panthalassa Intra-Oceanic Subduction During Mesozoic Times From Mantle Convection and Geoid Models. *Geochemistry, Geophysics, Geosystems*, *23*(11), e2022GC010514. https://doi.org/10.1029/2022GC010514

Liu, L., & Stegman, D. R. (2011). Segmentation of the Farallon slab. *Earth and Planetary Science Letters*, *311*(1), 1–10. https://doi.org/10.1016/j.epsl.2011.09.027

Mather, B. R., Müller, R. D., Zahirovic, S., Cannon, J., Chin, M., Ilano, L., Wright, N. M., Alfonso, C., Williams, S., Tetley, M., & Merdith, A. (2024). Deep time spatio-temporal data analysis using pyGPlates with PlateTectonicTools and GPlately. *Geoscience Data Journal*, *11*(1), 3–10. https://doi.org/10.1002/gdj3.185

McKenzie, D. P. (1969). Speculations on the consequences and causes of plate motions. *Geophysical Journal International*, *18*(1), 1–32. https://doi.org/10.1111/j.1365-246X.1969.tb00259.x

Mégnin, C., Bunge, H.-P., Romanowicz, B., & Richards, M. A. (1997). Imaging 3-D spherical convection models: What can seismic tomography tell us about mantle dynamics? *Geophysical Research Letters*, *24*(11), 1299–1302. https://doi.org/10.1029/97GL01256

Miller, K. G., Kominz, M. A., Browning, J. V., Wright, J. D., Mountain, G. S., Katz, M. E., Sugarman, P. J., Cramer, B. S., Christie-Blick, N., & Pekar, S. F. (2005). The Phanerozoic record of global sea-level change. *Science*, *310*(5752), 1293–1298. https://doi.org/10.1126/science.1116412

Müller, R. D., Cannon, J., Qin, X., Watson, R. J., Gurnis, M., Williams, S., Pfaffelmoser, T., Seton, M., Russell, S. H. J., & Zahirovic, S. (2018). GPlates: Building a virtual Earth through deep time. *Geochemistry, Geophysics, Geosystems*, *19*(7), 2243–2261. https://doi.org/10.1029/2018GC007584

Müller, R. D., Flament, N., Cannon, J., Tetley, M. G., Williams, S. E., Cao, X., Bodur, Ö. F., Zahirovic, S., & Merdith, A. (2022a). A tectonic-rules-based mantle reference frame since 1 billion years ago—implications for supercontinent cycles and plate–mantle system evolution. *Solid Earth*, *13*(7), 1127–1159. https://doi.org/10.5194/se-13-1127-2022

Müller, R. D., Mather, B., Dutkiewicz, A., Keller, T., Merdith, A., Gonzalez, C. M., Gorczyk, W., & Zahirovic, S. (2022b). Evolution of Earth's tectonic carbon conveyor belt. *Nature*, *605*(7911), 629–639. https://doi.org/10.1038/s41586-022-04420-x

Müller, R. D., Zahirovic, S., Williams, S. E., Cannon, J., Seton, M., Bower, D. J., Tetley, M. G., Heine, C., Le Breton, E., Liu, S., Russell, S. H. J., Yang, T., Leonard, J., & Gurnis, M. (2019). A global plate model including lithospheric deformation along major rifts and orogens since the Triassic. *Tectonics*, *38*(6), 1884–1907. https://doi.org/10.1029/2018TC005462

Nerlich, R., Colli, L., Ghelichkhan, S., Schuberth, B., & Bunge, H.-P. (2016). Constraining central Neo-Tethys Ocean reconstructions with mantle convection models. *Geophysical Research Letters*, *43*(18), 9595–9603. https://doi.org/10.1002/2016GL070524

Paulson, A., & Richards, M. A. (2009). On the resolution of radial viscosity structure in modelling long-wavelength postglacial rebound data. *Geophysical Journal International*, *179*(3), 1516–1526. https://doi.org/10.1111/j.1365-246X.2009.04362.x

Peng, D., & Liu, L. (2022). Quantifying slab sinking rates using global geodynamic models with data-assimilation. *Earth-Science Reviews*, *230*, 104039. https://doi.org/10.1016/j.earscirev.2022.104039

Peng, D., Liu, L., Hu, J., Li, S., & Liu, Y. (2021a). Formation of east Asian stagnant slabs due to a pressure-driven Cenozoic mantle wind following mesozoic subduction. *Geophysical Research Letters*, *48*(18), e2021GL094638. https://doi.org/10.1029/2021GL094638

Peng, D., Liu, L., & Wang, Y. (2021b). A newly discovered late-Cretaceous east Asian flat slab explains its unique lithospheric structure and tectonics. *Journal of Geophysical Research: Solid Earth*, *126*(10), e2021JB022103. https://doi.org/10.1029/2021JB022103

Piazzoni, A. S., Steinle-Neumann, G., Bunge, H.-P., & Dolejš, D. (2007). A mineralogical model for density and elasticity of the Earth's mantle. *Geochemistry, Geophysics, Geosystems*, *8*(11). https://doi.org/10.1029/2007GC001697

Rathgeber, F., Ham, D. A., Mitchell, L., Lange, M., Luporini, F., Mcrae, A. T. T., Bercea, G.-T., Markall, G. R., & Kelly, P. H. J. (2016). Firedrake: Automating the finite element method by composing abstractions. *ACM Transactions on Mathematical Software*, *43*(3), 24:1–24:27. https://doi.org/10.1145/2998441

Raymo, M. E., & Ruddiman, W. F. (1992). Tectonic forcing of late Cenozoic climate. *Nature*, *359*(6391), 117–122. https://doi.org/10.1038/359117a0

Ringwood, A. E. (1991). Phase transformations and their bearing on the constitution and dynamics of the mantle. *Geochimica et Cosmochimica Acta*, *55*(8), 2083–2110. https://doi.org/10.1016/0016-7037(91)90090-R

Ritsema, J., Deuss, A., van Heijst, H. J., & Woodhouse, J. H. (2011). S40RTS: A degree-40 shear-velocity model for the mantle from new Rayleigh wave dispersion, teleseismic traveltime and normal-mode splitting function measurements. *Geophysical Journal International*, *184*(3), 1223–1236. https://doi.org/10.1111/j.1365-246X.2010.04884.x

Ritsema, J., McNamara, A. K., & Bull, A. L. (2007). Tomographic filtering of geodynamic models: Implications for model interpretation and large-scale mantle structure. *Journal of Geophysical Research: Solid Earth*, *112*(B1). https://doi.org/10.1029/2006JB004566

Ritsema, J., van Heijst, H. J., & Woodhouse, J. H. (1999). Complex shear wave velocity structure imaged beneath Africa and Iceland. *Science*, *286*(5446), 1925–1928. https://doi.org/10.1126/science.286.5446.1925

Schuberth, B. S. A., Bunge, H.-P., & Ritsema, J. (2009). Tomographic filtering of high-resolution mantle circulation models: Can seismic heterogeneity be explained by temperature alone? *Geochemistry, Geophysics, Geosystems*, *10*(5). https://doi.org/10.1029/2009GC002401

Scotese, C. R., Song, H., Mills, B. J. W., & van der Meer, D. G. (2021). Phanerozoic paleotemperatures: The Earth's changing climate during the last 540 million years. *Earth-Science Reviews*, *215*, 103503. https://doi.org/10.1016/j.earscirev.2021.103503

Seton, M., Flament, N., Whittaker, J., Müller, R. D., Gurnis, M., & Bower, D. J. (2015). Ridge subduction sparked reorganization of the Pacific plate–mantle system 60–50 million years ago. *Geophysical Research Letters*, *42*(6), 1732–1740. https://doi.org/10.1002/2015GL063057

Simmons, N. A., Myers, S. C., Johannesson, G., Matzel, E., & Grand, S. P. (2015). Evidence for long-lived subduction of an ancient tectonic plate beneath the southern Indian Ocean. *Geophysical Research Letters*, *42*(21), 9270–9278. https://doi.org/10.1002/2015GL066237

Simmons, N. A., Schuberth, B. S. A., Myers, S. C., & Knapp, D. R. (2019). Resolution and covariance of the LLNL-G3D-JPS global seismic tomography model: Applications to travel time uncertainty and tomographic filtering of geodynamic models. *Geophysical Journal International*, *217*(3), 1543–1557. https://doi.org/10.1093/gji/ggz102

Stixrude, L., & Lithgow-Bertelloni, C. (2005). Thermodynamics of mantle minerals—I. Physical properties. *Geophysical Journal International*, *162*(2), 610–632. https://doi.org/10.1111/j.1365-246X.2005.02642.x

Stixrude, L., & Lithgow-Bertelloni, C. (2011). Thermodynamics of mantle minerals—II. Phase equilibria. *Geophysical Journal International*, *184*(3), 1180–1213. https://doi.org/10.1111/j.1365-246X.2010.04890.x

Stixrude, L., & Lithgow-Bertelloni, C. (2022). Thermal expansivity, heat capacity and bulk modulus of the mantle. *Geophysical Journal International*, *228*(2), 1119–1149. https://doi.org/10.1093/gji/ggab394

Stixrude, L., & Lithgow-Bertelloni, C. (2024). Thermodynamics of mantle minerals—III. The role of iron. *Geophysical Journal International*, *237*(3), 1699–1733. https://doi.org/10.1093/gji/ggae126

Stotz, I. L., Iaffaldano, G., & Davies, D. R. (2018). Pressure-driven Poiseuille flow: A major component of the torque-balance governing Pacific plate motion. *Geophysical Research Letters*, *45*(1), 117–125. https://doi.org/10.1002/2017GL075697

Styles, E., Goes, S., van Keken, P. E., Ritsema, J., & Smith, H. (2011). Synthetic images of dynamically predicted plumes and comparison with a global tomographic model. *Earth and Planetary Science Letters*, *311*(3), 351–363. https://doi.org/10.1016/j.epsl.2011.09.012

Su, J., Houser, C., Hernlund, J. W., & Deschamps, F. (2023). Tomographic filtering of shear and compressional wave models reveals uncorrelated variations in the lowermost mantle. *Geophysical Journal International*, *234*(3), 2114–2127. https://doi.org/10.1093/gji/ggad190

Trampert, J., Fichtner, A., & Ritsema, J. (2013). Resolution tests revisited: The power of random numbers. *Geophysical Journal International*, *192*, 676–680. https://doi.org/10.1093/gji/ggs057

van der Meer, D. G., van Hinsbergen, D. J. J., & Spakman, W. (2018). Atlas of the underworld: Slab remnants in the mantle, their sinking history, and a new outlook on lower mantle viscosity. *Tectonophysics*, *723*, 309–448. https://doi.org/10.1016/j.tecto.2017.10.004

Wang, W., Zhang, H., Brodholt, J. P., & Wu, Z. (2021). Elasticity of hydrous ringwoodite at mantle conditions: Implication for water distribution in the lowermost mantle transition zone. *Earth and Planetary Science Letters*, *554*, 116626. https://doi.org/10.1016/j.epsl.2020.116626

Workman, R. K., & Hart, S. R. (2005). Major and trace element composition of the depleted MORB mantle (DMM). *Earth and Planetary Science Letters*, *231*(1), 53–72. https://doi.org/10.1016/j.epsl.2004.12.005

Wu, J., Suppe, J., Lu, R., & Kanda, R. (2016). Philippine Sea and East Asian plate tectonics since 52 Ma constrained by new subducted slab reconstruction methods. *Journal of Geophysical Research: Solid Earth*, *121*(6), 4670–4741. https://doi.org/10.1002/2016JB012923

Young, A., Flament, N., Williams, S. E., Merdith, A., Cao, X., & Müller, R. D. (2022). Long-term Phanerozoic sea level change from solid Earth processes. *Earth and Planetary Science Letters*, *584*, 117451. https://doi.org/10.1016/j.epsl.2022.117451

Zahirovic, S., Eleish, A., Doss, S., Pall, J., Cannon, J., Pistone, M., Tetley, M. G., Young, A., & Fox, P. (2022). Subduction and carbonate platform interactions. *Geoscience Data Journal*, *9*(2), 371–383. https://doi.org/10.1002/gdj3.146

Zahirovic, S., Matthews, K. J., Flament, N., Müller, R. D., Hill, K. C., Seton, M., & Gurnis, M. (2016). Tectonic evolution and deep mantle structure of the eastern Tethys since the latest Jurassic. *Earth-Science Reviews*, *162*, 293–337. https://doi.org/10.1016/j.earscirev.2016.09.005

Zaroli, C., Koelemeijer, P., & Lambotte, S. (2017). Toward seeing the Earth's interior through unbiased tomographic lenses. *Geophysical Research Letters*, *44*(22). https://doi.org/10.1002/2017GL074996

Zhong, S., Zuber, M. T., Moresi, L., & Gurnis, M. (2000). Role of temperature-dependent viscosity and surface plates in spherical shell models of mantle convection. *Journal of Geophysical Research: Solid Earth*, *105*(B5), 11063–11082. https://doi.org/10.1029/2000JB900003

Zhou, W.-Y., Hao, M., Zhang, J. S., Chen, B., Wang, R., & Schmandt, B. (2022). Constraining composition and temperature variations in the mantle transition zone. *Nature Communications*, *13*(1), 1094. https://doi.org/10.1038/s41467-022-28709-7

3 | Testing Plate Reconstructions with Emergent Slab Geometry

Tom New[1], Maria Seton[1], R. Dietmar Müller[1], D. Rhodri Davies[2], Siavash Ghelichkhan[2], and Ben Mather[3]

[1] *EarthByte Group, School of Geosciences, The University of Sydney, NSW, Australia*
[2] *Research School of Earth Sciences, Australian National University, ACT, Australia*
[3] *School of Geography, Earth and Atmospheric Sciences, The University of Melbourne, VIC, Australia*

Abstract

Global mantle convection models driven by tectonic reconstructions now allow subduction geometry to emerge dynamically rather than being prescribed, offering new opportunities to more robustly test the compatibility between plate kinematic histories and present-day mantle structure. Here we evaluate slab morphology predicted by latest-generation G-ADOPT forward models against a suite of well-imaged subduction systems including the Aegean, Brasilia, Aleutian, Caribbean, Izu–Bonin, Mariana, Sunda, and Tonga–Kermadec–Hikurangi slabs. Modelled slabs are compared directly with two seismic tomography models and assessed for: depth; polarity and dip angle; lateral position and extent; and statistical misfit.

Several regions show good agreement–most notably the Aleutian, Sunda, and Brasilia slabs–demonstrating that simple plate-driven convection (e.g., intra-oceanic or island arc systems primarily controlled by slab rollback) can reproduce major features of the mantle's subduction record as imaged by seismic tomography. However, systematic misfits arise in cases involving strong trench advance or complex microplate interactions. In particular, the G-ADOPT implementation of slab polarity, which is inferred solely from trench migration direction, produces incorrect subduction polarity in the Aegean and Caribbean (where there is trench advance in the mantle frame) and contributes to dip errors elsewhere. Our results highlight both the strengths and limitations of emergent-geometry convection modelling and illustrate how slab morphology can be used to diagnose deficiencies in plate reconstructions, trench-migration histories, and geodynamic model assumptions. Together, these comparisons provide a framework for improving reconstruction–convection consistency in future global models.

1 Introduction

Reconstructing Earth's subduction history requires integrating plate tectonic reconstructions, mantle convection modelling, and seismic tomography, each capturing complementary aspects of

long-term mantle–lithosphere interaction (e.g., Bunge et al., 1998; Lithgow-Bertelloni & Richards, 1998; Seton et al., 2012). Tomography provides snapshots of present-day slab distribution in the mantle (e.g., Bijwaard & Spakman, 2000; Fukao & Obayashi, 2013; van der Meer et al., 2018), while plate reconstructions describe the surface kinematics that delivered those slabs to depth (e.g., Müller et al., 2019; Zahirovic et al., 2022). Mantle circulation models (MCMs) link these by predicting how reconstructed plate motions generate slab deformation, dip, polarity, stagnation, and sinking histories (e.g., Butterworth et al., 2014). Yet inconsistencies between reconstructions, geodynamic predictions, and tomography remain common, and identifying their causes is critical for understanding Earth evolution.

Earlier generations of global geodynamic models often imposed slab geometry—such as dip, polarity, and assimilation rates—directly (e.g., Spasojević & Gurnis, 2012; Bower et al., 2015), limiting their ability to fully evaluate consistencies with tectonic reconstructions. Recent frameworks such as G-ADOPT (Gibson et al., 2024) allow subduction geometry to emerge dynamically from plate kinematics and mantle rheology without predefined slab paths (e.g., Arnould et al., 2020; Davies et al., 2022). This development enables simulated slab morphology to serve as an independent test of reconstruction validity. However, it also introduces new sensitivities: in G-ADOPT, slab polarity is inferred from trench migration direction, which may misrepresent true subduction polarity during trench advance or complex plate interactions (cf. Braun & Beaumont, 1995; Schellart, 2004). Similarly, slab dip, curvature, or stagnation behaviour may reflect limitations in model rheology, density structure, or the accuracy of the input plate kinematics.

Here we systematically compare slab geometries predicted by latest-generation G-ADOPT models with seismic imaging across eight well-studied subduction systems: the Aegean, Brasilia, Aleutian, Caribbean, Izu–Bonin, Mariana, Sunda, and Tonga–Kermadec–Hikurangi regions. For each case, we synthesise geological interpretations (e.g., Jolivet & Brun, 2010; Goes et al., 2017), review reconstructed kinematics (e.g., Zahirovic et al., 2022), and evaluate model–tomography agreement with two tomography models (Ritsema et al., 2011; Simmons et al., 2015) in terms of: slab depth; polarity and dip; lateral position and extent; and statistical misfit. These two tomography models are chosen for the availability of resolution operators that allow tomographic filtering of the modelled slabs for more direct comparison (Zaroli et al., 2017; New et al., 2025a).

With these comparisons, we highlight both the strengths and the limitations of G-ADOPT, however we also aim to provide insight into the behaviour of emergent-geometry MCMs more broadly. By identifying where and why modelled slabs diverge from (or agree with) tomographic images, we can diagnose deficiencies in plate reconstructions, trench-migration histories, and geodynamic model assumptions. Ultimately, this work provides a framework for improving reconstruction–convection consistency in future global models, advancing our understanding of Earth's long-term tectonic and mantle evolution.

2 Methods

2.1 Plate reconstruction inputs

As the driving input of the MCM, we use the 410 Ma to present-day plate kinematic reconstruction of Zahirovic et al. (2022, hereafter *Z22*), which combined the reconstructions of Young et al. (2019, 410–250 Ma), Müller et al. (2019), and Cao et al. (2022, 250–0 Ma). This reconstruction bridges the typical divide between pre- and post-Pangea reconstructions that has typically existed, where pre-Pangea reconstructions have relied on palaeomagnetic reference frames, while post-Pangea reconstructions have used hotspot reference frames. *Z22* uses a palaeomagnetic reference frame

for both periods, then, following the method of Tetley et al. (2019), derives an absolute mantle reference frame that minimises true polar wander and net lithospheric rotation. This isolation of the plate–mantle system makes *Z22* particularly suitable for driving mantle convection models.

2.2 Mantle circulation model

The most common way to forward model mantle circulation is to impose surface velocity boundary conditions from a tectonic reconstruction onto a convecting mantle. At convergent plate boundaries in the reconstruction, subduction-related parameters are then prescribed as part of *data assimilation*, including, for example, subduction polarity, slab dip angle, crustal temperature (based on age), and chemical composition (e.g., Li et al., 2023). Recent mantle convection models allow subduction geometry to emerge dynamically from the imposed plate kinematics and mantle rheology alone, without prescribing slab geometry (e.g., Arnould et al., 2020; Davies et al., 2022). Consequently, the rheological properties of the lithosphere and mantle (e.g., viscosity contrasts, temperature–pressure relationships) and the kinematic consistency of the plate reconstruction (e.g., actual convergence at subducting margins, ridge jumps) exert a stronger control on slab morphology and, in turn, on overall mantle structure.

2.3 Tomographic comparison

To evaluate the slab morphology predicted by the MCM, we compare modelled slabs across a range of well-studied subduction systems with two global seismic tomography models: *S40RTS* (Ritsema et al., 2011) and *LLNL-G3D-JPS* (Simmons et al., 2015). These models were selected primarily due to the availability of a resolution operator for tomographic filtering of the modelled slabs, which allow for more direct comparison between modelled and imaged mantle structures, and we applied these resolution operators following the method of New et al. (2025a). *S40RTS* is a global S-wave velocity model derived from surface- and body-wave data up to spherical harmonic degree 40 (∼1000–1100 km wavelength), and has been the standard reference when tomographic filtering is employed (e.g., Schuberth et al., 2009; Davies et al., 2012; Nerlich et al., 2016; Koelemeijer et al., 2018). *LLNL-G3D-JPS* is a global, joint P- and S-wave tomography model. It achieves finer resolution than *S40RTS* (∼400 km in the upper mantle and transition zone, ∼800 km in the lower mantle), making it better-suited for imaging the slabs produced by both ongoing and past subduction, while also providing resolution operator for the P-wave model for comparison with a mantle model (e.g., Lin et al., 2022; New et al., 2025b).

2.4 Comparison metrics

To assess the agreement between modelled and imaged slabs, we evaluate several key features of slab morphology in our models compared to tomography:

(i) *Depth*: does the modelled slab reach the same depth as the imaged anomaly at present day?

(ii) *Dip and polarity*: does the modelled slab dip at a similar angle to the imaged anomaly and in the same direction?

(iii) *Lateral position and extent*: is the modelled slab located in the same horizontal position as the imaged anomaly, and does it have a similar lateral extent?

(iv) *Statistical misfit*: what are the ℓ^2 and Wasserstein misfits between the modelled and imaged slabs after tomographic filtering?

The ℓ^2-norm is defined the usual way (i.e., the square root of the sum of the squared differences). The Wasserstein metric, familiar from the field of optimal transport, can be thought of as the effort needed to transform one distribution into another. Both are calculated following tomographic filtering of the modelled slabs—with a somewhat arbitrary depth cut-off of 1500 km due to our focus here on slab morphology—as described in New et al. (2025b). Two things must be kept in mind when interpreting these metrics. First, they are relative measures; there is no threshold value for a good fit. Second, comparing across misfit categories is not meaningful; comparisons should be made between regions only. A summary of the qualitative and quantitative assessments for each region is provided in Table 1.

3 Results

Here, we summarise the interpretation of seismic tomography in the literature for each subduction system, describe the relevant aspects of the *Z22* reconstruction, and evaluate the agreement between modelled and imaged slabs according to the metrics outlined above, first for continental settings and then for oceanic/arc settings.

As examples of where the models perform well (Aleutian) and poorly (Caribbean) we show the palaeotrench locations and predicted temperature structure at key times in the past (Figures 1 and 3). For these anomalies, we also show the present-day tectonic setting, predicted temperature structure, tomographically filtered modelled seismic velocity structure, and seismic tomography (Figures 2 and 4). All figures of modelled seismic velocity structure use the same colour scale as the corresponding tomography figures for ease of comparison. Figures for all other anomalies are provided in the supplementary materials (Appendix B).

3.1 Continental settings

3.1.1 Aegean anomaly

The Aegean anomaly is located below southeastern Europe and is imaged by tomography from the Hellenic subduction system down to the lower mantle. It is well-studied, and is commonly interpreted as the subducting lithosphere of the African plate (e.g., Spakman et al., 1988; de Jonge et al., 1994; Piromallo & Morelli, 1997; van Hinsbergen et al., 2005; Chang et al., 2010).

In *Z22*, the African plate subducts beneath Eurasian lithosphere from 67 Ma to present day, following Le Breton et al. (2017) and Müller et al. (2019). According to this reconstruction, in the Eurasian reference frame there is minimal trench migration until 15 Ma, after which the trench retreats at 14.7 km Myr^{-1} until present day. In contrast, when viewed in the mantle frame, the first 52 Myr of subduction is characterised by rapid trench advance of 18.0 km Myr^{-1}. Up to the late Eocene, there is double subduction: the Adria microplate is sandwiched between the African and Eurasian plates, with Africa subducting beneath Adria and Adria beneath Eurasia. In the early Oligocene, the Mediterranean microplate initiates then steadily widens until it meets the Hellenic trench by present day (van Hinsbergen et al., 2014).

From this reconstruction, one expects a north-northeast dipping slab. However, subduction polarity in G-ADOPT is determined implicitly by the direction of trench migration and dip angle by the speed of migration, rather than both being explicitly imposed as in earlier mantle convection codes (e.g., CitComS). This results in slab morphology that is incompatible with the imaged Aegean anomaly (Figure B1). Although the slab reaches the correct depth at present day (1400 km), and dips at approximately the same angle from horizontal, the polarity is reversed, with the slab dipping

south-southwest instead of north-northeast. We find somewhat poor misfit metrics of $\ell^2 = 0.242$ and Wass. $= 0.355$ for *S40RTS*, and $\ell^2 = 0.243$ and Wass. $= 0.599$ for *LLNL-G3D-JPS*.

3.1.2 Brasilia anomaly

The Brasilia anomaly is located below northern to central South America and is imaged by tomography from the Nazca subduction system down to the lower mantle. It was interpreted by van der Meer et al. (2018) as the result of continuous subduction of the Farallon plate since at least the earliest Jurassic, with estimates of the onset of arc magmatism ranging from 200–145 Ma (Villagómez et al., 2011; Boekhout et al., 2012; Demouy et al., 2012). However, more recent interpretation of tomographic data suggests that subduction was not continuous since the Mesozoic, instead consisting of episodes of subduction and slab break-off, with the most recent period of subduction beginning in the late Cretaceous (Chen et al., 2019).

In *Z22*, subduction under South America begins from the very start of the model at 410 Ma with the Phoenix plate, which transitions to subduction of the Farallon plate in the Carboniferous as the Farallon–Phoenix mid-ocean ridge (MOR) migrates south, with trench retreat of 30.7 km Myr^{-1} in the mantle frame. During the Permian, there is minimal trench migration with only ~300 km of net retreat. Rapid trench retreat then resumes for a brief period of 20 Ma, followed by a long period of minimal migration until the middle Cretaceous. In the early Cretaceous, there are additionally a pair of back-arc microplates in the north. From 120 Ma to present day, there is steady trench retreat of 18.1 km Myr^{-1}. The tectonic reconstruction from the middle Cretaceous to present day of the Pacific plate and Andean margin is based on the models of Müller et al. (2019) and Torsvik et al. (2019).

The resulting slab morphology from the most recent period of subduction and trench retreat is—after tomographic filtering—broadly compatible with the Brasilia anomaly imaged by *LLNL-G3D-JPS* (Figure B2), despite the discrepancy in onset timing between *Z22* and Chen et al. (2019). The slab reaches nearly the correct depth at present day (1200 km versus 1350 km) and dips at approximately the same angle, with comparable volume. However, the slab is offset to the west compared to the imaged anomaly by 2–3°. The comparison with *S40RTS* is less favourable, however this is likely due to the lower resolution of that model—*S40RTS* does not recover a fast anomaly in the lithosphere/uppermost mantle beneath the Andean margin (i.e., a continuous slab from present-day subduction penetrating into the lower mantle), which is clearly imaged in most other tomographic models. We find relatively good misfits of $\ell^2 = 0.153$ and Wass. $= 0.334$ for *S40RTS*, and $\ell^2 = 0.174$ and Wass. $= 0.365$ for *LLNL-G3D-JPS*.

3.2 Arc settings

3.2.1 Aleutian anomaly

The Aleutian anomaly is located beneath the Aleutian island arc and is imaged by regional tomography models in the upper mantle (Gorbatov et al., 2000; Qi et al., 2007; Koulakov et al., 2011; Martin-Short et al., 2016), and in global tomography models down to the top of the lower mantle (e.g., *UU-P07,* van der Meer et al., 2018, *LLNL-G3D-JPS*, Figure 2). $^{40}Ar/^{39}Ar$ dating of Aleutian igneous rocks provides a minimum age of 46 Ma for the onset of subduction (Jicha et al., 2006; Chekhovich et al., 2014).

In *Z22*, subduction of proto-Pacific lithosphere beneath the North American and Eurasian plates is long-lived, however within the last 100 Myr two jumps in trench location occur; first at 67 Ma and again at 46 Ma (Figure 1a), where the second is the iniation of Aleutian subduction

as derived from aforementioned isotope dating. From this initiation time, there is trench retreat of 15.8 km Myr^{-1} throughout. Due to the curved geometry of the Aleutian trench, subduction is oblique near the western end of the arc, becoming progressively more orthogonal towards the east. From 83 Ma, the Kula plate subducts beneath the North American plate, then at 41 Ma the MORs bounding the Kula plate terminate (Wright et al., 2016), after which the Pacific plate subducts beneath North America (Croon et al., 2008; Wright et al., 2015). The western margin bounding the Kula plate is designated in GPlates as a MOR, however, from 73–55 Ma there is actually a small amount of oblique convergence across this margin, according to the plate velocities derived from Euler pole rotations of the respective plates, then from 55–48 Ma the convergence becomes much more rapid and perpendicular. On the eastern end of the arc, the Kamchatka microplate gradually rotates into its present-day orientation, where the Pacific plate subducts beneath it with 26.5 km Myr^{-1} of trench retreat (Wright et al., 2016).

The resulting present-day slab morphology is a good match to the imaged Aleutian anomaly, with comparable volume in the transition zone and uppermost lower mantle, and overproduction of slab material in the upper mantle (Figure 2). Tomographic filtering makes dip angle difficult to interpret (due to smearing), however the unfiltered temperature field has very similar dip angle to that imaged by *LLNL-G3D-JPS* of ∼40°. After tomographic filtering, the modelled slab achieves similar depth to the anomaly imaged by *LLNL-G3D-JPS* (∼750 km). The lateral extent of the Aleutian anomaly is 3–4° larger to the northeast than produced by the filtered model. The aforementioned convergence across the Kula–Pacific MOR is visible in the model as a cold downwelling by 50 Ma (Figure 1b). Although present, the Aleutian anomaly is not well-imaged by *S40RTS* due its lower resolution, resulting in non-slab-like morphology, and it does not penetrate below the transition zone, whereas the *S40RTS*-filtered slab does. The results from G-ADOPT are broadly similar to those of previous regional models, insofar as they produce a continuous north-dipping slab from the trench to the lower mantle (e.g., Creager & Boyd, 1991; Billen & Gurnis, 2003; Clark & Müller, 2008), however our model produces a much more detailed slab morphology. We find good misfit metrics of $\ell^2 = 0.159$ and Wass. $= 0.196$ for *S40RTS*, and $\ell^2 = 0.172$ and Wass. $= 0.593$ for *LLNL-G3D-JPS*.

3.2.2 Caribbean anomaly

The Caribbean anomaly is imaged in the upper mantle and transition zone, where the Atlantic plate subducts below the Caribbean plate along the Lesser Antilles subduction system. It is steeply westward dipping until 550–600 km depth, below which it becomes near-horizontal (van der Hilst & Spakman, 1989; van Benthem et al., 2013). The initiation of the Lesser Antilles arc, and accompanying basins, provides a minimum age of 45 Ma for the onset of subduction (Burke, 1988; Boschman et al., 2014). Deeper anomalies are imaged in the lower mantle, which have been interpreted as older episodes of subduction beneath the proto-Caribbean plate during the Mesozoic. They are discontinuous with the Caribbean anomaly, which may be explained by a STEP fault causing slab break-off in the early Eocene (van Benthem et al., 2013; van der Meer et al., 2018).

In *Z22*, the STEP fault transition from earlier subduction occurs at 53 Ma, where the trench jumps eastward by 400 km at its southern end. Subduction begins with ∼200 km of relatively rapid trench retreat until 45 Ma, followed by a period of no net migration until 30 Ma. There are then ∼275 km of slower trench advance up to present day (Figure 3a). Constraints on the circum-Caribbean region are from the plate model of Müller et al. (2016), which is itself based on Boschman et al. (2014) with minor modifications.

The Caribbean slab reaches approximately the correct depth at present day (700 km versus

Figure 1

Aleutian anomaly history. (a) Palaeotrench locations. (b), (c), (d) G-ADOPT temperature perturbation structure ΔT at 50, 40 *and* 20 Ma*, respectively. Dashed lines represent the* 410, 660 *and* 1000 km *discontinuities.*

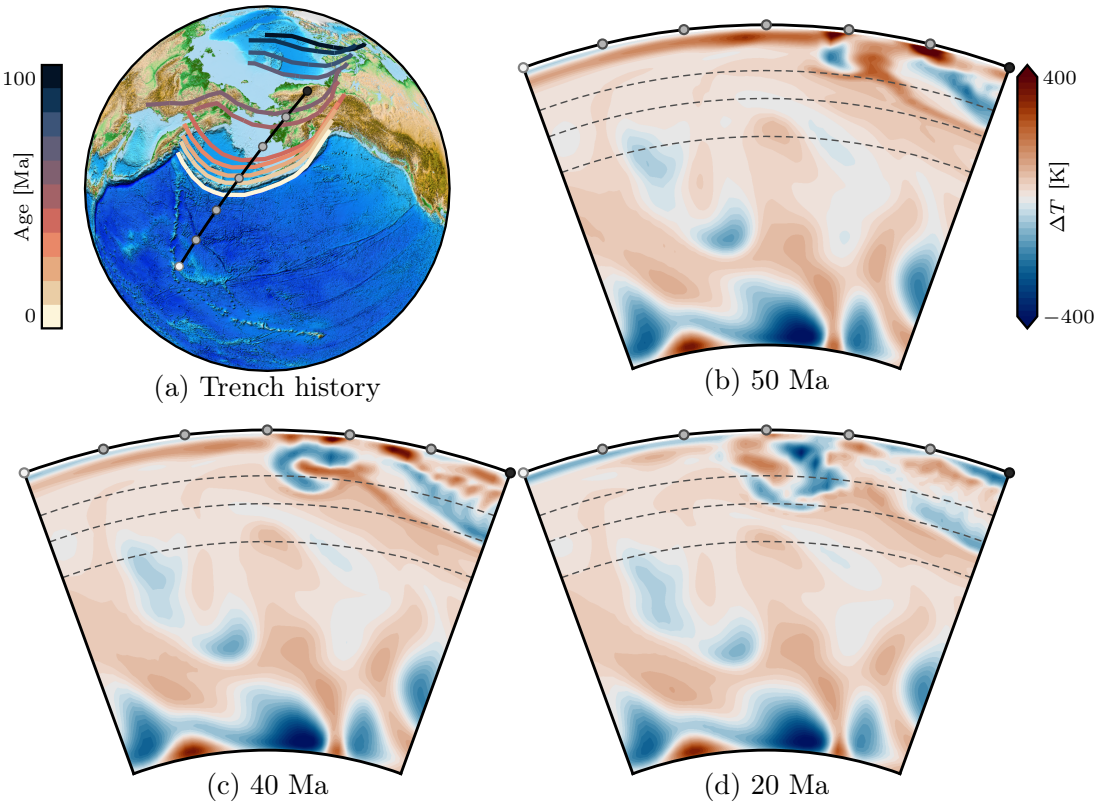

750 km), and has a similar dip angle from horizontal, but dips steeply eastward instead of the expected steep westward dip. Due to the very steep dip angle, the lateral position and extent of the slab matches fairly well in the upper mantle, despite the incorrect polarity. The modelled slab also does not achieve the near-horizontal geometry in the lower transition zone seen in tomographic models, instead penetrating deeper in the uppermost lower mantle. Despite this, the volume of the modelled slab is comparable to that of the imaged anomaly. There is a significant amount of slab material in the transition zone to lower mantle depths which can be attributed to long-lived Farallon subduction (Figures 3b–3d), and material at comparable depths and locations is imaged in tomography (Figures 4e and 4f). We find surprisingly good misfit metrics of $\ell^2 = 0.153$ and Wass. $= 0.371$ for *S40RTS*, and $\ell^2 = 0.122$ and Wass. $= 0.322$ for *LLNL-G3D-JPS*.

3.2.3 Izu-Bonin anomaly

The Izu-Bonin anomaly is well-imaged in tomography models, extending from the present-day trench to the bottom of the transition zone, where it then lies horizontally over at least 15° as projected to the surface (van der Hilst et al., 1991; Bijwaard et al., 1998; Gorbatov & Kennett, 2003; Sugioka et al., 2010; Fukao & Obayashi, 2013; Jaxybulatov et al., 2013). It was interpreted by van der Meer et al. (2018) as the result of Pacific subduction beneath the Philippine Sea plate since the early Eocene, with U/Pb and ^{40}Ar/^{39}Ar dating providing a minimum age of 52–51 Ma (Arculus et al., 2015; Ishizuka et al., 2018).

Figure 2

(a) The present-day tectonic setting of the Aleutian anomaly. (b) G-ADOPT temperature perturbation from layer mean ΔT. (c), (d) G-ADOPT seismic velocity perturbation $d\ln v_{S,P}$ from layer mean, filtered by S40RTS and LLNL-G3D-JPS respectively. (e), (f) Seismic tomography in S40RTS and LLNL-G3D-JPS.

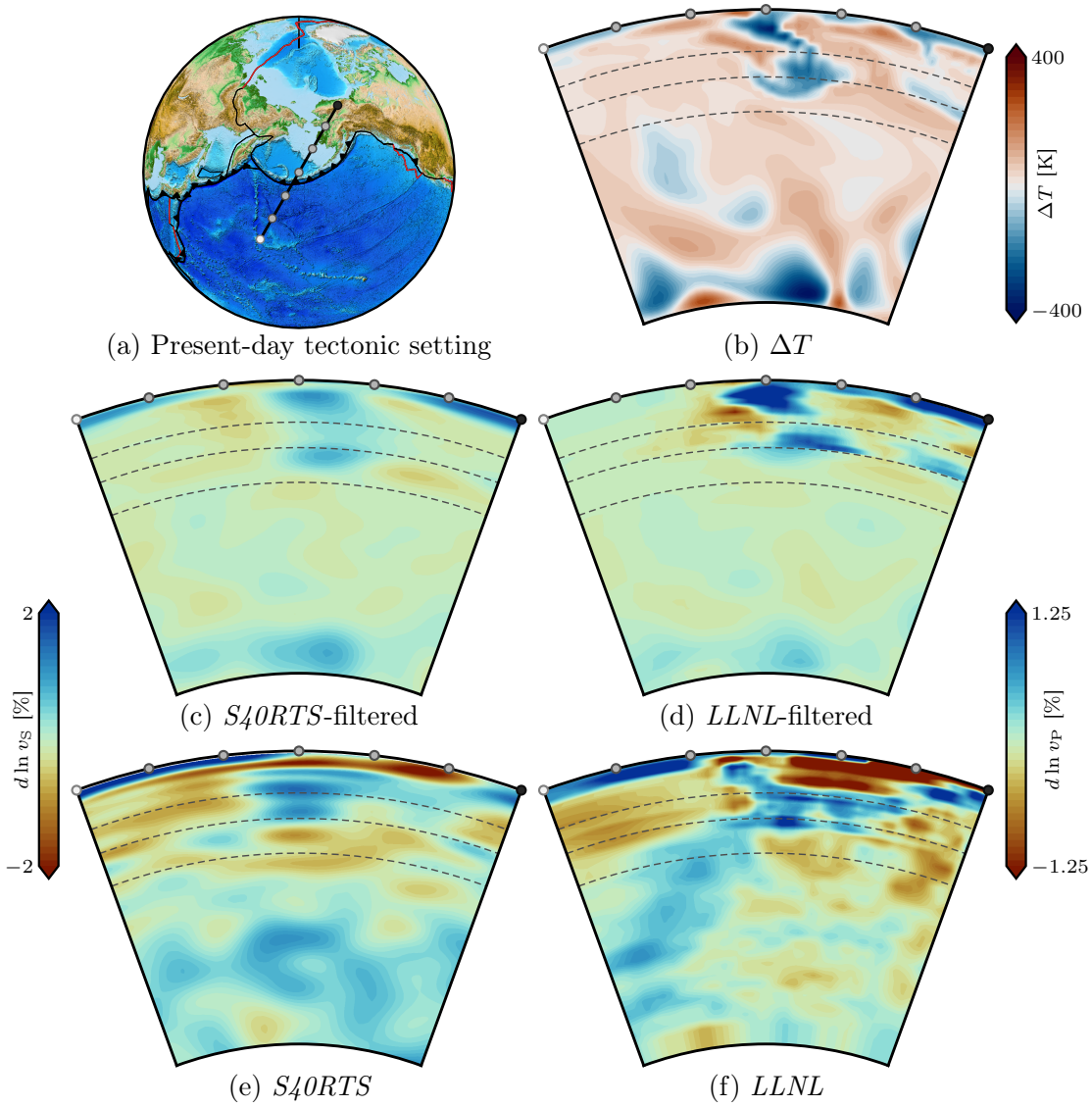

In *Z22*, the subduction zone, which eventually becomes the Izu-Bonin-Mariana trench, initiates at 55 Ma, trending NW–SE rather than the present-day N–S orientation. Over the next 20 Myr, the northern end of the trench experiences extremely rapid trench retreat at 102.5 km Myr^{-1}, while the southern end retreats at a slower rate of 27.5 unit, resulting in a NNW–SSE orientation of the trench by 35 Ma. Until present day, there is minimal net migration of the trench, however there are small oscillations between advance and retreat. The tectonic reconstruction of Southeast Asia and the western Pacific is based on Zahirovic et al. (2014) and Zahirovic et al. (2016). Deforming components of the reconstruction prior to 40 Ma are based on Yang et al. (2016), and from 40 Ma to present day on Bai et al. (2015).

The resulting slab morphology is a good match to the imaged anomaly from the Izu-Bonin trench down to the bottom of the transition zone, although the model only produces a short lateral

Figure 3

Caribbean anomaly history. (a) Palaeotrench locations. (b), (c), (d) G-ADOPT temperature perturbation structure ΔT at 100, 50 and 25 Ma, respectively.

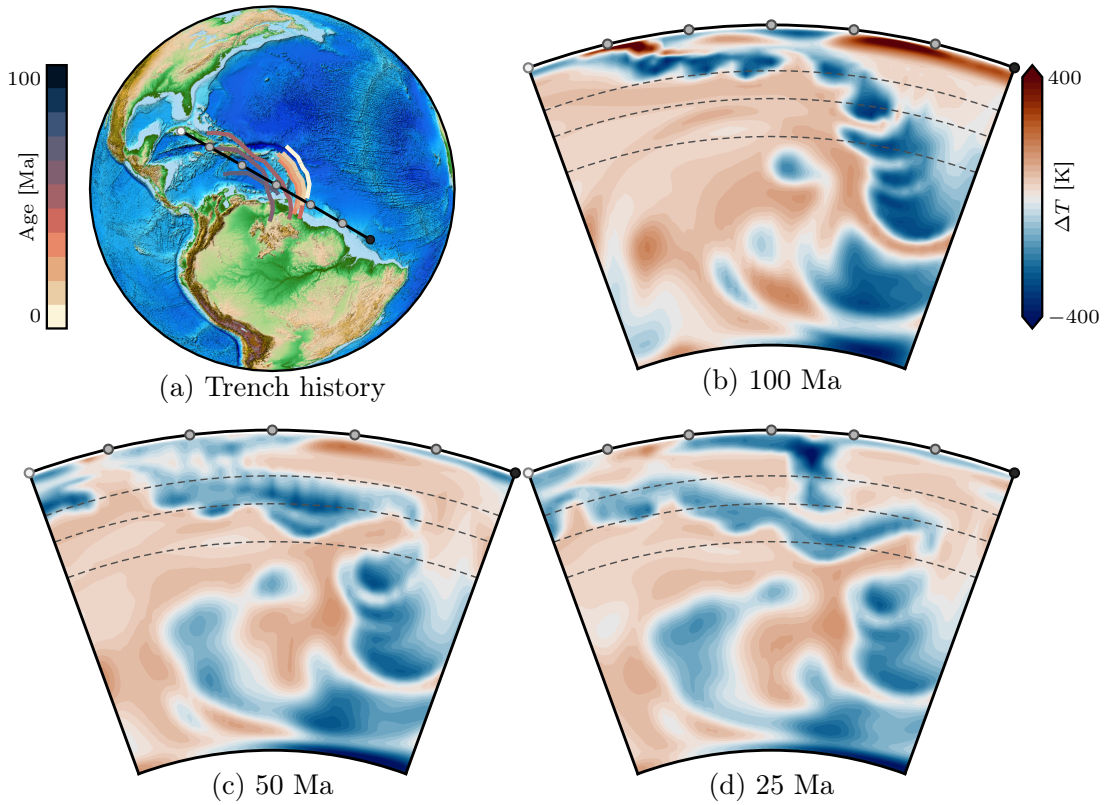

extent of stagnant slab behaviour (∼2° as projected to the surface compared to the ∼15° imaged; Figure B4). A dip trend from *UU-P07* is identified by van der Meer et al. (2018, though they do not quantify it, we assess it to be ∼45° below horizontal throughout the upper mantle). This is not reproduced in *Z22*, where the slab remains near-horizontal for the first 200–300 km depth, then steepens sharply to near-vertical until the bottom of the transition zone, before flattening again. This morphology, in contrast, bears a stronger resemblance to that imaged by *LLNL-G3D-JPS*, where, although the slab appears disconnected, there is the same horizontal-vertical-horizontal behaviour. We find poor misfits of $\ell^2 = 0.252$ and Wass. $= 0.655$ for *S40RTS*, and $\ell^2 = 0.277$ and Wass. $= 0.576$ for *LLNL-G3D-JPS*.

3.2.4 Mariana anomaly

The Mariana anomaly is just south of the Izu-Bonin anomaly (Section 3.2.3), and is therefore imaged in many of the same tomography models (e.g., Bijwaard et al., 1998; Gorbatov & Kennett, 2003; Fukao & Obayashi, 2013; Jaxybulatov et al., 2013). It was intepreted by van der Meer et al. (2018) to represent subducting Pacific lithosphere steeply dipping to the west. However unlike the Izu-Bonin slab, it does not exhibit stagnation in the transition zone, instead penetrating into the lower mantle. It is connected to the Izu-Bonin slab to the north until 300–400 km depth, but below this depth the anomalies are disconnected due a tear fault, originating from the Marcus–Necker ridge (Miller et al., 2004). To the south, the Mariana slab is similarly disconnected by a tear. As with the Izu-Bonin slab, U/Pb and $^{40}Ar/^{39}Ar$ dating provides a minimum age of 52–51 Ma for the

Figure 4

As in Figure 2 but for the Caribbean anomaly.

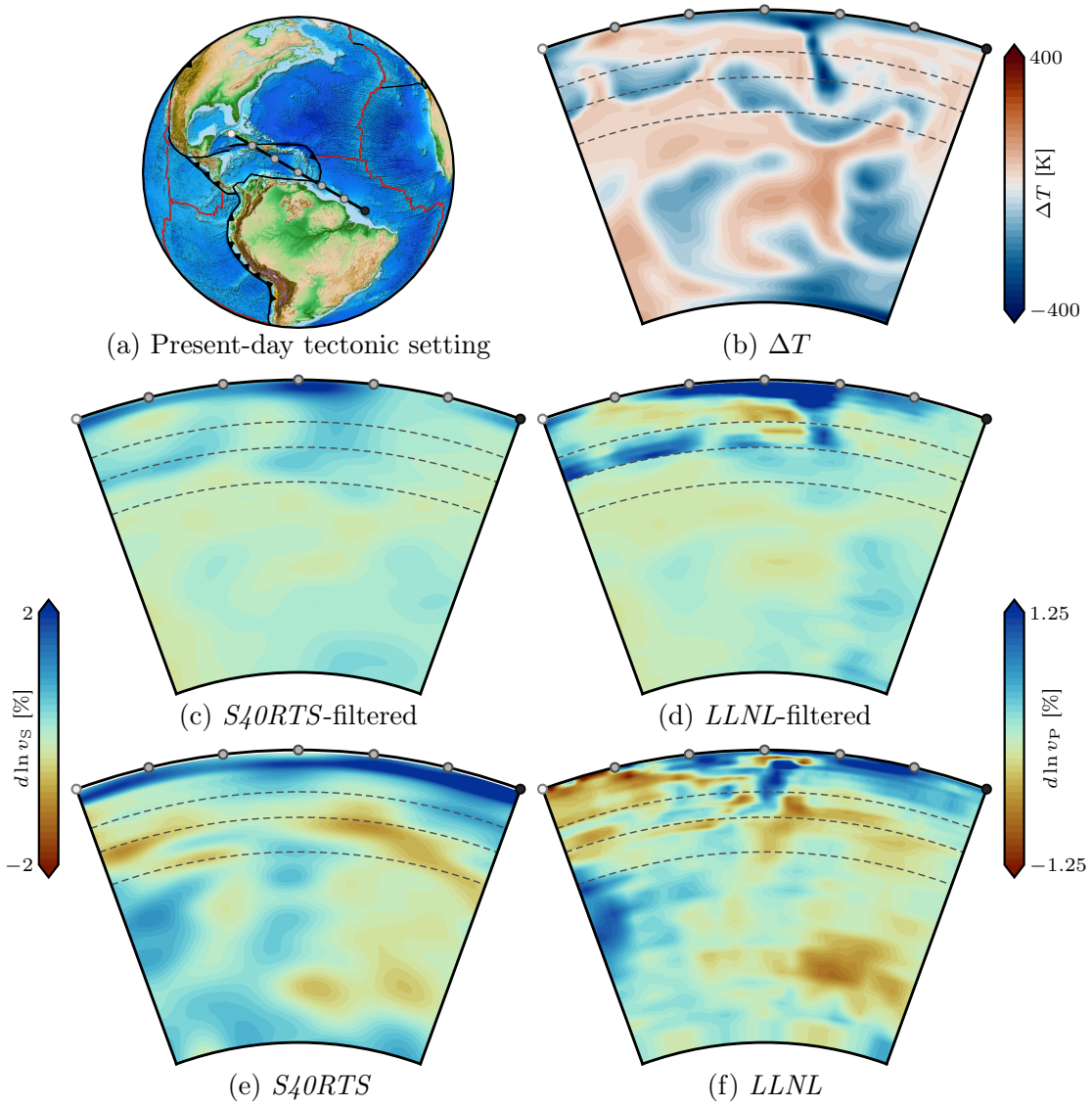

(a) Present-day tectonic setting (b) ΔT

(c) *S40RTS*-filtered (d) *LLNL*-filtered

(e) *S40RTS* (f) *LLNL*

onset of subduction.

Although it is part of the same subduction system as the Izu-Bonin slab, the tectonic history associated with the Mariana slab modelled in *Z22* is markedly different. Trench retreat during the first 20 Myr is much more moderate at a rate of 20 km Myr^{-1}. At this point, subduction terminates at the southern end of the trench, gradually propagating northward until 25 Ma, at which point the trench jumps westward by ∼500 km. There are then 5 Myr of rapid trench retreat at 67.0 km Myr^{-1}, followed by minimal net migration until 10 Ma. Then, until present day, there is rapid trench advance at 44.7 km Ma^{-1} until the trench achieves its present-day position.

The modelled slab penetrates down to the lower mantle, achieving a depth of 850 km. The dip angle is sub-horizontal in the upper mantle, steepening to near-vertical in the lower transition zone before shallowing again in the lower mantle (Figure B6). Except for the horizontal portion in the upper mantle, this morphology is similar to the anomaly imaged by *LLNL-G3D-JPS*, although the modelled slab is offset to the west by ∼3°, and is not as deep. We find relatively good misfits of

$\ell^2 = 0.172$ and Wass. $= 0.374$ for *S40RTS*, and $\ell^2 = 0.147$ and Wass. $= 0.327$ for *LLNL-G3D-JPS*.

3.2.5 Sunda anomaly

The Sunda anomaly is another widely-studied seismically fast body which—in the upper mantle—has been interpreted as Australian and Indian lithosphere actively subducting beneath Java–Sumatra (e.g., Fukao et al., 1992; Puspito et al., 1993; Puspito & Shimazaki, 1995; Widiyantoro & van der Hilst, 1996; Widiyantoro & Van Der Hilst, 1997; Widiyantoro et al., 2000; Replumaz et al., 2004; Pesicek et al., 2010; Spakman & Hall, 2010; Koulakov, 2013; Zahirovic et al., 2014; Hall & Spakman, 2015; Wu et al., 2016). It is imaged reaching the base of the transition zone, and below this depth is visually continuous in most tomography models with a deeper anomaly that reaches well into the lower mantle. Some authors have interpreted the deeper anomaly as contiguous with the Sunda slab (e.g., Replumaz et al., 2004; Zahirovic et al., 2014), while others suggest that the deeper anomaly originates from a different subduction episode altogether, based on its different strike (e.g., Hall & Spakman, 2015; Wu et al., 2016; van der Meer et al., 2018).

In *Z22*, there has been subduction under terranes that will eventually become part of the Sunda arc since the early Jurassic, however the current episode of subduction begins at 70 Ma, with minimal net trench migration until 45 Ma. There is then trench retreat at 32.1 km Myr^{-1} until 20 Ma, followed by just ∼150 km of trench advance until present day. The SW–NE striking subduction zone, which previous authors have associated with the deeper anomaly, is modelled in *Z22* from 70–48 Ma. However, for all but the final 5 Myr of age range, subduction is oblique—with the underlying plate moving NNE—rather than orthogonal. SE Asia is characterised by its famously complex assortment of back-arc spreading, subduction, and microplate activity. North of Sunda, subduction is opposite in polarity (south-dipping). The Izanagi and South Philippine Sea (SPS) lithosphere subduct beneath Eurasia until 47 Ma. After 47 Ma, rollback transfers subduction to the South China Sea–margin system (SPS beneath South China Sea lithosphere). Eventually, rollback causes the trench to meet the Eurasian-margin system and the subduction systems merge. To the northeast, there is also the north and south Celebes Sea plates, where Australian lithosphere subducts with rapid trench retreat until 25 Ma at which point it lines up with the Sunda trench. It then advances northward again until 10 Ma, when subduction terminates.

The resulting slab penetrates into the lower mantle to a depth of ∼1000 km dipping steeply to the northeast (Figure B8). Another, deeper slab remnant is also present under Java–Sumatra from ∼1000–1400 km depth, but it is discontinuous with the shallower slab. Interrogating model output through time (Figure B7), this deeper anomaly can be identified with the Southeast Asian slab graveyard, which has also been found in similar modelling studies (e.g., Zahirovic et al., 2016). This general morphology is similar to that imaged by *LLNL-G3D-JPS*, although in tomography, everything is ∼200–300 km shallower, and the shallower anomaly extends much further northeast, lying flat in the transition zone. We find moderate misfit values of $\ell^2 = 0.212$ and Wass. $= 0.248$ for *S40RTS*, and $\ell^2 = 0.173$ and Wass. $= 0.459$ for *LLNL-G3D-JPS*.

3.2.6 Tonga–Kermadec–Hikurangi anomaly

The Tonga–Kermadec–Hikurangi (TKH) anomaly is a north–south striking anomaly that has been interpreted as a single slab penetrating down to the uppermost lower mantle (e.g., van der Hilst, 1995; Bijwaard et al., 1998; Fukao et al., 2001; Hall & Spakman, 2002; Gorbatov & Kennett, 2003; Schellart et al., 2009; Fukao & Obayashi, 2013). This penetration occurs most prominently in the south. However, in the north, the slab appears to stagnate at the bottom of the transition zone, explained by increased trench retreat speed (van der Meer et al., 2018). There is a large disparity

between ages that have been proposed for the onset of subduction, ranging from 30 Ma (van de Lagemaat et al., 2018), to 45–50 Ma (Hall & Spakman, 2002; Wu et al., 2016) to 85 Ma (Schellart et al., 2006).

In *Z22*, subduction at the TKH trench begins at 45 Ma, consistent with the middle estimate above, with the Pacific plate subducting beneath the Australian plate. However, it is worth noting that proto-Pacific lithosphere has been continuously subducting, to various degrees, beneath the Australian margin since the beginning of the model at 410 Ma, with only a short break (where subduction is inverted), from 55–45 Ma. There is rapid trench retreat of 60.3 km Myr^{-1} at the northern end of the trench, decreasing to a more moderate 27.0 km Myr^{-1} at the southern end, where subduction is highly oblique. From 45–19 Ma, there are a series of microplates—variously bounded by back-arc spreading and secondary subduction—which eventually become the North Loyalty and South Fiji basins, and later the Lau Basin and Havre Trough (Matthews et al., 2015). From 38–33 Ma, the MOR which generates the North Loyalty basin actually has convergence across it, according to the plate rotations given in the reconstruction for this time range.

The resulting slab morphology is a fair match to the TKH anomaly imaged by both *S40RTS* and *LLNL-G3D-JPS*, with the slab penetrating into the uppermost lower mantle to a depth of ∼1200 km, albeit further to the west by ∼5° (Figure B10). There is similar morphology in both modelled and imaged slabs, with sub-horizontal behaviour in the upper mantle, which then steepens in the transition zone (although *LLNL-G3D-JPS* does not image much at all in the transition zone, *S40RTS* and other tomography models do). The deeper cold anomalies in the temperature perturbation field are much less strong than the anomaly produced in the upper mantle, and this is even more pronounced after tomographic filtering when compared directly to the imaged anomalies. However, despite this superficial similarity, the continuity of the modelled slab is caused by the accidental convergence across the MOR generating the North Loyalty basin from 38–33 Ma, which is unlikely to have occurred in reality given geological constraints. We find poor misfits of $\ell^2 = 0.235$ and Wass. $= 0.480$ for *S40RTS*, and $\ell^2 = 0.213$ and Wass. $= 0.558$ for *LLNL-G3D-JPS*.

4 Discussion

4.1 Regions of strong agreement: rollback-dominated systems

In several tectonic settings—most notably the Aleutian, Brasilia, Mariana, and Sunda regions—the G-ADOPT predictions broadly match tomographically imaged slab morphology, including dip direction, approximate depth range, and overall continuity. These systems share a common characteristic: subduction has been governed largely by trench retreat with relatively simple plate boundary geometries and limited overriding-plate deformation. Previous modelling work has shown that rollback-dominated subduction is comparatively straightforward for global MCMs to reproduce because slab dip and descent rate are controlled primarily by lithospheric buoyancy and trench-normal convergence (Schellart, 2004; Funiciello et al., 2008; Capitanio et al., 2010). Our results confirm that trench kinematics are relatively simple, emergent slab morphology can converge well with mantle structure inferred from tomography (Fukao & Obayashi, 2013; van der Meer et al., 2018).

4.2 Systematic failure during trench advance and polarity instability

The most persistent misfits arise in the Aegean and Caribbean, where the model predicts the incorrect subduction polarity relative to tomography. This behaviour directly reflects the current

Table 1

Summary of model–data comparisons for each subduction system studied. Because we are primarily interested in slab morphology in active subduction systems, we choose a (somewhat arbitrary) depth cut-off of 1500 km *for the misfit calculations.*

Anomaly	Depth	Dip/polarity	Lateral position	Lateral extent	Misfit			
					S40RTS		*LLNL*	
					ℓ^2	Wass.	ℓ^2	Wass.
Aegean	Good Slab reaches the correct present-day depth (1400 km).	Poor Trench-advance episodes causes reversed polarity (SSW-dipping).	V. poor Reversed polarity places the slab on the wrong side of SZ.	V. poor Wrong-way dip yields little overlap in with tomography.	0.242	0.355	0.243	0.599
Brasilia	Moderate Slab is ∼150 km too shallow.	Good Slab dip angle agrees closely with the tomographic anomaly.	Moderate Slab is offset westward by 2–3° relative to tomography.	Good Comparable to tomography after filtering.	0.153	0.334	0.174	0.365
Aleutian	Good Filtered slab reaches a similar depth to *LLNL* (∼750 km).	Good Unfiltered structure shows a similar dip to *LLNL* (∼40°).	Good Modelled slab aligns well with the imaged anomaly.	Good Extent similar, tomography extends 3–4° farther NE.	0.159	0.196	0.172	0.593
Caribbean	Good Slab depth matches closely (700 km vs 750 km imaged).	Moderate Dip is similar but polarity is reversed (E vs. W).	Good Steep dip preserves positional match despite polarity error.	Good Overall slab volume comparable to tomography.	0.153	0.371	0.122	0.322
Izu–Bonin	Good Slab matches tomography from the trench to base of UM.	Moderate Model misses the inferred ∼45° dip, showing stepped geometry.	Good Slab is colocated with the imaged anomaly down to TZ.	V. poor Only ∼2° of stagnant slab is produced versus ∼15° imaged.	0.252	0.655	0.277	0.576
Mariana	Moderate Slab penetrates to LM (850 km) but not as deep as imaged.	Good TZ steepening to near-vertical broadly consistent with *LLNL*.	Moderate Slab is offset ∼3° to the west relative to the imaged anomaly.	Moderate Laterally extensive but ∼5–6° less than imaged.	0.172	0.374	0.147	0.327
Sunda	Poor Comparable structure imaged ∼250 km shallower than model.	Good Steep northeast-dipping slab geometry is similar to *LLNL*.	Good Slab lies beneath Java–Sumatra in the expected location.	Moderate Tomography flatter TZ slab compared to model.	0.212	0.248	0.173	0.459
Tonga–Kermadec–Hikurangi	Moderate Slab penetrates to the uppermost lower mantle (to ∼1200 km) but not perfectly.	Good UM sub-horizontal/TZ steepening matches imaged morphology.	Moderate Slab is shifted ∼5° west of the imaged anomaly.	Moderate Apparent continuity/extent is partly artefactual and deeper anomalies weaken after filtering.	0.235	0.480	0.213	0.558

G-ADOPT implementation in which polarity is inferred solely from trench migration direction rather than from explicit upper-plate geometry or inherited subduction configuration. Geodynamic studies have long shown that trench advance inverts the usual force balance controlling slab dip, often steepening the slab or even reversing its polarity under certain boundary conditions (Braun & Beaumont, 1995; Schellart, 2005; Stegman et al., 2010b, 2010a). Because the model reads polarity from trench migration rather than from geological constraints, episodes of rapid trench advance in the reconstructions lead to physically implausible slab orientations. These mismatches therefore highlight a structural limitation within the modelling framework rather than an error in the input kinematic parameters (i.e. plate reconstructions themselves).

One solution may be to incorporate more geologic data, drawing inspiration from the so-called *tomotectonic* approach (e.g., Li et al., 2023). Introducing a different density profile in regions of known continental lithosphere may allow the correct dip polarity to arise naturally without artificially prescribing it, and without the order-of-magnitude-higher computational expense of billions of geochemical tracers (Peng et al., 2021).

4.3 Dip and stagnation misfits: rheological and kinematic sensitivities

In several subduction zones, including Izu–Bonin and Mariana, the model reproduces the overall depth extent of the slabs but mismatches the observed dip angle or stagnation behaviour. Previous geodynamic work has emphasised that slab dip is highly sensitive to the balance between negative buoyancy, mantle viscosity structure, and upper-plate motion (Goes et al., 2017; Holt et al., 2018; Holt & Royden, 2020). The failure of the model to reproduce shallow dips or stagnated geometries near the 660 km discontinuity may reflect (i) simplified mantle viscosity profiles that lack strong depth-dependent variations, (ii) insufficient slab weakening or hydration, or (iii) incomplete representation of microplate interactions that strongly modulate trench retreat. Slab stagnation above or below the transition zone, widely documented in tomography (Fukao & Obayashi, 2013), is particularly sensitive to both density structure and lower-mantle viscosity (Fukao et al., 2001; Richard & Bercovici, 2009), suggesting that part of the misfit may arise from mantle rheological assumptions within G-ADOPT.

4.4 Implications for plate reconstructions

Where reconstructed trench motions produce slab geometries that agree with tomography (e.g., Aleutian, Sunda, Brasilia), our results lend independent support to the underlying kinematic histories. This aligns with recent efforts to use mantle structure to evaluate reconstructions (van der Meer et al., 2010; Müller et al., 2019; Zahirovic et al., 2022). Conversely, in systems where the model grossly deviates from observations, two categories of mismatch emerge: (i) artefacts generated by the model's polarity logic, and (ii) plausible indicators of reconstruction uncertainty. Artefacts of polarity logic are evident in the Aegean and Caribbean, where there is non-negligible trench advance in the mantle frame. Reconstruction-related discrepancies include the magnitude of trench rollback in parts of IBM and TKH, and the misprescribed convergence of margins in the Aleutians and TKH (Figure 5). Distinguishing between these cases requires careful geological judgement, but our comparisons show that slab morphology can identify where reconstructions are likely robust and where they may require refinement.

The misfit metrics presented in Table 1 provide a quantitative basis for future refinement of reconstructions. For example, the relatively high misfit values in the Izu–Bonin and TKH systems suggest that trench kinematics or plate boundary configurations in these regions may be less certain than previously thought. However, such metrics should always be interpreted in the context of

Figure 5

Misprescribed margin type in (a) the Aleutians at 50 Ma *and (b) Tonga–Kermadec–Hikurangi at* 35 Ma. *Red lines are mid-ocean ridges, black lines with teeth are subduction zones, and grey arrows indicate plate motions in the mantle reference frame. In both cases, a margin in the centre of the figure is designated as a mid-ocean ridge in GPlates, however there is instead convergence across it.*

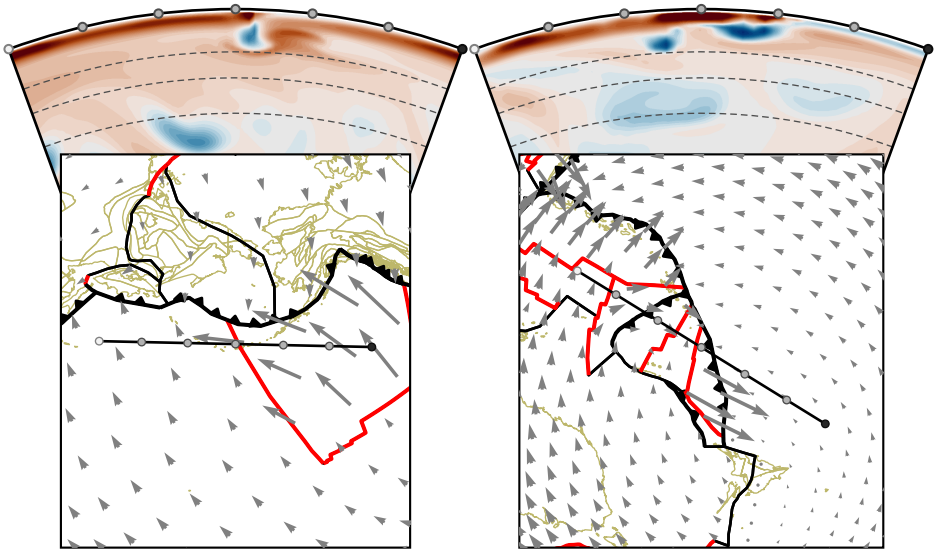

(a) Al at 50 Ma (b) TKH at 35 Ma

known model limitations, which will often require interrogation of MCM output through deep time. For example, the low misfit in the Caribbean system belies the fundamental polarity error discussed above.

4.5 Implications for modelling subduction in global convection frameworks

The results highlight several opportunities to improve reconstruction-driven global MCMs. First, slab polarity should be imposed or inferred from geological constraints rather than derived from trench migration alone, consistent with regional studies showing robust polarity persistence through complex trench motions (Lallemand et al., 2005). Second, viscosity and density profiles may require refinement to reproduce observed transition-zone stagnation patterns (Fukao et al., 2001; Fukao & Obayashi, 2013). Third, more accurate treatment of microplate geometries and overriding-plate dynamics may help reduce misfits in regions with trench curvature or plate-boundary reorganizations. More generally, our findings reinforce the need for coupled advances: improved reconstructions, more realistic rheologies, and physics-based criteria for subduction initiation, polarity, and tearing (Gurnis et al., 2018; Stern & Gerya, 2018). Reconstruction-driven global convection will only reach its full diagnostic potential when emergent slab geometry responds to physically meaningful tectonic parameters rather than simplified rules.

4.6 Importance of tomographic filtering

An important caveat on the use of seismic tomography in our benchmarks is that the two models we use (*S40RTS* and *LLNL-G3D-JPS*) are not equivalent in their resolving power. *S40RTS* is limited to spherical harmonic degree 40 (∼1000–1100 km wavelength), so it is effectively a low-pass view of mantle structure and tends to significantly smear, weaken, or even eliminate slab-scale features that are prominent in simulated mantle structure. This limitation is evident in some

of our regional comparisons (e.g., Aleutian, Sunda), where the match to *S40RTS* is noticeably poorer, likely reflecting resolution loss. By contrast, *LLNL-G3D-JPS* has substantially higher resolution (particularly in the upper mantle and transition zone: ∼400 km), making it better suited for evaluating slab morphology in more complex, small-to-medium scale settings (microplate interactions, slab tears, etc.). In this sense, *S40RTS* should be treated primarily as a conservative, large-scale reference (useful for first-order geometry and deep continuity), whereas *LLNL-G3D-JPS* is the more informative benchmark for diagnostic evaluation of regional slab morphology across the systems targeted here.

Relatedly, the resolution-operator workflow is central to why these two models were chosen: availability of resolution operators allows us to filter (degrade) modelled structure to what each tomography model can actually resolve, enabling fairer visual comparison and avoiding spuriously harsh misfits driven by unresolved fine structure. This is a major strength of the approach. The main drawback is practical: resolution operators are publicly available only for a small subset of global tomography models, which constrains broader MCM–tomography comparisons. A clear recommendation from this study is therefore that resolution operators become a standard companion product for future seismic tomography models. This would immediately allow the comparison framework developed here to be applied across a wider ensemble of modern tomographic models, improving the robustness of evaluating MCMs with tomography.

5 Conclusions

Our evaluation of slab morphology in this G-ADOPT MCM shows that dynamically emergent subduction geometry can reproduce many first-order features of the mantle's subduction record, but also exposes systematic limitations that must be addressed for such models to serve as robust tests of Earth's tectonic history. Regions dominated by trench retreat and relatively simple plate boundary configurations—such as the Aleutian, Brasilia, Sunda, and Tonga–Kermadec–Hikurangi systems—exhibit good agreement between modelled and tomographically imaged slab geometry, indicating that present-day mantle structure in these settings can be explained largely by reconstructed kinematics and lithospheric buoyancy forces.

In contrast, the model performs poorly in settings involving trench advance, extremely rapid rollback, or complex microplate interactions. The most consequential failure mode is incorrect subduction polarity, particularly pronounced in the Aegean and Caribbean regions, where polarity is incorrectly simulated because the model infers it solely from trench migration direction. Additional discrepancies in slab dip, segmentation, and stagnation behaviour point to sensitivities to mantle rheology, the representation of upper-plate dynamics, and uncertainties in reconstructed trench motions.

These findings emphasise two central conclusions. First, emergent-geometry global convection models can provide meaningful, independent tests of plate reconstructions, but only when key subduction parameters—especially polarity—are constrained appropriately. Second, mismatches between modelled and imaged slabs are informative: they highlight where reconstructions are incomplete, where model rheology is oversimplified, and where subduction behaviour cannot be captured without more realistic coupling between plates and the mantle.

By integrating geological interpretations, reconstructions, geodynamic predictions, and tomographic observations, this study demonstrates that slab morphology is a powerful diagnostic for assessing both the kinematic history of plates and the physical assumptions embedded in mantle convection models. Future work should combine improved reconstruction constraints, refined rheological formulations, and physics-based criteria for subduction initiation and polarity to advance

the reliability of global models that seek to reconcile Earth's surface evolution with its deep-mantle structure.

References

Arculus, R. J., Ishizuka, O., Bogus, K. A., Gurnis, M., Hickey-Vargas, R., Aljahdali, M. H., Bandini-Maeder, A. N., Barth, A. P., Brandl, P. A., Drab, L., do Monte Guerra, R., Hamada, M., Jiang, F., Kanayama, K., Kender, S., Kusano, Y., Li, H., Loudin, L. C., Maffione, M., … Zhang, Z. (2015). A record of spontaneous subduction initiation in the Izu–Bonin–Mariana arc. *Nature Geoscience*, *8*(9), 728–733. https://doi.org/10.1038/ngeo2515

Arnould, M., Coltice, N., Flament, N., & Mallard, C. (2020). Plate tectonics and mantle controls on plume dynamics. *Earth and Planetary Science Letters*, *547*, 116439. https://doi.org/10.1016/j.epsl.2020.116439

Bai, Y., Wu, S., Liu, Z., Müller, R. D., Williams, S. E., Zahirovic, S., & Dong, D. (2015). Full-fit reconstruction of the South China Sea conjugate margins. *Tectonophysics*, *661*, 121–135. https://doi.org/10.1016/j.tecto.2015.08.028

Bijwaard, H., & Spakman, W. (2000). Non-linear global P-wave tomography by iterated linearized inversion. *Geophysical Journal International*, *141*(1), 71–82. https://doi.org/10.1046/j.1365-246X.2000.00053.x

Bijwaard, H., Spakman, W., & Engdahl, E. R. (1998). Closing the gap between regional and global travel time tomography. *Journal of Geophysical Research: Solid Earth*, *103*(B12), 30055–30078. https://doi.org/10.1029/98JB02467

Billen, M. I., & Gurnis, M. (2003). Comparison of dynamic flow models for the Central Aleutian and Tonga–Kermadec subduction zones. *Geochemistry, Geophysics, Geosystems*, *4*(4). https://doi.org/10.1029/2001GC000295

Boekhout, F., Spikings, R., Sempere, T., Chiaradia, M., Ulianov, A., & Schaltegger, U. (2012). Mesozoic arc magmatism along the southern Peruvian margin during Gondwana breakup and dispersal. *Lithos*, *146–147*, 48–64. https://doi.org/10.1016/j.lithos.2012.04.015

Boschman, L. M., van Hinsbergen, D. J. J., Torsvik, T. H., Spakman, W., & Pindell, J. L. (2014). Kinematic reconstruction of the Caribbean region since the Early Jurassic. *Earth-Science Reviews*, *138*, 102–136. https://doi.org/10.1016/j.earscirev.2014.08.007

Bower, D. J., Gurnis, M., & Flament, N. (2015). Assimilating lithosphere and slab history in 4-D Earth models. *Physics of the Earth and Planetary Interiors*, *238*, 8–22. https://doi.org/10.1016/j.pepi.2014.10.013

Braun, J., & Beaumont, C. (1995). Three-dimensional numerical experiments of strain partitioning at oblique plate boundaries: Implications for contrasting tectonic styles in the southern Coast Ranges, California, and central South Island, New Zealand. *Journal of Geophysical Research: Solid Earth*, *100*(B9), 18059–18074. https://doi.org/10.1029/95JB01683

Bunge, H.-P., Richards, M. A., Lithgow-Bertelloni, C., Baumgardner, J. R., Grand, S. P., & Romanowicz, B. A. (1998). Time scales and heterogeneous structure in geodynamic Earth models. *Science*, *280*(5360), 91–95. https://doi.org/10.1126/science.280.5360.91

Burke, K. (1988). Tectonic evolution of the Caribbean. *Annual review of earth and planetary sciences*, *16*, 201–230. https://doi.org/10.1146/annurev.ea.16.050188.001221

Butterworth, N. P., Talsma, A. S., Müller, R. D., Seton, M., Bunge, H.-P., Schuberth, B. S. A., Shephard, G. E., & Heine, C. (2014). Geological, tomographic, kinematic and geodynamic constraints on the dynamics of sinking slabs. *Journal of Geodynamics*, *73*, 1–13. https://doi.org/10.1016/j.jog.2013.10.006

Cao, X., Zahirovic, S., Li, S., Suo, Y., Wang, P., Liu, J., & Müller, R. D. (2022). A deforming plate tectonic model of the South China Block since the Jurassic. *Gondwana Research*, *102*, 3–16. https://doi.org/10.1016/j.gr.2020.11.010

Capitanio, F. A., Stegman, D. R., Moresi, L. N., & Sharples, W. (2010). Upper plate controls on deep subduction, trench migrations and deformations at convergent margins. *Tectonophysics*, *483*(1), 80–92. https://doi.org/10.1016/j.tecto.2009.08.020

Chang, S.-J., Van Der Lee, S., Matzel, E., & Bedle, H. (2010). Radial anisotropy along the Tethyan margin. *Geophysical Journal International*, *182*(2), 1013–1024. https://doi.org/10.1111/j.1365-246X.2010.04662.x

Chekhovich, V. D., Sheremet, O. G., & Kononov, M. V. (2014). Strike-slip fault system in the Earth's crust of the Bering Sea: A relic of boundary between the Eurasian and North American lithospheric plates. *Geotectonics*, *48*(4), 255–272. https://doi.org/10.1134/S0016852114040037

Chen, Y.-W., Wu, J., & Suppe, J. (2019). Southward propagation of Nazca subduction along the Andes. *Nature*, *565*(7740), 441–447. https://doi.org/10.1038/s41586-018-0860-1

Clark, S. R., & Müller, R. D. (2008). Convection models in the Kamchatka region using imposed plate motion and thermal histories. *Journal of Geodynamics*, *46*(1), 1–9. https://doi.org/10.1016/j.jog.2008.02.002

Creager, K. C., & Boyd, T. M. (1991). The geometry of Aleutian subduction: Three-dimensional kinematic flow model. *Journal of Geophysical Research: Solid Earth*, *96*(B2), 2293–2307. https://doi.org/10.1029/90JB01918

Croon, M. B., Cande, S. C., & Stock, J. M. (2008). Revised Pacific–Antarctic plate motions and geophysics of the Menard Fracture Zone. *Geochemistry, Geophysics, Geosystems*, *9*(7). https://doi.org/10.1029/2008GC002019

Davies, D. R., Goes, S., Davies, J. H., Schuberth, B. S. A., Bunge, H.-P., & Ritsema, J. (2012). Reconciling dynamic and seismic models of Earth's lower mantle: The dominant role of thermal heterogeneity. *Earth and Planetary Science Letters*, *353–354*, 253–269. https://doi.org/10.1016/j.epsl.2012.08.016

Davies, D. R., Kramer, S. C., Ghelichkhan, S., & Gibson, A. (2022). Towards automatic finite-element methods for geodynamics via Firedrake. *Geoscientific Model Development*, *15*(13), 5127–5166. https://doi.org/10.5194/gmd-15-5127-2022

de Jonge, M. R., Wortel, M. J. R., & Spakman, W. (1994). Regional scale tectonic evolution and the seismic velocity structure of the lithosphere and upper mantle: The Mediterranean region. *Journal of Geophysical Research: Solid Earth*, *99*(B6), 12091–12108. https://doi.org/10.1029/94JB00648

Demouy, S., Paquette, J.-L., de Saint Blanquat, M., Benoit, M., Belousova, E. A., O'Reilly, S. Y., García, F., Tejada, L. C., Gallegos, R., & Sempere, T. (2012). Spatial and temporal evolution of Liassic to Paleocene arc activity in southern Peru unraveled by zircon U–Pb and Hf in-situ data on plutonic rocks. *Lithos*, *155*, 183–200. https://doi.org/10.1016/j.lithos.2012.09.001

Fukao, Y., Obayashi, M., Inoue, H., & Nenbai, M. (1992). Subducting slabs stagnant in the mantle transition zone. *Journal of Geophysical Research*, *97*(B4), 4809–4822. https://doi.org/10.1029/91JB02749

Fukao, Y., & Obayashi, M. (2013). Subducted slabs stagnant above, penetrating through, and trapped below the 660 km discontinuity. *Journal of Geophysical Research: Solid Earth*, *118*(11), 5920–5938. https://doi.org/10.1002/2013JB010466

Fukao, Y., Widiyantoro, S., & Obayashi, M. (2001). Stagnant slabs in the upper and lower mantle transition region. *Reviews of Geophysics*, *39*(3), 291–323. https://doi.org/10.1029/1999RG000068

Funiciello, F., Faccenna, C., Heuret, A., Lallemand, S., Di Giuseppe, E., & Becker, T. W. (2008). Trench migration, net rotation and slab–mantle coupling. *Earth and Planetary Science Letters*, *271*(1), 233–240. https://doi.org/10.1016/j.epsl.2008.04.006

Gibson, A., Davies, D. R., Kramer, S., Gelichkhan, S., Turner, R., Duvernay, T., & Scott, W. (2024, June). G-ADOPT. https://doi.org/10.5281/zenodo.5644391

Goes, S., Agrusta, R., van Hunen, J., & Garel, F. (2017). Subduction–transition zone interaction: A review. *Geosphere*, *13*(3), 644–664. https://doi.org/10.1130/GES01476.1

Gorbatov, A., & Kennett, B. L. N. (2003). Joint bulk-sound and shear tomography for Western Pacific subduction zones. *Earth and Planetary Science Letters*, *210*(3), 527–543. https://doi.org/10.1016/S0012-821X(03)00165-1

Gorbatov, A., Widiyantoro, S., Fukao, Y., & Gordeev, E. (2000). Signature of remnant slabs in the North Pacific from P-wave tomography. *Geophysical Journal International*, *142*(1), 27–36. https://doi.org/10.1046/j.1365-246x.2000.00122.x

Gurnis, M., Yang, T., Cannon, J., Turner, M., Williams, S., Flament, N., & Müller, R. D. (2018). Global tectonic reconstructions with continuously deforming and evolving rigid plates. *Computers & Geosciences*, *116*, 32–41. https://doi.org/10.1016/j.cageo.2018.04.007

Hall, R., & Spakman, W. (2002). Subducted slabs beneath the eastern Indonesia–Tonga region: Insights from tomography. *Earth and Planetary Science Letters*, *201*(2), 321–336. https://doi.org/10.1016/S0012-821X(02)00705-7

Hall, R., & Spakman, W. (2015). Mantle structure and tectonic history of SE Asia. *Tectonophysics*, *658*, 14–45. https://doi.org/10.1016/j.tecto.2015.07.003

Holt, A. F., & Royden, L. H. (2020). Subduction dynamics and mantle pressure: 2. Towards a global understanding of slab dip and upper mantle circulation. *Geochemistry, Geophysics, Geosystems*, *21*(7), e2019GC008771. https://doi.org/10.1029/2019GC008771

Holt, A. F., Royden, L. H., Becker, T. W., & Faccenna, C. (2018). Slab interactions in 3-D subduction settings: The Philippine Sea Plate region. *Earth and Planetary Science Letters*, *489*, 72–83. https://doi.org/10.1016/j.epsl.2018.02.024

Ishizuka, O., Hickey-Vargas, R., Arculus, R. J., Yogodzinski, G. M., Savov, I. P., Kusano, Y., McCarthy, A., Brandl, P. A., & Sudo, M. (2018). Age of Izu–Bonin–Mariana arc basement. *Earth and Planetary Science Letters*, *481*, 80–90. https://doi.org/10.1016/j.epsl.2017.10.023

Jaxybulatov, K., Koulakov, I., & Dobretsov, N. L. (2013). Segmentation of the Izu–Bonin and Mariana slabs based on the analysis of the Benioff seismicity distribution and regional tomography results. *Solid Earth*, *4*(1), 59–73. https://doi.org/10.5194/se-4-59-2013

Jicha, B. R., Scholl, D. W., Singer, B. S., Yogodzinski, G. M., & Kay, S. M. (2006). Revised age of Aleutian Island Arc formation implies high rate of magma production. *Geology*, *34*(8), 661–664. https://doi.org/10.1130/G22433.1

Jolivet, L., & Brun, J.-P. (2010). Cenozoic geodynamic evolution of the Aegean. *International Journal of Earth Sciences*, *99*(1), 109–138. https://doi.org/10.1007/s00531-008-0366-4

Koelemeijer, P., Schuberth, B. S. A., Davies, D. R., Deuss, A., & Ritsema, J. (2018). Constraints on the presence of post-perovskite in Earth's lowermost mantle from tomographic-geodynamic model comparisons. *Earth and Planetary Science Letters*, *494*, 226–238. https://doi.org/10.1016/j.epsl.2018.04.056

Koulakov, I. (2013). Studying deep sources of volcanism using multiscale seismic tomography. *Journal of Volcanology and Geothermal Research*, *257*, 205–226. https://doi.org/10.1016/j.jvolgeores.2013.03.012

Koulakov, I., Dobretsov, N., Bushenkova, N., & Yakovlev, A. (2011). Slab shape in subduction zones beneath the Kurile–Kamchatka and Aleutian arcs based on regional tomography results. *Russian Geology and Geophysics*, *52*(6), 650–667. https://doi.org/10.1016/j.rgg.2011.05.008

Lallemand, S., Heuret, A., & Boutelier, D. (2005). On the relationships between slab dip, back-arc stress, upper plate absolute motion, and crustal nature in subduction zones. *Geochemistry, Geophysics, Geosystems*, *6*(9). https://doi.org/10.1029/2005GC000917

Le Breton, E., Handy, M. R., Molli, G., & Ustaszewski, K. (2017). Post-20 Ma motion of the Adriatic plate: New constraints from surrounding orogens and implications for crust–mantle decoupling. *Tectonics*, *36*(12), 3135–3154. https://doi.org/10.1002/2016TC004443

Li, Y., Liu, L., Peng, D., Dong, H., & Li, S. (2023). Evaluating tomotectonic plate reconstructions using geodynamic models with data assimilation, the case for North America. *Earth-Science Reviews*, *244*, 104518. https://doi.org/10.1016/j.earscirev.2023.104518

Lin, Y.-A., Colli, L., & Wu, J. (2022). NW Pacific-Panthalassa Intra-Oceanic Subduction During Mesozoic Times From Mantle Convection and Geoid Models. *Geochemistry, Geophysics, Geosystems*, *23*(11), e2022GC010514. https://doi.org/10.1029/2022GC010514

Lithgow-Bertelloni, C., & Richards, M. A. (1998). The dynamics of Cenozoic and Mesozoic plate motions. *Reviews of Geophysics*, *36*(1), 27–78. https://doi.org/10.1029/97RG02282

Martin-Short, R., Allen, R. M., & Bastow, I. D. (2016). Subduction geometry beneath south central Alaska and its relationship to volcanism. *Geophysical Research Letters*, *43*(18), 9509–9517. https://doi.org/10.1002/2016GL070580

Matthews, K. J., Williams, S. E., Whittaker, J. M., Müller, R. D., Seton, M., & Clarke, G. L. (2015). Geologic and kinematic constraints on late Cretaceous to mid Eocene plate boundaries in the southwest Pacific. *Earth-Science Reviews*, *140*, 72–107. https://doi.org/10.1016/j.earscirev.2014.10.008

Miller, M. S., Kennett, B. L. N., & Lister, G. S. (2004). Imaging changes in morphology, geometry, and physical properties of the subducting Pacific plate along the Izu–Bonin–Mariana arc. *Earth and Planetary Science Letters*, *224*(3), 363–370. https://doi.org/10.1016/j.epsl.2004.05.018

Müller, R. D., Seton, M., Zahirovic, S., Williams, S. E., Matthews, K. J., Wright, N. M., Shephard, G. E., Maloney, K. T., Barnett-Moore, N., Hosseinpour, M., Bower, D. J., & Cannon, J. (2016). Ocean basin evolution and global-scale plate reorganization events since Pangea breakup. *Annual Review of Earth and Planetary Sciences*, *44*(1), 107–138. https://doi.org/10.1146/annurev-earth-060115-012211

Müller, R. D., Zahirovic, S., Williams, S. E., Cannon, J., Seton, M., Bower, D. J., Tetley, M. G., Heine, C., Le Breton, E., Liu, S., Russell, S. H. J., Yang, T., Leonard, J., & Gurnis, M. (2019). A global plate model including lithospheric deformation along major rifts and orogens since the Triassic. *Tectonics*, *38*(6), 1884–1907. https://doi.org/10.1029/2018TC005462

Nerlich, R., Colli, L., Ghelichkhan, S., Schuberth, B., & Bunge, H.-P. (2016). Constraining central Neo-Tethys Ocean reconstructions with mantle convection models. *Geophysical Research Letters*, *43*(18), 9595–9603. https://doi.org/10.1002/2016GL070524

New, T., Ghelichkhan, S., Davies, D. R., Seton, M., Mather, B., & Müller, R. D. (2025a). Calibrating plate reconstructions with global mantle convection models. *Manuscript in revision, Geochemistry, Geophysics, Geosystems.*

New, T., Seton, M., Mather, B., Müller, R. D., Ghelichkhan, S., & Davies, D. R. (2025b). Coupled plate–mantle models support a 25 Ma Ontong–Java collision. *Prepared for submission to Earth and Planetary Science Letters.*

Peng, D., Liu, L., & Wang, Y. (2021). A newly discovered late-Cretaceous east Asian flat slab explains its unique lithospheric structure and tectonics. *Journal of Geophysical Research: Solid Earth*, *126*(10), e2021JB022103. https://doi.org/10.1029/2021JB022103

Pesicek, J., Thurber, C., Widiyantoro, S., Zhang, H., DeShon, H., & Engdahl, E. (2010). Sharpening the tomographic image of the subducting slab below Sumatra, the Andaman Islands and Burma. *Geophysical Journal International*, *182*(1), 433–453. https://doi.org/10.1111/j.1365-246X.2010.04630.x

Piromallo, C., & Morelli, A. (1997). Imaging the Mediterranean upper mantle by P-wave travel time tomography. *Annals of Geophysics*, *40*(4).

Puspito, N. T., & Shimazaki, K. (1995). Mantle structure and seismotectonics of the Sunda and Banda arcs. *Tectonophysics*, *251*(1), 215–228. https://doi.org/10.1016/0040-1951(95)00063-1

Puspito, N. T., Yamanaka, Y., Miyatake, T., Shimazaki, K., & Hirahara, K. (1993). Three-dimensional P-wave velocity structure beneath the Indonesian region. *Tectonophysics*, *220*(1), 175–192. https://doi.org/10.1016/0040-1951(93)90230-H

Qi, C., Zhao, D., & Chen, Y. (2007). Search for deep slab segments under Alaska. *Physics of the Earth and Planetary Interiors*, *165*(1), 68–82. https://doi.org/10.1016/j.pepi.2007.08.004

Replumaz, A., Kárason, H., van der Hilst, R. D., Besse, J., & Tapponnier, P. (2004). 4-D evolution of SE Asia's mantle from geological reconstructions and seismic tomography. *Earth and Planetary Science Letters*, *221*(1), 103–115. https://doi.org/10.1016/S0012-821X(04)00070-6

Richard, G. C., & Bercovici, D. (2009). Water-induced convection in the Earth's mantle transition zone. *Journal of Geophysical Research: Solid Earth*, *114*(B1). https://doi.org/10.1029/2008JB005734

Ritsema, J., Deuss, A., van Heijst, H. J., & Woodhouse, J. H. (2011). S40RTS: A degree-40 shear-velocity model for the mantle from new Rayleigh wave dispersion, teleseismic traveltime and normal-mode splitting function measurements. *Geophysical Journal International*, *184*(3), 1223–1236. https://doi.org/10.1111/j.1365-246X.2010.04884.x

Schellart, W. P. (2004). Kinematics of subduction and subduction-induced flow in the upper mantle. *Journal of Geophysical Research: Solid Earth*, *109*(B7). https://doi.org/10.1029/2004JB002970

Schellart, W. P. (2005). Influence of the subducting plate velocity on the geometry of the slab and migration of the subduction hinge. *Earth and Planetary Science Letters*, *231*(3), 197–219. https://doi.org/10.1016/j.epsl.2004.12.019

Schellart, W. P., Kennett, B. L. N., Spakman, W., & Amaru, M. (2009). Plate reconstructions and tomography reveal a fossil lower mantle slab below the Tasman Sea. *Earth and Planetary Science Letters*, *278*(3), 143–151. https://doi.org/10.1016/j.epsl.2008.11.004

Schellart, W. P., Lister, G. S., & Toy, V. G. (2006). A late Cretaceous and Cenozoic reconstruction of the Southwest Pacific region: Tectonics controlled by subduction and slab rollback processes. *Earth-Science Reviews*, *76*(3), 191–233. https://doi.org/10.1016/j.earscirev.2006.01.002

Schuberth, B. S. A., Bunge, H.-P., & Ritsema, J. (2009). Tomographic filtering of high-resolution mantle circulation models: Can seismic heterogeneity be explained by temperature alone? *Geochemistry, Geophysics, Geosystems*, *10*(5). https://doi.org/10.1029/2009GC002401

Seton, M., Müller, R. D., Zahirovic, S., Gaina, C., Torsvik, T., Shephard, G., Talsma, A., Gurnis, M., Turner, M., Maus, S., & Chandler, M. (2012). Global continental and ocean basin reconstructions since 200 Ma. *Earth-Science Reviews*, *113*(3), 212–270. https://doi.org/10.1016/j.earscirev.2012.03.002

Simmons, N. A., Myers, S. C., Johannesson, G., Matzel, E., & Grand, S. P. (2015). Evidence for long-lived subduction of an ancient tectonic plate beneath the southern Indian Ocean. *Geophysical Research Letters*, *42*(21), 9270–9278. https://doi.org/10.1002/2015GL066237

Spakman, W., Wortel, M. J. R., & Vlaar, N. J. (1988). The Hellenic Subduction Zone: A tomographic image and its geodynamic implications. *Geophysical Research Letters*, *15*(1), 60–63. https://doi.org/10.1029/GL015i001p00060

Spakman, W., & Hall, R. (2010). Surface deformation and slab–mantle interaction during Banda arc subduction rollback. *Nature Geoscience*, *3*(8), 562–566. https://doi.org/10.1038/ngeo917

Spasojević, S., & Gurnis, M. (2012). Sea level and vertical motion of continents from dynamic earth models since the Late Cretaceous. *AAPG Bulletin*, *96*(11), 2037–2064. https://doi.org/10.1306/03261211121

Stegman, D. R., Farrington, R., Capitanio, F. A., & Schellart, W. P. (2010a). A regime diagram for subduction styles from 3-D numerical models of free subduction. *Tectonophysics*, *483*(1), 29–45. https://doi.org/10.1016/j.tecto.2009.08.041

Stegman, D. R., Schellart, W. P., & Freeman, J. (2010b). Competing influences of plate width and far-field boundary conditions on trench migration and morphology of subducted slabs in the upper mantle. *Tectonophysics*, *483*(1), 46–57. https://doi.org/10.1016/j.tecto.2009.08.026

Stern, R. J., & Gerya, T. (2018). Subduction initiation in nature and models: A review. *Tectonophysics*, *746*, 173–198. https://doi.org/10.1016/j.tecto.2017.10.014

Sugioka, H., Suetsugu, D., Obayashi, M., Fukao, Y., & Gao, Y. (2010). Fast P- and S-wave velocities associated with the "cold" stagnant slab beneath the northern Philippine Sea. *Physics of the Earth and Planetary Interiors*, *179*(1), 1–6. https://doi.org/10.1016/j.pepi.2010.01.006

Tetley, M. G., Williams, S. E., Gurnis, M., Flament, N., & Müller, R. D. (2019). Constraining absolute plate motions since the Triassic. *Journal of Geophysical Research: Solid Earth*, *124*(7), 7231–7258. https://doi.org/10.1029/2019JB017442

Torsvik, T. H., Steinberger, B., Shephard, G. E., Doubrovine, P. V., Gaina, C., Domeier, M., Conrad, C. P., & Sager, W. W. (2019). Pacific–Panthalassic reconstructions: Overview, errata and the way forward. *Geochemistry, Geophysics, Geosystems*, *20*(7), 3659–3689. https://doi.org/10.1029/2019GC008402

van Benthem, S., Govers, R., Spakman, W., & Wortel, R. (2013). Tectonic evolution and mantle structure of the Caribbean. *Journal of Geophysical Research: Solid Earth*, *118*(6), 3019–3036. https://doi.org/10.1002/jgrb.50235

van de Lagemaat, S. H. A., van Hinsbergen, D. J. J., Boschman, L. M., Kamp, P. J. J., & Spakman, W. (2018). Southwest Pacific absolute plate kinematic reconstruction reveals major Cenozoic Tonga–Kermadec slab dragging. *Tectonics*, *37*(8), 2647–2674. https://doi.org/10.1029/2017TC004901

van der Hilst, R. D., Engdahl, R., Spakman, W., & Nolet, G. (1991). Tomographic imaging of subducted lithosphere below northwest Pacific island arcs. *Nature*, *353*(6339), 37–43. https://doi.org/10.1038/353037a0

van der Hilst, R. D., & Spakman, W. (1989). Importance of the reference model in linearized tomography and images of subduction below the Caribbean plate. *Geophysical Research Letters*, *16*(10), 1093–1096. https://doi.org/10.1029/GL016i010p01093

van der Hilst, R. (1995). Complex morphology of subducted lithosphere in the mantle beneath the Tonga trench. *Nature*, *374*(6518), 154–157. https://doi.org/10.1038/374154a0

van der Meer, D. G., Spakman, W., van Hinsbergen, D. J. J., Amaru, M. L., & Torsvik, T. H. (2010). Towards absolute plate motions constrained by lower-mantle slab remnants. *Nature Geoscience*, *3*(1), 36–40. https://doi.org/10.1038/ngeo708

van der Meer, D. G., van Hinsbergen, D. J. J., & Spakman, W. (2018). Atlas of the underworld: Slab remnants in the mantle, their sinking history, and a new outlook on lower mantle viscosity. *Tectonophysics*, *723*, 309–448. https://doi.org/10.1016/j.tecto.2017.10.004

van Hinsbergen, D. J. J., Vissers, R. L. M., & Spakman, W. (2014). Origin and consequences of western Mediterranean subduction, rollback, and slab segmentation. *Tectonics*, *33*(4), 393–419. https://doi.org/10.1002/2013TC003349

van Hinsbergen, D. J. J., Hafkenscheid, E., Spakman, W., Meulenkamp, J., & Wortel, R. (2005). Nappe stacking resulting from subduction of oceanic and continental lithosphere below Greece. *Geology*, *33*(4), 325–328. https://doi.org/10.1130/G20878.1

Villagómez, D., Spikings, R., Magna, T., Kammer, A., Winkler, W., & Beltrán, A. (2011). Geochronology, geochemistry and tectonic evolution of the Western and Central cordilleras of Colombia. *Lithos*, *125*(3), 875–896. https://doi.org/10.1016/j.lithos.2011.05.003

Widiyantoro, S., Gorbatov, A., Kennett, B. L. N., & Fukao, Y. (2000). Improving global shear wave traveltime tomography using three-dimensional ray tracing and iterative inversion. *Geophysical Journal International*, *141*(3), 747–758. https://doi.org/10.1046/j.1365-246x.2000.00112.x

Widiyantoro, S., & Van Der Hilst, R. (1997). Mantle structure beneath Indonesia inferred from high-resolution tomographic imaging. *Geophysical Journal International*, *130*(1), 167–182. https://doi.org/10.1111/j.1365-246X.1997.tb00996.x

Widiyantoro, S., & van der Hilst, R. (1996). Structure and evolution of lithospheric slab beneath the Sunda arc, Indonesia. *Science*, *271*(5255), 1566–1570. https://doi.org/10.1126/science.271.5255.1566

Wright, N. M., Müller, R. D., Seton, M., & Williams, S. E. (2015). Revision of Paleogene plate motions in the Pacific and implications for the Hawaiian-Emperor bend. *Geology*, *43*(5), 455–458. https://doi.org/10.1130/G36303.1

Wright, N. M., Seton, M., Williams, S. E., & Müller, R. D. (2016). The Late Cretaceous to recent tectonic history of the Pacific Ocean basin. *Earth-Science Reviews*, *154*, 138–173. https://doi.org/10.1016/j.earscirev.2015.11.015

Wu, J., Suppe, J., Lu, R., & Kanda, R. (2016). Philippine Sea and East Asian plate tectonics since 52 Ma constrained by new subducted slab reconstruction methods. *Journal of Geophysical Research: Solid Earth*, *121*(6), 4670–4741. https://doi.org/10.1002/2016JB012923

Yang, T., Gurnis, M., & Zahirovic, S. (2016). Mantle-induced subsidence and compression in SE Asia since the early Miocene. *Geophysical Research Letters*, *43*(5), 1901–1909. https://doi.org/10.1002/2016GL068050

Young, A., Flament, N., Maloney, K., Williams, S., Matthews, K., Zahirovic, S., & Müller, R. D. (2019). Global kinematics of tectonic plates and subduction zones since the late Paleozoic Era. *Geoscience Frontiers*, *10*(3), 989–1013. https://doi.org/10.1016/j.gsf.2018.05.011

Zahirovic, S., Seton, M., & Müller, R. D. (2014). The Cretaceous and Cenozoic tectonic evolution of Southeast Asia. *Solid Earth*, *5*(1), 227–273. https://doi.org/10.5194/se-5-227-2014

Zahirovic, S., Eleish, A., Doss, S., Pall, J., Cannon, J., Pistone, M., Tetley, M. G., Young, A., & Fox, P. (2022). Subduction and carbonate platform interactions. *Geoscience Data Journal*, *9*(2), 371–383. https://doi.org/10.1002/gdj3.146

Zahirovic, S., Matthews, K. J., Flament, N., Müller, R. D., Hill, K. C., Seton, M., & Gurnis, M. (2016). Tectonic evolution and deep mantle structure of the eastern Tethys since the latest Jurassic. *Earth-Science Reviews*, *162*, 293–337. https://doi.org/10.1016/j.earscirev.2016.09.005

Zaroli, C., Koelemeijer, P., & Lambotte, S. (2017). Toward seeing the Earth's interior through unbiased tomographic lenses. *Geophysical Research Letters*, *44*(22). https://doi.org/10.1002/2017GL074996

4 | Coupled Plate–Mantle Models Support a 25 Ma Ontong–Java Collision

Tom New[1], Maria Seton[1], Ben Mather[2], R. Dietmar Müller[1], Siavash Ghelichkhan[3], and D. Rhodri Davies[3]

[1] *EarthByte Group, School of Geosciences, The University of Sydney, NSW, Australia*
[2] *School of Geography, Earth and Atmospheric Sciences, The University of Melbourne, VIC, Australia*
[3] *Research School of Earth Sciences, Australian National University, ACT, Australia*

Abstract

The collision between the Ontong–Java Plateau and the Melanesian arc subduction system in the southwest Pacific has been proposed to have occurred at either 25 Ma or 12 Ma, with significant implications for regional tectonics, subduction polarity reversal, and global plate reorganisation events. To assess these competing reconstructions with an independent methodology, we implemented each as a topological plate model in GPlates and coupled them to a global mantle circulation model in G-ADOPT. We converted the predicted present-day mantle temperature fields to seismic velocity using mineral physics models, applied tomographic resolution operators, and compared the results to a suite of seismic tomography models. We also applied statistical tests in the ℓ^2-norm and, new to this application, the Wasserstein metric to quantify the similarity between modelled and observed mantle structure.

We find that the 25 Ma collision model better reproduces tomographically imaged mantle structure below the collision zone, producing slab material at the appropriate depths in the transition zone to uppermost mantle which the 12 Ma model does not. The earlier collision model also yields 10–28 % lower misfit scores across all comparison metrics and tomography models. Our results therefore support a 25 Ma collision between the Ontong–Java Plateau and the Melanesian arc subduction system, coinciding with the proposed 25 Ma plate reorganisation.

1 Introduction

The Ontong–Java Plateau (OJP) is the world's largest and most voluminous oceanic igneous province, which erupted between 122 and 108 million years ago (Larson & Erba, 1999; Sikora & Bergen, 2004; Davidson et al., 2023). After its emplacement, the OJP travelled westward with the Pacific plate, eventually colliding with the Australian plate margin in the southwest Pacific (Wright et al., 2015), along the Melanesian arc subduction system (MSS; Figure 1). This collision is thought to have triggered significant regional tectonic changes, including a global plate reorganization event

Figure 1

The present-day tectonic setting of the Ontong–Java plateau (pink) and Melanesian arc subduction system (red) in the southwest Pacific after Zahirovic et al. (2022). Black lines indicate convergent or transform margins and red lines indicate divergent margins. Relief model is ETOPO1 (NOAA National Geophysical Data Center, 2009).

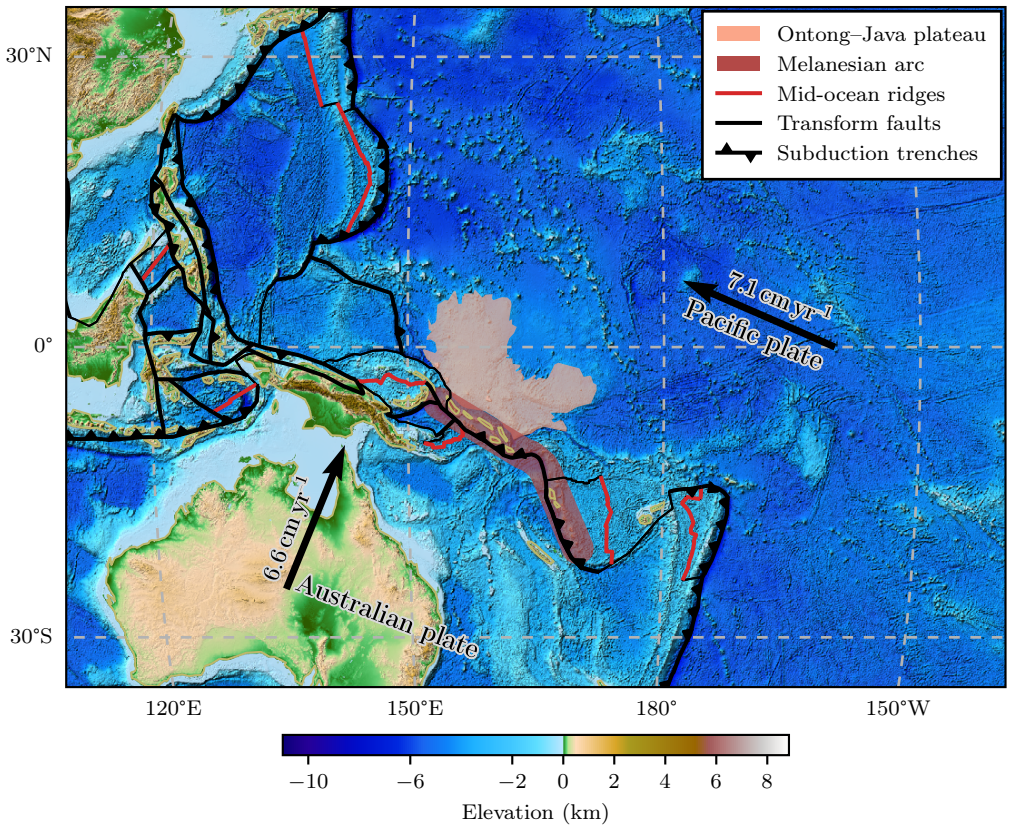

(GPRE) around 25 million years ago, (Stern, 2004; Knesel et al., 2008), a regional flare-up in mineralisation (Holm et al., 2013, 2019), and an abrupt shift in the Australian plate's motion (Knesel et al., 2008).

However, the precise timing, polarity, and dynamics of subduction during this event remain uncertain, particularly along the north-northeastern margins of the Australian plate, where much of the oceanic record has been subducted and onshore geological data are sparse due to challenging terrain and limited access. This debate has resolved into two main camps for the timing of collision and polarity reversal, the so-called *soft-docking* and *hard-docking* scenarios.

In the *soft-docking* camp, the OJP is thought to have reached the Australia–Pacific margin around 25 million years ago, followed by a ∼12 Myr-long period with relatively little subduction, due to the thicker and less ductile igneous material of the OJP jamming the subduction zone, evidenced by a gap in back-arc volcanism in the stratigraphic record (Petterson et al., 1997; Hall, 2002; Schellart et al., 2006). Similar age constraints for the OJP's arrival have been inferred from a short-lived slowdown in motion of the Australian plate from 26–23 Ma (Knesel et al., 2008). In this view, NE-dipping subduction of the Australian plate along the South Solomon Trench began from 15–8 Ma (Figure 2; Petterson et al., 1999; Schellart et al., 2006).

On the other hand, the *hard-docking* camp holds that the transition from SW- to NE-dipping subduction occurred more recently and much faster, over a period of just a few million years. Multichannel seismic reflection data from a joint US–Japan research voyage, together with onshore

geology, point to a much later termination of Pacific subduction (Cowley et al., 2004; Mann & Taira, 2004; Phinney et al., 2004). Intra-arc rifting produced asymmetrical, normal-fault-bounded basins until at least ∼11 Ma, with extension ending by 5 Ma as earlier rifts were folded and inverted. Subduction then initiated in the South Solomon Trench from 4–2 Ma, evidenced by new arc volcanism above the subducting Australian plate (Figure 3; Mann & Taira, 2004).

Beyond the timing of the main OJP–MSS collision, Musgrave (1990, 2013) has argued that geological and paleomagnetic data support the OJP being much larger, and that it experienced north–south rifting on its western margin during the 120 Ma Pacific reorganisation; the event which also rifted it apart from the Hikurangi and Manihiki plateaus (Taylor, 2006; Tejada et al., 2023). This additional rifted portion of the OJP, the so-called *Malaita terrane*, reached the subduction zone as early as 35 million years ago, accreting onto Malaita. However, this series of events is not mutually exclusive with either scenario, and our primary focus is distinguishing between them.

The two end-member scenarios imply different sequences of subduction initiation, trench migration, and arc development. Because geological and geophysical constraints are sparse or conflicting, we instead use present-day mantle structure as an independent test. Subducted slabs are generally accepted to be colder and therefore seismically faster than the surrounding mantle, and so their present-day locations can be imaged by seismic tomography. By running geodynamic mantle circulation models (MCMs) forced by plate tectonic reconstructions, the predicted present-day locations of slabs can be compared with tomography to assess the validity of each reconstruction (e.g., Flament et al., 2015; Seton et al., 2015; Nerlich et al., 2016; Lin et al., 2022).

However, there are practical issues regarding the validity of comparing modelled mantle temperature structure to seismic tomography. The conversion from temperature to seismic velocity is non-trivial, involving mineral physics (Stixrude & Lithgow-Bertelloni, 2005, 2011, 2024) and anelastic effects (Cammarano et al., 2003; Goes et al., 2004). Furthermore, tomography models do not have uniform resolving power throughout the mantle, and so some features may be poorly imaged or entirely missing (Ritsema et al., 2007; Zaroli et al., 2017). Finally, a common challenge is actually determining the similarity between modelled and observed structures. Many authors make a qualitative comparison by choosing a temperature contour to represent modelled structure then overlaying this on tomography in cross-section (e.g., Flament et al., 2015; Seton et al., 2015; Nerlich et al., 2016) or vice-versa (e.g., Lin et al., 2022). Quantitative comparisons are often made using an ℓ^2-norm (e.g., Lin et al., 2022) or vote maps (e.g., Shephard et al., 2017), however both of these metrics have limitations in their ability to capture spatial correlation in the total absence of overlap.

In this study we test whether our predicted mantle structure supports a 25 Ma versus a 12 Ma OJP–MSS collision scenario by implementing the two main competing reconstructions for the collision as topological plate models in GPlates (Müller et al., 2018), and coupling them to a global MCM implemented in G-ADOPT (Davies et al., 2022; Ghelichkhan et al., 2024). We then convert the predicted present-day mantle temperature to seismic velocity using mineral physics models, apply tomographic resolution operators, and compare the results to a suite of seismic tomography models in cross-section using both the ℓ^2-norm and the Wasserstein metric. Through this integrated approach, we aim to assess which reconstruction produces a predicted mantle structure that best explains the observed present-day mantle structure beneath the southwest Pacific and therefore the implication of the collision and subduction polarity reversal on regional and global tectonic and geodynamic changes.

Figure 2

The most widely-accepted reconstruction of the collision between the Ontong–Java plateau (OJP) and the Melanesian arc subduction system (MSS). At 85 Ma*, many spreading ridges which previously subdivided the proto-Pacific plate terminate, and the MSS and its back-arc basins initiate. At* 25 Ma*, the OJP collides with the MSS. Subduction polarity reversal finishes by* ∼12 Ma*, with the Australian plate now subducting under the Pacific plate. Australia-fixed reference frame. Global tectonic model after Zahirovic et al. (2022), which is locally based on the* 25 Ma *collision model of Hall (2002).*

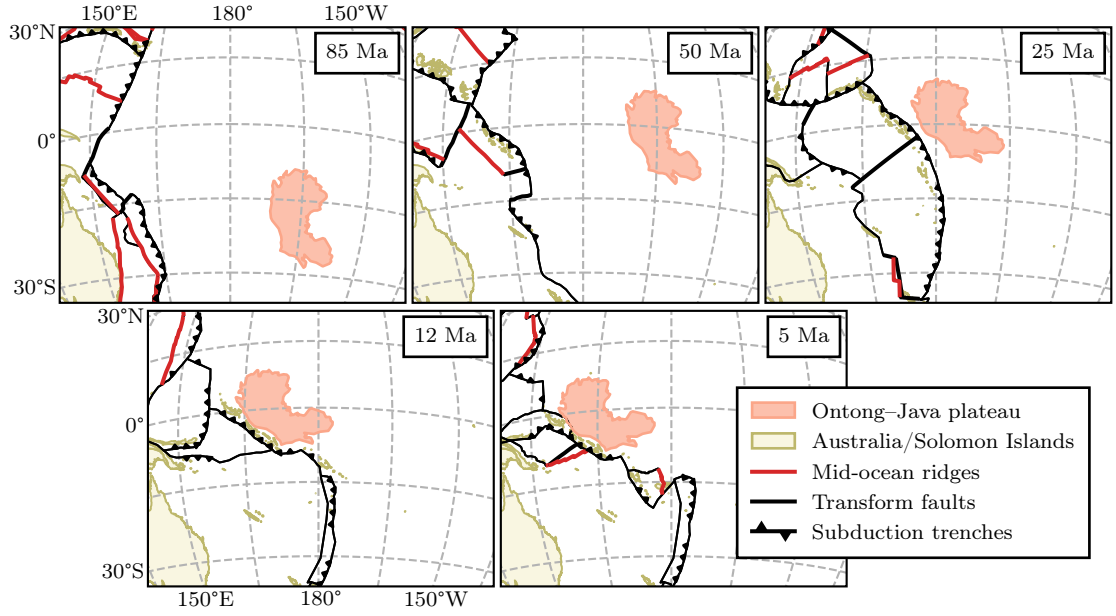

Figure 3

The alternate reconstruction for the OJP–MSS collision proposed by Mann and Taira (2004). When the MSS forms at 85 Ma *rollback is much slower, and so by* 50 Ma *the island arc has already reached its present-day latitude. From* 50–20 Ma *there is a small amount of extension and anticlockwise rotation of the arc. At* 12 Ma *the OJP finally reaches the MSS, initiating polarity reversal, which is complete by* 5 Ma*. Australia-fixed reference frame. Global tectonic model after Zahirovic et al. (2022), with local alterations to match the reconstruction of Mann and Taira (2004).*

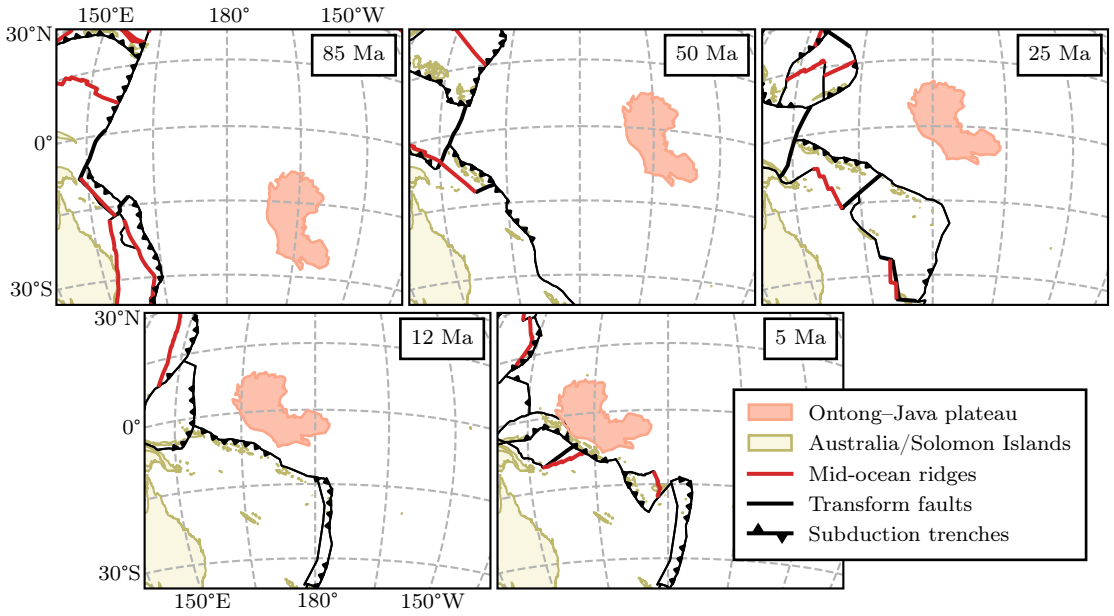

2 Methodology

2.1 Topological plate model

To assess the competing models for the OJP–MSS collision, we first implemented the two primary reconstructions as topological plate models using GPlates (Müller et al., 2018). Using the plate tectonic model of Zahirovic et al. (2022) as a base (which we refer to as *Z22*), we made alterations to the model to suit each of the reconstructions.

In the southwest Pacific, *Z22* is functionally identical to a reconstruction that imposes collision at ∼25 Ma. While what is implemented in Zahirovic et al. (2022) is the model of Seton et al. (2016), it is based on the 25 Ma collision as reflected in Hall (2002). Thus, only very minor corrections needed to be made to ensure the correct closure of topological networks in the plate model.

To satisfy the constraints offered by Musgrave (2013) of an earlier phase of collision with a rifted-off segment of the OJP, we adjusted the *Z22* base reconstruction to include a new spreading ridge running NNW–SSE through the proto-Pacific plate at 120 Ma. Since this ridge, if it existed, would be entirely subducted away at present day, we modelled its terminatation at 85 Ma to correspond to the cessation of spreading along all the spreading ridges associated with the break-up of the Ontong–Java–Nui Plateau. While the MCM output of this model was indiscernible from that of*Z22*—and hence we do not focus on it in this study—our implementation of this 35 Ma event was very simplistic, and a more in-depth reconstruction would be needed to properly test it.

To implement the reconstruction of Mann and Taira (2004), extensive changes to *Z22* in the SW Pacific were necessary; we refer to this alternate reconstruction as *Z22M04* Figure 3. Since the relative motions of the proto-Pacific (Croon et al., 2008; Wright et al., 2015; Torsvik et al., 2019) and Australian plates (Williams et al., 2011) are well-constrained from 120–0 Ma, the only degree of freedom to alter the timing of the collision is the trench retreat speed of the MSS. In *Z22M04*, the OJP–MSS collision occurs much later compared to the reference model so from 85–50 Ma the MSS' retreat speed was reduced accordingly (from 37.1 km Myr^{-1} to 13.4 km Myr^{-1}). *Z22M04* also has the collision of the OJP with the MSS occur at an even more oblique angle than *Z22* (∼69° instead of ∼63°). Therefore, from 50–12 Ma the retreat of the Melanesian arc at its western end slows down significantly, which accommodates the necessary rotation to create the oblique collision. Due to its new position relative to the Australian and Pacific plates, the MSS now begins its collision with the OJP at ∼12 Ma, with the polarity reversal nearing completion by 5 Ma.

2.2 Geodynamic mantle circulation model

To compare the validity of each reconstruction, we coupled their corresponding plate models in pyGPlates to a global mantle convection simulator, implemented in G-ADOPT. pyGPlates (Mather et al., 2024) is an open-source Python library for analysing and visualising reconstructions generated with GPlates (Müller et al., 2018). G-ADOPT (Davies et al., 2022; Ghelichkhan et al., 2024) builds on Firedrake, an automated finite-element system (Rathgeber et al., 2016), and has been extensively validated and benchmarked for global mantle flow (Davies et al., 2022).

G-ADOPT has several features which make it a desirable choice for use in computational geodynamics. First, its high-level interface is entirely in Python 3, with which many geoscientists are already familiar and has a low barrier-to-entry for those who are not. Second, G-ADOPT separates the tasks of implementing a finite element model and solving it. A model is implemented using Unified Form Language (UFL), which allows for a much more natural translation of mathematical formulae into code. Then, under-the-hood, the UFL equations are translated into C/C++ code

and solved by PETSc (Balay et al., 1997), performing automatically for the user sophisticated performance optimisations that few would have the resources to code explicitly. Third, it is built with parallelisation in mind, making it relatively easy to run on high performance computing clusters.

The model is first spun-up with free-slip, isothermal boundary conditions at the surface (300 K) and core–mantle boundary (4000 K) until a quasi-steady state is achieved after approximately 500 Myr. Plate velocities from pyGPlates are then assimilated from 410 Ma to the present day. This coupled framework provides the synthetic mantle temperature fields that we subsequently convert to seismic velocities for comparison with seismic tomography. An extended description of the MCM set-up, including material properties, is provided in the supplementary materials (Appendix C).

2.3 Comparison to seismic tomography

We assess the validity of our reconstructions in several ways, some common in the literature, some uncommon, and one which has not before been used for this application. First, we qualitatively assess—in vertical cross-sections through the Solomons and Vanuatu—the similarities and differences in the seismic velocity fields among our geodynamic models and a broad range of seismic tomography models. Next, in order to make these comparisons more robust, we apply the resolution operators from those tomography models which have them to our geodynamic models, allowing us to view our models with the appropriate local resolution. Lastly, we compute comparison metrics between our models and seismic tomography; first the ℓ^2-norm, and second the Wasserstein metric.

2.3.1 Seismic tomography

For our comparison of seismic tomography models in the region, we first choose those which have published resolution operators in order to facilitate a quantitative comparison with our mantle circulation models: *LLNL-G3D-JPS* and *S40RTS*. We additionally select three other tomography models: *OJP_P*, *TX2019slab*, and *MIT-P08* to assess the robustness of the features between a wider variety of models.

S40RTS (Ritsema et al., 2011) is a global S-wave velocity model parameterised in spherical harmonics to degree 40 with vertical splines. For over a decade, it was the standard reference for tomographic filtering, largely because its resolution operator was made available (Ritsema et al., 2007). Despite its relatively coarse nominal resolution of ∼1100 km (Trampert et al., 2013), *S40RTS* has been widely used to compare mantle circulation models with tomography, particularly in studies of slab morphology, sinking rates, and deep mantle structure. Its longevity makes it a valuable baseline against which to test newer approaches.

LLNL-G3D-JPS (Simmons et al., 2015) is a more recent global joint P- and S-wave velocity model built using a multi-resolution regional parametrisation. It achieves substantially finer effective resolution than *S40RTS*: ∼400 km in the upper mantle (UM) and transition zone (TZ) and ∼800 km in the lower mantle (LM; Simmons et al., 2019). Crucially, it is one of the very few P-wave models published with a resolution operator, making it an ideal benchmark for filtering synthetic mantle fields into the space constrained by P-wave data.

OJP_P (Obayashi et al., 2021) is a regionally focused multi-frequency P-wave tomography model from a ∼2-year seafloor/island campaign around the OJP that resolves UM and TZ architecture. It images fast anomalies beneath the centre of the plateau and its eastern margin, which has been interpreted as thick lithosphere and a remnant dipping Pacific slab and a broad stagnant Pacific slab in the TZ formed during rapid trench retreat from 48–25 Ma.

TX2019slab (Lu et al., 2019) is a global jointly inverted P– and S–wave tomography model that explicitly incorporates a 3D thermal model of subducting slabs in the starting Earth model and simultaneously inverts for velocity and earthquake locations to reduce slab-induced mislocation biases. Compared with prior global models, it recovers higher-amplitude, better-resolved slabs, making it particularly suitable for interpreting slab morphology.

GLAD-M35 (Cui et al., 2024) is the final generation of a series of joint P- and S-wave global adjoint tomography models, which strengthens constraints on global P-wave heterogeneity, substantially reducing P-wave misfit (and long-distance bias) compared to prior models. It also delivers uncertainty and resolution maps, enabling more robust interpretation of mantle structure. However, as no resolution operator has been published, we only use it for qualitative comparison.

2.3.2 Conversion to seismic speed

Mantle mineral physics models (Stixrude & Lithgow-Bertelloni, 2005; Piazzoni et al., 2007; Stixrude & Lithgow-Bertelloni, 2011, 2024) provide the link between the temperature and pressure fields predicted by mantle circulation models and the seismic heterogeneities imaged by tomography. Pressure effects vary predictably with depth (Cammarano et al., 2005), but the influence of temperature is more complex, involving both elastic and anelastic contributions. Using MMA-EoS (an open-source phase equilibrium solver; Chust et al., 2017), we implemented the solution parameters of Stixrude and Lithgow-Bertelloni (2024) to generate look-up tables for a homogenous pyrolitic mantle, under the assumption that the largest seismic anomalies have a predominantly thermal origin (Ringwood, 1991; Schuberth et al., 2009; Davies et al., 2012). While chemical heterogeneity undoubtedly contributes to seismic structure (e.g., Wang et al., 2021; Goes et al., 2022; Zhou et al., 2022), this thermal assumption is consistent with our coupled model, which only includes thermal anomalies.

To ensure robust application in geodynamic simulations, we regularised the thermodynamic tables by filtering the temperature–velocity relationship. Sharp, non-physical variations can produce abrupt jumps in seismic velocity that are not consistent with underlying mantle behaviour. We therefore constrained the gradient to the interval $[-1.5, 0.0]$ for S-waves and $[-\infty, 0.0]$ for P-waves, removing excessively steep slopes or gradients. Out-of-range values were replaced via inverse-distance weighted interpolation from neighbouring in-range points. The filtered gradient field was then reintegrated to reconstruct velocity tables anchored to the reference adiabat at each depth. This procedure yields a smooth, monotonic relationship between temperature and seismic velocity which is suitable for geodynamic applications.

We also account for viscoelastic relaxation, which modifies seismic wave speeds at mantle conditions. Given the uncertainty in attenuation, we adopt the Q6 parametrisation of Cammarano et al. (2003), which represents a moderate anelastic response (Table C1). This correction modestly amplifies seismic velocity perturbations, with a depth- and temperature- effect that is nonlinear (Figure C2).

This workflow—conversion of temperature fields to seismic velocity, gradient regularisation, and anelastic correction—has been encapsulated in G-DRIFT, a companion library to G-ADOPT, available at github.com/g-adopt/g-drift/.

2.3.3 Resolution operator

To evaluate how tomographic resolution shapes the appearance of synthetic mantle structure, we apply resolution operators from two widely used global models: *S40RTS* for S-waves and *LLNL-G3D-JPS* for P-waves (although *LLNL* is a joint P- and S-wave model, the resolution operator is

only available for P-waves at this time). These models provide complementary perspectives, since S- and P-waves differ in their sensitivities to temperature, composition, and anelastic effects.

Before either resolution operator $\mathcal{R}$ can be applied to a synthetic mantle model m, the model must first be reparametrised into the same basis as the tomography model, which we denote $\tilde{m}$. For *LLNL-G3D-JPS*, this involves downsampling onto the model's native tessellated triangular mesh (about one million nodes). For *S40RTS*, our synthetic seismic velocity structure is expanded into spherical harmonics up to degree 40. In both cases, the filtered model $\tilde{m}'$ is obtained through matrix–vector multiplication:

$$\tilde{m}' = \mathcal{R}\tilde{m}. \tag{1}$$

Programmatically, applying $\mathcal{R}$ is non-trivial. For *LLNL-G3D-JPS*, the operator contains on the order of 10^{12} elements; the LLNL_ToFi_3 script (github.com/tom-new/LLNL_ToFi_3/), which updates the implementation of Simmons et al. (2019) to Python 3 and provides an implementation compatible with Firedrake, exploits sparsity and parallelism to make the calculation tractable. For *S40RTS*, open-source filtering software is not currently available and hence we cannot provide it here. Nevertheless, by applying both operators we are able to examine how P- and S-wave resolution differently filter synthetic mantle anomalies, providing complementary insights into slab geometry and dynamics. It is important to note that in principle this stage of post-processing is easy to replace with the resolution operator for any other seismic tomography model.

2.3.4 Comparison metrics

We compute the ℓ^2 misfit between each of the processed models and the target tomography, where the ℓ^2-norm is defined in the usual manner (i.e., the square root of the sum of the squared differences). For S-wave comparisons we use *S40RTS*, while for P-wave comparisons we use *LLNL-G3D-JPS*. The ℓ^2-norm provides a convenient summary metric, but it has limitations as a measure of spatial correlation. Once two anomalies no longer overlap the norm saturates and cannot distinguish between larger separation distances (Figure 4).

For this reason, we also adopt the Wasserstein metric (also known as the Kantorovich–Rubinstein metric or earth mover's distance) which is sensitive not only to overlap extent, but also separation distance (Figure 4). This fact, in principle, makes the Wasserstein metric more geophysically meaningful, as it can measure displacement of slabs or plumes rather than just the presence or absence of overlap. This metric is familiar from the optimal transport problem in mathematics and computer science (Kantorovich, 1939; Vaserstein, 1969), but seldom used in geoscience and, to the authors' knowledge, has never been used in place of the ℓ^2-norm for this application. Its advantage over the ℓ^2-norm can be clearly seen when considering the similarity scores of the images in Figure 4; I_2 is four times further away from the reference feature I_0 than I_1, but its misfit according to the ℓ^2-norm is only twice as large, while the Wasserstein metric correctly scales the misfit. Similarly, I_3 is twice as far from I_0 as I_2 is from I_0, but the ℓ^2-norm does not distinguish between them, while the Wasserstein metric does.

The Wasserstein metric is commonly described as quantifying the amount of work done to move some number piles of dirt of various sizes into some number of holes of various sizes (hence the name earth mover's distance). However, this physical analogy is slightly misleading for two reasons. First, the total mass must be conserved between the initial and final states (no dirt can be created or destroyed). Second, the Wasserstein metric only accepts non-negative distributions. Therefore, the metric can more appropriately thought of as the work needed to move between different configurations of dirt piles, with the same total amount of dirt in each.

These constraints are problematic for our application; geodynamic and tomography models

Table 1

Summary of advantages and disadvantages of the ℓ^2-norm and Wasserstein metric.

Comparison method	Advantages	Disadvantages
ℓ^2-norm	Convenient summary metric	Does not require special normalisation
Wasserstein metric	Sensitive to overlap and separation distance	Requires non-negative distributions and equal total mass

Figure 4

Comparison between ℓ^2-norm and Wasserstein metric between a 2-dimensional Gaussian reference feature I_0 with mean $(-0.5, -0.5)$ and Gaussian features $I_{1,2,3}$ whose means are increasingly separated from the reference feature. A similarity of 0 indicates a perfect match, while larger values indicate greater dissimilarity.

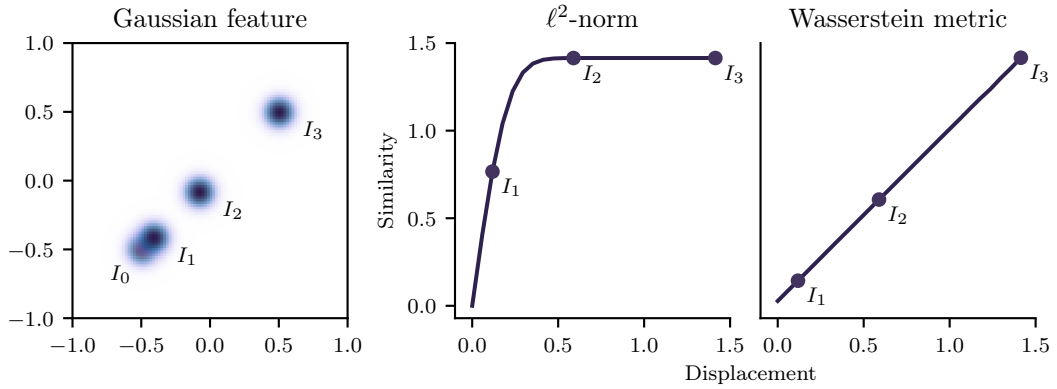

Note. For an animated version of this figure, visit github.com/tom-new/l2-vs-wass/.

of seismic velocity perturbation have both positive and negative values, and the total mass in a cross-section is unlikely to be the same between models. We therefore compute the Wasserstein similarity between only the magnitude of fast perturbations, with the total positive mass normalised to 1. This scaling removes global amplification or damping and focuses the comparison on relative spatial patterns (Table 1).

For both metrics, we compute similarity scores in vertical cross-sections through the Melanesian arc at five locations (A–E; Figures 8 and 9) limiting our analysis to the UM and TZ (depths from 0–1200 km) to focus the comparison on recent slab structure (i.e., that which has been produced by the MSS since its initiation at 85 Ma).

3 Results

3.1 Seismic tomography models

Although most of LM structure is quite different between models, a large region of slow material presents in the lowermost mantle across all models, likely representing the edge of the Pacific LLSVP. However, lower mantle structure is not the focus of this study. On the other hand, there is good consistency between the chosen tomography models in UM and TZ structure (Figure 5). The main feature observed across all tomography models and cross-sections is a 200–400 km-thick,

Figure 5

Comparison of five seismic tomography models in cross-section through the Melanesian arc. From left to right: LLNL-G3D-JPS, S40RTS, OJP_P, TX2019slab, and GLAD-M35. For S40RTS, S-wave velocity perturbations ($d\ln v_S$) are shown with x=1.5, while for all other models P-wave velocity perturbations ($d\ln v_P$) are shown with x=1.

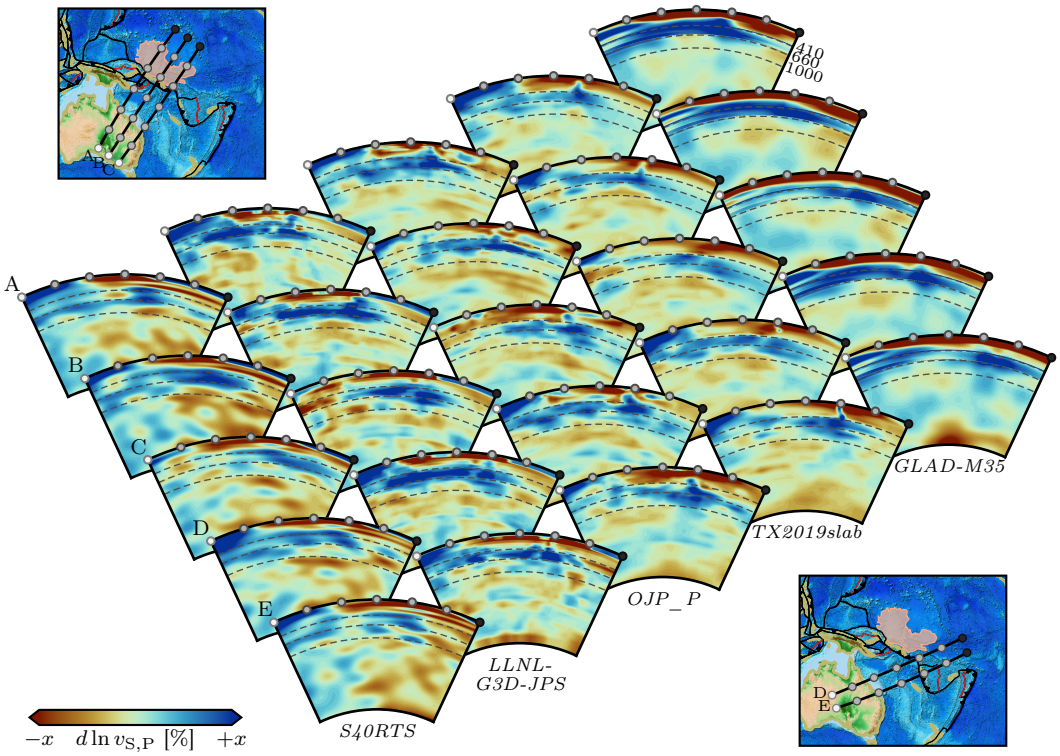

approximately 2500 km-long, seismically fast region in the UM/TZ starting under Australia (between the 2nd and 3rd pips) and ending under the Melanesian arc. Previous studies have interpreted this anomaly as a stagnant slab in the TZ (Obayashi et al., 2021). This anomaly shortens in its SW extent by a few hundred kilometres as cross-sections move SE (i.e., A to C).

3.2 Temporal evolution of modelled slabs

Before comparing the present-day results of our MCMs in each reconstruction, we first present the temporal evolution of the temperature field of each model in a representative cross-section, alongside the reconstruction in the mantle reference frame, in order to identify which cold anomalies in our model are associated with which subduction events (Figures 6 and 7).

The *Z22* reconstruction features unusually rapid (37 km Myr^{-1}) northeasterly trench migration of the proto-MSS from its initiation at 85 Ma until its first contact with the OJP at 25 Ma (Figure 6). Independent constraints require back-arc spreading and inverted secondary subduction associated with the Coral Sea (Seton et al., 2016). In our MCM, the subducted material from the proto-MSS that accumulates between 85–50 Ma does not sink very deeply under gravity because it is advected with the rapidly migrating trench; instead, it is separated from younger subduction (50–0 Ma) by this inverted secondary subduction system. From 25 Ma to present, the reconstruction implies almost no motion of the MSS relative to the mantle frame, so slab material subducted at the MSS during this interval sinks nearly vertically in our MCM, reaching the top of the TZ by 20 Ma and penetrating below the TZ by present day.

In contrast, *Z22M04* has much slower (13 km Myr^{-1}) trench migration from 85–12 Ma (Fig-

ure 7). In our MCM, this slower trench retreat allows earlier subducted material to sink more nearly vertically, so the secondary subduction associated with the Coral Sea does not disrupt the continuity of the subducted slab. However, there is significant thinning from 20–10 Ma, which, once tomographically filtered, becomes invisible (New et al., 2025). Because trench retreat continues until 10 Ma there are only 10 Myr of purely vertical sinking under the MSS, so by present day the slab material is only beginning to enter the TZ.

3.3 Qualitative comparison and statistical validation

With an understanding of the history of various slab material in our MCMs, we are now in a position to compare the present-day modelled mantle structure in *Z22* and *Z22M04* to that imaged by seismic tomography. Given the limitations of comparing thermal models directly with seismic images as previously noted (New et al., 2025), we instead report fully post-processed outputs—temperatures converted to seismic velocities and subsequently processed through tomographic filtering.

Once converted to seismic velocity and tomographically filtered, the recovered slab morphology is notably different, because most fast anomalies become broadened (Figures 8 and 9). In both *S40RTS*- and *LLNL*-filtering, the slab under the OJP is of comparable depth to tomography, however for *Z22M04* this is only the case with *S40RTS*-filtering. On the other hand, *Z22M04* is the only model which recovers slab material in the UM/TZ between the 2nd and 3rd cross-section pips; very little slab material is preserved in the TZ in *Z22* in this location. That which is preserved is only present in the uppermost-mantle, and therefore is better interpreted as the signature of Australian crustal material. *Z22M04* also recovers the SW shortening of slab material as cross-sections move SE.

Considering slab material generated in our models directly underneath the OJP–MSS collision region, and therefore associated with the most recent subduction (denoted **S1** in Figures 8 and 9), *Z22* produces slab material with basal depths at or just below the bottom of the TZ, in good agreement with the fast anomalies imaged by *S40RTS* and *LLNL-G3D-JPS*. In contrast, slab material in *Z22M04* attains basal depths ∼250 km shallower, reaching only the top of the TZ or just beginning to penetrate into it. Neither model, however, reproduces slab **S1** with the full lateral extent inferred from tomography: in our models, slabs are ∼8° long, whereas in tomography slab **S1** extends at least 12° (and potentially farther, depending on one's judgement of slab continuity). Slab material associated with subduction from 85–50 Ma (denoted **S2** in Figures 8 and 9) is heavily suppressed in *Z22* after filtering, but recovered well in *Z22M04*.

We also explored the statistical misfit between our two models and tomography. *Z22* is a better fit to tomography than *Z22M04* according to the ℓ^2-norm for both *S40RTS*-filtered and *LLNL*-filtered comparisons, with a 10 % better mean similarity score for both (Table 2). This difference in similarity scores between the two models is more pronounced when using the Wasserstein metric—with 28 % and 22 % better similarity for *S40RTS* and *LLNL-G3D-JPS*, respectively—indicating that *Z22* not only has a better overlap with fast tomographic anomalies, but also a closer spatial alignment. (Note that the scores for the ℓ^2-norm and Wasserstein metric are not directly comparable to each other, as they measure different things; see Table 1).

Figure 6

Development of temperature perturbation from layer mean (ΔT) through time in the southwest Pacific for Z22. Reconstruction shown in mantle reference frame. **a***) Stagnation of slab material from* 50–25 Ma *due to continuous and rapid trench retreat.* **b***) From* 25 Ma*, minimal trench retreat occurs, allowing for vertical sinking.* **c***) Slab penetrates the bottom of the TZ.*

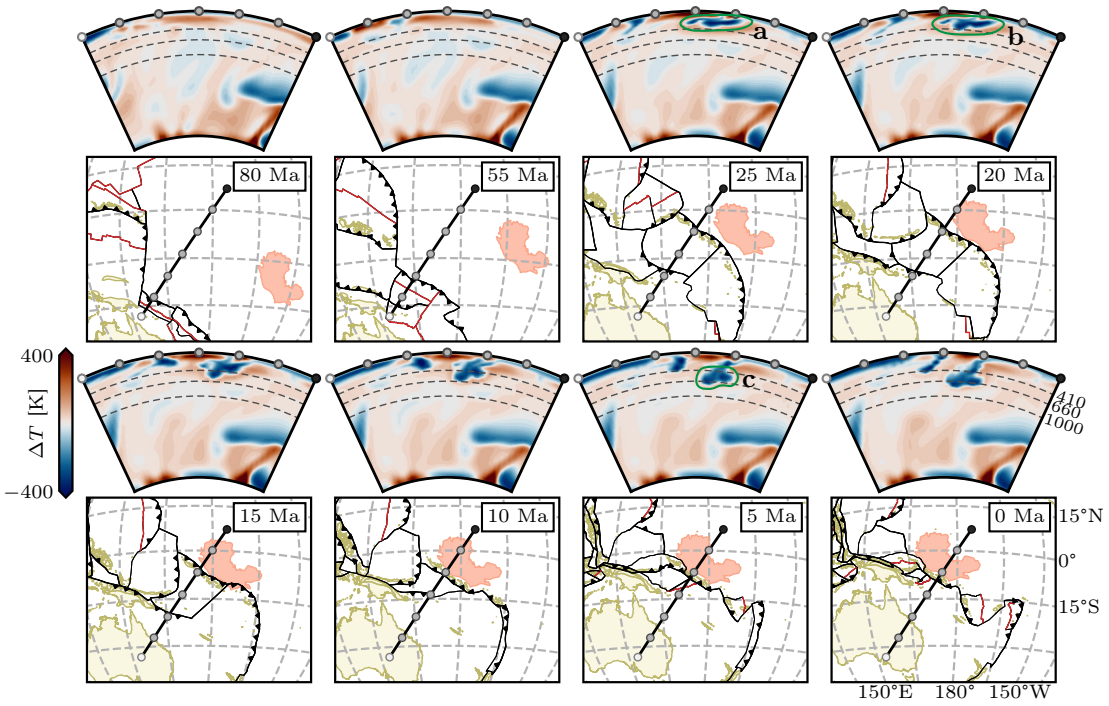

Figure 7

Development of temperature perturbation from layer mean (ΔT) through time in the southwest Pacific for Z22M04. Reconstruction shown in mantle reference frame. **a***) Part-sinking, part-stagnation of slab material due to continuous but slower trench retreat from* 50–10 Ma*.* **b***) Vertical sinking of slab material from* 10 Ma *just penetrating the top of the TZ.*

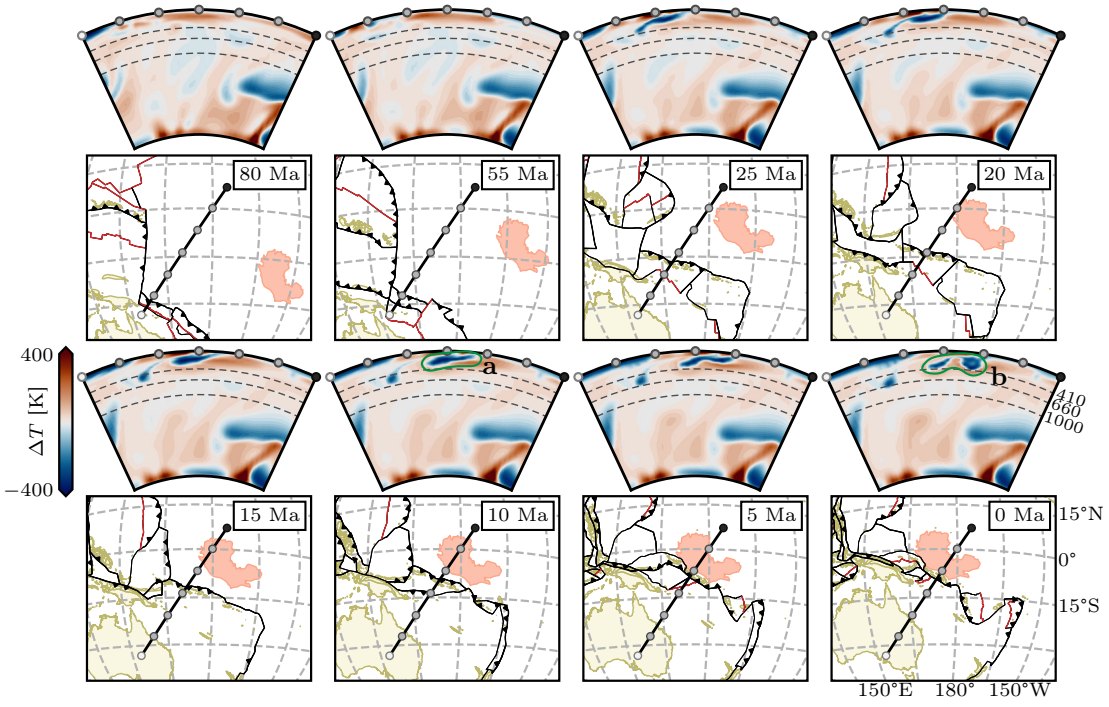

Table 2

The ℓ^2-norm and Wasserstein metric similarity scores between Z22 and Z22M04 and seismic tomography models S40RTS and LLNL-G3D-JPS in cross-sections A–E through the Melanesian arc in Figures 8 and 9. Similarity scores have been normalised to be in the range [0, 1], but ℓ^2 and Wassertstein scores are not directly comparable. Lower is better.

Model	Cross-section	*S40RTS*-filtered		*LLNL*-filtered	
		ℓ^2-norm	Wass.	ℓ^2-norm	Wass.
Z22	A	0.214	0.550	0.156	0.742
	B	0.204	0.642	0.136	0.601
	C	0.171	0.779	0.133	0.751
	D	0.207	0.452	0.163	0.660
	E	0.185	0.365	0.190	0.535
	Mean	0.196	0.558	0.156	0.658
Z22M04	A	0.241	0.748	0.170	0.931
	B	0.220	0.944	0.159	0.907
	C	0.199	0.952	0.161	0.849
	D	0.224	0.505	0.179	0.636
	E	0.204	0.724	0.194	0.891
	Mean	0.218	0.775	0.173	0.843
Difference	$100\left(1-\frac{Z22}{Z22M04}\right)$	10 %	28 %	10 %	22 %

4 Discussion

4.1 Implications for OJP–MSS collision and subduction polarity reversal timing

Across all tomography models considered, fast anomalies interpreted as MSS-related slab material form a laterally continuous, 200–400 km-thick band in the upper mantle and transition zone extending from beneath eastern Australia to the present-day Melanesian arc. Our results indicate that the *Z22* reconstruction, with a 25 Ma collision between the OJP and the MSS, provides a better fit to the seismic tomography data.

Specifically, *Z22* reproduces the location and depth of slab material beneath the OJP–MSS region, particularly in the TZ, more accurately than the later collision model (*Z22M04*). The *Z22* model shows significant slab material at the correct depths, in line with seismic imaging of fast anomalies beneath the region. Because the depth extent and continuity of the imaged fast anomalies require sufficient time for post-reversal subduction to generate and advect slab material into the TZ, the improved match of *Z22* implies an earlier subduction polarity reversal at ∼12 Ma, rather than a very recent (∼1–2 Ma) reversal.

In contrast, the *Z22M04* model fails to replicate this slab material in the TZ and instead places it at shallower depths, which does not align with tomography. This difference between the reconstructions among the cross-sections in Figures 8 and 9 is quantified by the misfit results from both *S40RTS* and *LLNL-G3D-JPS* tomography models (Table 2), where *Z22* performs significantly better in both ℓ^2-norm and Wasserstein metric comparisons (10–28 % lower misfit depending on metric and tomography model).

Figure 8

Z22 and Z22M04 in cross-section through the Melanesian arc comparing S-wave velocity perturbation ($d\ln v_S$) in S40RTS-filtered G-ADOPT output and S40RTS. **S1***) Slab generated by the MSS from* 50–0 Ma. **S2***) Slab material from proto-MSS subduction from* 85–50 Ma.

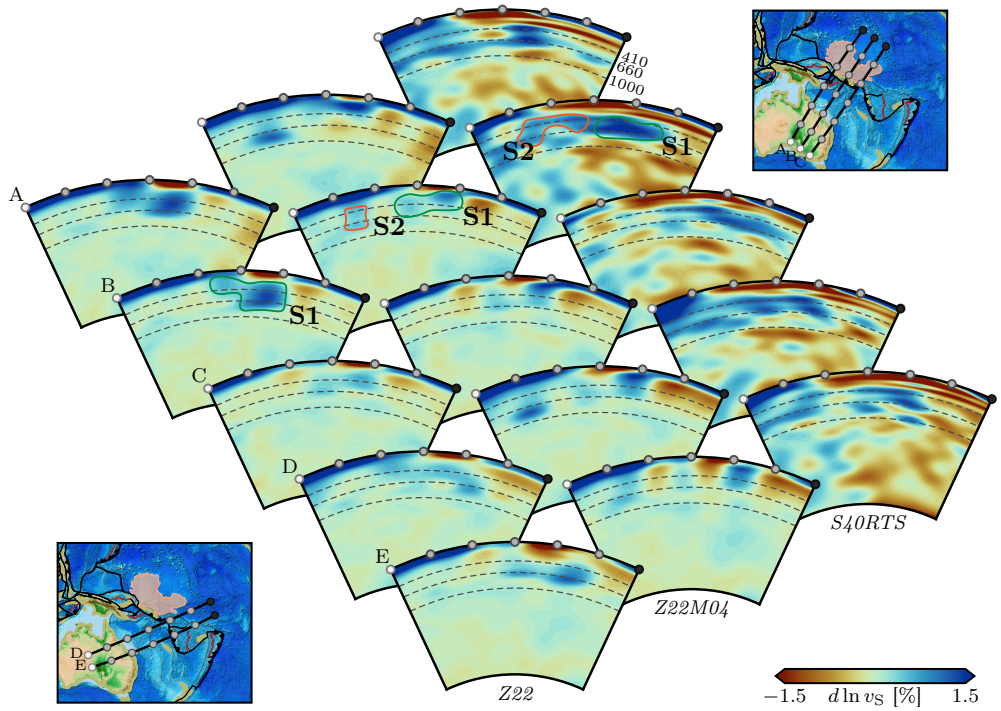

Figure 9

Z22 and Z22M04 in cross-section through the Melanesian arc comparing P-wave velocity perturbation ($d\ln v_P$) in LLNL-filtered G-ADOPT output and LLNL-G3D-JPS. **S1***) Slab generated by the MSS from* 50–0 Ma. **S2***) Slab material from proto-MSS subduction from* 85–50 Ma.

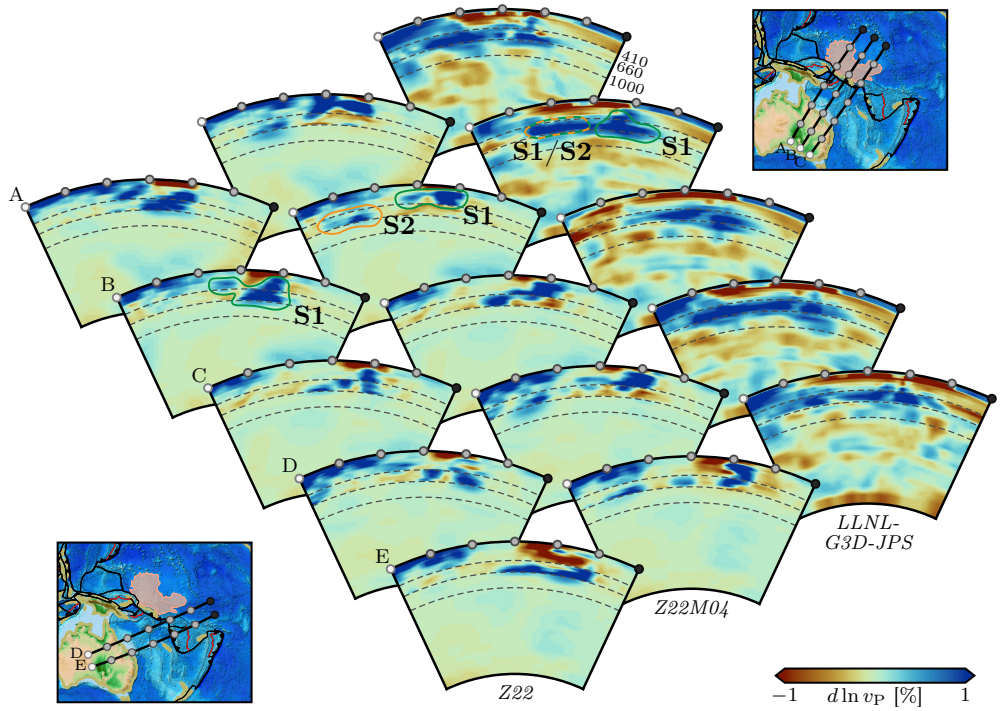

4.2 Implications for regional and global tectonic and geodynamic signatures

The collision of the >40 km-thick, buoyant OJP (Neal et al., 1997) with the MSS has been invoked to explain both a regional and global plate reorganisation event (Knesel et al., 2008). However, this argument hinges on the precise timing of the collision as a causal event. If the initial collision occurred between 26 and 20 Ma, the timing for a reorganisation around 25 Ma works. If it instead occurred between 12 and 8 Ma, the sequence of events cannot be reconciled. While our results from geodynamic modelling support the soft-docking model with timing of collision at 25 Ma, it remains an open question whether this collision caused significant enough change in subduction and/or mantle flow to trigger a GPRE.

GPREs are reflected in near synchronous changes in spreading rates and directions, subduction behaviour and intraplate deformation across all the ocean basins and continental margins (Matthews et al., 2012), while regional plate reorganisation events (RPREs) occur in a more geographically restricted domain. Consistent with this distinction, recent numerical modelling results (Janin et al., 2025) demonstrate that RPREs and GPREs not only manifest in different ways but are attributed to different plate boundary arrangements. RPREs are brief and locally confined, typically arising from changes along one or a few plate boundaries, while global events are far rarer and linked to the creation or destruction of plate boundaries several thousands of kilometres long, accompanied by shifts in mantle circulation and with effects that last for over 20 Myr (Janin et al., 2025).

There is evidence in the geological record for tectonic changes at around 25 Ma centred on the Pacific and Australian plates, including a slow-down in the motion of the Australian plate (Knesel et al., 2008), the onset of microplates along the fast-spreading East Pacific Rise (Mammerickx & Klitgord, 1982; Tebbens & Cande, 1997), southward offsets in the Cobb, Hawaiian, and Louisville hotspot chains seamount chains across the Pacific (Kroenke et al., 2004) and changes along the east Australia, Tasmantid (Knesel et al., 2008) and Lord Howe (Seton et al., 2019) seamount chains. In the Indian Ocean, there is evidence of a change in the collision regime along the Indian-Eurasia boundary (van Hinsbergen et al., 2012) but there is little evidence reflected in the seafloor spreading record at that time. There are no indicators of plate tectonic changes in the seafloor spreading record in the Atlantic Ocean.

A potentially analogous GPRE occurred between 105 and 100 Ma, evidenced by a host of contemporaneous tectonic events, and was likely precipitated by cessation of subduction along the eastern Gondwanan margin (Matthews et al., 2012). It has been suggested that the cause of cessation was the collision of the Hikurangi plateau, choking the east Gondwana subduction zone (Davy et al., 2008). However, it is debated whether such a small plateau—relative to the length of subduction zone which became inactive—could be solely responsible (Matthews et al., 2012). On one hand, the OJP is much larger than the Hikurangi plateau (2500 km versus 1100 km), but on the other, the length of change to the MSS is much shorter compared to that which occurred to the eastern Gondwanan margin (3000 km versus 7000 km). Moreover, a GPRE likely requires global-scale creation/destruction of plate boundaries together with prolonged changes in mantle flow (Janin et al., 2025), which is not the case in the late-Oligocene.

While this suggests that the plate reorganisation was not global in scope and effect, it does appear that there was an RPRE that affected the Pacific and Australian plates, consistent with the collision of the OJP along the northeasternmost margin of the Australian plate at 25 Ma. However, to further explore whether there is in fact a causal link between the OJP–MSS collision and changes to the plate–mantle system would require a more explicit experiment—for example through geodynamic modelling—that assesses the induced changes in subduction behaviour and mantle flow due to a collider the size, shape and thickness of the OJP.

4.3 Future work

The presence of a subduction-related fast anomaly from 800–1400 km depth under southeastern Australia has been invoked to explain the depression of the Lake Eyre basin via negative dynamic topography. This anomaly has been linked to a ∼4000 km-wide subduction zone, located slightly further southeast than S2 in *Z22M04* (Figures 8 and 9), that was active from 70–45 Ma (Schellart & Spakman, 2015). Given the proximity of the fast anomaly that develops in *Z22M04* from the MSS, we suggest that introducing such a subduction zone may reconcile two key constraints: (i) the ∼25 Ma OJP–MSS collision timing required to reproduce present-day tomographic structure beneath the MSS, and (ii) the negative dynamic topography hypothesis for Lake Eyre. In this framework, S2 in *Z22M04* is not directly compatible with *Z22*; however, a subduction zone located further south than S2 may be tectonically consistent with *Z22*. That is, S2 from *Z22M04* is not compatible with *Z22*, but a different subduction zone further south than S2 in *Z22M04* may be tectonically/geologically compatible with *Z22*. Similarly located slab material has been found in past global circulation models (Zahirovic et al., 2016). A particularly promising avenue for future work is therefore to explore the dynamic topography signal in a global MCM that includes a subduction zone extant from 70–45 Ma beneath the present-day Lake Eyre region, which would allow a direct test of the proposal that the depression of Lake Eyre is due to negative dynamic topography from subduction-related mantle flow, as proposed by Schellart and Spakman (2015).

Copper (Cu) porphyry deposits host 70 % of discovered global Cu resources and 20 % of global gold resources (Cooke et al., 2005; Sillitoe, 2010). Although most of these deposits occur in continental settings, a substantial number are developed in island-arc environments, including the Melanesian arc (Holm et al., 2019), and their importance is likely to grow as global demand increases. The formation of porphyry deposits is closely linked to subduction-zone processes (Sillitoe, 1972). The distribution of these deposits—both those already discovered and those yet to be found—is therefore sensitive to the dynamics and timing of subduction in the MSS. Our results, which provide an independent test of OJP–MSS collision timing, suggest that the initial collision occurred in the late Oligocene to early Miocene, consistent with the ages of porphyry-generating magmatic pulses in the Melanesian arc from 25–20 Ma (Holm et al., 2013). Nevertheless, further onshore field studies in the Melanesian arc are required to better constrain its porphyry prospectivity.

5 Conclusions

This study uses an integrated geodynamic modelling framework to test two competing reconstructions for the collision between the Ontong–Java plateau (OJP) and the Melanesian Arc subduction system (MSS). Our results strongly favour the 25 million-year-old collision scenario (*Z22*), as it provides a better fit to seismic tomography data compared to the 12 million-year-old collision model (*Z22M04*). The *Z22* model accurately reproduces the observed slab material in the upper mantle and transition zone, with a significant reduction in misfit compared to the alternative model.

These findings support the idea that the OJP–MSS collision at 25 million years ago played a key role in driving regional tectonic changes in the southwest Pacific, contributing to a reorganisation of plate motions. However, the impact of this collision on global plate dynamics remains uncertain, as GPREs are typically associated with much larger scale events. Further research could expand on these findings by exploring the potential links between the OJP–MSS collision and dynamic topography beneath regions like Lake Eyre. Additionally, the methodology developed in this study—combining topological plate reconstructions, mantle convection simulations, and robust seismic tomography comparisons—offers a powerful approach for discriminating between competing

tectonic models and could be applied to other subduction systems with unresolved plate kinematics.

References

Balay, S., Gropp, W. D., McInnes, L. C., & Smith, B. F. (1997). Efficient Management of Parallelism in Object-Oriented Numerical Software Libraries. In E. Arge, A. M. Bruaset, & H. P. Langtangen (Eds.), *Modern Software Tools for Scientific Computing* (pp. 163–202). Birkhäuser Boston. https://doi.org/10.1007/978-1-4612-1986-6_8

Cammarano, F., Goes, S., Deuss, A., & Giardini, D. (2005). Is a pyrolitic adiabatic mantle compatible with seismic data? *Earth and Planetary Science Letters*, *232*(3), 227–243. https://doi.org/10.1016/j.epsl.2005.01.031

Cammarano, F., Goes, S., Vacher, P., & Giardini, D. (2003). Inferring upper-mantle temperatures from seismic velocities. *Physics of the Earth and Planetary Interiors*, *138*(3), 197–222. https://doi.org/10.1016/S0031-9201(03)00156-0

Chust, T. C., Steinle-Neumann, G., Dolejš, D., Schuberth, B. S. A., & Bunge, H.-P. (2017). MMA-EoS: A computational framework for mineralogical thermodynamics. *Journal of Geophysical Research: Solid Earth*, *122*(12), 9881–9920. https://doi.org/10.1002/2017JB014501

Cooke, D. R., Hollings, P., & Walshe, J. L. (2005). Giant porphyry deposits: Characteristics, distribution, and tectonic controls. *Economic Geology*, *100*(5), 801–818. https://doi.org/10.2113/gsecongeo.100.5.801

Cowley, S., Mann, P., Coffin, M., & Shipley, T. H. (2004). Oligocene to recent tectonic history of the Central Solomon intra-arc basin as determined from marine seismic reflection data and compilation of onland geology. *Tectonophysics*, *389*(3-4), 267–307. https://doi.org/10.1016/j.tecto.2004.01.008

Croon, M. B., Cande, S. C., & Stock, J. M. (2008). Revised Pacific–Antarctic plate motions and geophysics of the Menard Fracture Zone. *Geochemistry, Geophysics, Geosystems*, *9*(7). https://doi.org/10.1029/2008GC002019

Cui, C., Lei, W., Liu, Q., Peter, D., Bozdağ, E., Tromp, J., Hill, J., Podhorszki, N., & Pugmire, D. (2024). GLAD-M35: A joint P and S global tomographic model with uncertainty quantification. *Geophysical Journal International*, *239*(1), 478–502. https://doi.org/10.1093/gji/ggae270

Davidson, P. C., Koppers, A. A. P., Sano, T., & Hanyu, T. (2023). A younger and protracted emplacement of the Ontong Java Plateau. *Science*, *380*(6650), 1185–1188. https://doi.org/10.1126/science.ade8666

Davies, D. R., Goes, S., Davies, J. H., Schuberth, B. S. A., Bunge, H.-P., & Ritsema, J. (2012). Reconciling dynamic and seismic models of Earth's lower mantle: The dominant role of thermal heterogeneity. *Earth and Planetary Science Letters*, *353–354*, 253–269. https://doi.org/10.1016/j.epsl.2012.08.016

Davies, D. R., Kramer, S. C., Ghelichkhan, S., & Gibson, A. (2022). Towards automatic finite-element methods for geodynamics via Firedrake. *Geoscientific Model Development*, *15*(13), 5127–5166. https://doi.org/10.5194/gmd-15-5127-2022

Davy, B., Hoernle, K., & Werner, R. (2008). Hikurangi plateau: Crustal structure, rifted formation, and Gondwana subduction history. *Geochemistry, Geophysics, Geosystems*, *9*(7). https://doi.org/10.1029/2007GC001855

Flament, N., Gurnis, M., Müller, R. D., Bower, D. J., & Husson, L. (2015). Influence of subduction history on South American topography. *Earth and Planetary Science Letters*, *430*, 9–18. https://doi.org/10.1016/j.epsl.2015.08.006

Ghelichkhan, S., Gibson, A., Davies, D. R., Kramer, S. C., & Ham, D. A. (2024). Automatic adjoint-based inversion schemes for geodynamics: Reconstructing the evolution of Earth's mantle in space and time. *Geoscientific Model Development*, *17*(13), 5057–5086. https://doi.org/10.5194/gmd-17-5057-2024

Goes, S., Cammarano, F., & Hansen, U. (2004). Synthetic seismic signature of thermal mantle plumes. *Earth and Planetary Science Letters*, *218*(3), 403–419. https://doi.org/10.1016/S0012-821X(03)00680-0

Goes, S., Yu, C., Ballmer, M. D., Yan, J., & van der Hilst, R. D. (2022). Compositional heterogeneity in the mantle transition zone. *Nature Reviews Earth & Environment*, *3*(8), 533–550. https://doi.org/10.1038/s43017-022-00312-w

Hall, R. (2002). Cenozoic geological and plate tectonic evolution of SE Asia and the SW Pacific: Computer-based reconstructions, model and animations. *Journal of Asian Earth Sciences*, *20*(4), 353–431. https://doi.org/10.1016/S1367-9120(01)00069-4

Holm, R. J., Spandler, C., & Richards, S. W. (2013). Melanesian arc far-field response to collision of the Ontong Java Plateau: Geochronology and petrogenesis of the Simuku Igneous Complex, New Britain, Papua New Guinea. *Tectonophysics*, *603*, 189–212. https://doi.org/10.1016/j.tecto.2013.05.029

Holm, R. J., Tapster, S., Jelsma, H. A., Rosenbaum, G., & Mark, D. F. (2019). Tectonic evolution and copper-gold metallogenesis of the Papua New Guinea and Solomon Islands region. *Ore Geology Reviews*, *104*, 208–226. https://doi.org/10.1016/j.oregeorev.2018.11.007

Janin, A., Coltice, N., Chamot-Rooke, N., & Tierny, J. (2025). Geodynamics of a global plate reorganization from topological data analysis. *Nature Geoscience*, *18*(10), 1041–1047. https://doi.org/10.1038/s41561-025-01772-7

Kantorovich, L. V. (1939). Mathematical methods of organizing and planning production. *Management Science*, *6*(4), 366–422. https://doi.org/10.1287/mnsc.6.4.366

Knesel, K. M., Cohen, B. E., Vasconcelos, P. M., & Thiede, D. S. (2008). Rapid change in drift of the Australian plate records collision with Ontong Java plateau. *Nature*, *454*(7205), 754–757. https://doi.org/10.1038/nature07138

Kroenke, L. W., Wessel, P., & Sterling, A. (2004). Motion of the Ontong Java Plateau in the hot-spot frame of reference: 122 Ma–present. In J. G. Fitton, J. J. Mahoney, P. J. Wallace, & A. D. Saunders (Eds.), *Origin and Evolution of the Ontong Java Plateau* (pp. 9–20, Vol. 229). Geological Society of London. https://doi.org/10.1144/GSL.SP.2004.229.01.02

Larson, R. L., & Erba, E. (1999). Onset of the Mid-Cretaceous greenhouse in the Barremian–Aptian: Igneous events and the biological, sedimentary, and geochemical responses. *Paleoceanography*, *14*(6), 663–678. https://doi.org/10.1029/1999PA900040

Lin, Y.-A., Colli, L., & Wu, J. (2022). NW Pacific-Panthalassa Intra-Oceanic Subduction During Mesozoic Times From Mantle Convection and Geoid Models. *Geochemistry, Geophysics, Geosystems*, *23*(11), e2022GC010514. https://doi.org/10.1029/2022GC010514

Lu, C., Grand, S. P., Lai, H., & Garnero, E. J. (2019). TX2019slab: A new P and S tomography model incorporating subducting slabs. *Journal of Geophysical Research: Solid Earth*, *124*(11), 11549–11567. https://doi.org/10.1029/2019JB017448

Mammerickx, J., & Klitgord, K. D. (1982). Northern East Pacific Rise: Evolution from 25 m.y. B.P. to the present. *Journal of Geophysical Research: Solid Earth*, *87*(B8), 6751–6759. https://doi.org/10.1029/JB087iB08p06751

Mann, P., & Taira, A. (2004). Global tectonic significance of the Solomon Islands and Ontong Java Plateau convergent zone. *Tectonophysics*, *389*(3), 137–190. https://doi.org/10.1016/j.tecto.2003.10.024

Mather, B. R., Müller, R. D., Zahirovic, S., Cannon, J., Chin, M., Ilano, L., Wright, N. M., Alfonso, C., Williams, S., Tetley, M., & Merdith, A. (2024). Deep time spatio-temporal data analysis using pyGPlates with PlateTectonicTools and GPlately. *Geoscience Data Journal*, *11*(1), 3–10. https://doi.org/10.1002/gdj3.185

Matthews, K. J., Seton, M., & Müller, R. D. (2012). A global-scale plate reorganization event at 105–100 Ma. *Earth and Planetary Science Letters*, *355–356*, 283–298. https://doi.org/10.1016/j.epsl.2012.08.023

Müller, R. D., Cannon, J., Qin, X., Watson, R. J., Gurnis, M., Williams, S., Pfaffelmoser, T., Seton, M., Russell, S. H. J., & Zahirovic, S. (2018). GPlates: Building a virtual Earth through deep time. *Geochemistry, Geophysics, Geosystems*, *19*(7), 2243–2261. https://doi.org/10.1029/2018GC007584

Musgrave, R. J. (1990). Paleomagnetism and tectonics of Malaita, Solomon Islands. *Tectonics*, *9*(4), 735–759. https://doi.org/10.1029/TC009i004p00735

Musgrave, R. J. (2013). Evidence for late Eocene emplacement of the Malaita Terrane, Solomon Islands: Implications for an even larger Ontong Java Nui oceanic plateau. *Journal of Geophysical Research: Solid Earth*, *118*(6), 2670–2686. https://doi.org/10.1002/jgrb.50153

Neal, C. R., Mahoney, J. J., Kroenke, L. W., Duncan, R. A., & Petterson, M. G. (1997). The Ontong Java Plateau. *Geophysical Monograph*, *100*, 183–216.

Nerlich, R., Colli, L., Ghelichkhan, S., Schuberth, B., & Bunge, H.-P. (2016). Constraining central Neo-Tethys Ocean reconstructions with mantle convection models. *Geophysical Research Letters*, *43*(18), 9595–9603. https://doi.org/10.1002/2016GL070524

New, T., Ghelichkhan, S., Davies, D. R., Seton, M., Mather, B., & Müller, R. D. (2025). Calibrating plate reconstructions with global mantle convection models. *Manuscript in revision, Geochemistry, Geophysics, Geosystems.*

NOAA National Geophysical Data Center. (2009). *ETOPO1 1 Arc-Minute Global Relief Model*. NOAA National Centers for Environmental Information. https://doi.org/10.7289/V5C8276M

Obayashi, M., Yoshimitsu, J., Suetsugu, D., Shiobara, H., Sugioka, H., Ito, A., Isse, T., Ishihara, Y., Tanaka, S., & Tonegawa, T. (2021). Interrelation of the stagnant slab, Ontong Java Plateau, and intraplate volcanism as inferred from seismic tomography. *Scientific Reports*, *11*(1), 20966. https://doi.org/10.1038/s41598-021-99833-5

Petterson, M., Babbs, T., Neal, C., Mahoney, J., Saunders, A., Duncan, R., Tolia, D., Magu, R., Qopoto, C., Mahoa, H., & Natogga, D. (1999). Geological–tectonic framework of Solomon Islands, SW Pacific: Crustal accretion and growth within an intra-oceanic setting. *Tectonophysics*, *301*(1-2), 35–60. https://doi.org/10.1016/S0040-1951(98)00214-5

Petterson, M., Neal, C., Mahoney, J., Kroenke, L., Saunders, A., Babbs, T., Duncan, R., Tolia, D., & McGrail, B. (1997). Structure and deformation of north and central Malaita, Solomon Islands: Tectonic implications for the Ontong Java Plateau–Solomon arc collision, and for the fate of oceanic plateaus. *Tectonophysics*, *283*(1-4), 1–33. https://doi.org/10.1016/S0040-1951(97)00206-0

Phinney, E. J., Mann, P., Coffin, M. F., & Shipley, T. H. (2004). Sequence stratigraphy, structural style, and age of deformation of the Malaita accretionary prism (Solomon arc–Ontong Java Plateau convergent zone). *Tectonophysics*, *389*(3-4), 221–246. https://doi.org/10.1016/j.tecto.2003.10.025

Piazzoni, A. S., Steinle-Neumann, G., Bunge, H.-P., & Dolejš, D. (2007). A mineralogical model for density and elasticity of the Earth's mantle. *Geochemistry, Geophysics, Geosystems*, *8*(11). https://doi.org/10.1029/2007GC001697

Rathgeber, F., Ham, D. A., Mitchell, L., Lange, M., Luporini, F., Mcrae, A. T. T., Bercea, G.-T., Markall, G. R., & Kelly, P. H. J. (2016). Firedrake: Automating the finite element method by composing abstractions. *ACM Transactions on Mathematical Software*, *43*(3), 24:1–24:27. https://doi.org/10.1145/2998441

Ringwood, A. E. (1991). Phase transformations and their bearing on the constitution and dynamics of the mantle. *Geochimica et Cosmochimica Acta*, *55*(8), 2083–2110. https://doi.org/10.1016/0016-7037(91)90090-R

Ritsema, J., Deuss, A., van Heijst, H. J., & Woodhouse, J. H. (2011). S40RTS: A degree-40 shear-velocity model for the mantle from new Rayleigh wave dispersion, teleseismic traveltime and normal-mode splitting function measurements. *Geophysical Journal International*, *184*(3), 1223–1236. https://doi.org/10.1111/j.1365-246X.2010.04884.x

Ritsema, J., McNamara, A. K., & Bull, A. L. (2007). Tomographic filtering of geodynamic models: Implications for model interpretation and large-scale mantle structure. *Journal of Geophysical Research: Solid Earth*, *112*(B1). https://doi.org/10.1029/2006JB004566

Schellart, W. P., Lister, G. S., & Toy, V. G. (2006). A late Cretaceous and Cenozoic reconstruction of the Southwest Pacific region: Tectonics controlled by subduction and slab rollback processes. *Earth-Science Reviews*, *76*(3), 191–233. https://doi.org/10.1016/j.earscirev.2006.01.002

Schellart, W. P., & Spakman, W. (2015). Australian plate motion and topography linked to fossil New Guinea slab below Lake Eyre. *Earth and Planetary Science Letters*, *421*, 107–116. https://doi.org/10.1016/j.epsl.2015.03.036

Schuberth, B. S. A., Bunge, H.-P., & Ritsema, J. (2009). Tomographic filtering of high-resolution mantle circulation models: Can seismic heterogeneity be explained by temperature alone? *Geochemistry, Geophysics, Geosystems*, *10*(5). https://doi.org/10.1029/2009GC002401

Seton, M., Flament, N., Whittaker, J., Müller, R. D., Gurnis, M., & Bower, D. J. (2015). Ridge subduction sparked reorganization of the Pacific plate–mantle system 60–50 million years ago. *Geophysical Research Letters*, *42*(6), 1732–1740. https://doi.org/10.1002/2015GL063057

Seton, M., Mortimer, N., Williams, S., Quilty, P., Gans, P., Meffre, S., Micklethwaite, S., Zahirovic, S., Moore, J., & Matthews, K. J. (2016). Melanesian back-arc basin and arc development: Constraints from the eastern Coral Sea. *Gondwana Research*, *39*, 77–95. https://doi.org/10.1016/j.gr.2016.06.011

Seton, M., Williams, S., Mortimer, N., Meffre, S., Micklethwaite, S., & Zahirovic, S. (2019). Magma production along the Lord Howe Seamount Chain, northern Zealandia. *Geological Magazine*, *156*(9), 1605–1617. https://doi.org/10.1017/S0016756818000912

Shephard, G. E., Matthews, K. J., Hosseini, K., & Domeier, M. (2017). On the consistency of seismically imaged lower mantle slabs. *Scientific Reports*, *7*(1), 10976. https://doi.org/10.1038/s41598-017-11039-w

Sikora, P. J., & Bergen, J. A. (2004). Lower Cretaceous planktonic foraminiferal and nannofossil biostratigraphy of Ontong Java Plateau sites from DSDP Leg 30 and ODP Leg 192. *Geological Society, London, Special Publications*, *229*(1), 83–111. https://doi.org/10.1144/GSL.SP.2004.229.01.07

Sillitoe, R. H. (1972). A plate tectonic model for the origin of porphyry copper deposits. *Economic Geology*, *67*(2), 184–197. https://doi.org/10.2113/gsecongeo.67.2.184

Sillitoe, R. H. (2010). Porphyry Copper Systems. *Economic Geology*, *105*(1), 3–41. https://doi.org/10.2113/gsecongeo.105.1.3

Simmons, N. A., Myers, S. C., Johannesson, G., Matzel, E., & Grand, S. P. (2015). Evidence for long-lived subduction of an ancient tectonic plate beneath the southern Indian Ocean. *Geophysical Research Letters*, *42*(21), 9270–9278. https://doi.org/10.1002/2015GL066237

Simmons, N. A., Schuberth, B. S. A., Myers, S. C., & Knapp, D. R. (2019). Resolution and covariance of the LLNL-G3D-JPS global seismic tomography model: Applications to travel time uncertainty and tomographic filtering of geodynamic models. *Geophysical Journal International*, *217*(3), 1543–1557. https://doi.org/10.1093/gji/ggz102

Stern, R. J. (2004). Subduction initiation: Spontaneous and induced. *Earth and Planetary Science Letters*, *226*(3), 275–292. https://doi.org/10.1016/j.epsl.2004.08.007

Stixrude, L., & Lithgow-Bertelloni, C. (2005). Thermodynamics of mantle minerals—I. Physical properties. *Geophysical Journal International*, *162*(2), 610–632. https://doi.org/10.1111/j.1365-246X.2005.02642.x

Stixrude, L., & Lithgow-Bertelloni, C. (2011). Thermodynamics of mantle minerals—II. Phase equilibria. *Geophysical Journal International*, *184*(3), 1180–1213. https://doi.org/10.1111/j.1365-246X.2010.04890.x

Stixrude, L., & Lithgow-Bertelloni, C. (2024). Thermodynamics of mantle minerals—III. The role of iron. *Geophysical Journal International*, *237*(3), 1699–1733. https://doi.org/10.1093/gji/ggae126

Taylor, B. (2006). The single largest oceanic plateau: Ontong Java–Manihiki–Hikurangi. *Earth and Planetary Science Letters*, *241*(3-4), 372–380. https://doi.org/10.1016/j.epsl.2005.11.049

Tebbens, S. F., & Cande, S. C. (1997). Southeast Pacific tectonic evolution from Early Oligocene to Present. *Journal of Geophysical Research: Solid Earth*, *102*(B6), 12061–12084. https://doi.org/10.1029/96JB02582

Tejada, M. L. G., Sano, T., Hanyu, T., Koppers, A. a. P., Nakanishi, M., Miyazaki, T., Ishikawa, A., Tani, K., Shimizu, S., Shimizu, K., Vaglarov, B., & Chang, Q. (2023). New evidence for the Ontong Java Nui hypothesis. *Scientific Reports*, *13*(1), 8486. https://doi.org/10.1038/s41598-023-33724-9

Torsvik, T. H., Steinberger, B., Shephard, G. E., Doubrovine, P. V., Gaina, C., Domeier, M., Conrad, C. P., & Sager, W. W. (2019). Pacific–Panthalassic reconstructions: Overview, errata and the way forward. *Geochemistry, Geophysics, Geosystems*, *20*(7), 3659–3689. https://doi.org/10.1029/2019GC008402

Trampert, J., Fichtner, A., & Ritsema, J. (2013). Resolution tests revisited: The power of random numbers. *Geophysical Journal International*, *192*, 676–680. https://doi.org/10.1093/gji/ggs057

van Hinsbergen, D. J. J., Lippert, P. C., Dupont-Nivet, G., McQuarrie, N., Doubrovine, P. V., Spakman, W., & Torsvik, T. H. (2012). Greater India Basin hypothesis and a two-stage Cenozoic collision between India and Asia. *Proceedings of the National Academy of Sciences*, *109*(20), 7659–7664. https://doi.org/10.1073/pnas.1117262109

Vaserstein, L. N. (1969). Markov processes over denumerable products of spaces, describing large systems of automata. *Problemy Peredachi Informatsii*, *5*(3), 64–72.

Wang, W., Zhang, H., Brodholt, J. P., & Wu, Z. (2021). Elasticity of hydrous ringwoodite at mantle conditions: Implication for water distribution in the lowermost mantle transition zone. *Earth and Planetary Science Letters*, *554*, 116626. https://doi.org/10.1016/j.epsl.2020.116626

Williams, S. E., Whittaker, J. M., & Müller, R. D. (2011). Full-fit, palinspastic reconstruction of the conjugate Australian–Antarctic margins. *Tectonics*, *30*(6). https://doi.org/10.1029/2011TC002912

Wright, N. M., Müller, R. D., Seton, M., & Williams, S. E. (2015). Revision of Paleogene plate motions in the Pacific and implications for the Hawaiian-Emperor bend. *Geology*, *43*(5), 455–458. https://doi.org/10.1130/G36303.1

Zahirovic, S., Eleish, A., Doss, S., Pall, J., Cannon, J., Pistone, M., Tetley, M. G., Young, A., & Fox, P. (2022). Subduction and carbonate platform interactions. *Geoscience Data Journal*, *9*(2), 371–383. https://doi.org/10.1002/gdj3.146

Zahirovic, S., Matthews, K. J., Flament, N., Müller, R. D., Hill, K. C., Seton, M., & Gurnis, M. (2016). Tectonic evolution and deep mantle structure of the eastern Tethys since the latest Jurassic. *Earth-Science Reviews*, *162*, 293–337. https://doi.org/10.1016/j.earscirev.2016.09.005

Zaroli, C., Koelemeijer, P., & Lambotte, S. (2017). Toward seeing the Earth's interior through unbiased tomographic lenses. *Geophysical Research Letters*, *44*(22). https://doi.org/10.1002/2017GL074996

Zhou, W.-Y., Hao, M., Zhang, J. S., Chen, B., Wang, R., & Schmandt, B. (2022). Constraining composition and temperature variations in the mantle transition zone. *Nature Communications*, *13*(1), 1094. https://doi.org/10.1038/s41467-022-28709-7

5 | Discussion

In this thesis, I develop new workflows to overcome three major limitations common to previous studies that use mantle circulation models (MCMs) to calibrate tectonic reconstructions—namely, accounting for nonlinearity in the temperature–velocity relationship, imaging the modelled mantle structure through the same lens as seismic tomography, and introducing a statistical method to measure the magnitude of displacement between seismic anomalies. I also explore the strengths and weaknesses of G-ADOPT MCMs in which slab geometry arises dynamically from the kinematics of the imposed tectonic reconstruction, rather than being prescribed at the surface according to constraints inferred from geology and tomography. These studies demonstrate that applying tomographic filtering to mantle circulation models significantly alters the interpretation of slab morphology. Additionally, the integration of the Wasserstein metric allows for a more appropriate assessment of the fit between modelled and imaged slabs.

I apply the learnings from these investigations to a case study: the collision of the Ontong–Java plateau (OJP) with the Melanesian arc subduction system (MSS), with implications for global plate reorganisations. This event provides an ideal test case for the methodologies I developed. The ambiguous geological and geophysical constraints on the evolution of the MSS mean that predictions of mantle structure derived from two MCMs, each forced by a different tectonic reconstruction, provide an independent line of evidence to distinguish between the competing hypotheses in the literature. Furthermore, the relatively simple, rollback-dominated, oceanic arc regime of the collision is similar to other settings in which G-ADOPT models perform well when compared against images of slab morphology from seismic tomography models. Using my new workflows, I found that the predictions from G-ADOPT models support an earlier (∼25 Ma) timing for the OJP–MSS collision rather than a later (∼12 Ma), with significantly lower misfit–by 10–28 %—across all comparison metrics and cross-sections through the region.

1 Model–tomography comparisons

Using coupled plate tectonic–mantle circulation models to differentiate between competing tectonic reconstructions is an appealing and powerful method by which to obtain an independent line of evidence (e.g., Liu & Stegman, 2011; Flament et al., 2015; Seton et al., 2015; Zahirovic et al., 2016; Harrington et al., 2017; Hu et al., 2018a, 2018b; Peng et al., 2021a, 2021b). Chapter 2 demonstrates clearly the importance of tomographically filtering the predictions made by such MCMs to avoid over-indexing on differences (or similarities) between predicted and imaged slab morphologies. For example, cold anomalies (i.e., slabs) in a model's temperature structure may be:

- *Initially continuous, but broken into separate bodies.* This apparent segmentation emerges where the local resolution length increases and the anomaly's peak amplitude is pushed below the colour scale or noise floor, leaving gaps. Because the resolution operator is spatially variable and often anisotropic, the same feature can remain coherent in one region and

fragment in another. Interpreted naïvely, this pattern could mimic slab tearing or along-strike offsets that are not present in the synthetic model.

- *Initially discontinuous, but connected into a single body.* Here, poor local resolution causes amplitude to leak into low-signal regions, creating an artificial bridge. The effect is strongest where adjacent anomalies are closer than the local resolution length, and can be misread as mechanical continuity (e.g., an uninterrupted slab segment or channelised upwelling).

- *Increased in size but damped.* Convolution with the operator's point–spread function broadens narrow features (vertical and/or lateral smearing) while reducing peak amplitude. The net effect is an apparently more voluminous but intrinsically weaker anomaly, reflecting wavelength-dependent damping: short-wavelength structure is preferentially broadened and attenuated.

- *Reduced in size or eliminated.* Where anomaly wavelengths fall below the local resolution, or where neighbouring signals interfere destructively, the operator suppresses the feature to below detectability, yielding false negatives for genuine but fine-scale structure.

Acknowledging these complications is critical to avoid compromising the geodynamic and tectonic interpretations inferred when comparing predicted to imaged structure. It is easy to imagine such a scenario. Suppose there is a subduction system where onshore geology indicates a ∼10 Myr break or significant reduction in subduction rate (e.g., a gap in back-arc volcanism), but tomographic images of the corresponding anomaly reveal a contiguous slab from the surface to the bottom of the transition zone. Was the reduced subduction rate just not enough to be visible in tomography? Or did subduction continue as normal, and the apparent gap in volcanism caused by it simply not being preserved in the stratigraphic record? (The attentive reader will notice a striking similarity with the Ontong–Java plateau collision.)

Researchers create a tectonic model for each hypothesis, and conclude—based on the fact that their first reconstruction produces a slab break—that a slowdown in subduction is incompatible with tomography. However, once tomographically filtered, the slab break in the synthetic mantle structure might well vanish, indicating that the two sets of observations (geology and tomography) are compatible with each other.

An important caveat on the use of seismic tomography in this thesis is that the two models I use (*S40RTS* and *LLNL-G3D-JPS*) are not equivalent in their resolving power. *S40RTS* is limited to spherical harmonic degree 40 (∼1000–1100 km wavelength), so it is effectively a low-pass view of mantle structure and tends to significantly smear, weaken, or even eliminate slab-scale features that are prominent in simulated mantle structure. This limitation is evident in some of the regional comparisons (e.g., Aleutian, Sunda), where the match to *S40RTS* is noticeably poorer, likely reflecting resolution loss. By contrast, *LLNL-G3D-JPS* has substantially higher resolution (particularly in the upper mantle and transition zone: ∼400 km), making it better suited for evaluating slab morphology in more complex, small-to-medium scale settings (microplate interactions, slab tears, etc.). In this sense, *S40RTS* should be treated primarily as a conservative, large-scale reference (useful for first-order geometry and deep continuity), whereas *LLNL-G3D-JPS* is the more informative benchmark for diagnostic evaluation of regional slab morphology across the systems targeted here.

Relatedly, the resolution-operator workflow is central to why these two models were chosen: availability of resolution operators allows filtering (degradation) of modelled structure to what each tomography model can actually resolve, enabling fairer visual comparison and avoiding spuriously harsh misfits driven by unresolved fine structure. This is a major strength of the approach. The

main drawback is practical: resolution operators are publicly available only for a small subset of global tomography models, which constrains broader MCM–tomography comparisons. A clear recommendation from this thesis is therefore that resolution operators become a standard companion product for future seismic tomography models. This would immediately allow the comparison framework developed here to be applied across a wider ensemble of modern tomographic models, improving the robustness of evaluating MCMs with tomography.

The introduction of the Wasserstein metric for measuring model–tomography misfits is particularly useful in this context. Predictions of mantle structure made by MCMs driven by different candidate reconstructions are often more similar to one another than they are to tomography. If they also have little to no pointwise overlap, traditional measures of misfit saturate, while the Wasserstein metric remains able to distinguish between them.

2 Geodynamic models and kinematically-consistent plate reconstructions

Mantle circulation models in which slab geometry arises dynamically (e.g., Arnould et al., 2020; Peng et al., 2021a, 2021b; Davies et al., 2022; Li et al., 2023; New et al., 2025a) instead of being prescribed at the surface (e.g., Schuberth et al., 2009; Steinberger et al., 2012; Bower et al., 2015; Zahirovic et al., 2016; Hu et al., 2018b; Mao & Zhong, 2018) offer a powerful approach for modelling mantle dynamics in deep time (i.e., where there is no tomography and limited geology from which to infer slab dip angles).

However, this approach is not without challenges. Chapter 3 demonstrates how this methodology can have difficulty achieving sensible slab geometries under certain subduction regimes. Because the model reads polarity from trench migration rather than from geological constraints, episodes of rapid trench advance in reconstructions may lead to physically implausible slab orientations—particularly in continental subduction settings, where the absence of buoyant continental lithosphere allows incorrect dip polarity to develop. A second limitation concerns the lower mantle, where the prescribed viscosity profile of the models used in Chapters 3 and 4 (described in Appendix C) increases too steeply with depth. As a consequence, slab-like anomalies sink unrealistically slowly once they enter the middle of the lower mantle, and material subducted in the more distant past accumulates at depths shallower than expected from tomographic and plate-reconstruction constraints. These mismatches highlight structural limitations within the modelling framework rather than errors in the reconstructions themselves. Importantly, the conclusions of Chapters 3 and 4 are robust to the latter limitation: both chapters concern slabs whose subduction initiated within approximately the last 100 Ma, and the analysis is confined to slab behaviour in the upper mantle and transition zone, which is governed by the upper mantle and transition zone viscosity structure rather than the deeper profile.

Conversely, in systems where subduction history is not complicated by trench advance, mismatches between model predictions and expectations may be plausible indicators of uncertainties or errors in the underlying tectonic reconstruction. For example, a subduction system not generating sufficient slab volume may mean that slab rollback in the reconstruction is implausibly fast, or unexpected slab material may indicate an error in the plate rotations which has led to convergence across supposedly diverging margin. In geodynamic models with a prescriptivist approach to slab geometry such inconsistencies may be masked, but in models where slab geometry arises dynamically they serve as a heads-up that something is awry in the reconstruction.

Both limitations are addressed in the newest generation of G-ADOPT models, described in Section 3. The lower mantle viscosity profile has been revised, and continental lithosphere is now implemented via a distinct rheology in regions of known continental lithosphere, reconstructed

through time with pyGPlates. The latter draws inspiration from the so-called *tomotectonic* approach of incorporating more geologic data into geodynamic models (e.g., Li et al., 2023), and was motivated in part by the spurious trench advance described above: allowing the correct dip polarity to arise naturally avoids artificially prescribing it, without the order-of-magnitude-higher computational expense of billions of geochemical tracers (Peng et al., 2021b). A practical constraint on incorporating these improvements throughout the thesis, however, was the computational expense of mantle circulation models: each model generation requires millions of SU on Gadi, limiting both the number of generations that could be run within the project and the scope for re-running earlier analyses as the models evolved. Chapter 2 therefore makes use of this newest generation, while Chapters 3 and 4 use the earlier generation. Extending those analyses with the newest models—in particular, to older subduction systems whose slabs now reside in the lower mantle, and to assess whether the improved continental behaviour also refines slab morphologies in the settings examined—remains a natural direction for future work.

Overall, reconstruction-driven convection successfully reproduces slab morphology in settings dominated by rollback and simple trench geometry, but struggles when trench advance or upper-plate complexity dominates. Mismatches therefore serve not as failures but as informative diagnostics: they reveal deficiencies in the modelling framework, highlight where reconstructions require reassessment, and point toward physical processes that must be incorporated in future models—a path on which the implementation of continental lithosphere marks a first step. Slab morphology thus emerges as a powerful integrative constraint linking plate tectonics, mantle dynamics, and deep Earth structure.

3 Future outlook

Global plate reorganisation events (GPREs) can be viewed as scaled-up expressions of the same coupled plate–mantle interactions observed in regional reorganisations, such as the collision of the Ontong–Java plateau against the Melanesian arc, where there are relatively abrupt changes in plate-boundary configuration, subduction dynamics, and the balance of plate-driving forces. One such event is the ∼100 Ma GPRE that precipitated in the Pacific Ocean (Matthews et al., 2012). A number of drivers for this event have been proposed, including cessation of Pacific subduction beneath Gondwana due to ridge–trench interaction (Bradshaw, 1989), cessation (Olierook et al., 2020) or initiation (Gürer et al., 2022) of Tethyan subduction, plate capture (Luyendyk, 1995), and plume push from the Bouvet plume (Matthews et al., 2012). The Cretaceous collision of the Hikurangi plateau (HP) with the southern Gondwanan margin is thought to have to terminated long-lived subduction. However, most global plate reconstructions model the HP–Gondwana collision between 85 and 80 Ma, leading to it being overlooked as a potential cause for the ∼105 Ma GPRE.

Another is the ∼50 Ma GPRE—best visualised by the bend in the Hawai'i–Emperor seamount chain. The change in Pacific plate motion associated with the bend was at least partly driven by changes in mantle flow under the Pacific (Molnar & Atwater, 1973; Tarduno et al., 2003; Tarduno et al., 2009). Studies using coupled plate tectonic–mantle circulation models have shown that subduction cessation and the consequent reduction in slab pull also played an important role (e.g., Seton et al., 2015; Hu et al., 2022), which confirm the results from other studies that a change in plume motion alone cannot account for the seamount chain bend (Torsvik et al., 2017). Their results support changes in the subduction geometry of the circum-Pacific plate network having a significant impact on the coupled plate–mantle system, initiating the ∼50 Ma GPRE.

The workflows I developed in this thesis and demonstrate with the case study in Chapter 4 provide a powerful toolbox for future investigations to test the compatibility of these hypotheses

with present-day seismic observations of mantle structure, especially when considering end-member variations where differences between competing reconstructions is likely to lead to larger differences in predicted mantle structure.

Adjoint experiments may be also be a powerful tool for testing GPREs because they treat reorganisation as an inverse problem. Instead of prescribing disputed events (e.g., collision timing, subduction initiation/cessation, plume forcing) and predicting outcomes at present day, they assimilate the observed plate-motion change—along with other known constraints—to infer which time–space changes in slab pull, coupling, viscosity structure, and plume forcing are most responsible. The temperature–seismic-velocity conversion and tomographic filtering workflows developed in this thesis will be crucial for using adjoint models to investigate GPREs (and other events). They allow gradient descent to move toward the imaged mantle in observation space, rather than trying to force the initial conditions to reproduce tomographic spatial heterogeneity. At the same time, the key to a good adjoint model is a good forward model, which means the strengths and weaknesses of the G-ADOPT models discussed in Chapter 3 will also be important moving forward.

6 | Conclusions

In this thesis, I demonstrate many of the challenges associated with using mantle circulation models to differentiate between candidate tectonic reconstructions by comparison with seismic tomography—namely: (i) nonlinearity in the temperature–seismic velocity relationship, (ii) heterogeneity in the spatial resolution of seismic tomography models, and (iii) inability of traditional, pointwise misfit metrics to differentiate between non-overlapping anomalies. I develop a new workflow to account for the anelastic seismic response of mantle minerals, which introduces significant nonlinearity in the temperature–velocity relationship, and to apply the resolution operators of the *S40RTS* and *LLNL-G3D-JPS* tomography models, which allow synthetic predictions of mantle structure to be viewed through the same spatial resolution lens as seismic tomography. Where possible, these workflows have been made freely available for use in future experiments. I demonstrate that applying these post-processing workflows can change the categorical interpretation of upper-mantle–transition-zone slab morphology, for example the introduction of continuity to discontinuous slabs, and vice versa. I also investigate the performance of G-ADOPT mantle circulation models in a variety of well-studied and well-constrained subduction systems. G-ADOPT simulations do not predict the expected slab morphology in subduction regimes dominated by mantle-frame trench advance (e.g., Aegean, Caribbean) or extremely fast rollback (e.g., Izu–Bonin). However, they perform well in oceanic/arc settings with low to moderate rollback speeds, with predicted upper-mantle and transition-zone structure matching that imaged by seismic tomography in the Aleutian, Mariana, Sunda, and Tonga–Kermadec–Hikurangi subduction systems.

I apply these findings to a case study: the collision of the Ontong–Java plateau (OJP) with the Melanesian subduction system (MSS). Using the global tectonic reconstruction of Zahirovic et al. (2022) which already models the OJP–MSS collision at ∼25 Ma as a base (*Z22*), I derive an alternate reconstruction for a younger collision timing at ∼12 Ma (*Z22M04*). My results strongly favour the *Z22* scenario, as it more accurately reproduces slab material in the upper mantle transition zone under the OJP–MSS region, with a significant reduction in misfit as compared to the *Z22M04* scenario. These findings support the idea the collision played a key role in driving the regional reorganisation of plate motions ∼25 million years ago in the southwest Pacific. However, its role in a potential *global* plate reorganisation event remains uncertain—such events are typically associated with much larger changes to the plate circuit than were needed to reproduce observed present-day mantle structure. On the other hand, this experiment can be seen as a test-case, developing necessary tools to investigating the key factors in well-established global reorganisations of the plate circuit (i.e., the ∼50 and ∼105 Ma reorganisation events).

A | Supplement to Chapter 2

1 Mantle circulation model reference state

Table A1

Reference-state thermodynamic profiles of the mantle circulation model: depth z, temperature $\bar{T}$, density $\bar{\rho}$, gravitational acceleration $\bar{g}$, thermal expansivity $\bar{\alpha}$, isothermal compressibility $\bar{\beta}$, Grüneisen parameter $\bar{\gamma}$, molar isobaric heat capacity $\bar{C}_p$, molar isochoric heat capacity $\bar{C}_v$, and molar volume $\bar{V}$. Specific heat capacities and volume follow from the molar values via the mean molar mass $M = 0.133\,54\,\mathrm{kg\,mol^{-1}}$.

z [km]	$\bar{T}$ [K]	$\bar{\rho}$ [kg m^{-3}]	$\bar{g}$ [m s^{-2}]	$\bar{\alpha}$ [K^{-1}] [$\times 10^{-5}$]	$\bar{\beta}$ [Pa^{-1}] [$\times 10^{-12}$]	$\bar{\gamma}$	$\bar{C}_p$ [J mol^{-1} K^{-1}]	$\bar{C}_v$ [J mol^{-1} K^{-1}]	$\bar{V}$ [m^3 mol^{-1}] [$\times 10^{-5}$]
0	1600	3200	9.83	4.177	11.278	1.010	166.9	156.2	4.171
11	1606	3217	9.83	4.093	11.052	1.005	166.7	156.2	4.157
23	1612	3228	9.84	4.011	10.830	0.999	166.4	156.2	4.142
34	1617	3238	9.84	3.930	10.611	0.994	166.2	156.2	4.127
45	1622	3249	9.85	3.851	10.397	0.989	166.0	156.2	4.112
56	1627	3260	9.85	3.774	10.186	0.985	165.8	156.2	4.097
68	1632	3272	9.85	3.698	9.979	0.980	165.6	156.2	4.083
79	1638	3283	9.86	3.625	9.775	0.976	165.4	156.2	4.068
90	1642	3295	9.86	3.553	9.575	0.972	165.2	156.2	4.053
102	1648	3307	9.87	3.483	9.380	0.968	165.0	156.2	4.038
113	1652	3319	9.87	3.415	9.187	0.965	164.8	156.2	4.023
124	1657	3331	9.88	3.348	8.999	0.962	164.6	156.2	4.007
135	1662	3344	9.88	3.284	8.814	0.959	164.5	156.2	3.992
147	1667	3356	9.88	3.221	8.633	0.956	164.3	156.2	3.977
158	1672	3369	9.89	3.160	8.456	0.953	164.2	156.2	3.962
169	1676	3382	9.89	3.100	8.283	0.951	164.0	156.2	3.947
181	1681	3395	9.90	3.043	8.113	0.949	163.8	156.2	3.931
192	1686	3408	9.90	2.987	7.947	0.947	163.7	156.2	3.916
203	1690	3422	9.91	2.933	7.785	0.946	163.6	156.2	3.900
214	1695	3435	9.91	2.881	7.626	0.944	163.4	156.2	3.885
226	1699	3449	9.91	2.830	7.472	0.943	163.3	156.2	3.870
237	1704	3463	9.92	2.782	7.321	0.942	163.2	156.2	3.854
248	1708	3477	9.92	2.735	7.173	0.942	163.1	156.2	3.838
260	1712	3492	9.92	2.690	7.030	0.941	163.0	156.2	3.823
271	1716	3506	9.93	2.647	6.890	0.941	162.9	156.2	3.807
288	1723	3527	9.93	2.591	6.709	0.942	162.8	156.2	3.785
299	1727	3541	9.94	2.559	6.604	0.943	162.7	156.2	3.771
310	1731	3555	9.94	2.531	6.501	0.945	162.7	156.2	3.757
322	1735	3570	9.95	2.507	6.399	0.948	162.7	156.2	3.741
333	1739	3586	9.95	2.482	6.300	0.950	162.6	156.2	3.726
344	1743	3601	9.95	2.457	6.203	0.951	162.6	156.2	3.710

Table A1 (continued)

z [km]	$\bar{T}$ [K]	$\bar{\rho}$ [kg m^{-3}]	$\bar{g}$ [m s^{-2}]	$\bar{\alpha}$ [K^{-1}] [$\times 10^{-5}$]	$\bar{\beta}$ [Pa^{-1}] [$\times 10^{-12}$]	$\bar{\gamma}$	$\bar{C}_p$ [J mol^{-1} K^{-1}]	$\bar{C}_v$ [J mol^{-1} K^{-1}]	$\bar{V}$ [m^3 mol^{-1}] [$\times 10^{-5}$]
356	1747	3617	9.96	2.431	6.104	0.953	162.5	156.2	3.694
367	1750	3633	9.96	2.406	6.001	0.954	162.4	156.2	3.679
378	1754	3649	9.96	2.380	5.899	0.956	162.4	156.2	3.663
389	1758	3663	9.97	2.348	5.799	0.954	162.3	156.2	3.648
401	1762	3673	9.97	2.306	5.702	0.947	162.1	156.1	3.636
412	1765	3686	9.97	2.268	5.605	0.942	162.0	156.1	3.623
423	1769	3699	9.98	2.233	5.507	0.938	161.9	156.1	3.609
435	1772	3714	9.98	2.202	5.410	0.936	161.8	156.1	3.595
446	1776	3729	9.98	2.174	5.313	0.936	161.7	156.1	3.579
457	1780	3746	9.98	2.148	5.217	0.936	161.7	156.1	3.563
468	1783	3764	9.99	2.126	5.122	0.939	161.6	156.1	3.546
480	1787	3783	9.99	2.109	5.029	0.943	161.6	156.1	3.528
491	1790	3803	9.99	2.095	4.937	0.950	161.7	156.1	3.510
502	1794	3824	9.99	2.084	4.846	0.958	161.7	156.1	3.490
514	1797	3847	10.00	2.077	4.758	0.967	161.8	156.1	3.470
525	1801	3870	10.00	2.073	4.671	0.979	161.9	156.1	3.450
536	1804	3894	10.00	2.072	4.585	0.991	162.0	156.1	3.430
548	1808	3918	10.00	2.073	4.503	1.005	162.1	156.1	3.409
559	1811	3943	10.00	2.076	4.422	1.019	162.2	156.1	3.388
570	1815	3968	10.01	2.080	4.345	1.035	162.4	156.1	3.367
581	1818	3994	10.01	2.087	4.271	1.051	162.5	156.1	3.346
593	1822	4019	10.01	2.095	4.200	1.067	162.7	156.1	3.326
604	1826	4045	10.01	2.104	4.132	1.084	162.8	156.1	3.305
615	1829	4070	10.01	2.114	4.069	1.101	163.0	156.1	3.285
627	1833	4095	10.01	2.129	4.009	1.120	163.2	156.1	3.266
638	1837	4119	10.01	2.144	3.954	1.138	163.4	156.1	3.247
649	1841	4143	10.01	2.163	3.903	1.157	163.6	156.1	3.228
660	1844	4166	10.01	2.181	3.858	1.176	163.8	156.1	3.211
672	1848	4189	10.01	2.200	3.817	1.195	164.0	156.1	3.194
683	1852	4210	10.01	2.219	3.780	1.213	164.2	156.1	3.178
694	1856	4234	10.01	2.239	3.735	1.233	164.4	156.1	3.161
706	1860	4258	10.01	2.261	3.685	1.254	164.7	156.1	3.142
717	1864	4282	10.01	2.284	3.636	1.275	164.9	156.1	3.124
728	1868	4305	10.01	2.306	3.590	1.296	165.1	156.1	3.107
739	1872	4328	10.01	2.327	3.545	1.316	165.3	156.1	3.090
751	1876	4350	10.01	2.349	3.502	1.335	165.5	156.1	3.073
762	1880	4371	10.01	2.370	3.462	1.355	165.7	156.1	3.058
773	1884	4391	10.00	2.390	3.425	1.373	165.9	156.1	3.043
785	1889	4410	10.00	2.409	3.390	1.390	166.1	156.1	3.029
796	1893	4428	10.00	2.427	3.359	1.407	166.3	156.1	3.016
807	1897	4445	10.00	2.441	3.327	1.421	166.5	156.1	3.004
818	1901	4462	10.00	2.451	3.294	1.434	166.6	156.1	2.992
830	1905	4477	10.00	2.458	3.263	1.445	166.7	156.1	2.981
841	1910	4491	9.99	2.462	3.234	1.454	166.8	156.1	2.971
852	1914	4504	9.99	2.462	3.207	1.461	166.8	156.1	2.962
864	1918	4516	9.99	2.459	3.182	1.466	166.8	156.1	2.954
875	1922	4526	9.99	2.453	3.160	1.469	166.8	156.1	2.947
886	1926	4534	9.99	2.443	3.140	1.470	166.8	156.1	2.942
897	1931	4540	9.99	2.430	3.122	1.468	166.8	156.1	2.938
909	1935	4546	9.98	2.413	3.106	1.465	166.7	156.1	2.935
920	1939	4549	9.98	2.392	3.091	1.459	166.6	156.1	2.933
931	1943	4552	9.98	2.368	3.078	1.450	166.4	156.1	2.932
943	1947	4552	9.98	2.339	3.066	1.440	166.3	156.1	2.932
954	1951	4554	9.98	2.314	3.054	1.431	166.2	156.1	2.932

Table A1 (continued)

z [km]	$\bar{T}$ [K]	$\bar{\rho}$ [kg m^{-3}]	$\bar{g}$ [m s^{-2}]	$\bar{\alpha}$ [K^{-1}] [$\times 10^{-5}$]	$\bar{\beta}$ [Pa^{-1}] [$\times 10^{-12}$]	$\bar{\gamma}$	$\bar{C}_p$ [J mol^{-1} K^{-1}]	$\bar{C}_v$ [J mol^{-1} K^{-1}]	$\bar{V}$ [m^3 mol^{-1}] [$\times 10^{-5}$]
965	1955	4560	9.98	2.300	3.039	1.428	166.1	156.1	2.928
976	1960	4565	9.97	2.286	3.024	1.425	166.1	156.1	2.925
988	1964	4571	9.97	2.272	3.010	1.421	166.0	156.1	2.921
999	1968	4576	9.97	2.259	2.995	1.418	166.0	156.1	2.918
1010	1972	4582	9.97	2.245	2.980	1.415	165.9	156.1	2.914
1022	1976	4588	9.97	2.233	2.965	1.413	165.9	156.1	2.910
1033	1980	4595	9.97	2.221	2.949	1.411	165.8	156.1	2.906
1044	1984	4602	9.96	2.210	2.933	1.410	165.8	156.1	2.902
1056	1988	4608	9.96	2.199	2.917	1.408	165.7	156.1	2.898
1067	1992	4615	9.96	2.188	2.901	1.406	165.7	156.1	2.894
1078	1996	4621	9.96	2.177	2.885	1.405	165.7	156.1	2.890
1089	2000	4628	9.96	2.166	2.870	1.403	165.6	156.1	2.885
1101	2003	4635	9.96	2.155	2.854	1.402	165.6	156.1	2.881
1112	2007	4641	9.96	2.144	2.839	1.400	165.5	156.1	2.877
1123	2011	4648	9.96	2.134	2.824	1.399	165.5	156.1	2.873
1135	2015	4654	9.95	2.124	2.810	1.397	165.5	156.1	2.869
1146	2019	4660	9.95	2.114	2.795	1.396	165.4	156.1	2.865
1157	2023	4667	9.95	2.104	2.781	1.394	165.4	156.1	2.861
1168	2027	4673	9.95	2.093	2.766	1.393	165.4	156.1	2.857
1180	2030	4680	9.95	2.083	2.752	1.391	165.3	156.1	2.854
1191	2034	4686	9.95	2.073	2.738	1.390	165.3	156.1	2.850
1202	2038	4693	9.95	2.064	2.724	1.389	165.2	156.1	2.846
1214	2042	4699	9.95	2.054	2.710	1.387	165.2	156.1	2.842
1225	2046	4705	9.95	2.044	2.696	1.386	165.2	156.1	2.838
1236	2050	4712	9.95	2.035	2.683	1.384	165.1	156.1	2.834
1247	2053	4718	9.94	2.025	2.669	1.383	165.1	156.1	2.830
1259	2057	4724	9.94	2.016	2.656	1.381	165.1	156.1	2.827
1270	2061	4731	9.94	2.007	2.643	1.380	165.0	156.1	2.823
1281	2065	4737	9.94	1.998	2.630	1.379	165.0	156.1	2.819
1293	2068	4743	9.94	1.989	2.618	1.377	165.0	156.1	2.815
1304	2072	4749	9.94	1.980	2.605	1.376	164.9	156.1	2.812
1315	2076	4756	9.94	1.971	2.592	1.375	164.9	156.1	2.808
1326	2080	4762	9.94	1.962	2.580	1.373	164.9	156.1	2.804
1338	2083	4768	9.94	1.954	2.567	1.372	164.8	156.1	2.801
1349	2087	4774	9.94	1.945	2.555	1.371	164.8	156.1	2.797
1360	2091	4781	9.94	1.936	2.542	1.369	164.8	156.1	2.793
1372	2094	4787	9.94	1.928	2.530	1.368	164.7	156.1	2.790
1383	2098	4793	9.94	1.919	2.518	1.367	164.7	156.1	2.786
1394	2102	4799	9.94	1.911	2.506	1.365	164.7	156.1	2.783
1406	2105	4805	9.94	1.903	2.495	1.364	164.6	156.1	2.779
1417	2109	4811	9.94	1.895	2.484	1.363	164.6	156.1	2.776
1428	2113	4817	9.94	1.887	2.472	1.362	164.6	156.1	2.772
1439	2116	4823	9.93	1.879	2.461	1.361	164.6	156.1	2.769
1451	2120	4829	9.93	1.871	2.450	1.359	164.6	156.1	2.765
1462	2124	4835	9.93	1.864	2.439	1.358	164.5	156.1	2.762
1473	2127	4841	9.93	1.856	2.428	1.357	164.5	156.1	2.758
1484	2131	4847	9.93	1.848	2.417	1.356	164.5	156.1	2.755
1496	2134	4853	9.93	1.841	2.406	1.355	164.5	156.1	2.752
1507	2138	4859	9.93	1.833	2.395	1.353	164.4	156.1	2.748
1518	2141	4865	9.93	1.826	2.384	1.352	164.4	156.1	2.745
1530	2145	4871	9.93	1.818	2.374	1.351	164.4	156.1	2.741
1541	2148	4878	9.93	1.811	2.363	1.350	164.3	156.1	2.738
1552	2152	4884	9.93	1.803	2.352	1.349	164.3	156.1	2.734
1564	2156	4890	9.94	1.796	2.342	1.347	164.3	156.1	2.731

Table A1 (continued)

z [km]	$\bar{T}$ [K]	$\bar{\rho}$ [kg m^{-3}]	$\bar{g}$ [m s^{-2}]	$\bar{\alpha}$ [K^{-1}] [$\times 10^{-5}$]	$\bar{\beta}$ [Pa^{-1}] [$\times 10^{-12}$]	$\bar{\gamma}$	$\bar{C}_p$ [J mol^{-1} K^{-1}]	$\bar{C}_v$ [J mol^{-1} K^{-1}]	$\bar{V}$ [m^3 mol^{-1}] [$\times 10^{-5}$]
1575	2159	4896	9.94	1.788	2.331	1.346	164.2	156.1	2.728
1586	2163	4902	9.94	1.781	2.321	1.345	164.2	156.1	2.724
1597	2166	4907	9.94	1.774	2.311	1.344	164.2	156.1	2.721
1609	2170	4913	9.94	1.767	2.301	1.343	164.2	156.1	2.718
1620	2173	4919	9.94	1.760	2.291	1.342	164.2	156.1	2.715
1631	2177	4925	9.94	1.754	2.281	1.340	164.1	156.1	2.711
1643	2180	4931	9.94	1.747	2.272	1.339	164.1	156.1	2.708
1654	2184	4937	9.94	1.740	2.262	1.338	164.1	156.1	2.705
1665	2187	4943	9.94	1.733	2.252	1.337	164.1	156.1	2.702
1676	2190	4949	9.94	1.726	2.243	1.336	164.0	156.1	2.698
1688	2194	4955	9.94	1.720	2.233	1.335	164.0	156.1	2.695
1699	2197	4961	9.94	1.713	2.223	1.334	164.0	156.1	2.692
1710	2201	4967	9.94	1.706	2.214	1.333	163.9	156.1	2.689
1722	2204	4973	9.95	1.699	2.204	1.331	163.9	156.1	2.685
1733	2208	4978	9.95	1.693	2.195	1.330	163.9	156.1	2.682
1744	2211	4984	9.95	1.687	2.186	1.329	163.9	156.1	2.679
1755	2215	4990	9.95	1.680	2.177	1.328	163.8	156.1	2.676
1767	2218	4996	9.95	1.674	2.168	1.327	163.8	156.1	2.673
1778	2221	5002	9.95	1.668	2.159	1.326	163.8	156.1	2.670
1789	2225	5007	9.95	1.662	2.150	1.325	163.8	156.1	2.667
1801	2228	5013	9.96	1.656	2.141	1.324	163.8	156.1	2.664
1812	2232	5019	9.96	1.650	2.133	1.323	163.7	156.1	2.661
1823	2235	5024	9.96	1.643	2.124	1.322	163.7	156.1	2.658
1834	2238	5030	9.96	1.637	2.115	1.321	163.7	156.1	2.655
1846	2242	5036	9.96	1.631	2.107	1.320	163.7	156.1	2.652
1857	2245	5042	9.96	1.625	2.098	1.319	163.6	156.1	2.649
1868	2248	5048	9.97	1.619	2.090	1.318	163.6	156.1	2.646
1880	2252	5053	9.97	1.614	2.081	1.317	163.6	156.1	2.643
1891	2255	5059	9.97	1.608	2.073	1.316	163.6	156.1	2.640
1902	2258	5065	9.97	1.602	2.065	1.315	163.6	156.1	2.637
1914	2262	5071	9.98	1.596	2.057	1.314	163.5	156.1	2.634
1925	2265	5076	9.98	1.591	2.049	1.313	163.5	156.1	2.631
1936	2268	5082	9.98	1.585	2.041	1.312	163.5	156.1	2.628
1947	2272	5088	9.98	1.579	2.033	1.311	163.5	156.1	2.625
1959	2275	5093	9.99	1.574	2.025	1.310	163.4	156.1	2.622
1970	2278	5099	9.99	1.568	2.017	1.309	163.4	156.1	2.619
1981	2282	5104	9.99	1.563	2.009	1.308	163.4	156.1	2.616
1992	2285	5110	10.00	1.557	2.001	1.307	163.4	156.1	2.613
2004	2288	5116	10.00	1.552	1.993	1.306	163.4	156.1	2.610
2015	2292	5121	10.00	1.547	1.986	1.305	163.3	156.1	2.607
2026	2295	5127	10.01	1.541	1.978	1.304	163.3	156.1	2.605
2038	2298	5133	10.01	1.536	1.971	1.303	163.3	156.1	2.602
2049	2302	5138	10.01	1.531	1.963	1.302	163.3	156.1	2.599
2060	2305	5144	10.02	1.525	1.955	1.302	163.3	156.1	2.596
2072	2308	5150	10.02	1.520	1.948	1.301	163.2	156.1	2.593
2083	2311	5155	10.02	1.515	1.940	1.300	163.2	156.1	2.590
2094	2315	5161	10.03	1.510	1.933	1.299	163.2	156.1	2.587
2105	2318	5166	10.03	1.505	1.926	1.298	163.2	156.1	2.585
2117	2321	5172	10.04	1.499	1.919	1.297	163.2	156.1	2.582
2128	2324	5178	10.04	1.495	1.911	1.296	163.1	156.1	2.579
2139	2328	5183	10.04	1.490	1.904	1.295	163.1	156.1	2.576
2151	2331	5189	10.05	1.485	1.897	1.294	163.1	156.1	2.574
2162	2334	5194	10.05	1.480	1.890	1.293	163.1	156.1	2.571
2173	2337	5200	10.06	1.475	1.883	1.292	163.1	156.1	2.568

Table A1 (continued)

z [km]	$\bar{T}$ [K]	$\bar{\rho}$ [kg m^{-3}]	$\bar{g}$ [m s^{-2}]	$\bar{\alpha}$ [K^{-1}] [$\times 10^{-5}$]	$\bar{\beta}$ [Pa^{-1}] [$\times 10^{-12}$]	$\bar{\gamma}$	$\bar{C}_p$ [J mol^{-1} K^{-1}]	$\bar{C}_v$ [J mol^{-1} K^{-1}]	$\bar{V}$ [m^3 mol^{-1}] [$\times 10^{-5}$]
2184	2341	5205	10.06	1.470	1.876	1.292	163.1	156.1	2.565
2196	2344	5211	10.07	1.465	1.869	1.291	163.0	156.1	2.563
2207	2347	5216	10.07	1.460	1.863	1.290	163.0	156.1	2.560
2218	2350	5222	10.08	1.456	1.856	1.289	163.0	156.1	2.557
2230	2353	5227	10.08	1.451	1.849	1.288	163.0	156.1	2.555
2241	2357	5233	10.09	1.446	1.842	1.287	162.9	156.1	2.552
2252	2360	5239	10.09	1.441	1.835	1.286	162.9	156.1	2.549
2264	2363	5244	10.10	1.437	1.829	1.285	162.9	156.1	2.546
2275	2366	5250	10.11	1.432	1.822	1.284	162.9	156.1	2.544
2286	2369	5255	10.11	1.427	1.816	1.284	162.9	156.1	2.541
2297	2373	5259	10.12	1.423	1.809	1.283	162.9	156.1	2.539
2309	2376	5264	10.12	1.418	1.802	1.282	162.9	156.1	2.537
2320	2379	5268	10.13	1.414	1.796	1.282	162.8	156.1	2.535
2331	2382	5273	10.14	1.409	1.790	1.281	162.8	156.1	2.532
2342	2385	5278	10.14	1.405	1.783	1.280	162.8	156.1	2.530
2354	2388	5283	10.15	1.400	1.777	1.280	162.8	156.1	2.528
2365	2392	5288	10.16	1.396	1.770	1.279	162.8	156.1	2.525
2376	2395	5293	10.16	1.391	1.764	1.278	162.8	156.1	2.523
2388	2398	5298	10.17	1.387	1.758	1.277	162.8	156.1	2.520
2399	2401	5304	10.18	1.383	1.752	1.276	162.8	156.1	2.517
2410	2404	5310	10.19	1.379	1.746	1.276	162.7	156.1	2.514
2422	2407	5317	10.19	1.374	1.740	1.274	162.7	156.1	2.511
2433	2410	5324	10.20	1.370	1.734	1.273	162.7	156.1	2.508
2444	2414	5331	10.21	1.366	1.728	1.272	162.7	156.1	2.505
2455	2417	5338	10.22	1.362	1.722	1.271	162.7	156.1	2.501
2467	2420	5346	10.23	1.358	1.716	1.270	162.6	156.1	2.498
2478	2423	5354	10.23	1.354	1.710	1.268	162.6	156.1	2.494
2489	2426	5363	10.24	1.350	1.705	1.267	162.6	156.0	2.490
2500	2429	5371	10.25	1.346	1.699	1.266	162.6	156.0	2.486
2512	2432	5380	10.26	1.342	1.693	1.264	162.5	156.0	2.482
2523	2435	5389	10.27	1.338	1.688	1.262	162.5	156.0	2.478
2534	2438	5398	10.28	1.335	1.682	1.261	162.5	156.0	2.474
2546	2442	5408	10.29	1.331	1.677	1.259	162.5	156.0	2.470
2557	2445	5417	10.30	1.327	1.672	1.258	162.4	156.0	2.466
2568	2448	5426	10.31	1.324	1.667	1.256	162.4	156.0	2.461
2580	2451	5436	10.32	1.320	1.661	1.254	162.4	156.0	2.457
2591	2454	5446	10.33	1.316	1.656	1.253	162.4	156.0	2.452
2602	2457	5455	10.34	1.313	1.651	1.251	162.3	156.0	2.448
2613	2460	5465	10.35	1.309	1.646	1.249	162.3	156.0	2.444
2619	2462	5469	10.36	1.307	1.643	1.248	162.3	156.0	2.442
2630	2465	5478	10.37	1.303	1.638	1.247	162.3	156.0	2.438
2642	2468	5486	10.38	1.300	1.633	1.245	162.2	156.0	2.434
2653	2471	5494	10.39	1.296	1.628	1.244	162.2	155.9	2.431
2664	2474	5502	10.40	1.292	1.623	1.242	162.2	155.9	2.427
2676	2477	5511	10.41	1.289	1.617	1.241	162.2	155.9	2.423
2687	2480	5519	10.43	1.285	1.612	1.239	162.2	155.9	2.420
2698	2483	5527	10.44	1.281	1.607	1.238	162.1	155.9	2.416
2709	2486	5536	10.45	1.278	1.603	1.236	162.1	155.9	2.413
2721	2489	5544	10.46	1.274	1.598	1.235	162.1	155.9	2.409
2732	2492	5552	10.48	1.270	1.593	1.233	162.1	155.9	2.405
2743	2495	5560	10.49	1.267	1.588	1.232	162.0	155.9	2.402
2754	2498	5568	10.50	1.263	1.583	1.230	162.0	155.9	2.398
2766	2501	5576	10.52	1.260	1.578	1.228	162.0	155.9	2.395
2777	2504	5585	10.53	1.256	1.573	1.227	162.0	155.9	2.391

Table A1 (continued)

z [km]	$\bar{T}$ [K]	$\bar{\rho}$ [kg m^{-3}]	$\bar{g}$ [m s^{-2}]	$\bar{\alpha}$ [K^{-1}] [$\times 10^{-5}$]	$\bar{\beta}$ [Pa^{-1}] [$\times 10^{-12}$]	$\bar{\gamma}$	$\bar{C}_p$ [J mol^{-1} K^{-1}]	$\bar{C}_v$ [J mol^{-1} K^{-1}]	$\bar{V}$ [m^3 mol^{-1}] [$\times 10^{-5}$]
2788	2507	5593	10.55	1.252	1.569	1.225	161.9	155.9	2.388
2800	2510	5601	10.56	1.249	1.564	1.224	161.9	155.9	2.384
2811	2513	5609	10.57	1.245	1.560	1.222	161.9	155.9	2.381
2822	2516	5617	10.59	1.242	1.555	1.220	161.9	155.9	2.377
2834	2520	5625	10.60	1.238	1.550	1.219	161.8	155.9	2.374
2845	2522	5633	10.62	1.235	1.546	1.217	161.8	155.9	2.370
2856	2526	5641	10.63	1.231	1.541	1.216	161.8	155.9	2.367
2867	2528	5649	10.65	1.228	1.537	1.214	161.8	155.9	2.364
2879	2532	5657	10.66	1.225	1.532	1.212	161.8	155.9	2.360
2890	2535	5665	10.68	1.221	1.528	1.211	161.7	155.9	2.357

2 Post-processing code details

This appendix documents the software underpinning the seismic velocity conversion and tomographic filtering workflows developed in this thesis (Chapter 2). Its purpose is twofold: to make the thesis self-contained by describing the structure, function, and provenance of each component, and to enable readers to reproduce the results or build upon the workflows without prior involvement in the work. Four repositories are described. The first (Section 2.1) is the end-to-end pipeline that I developed, maintain, and used to produce the results in this thesis; it orchestrates the three library packages described in Sections 2.2–2.4. As set out in the statement of contributions, I developed and validated the original workflows for tomographic filtering on which the srts and llnltofi packages are based; these were subsequently refactored by S.G. into the portable, tested, and documented packages described below. Because modern scientific software is developed collaboratively under version control, the definitive record of individual authorship is the commit history of each repository, which attributes every change to its author. The exact versions of all four codes used to produce the results in this thesis have been archived with persistent identifiers (Section 2.5).

2.1 The convection-to-seismic pipeline

Repository. https://github.com/tom-new/convection-to-seismic

Purpose. This repository, which I developed, contains the complete workflow for post-processing mantle convection simulation output into synthetic seismic observables that can be compared directly, and fairly, with global tomographic models. It converts the simulated temperature field to absolute seismic velocities (v_S, v_P) via a thermodynamic look-up table with gradient regularisation and anelastic corrections, applies the resolution operators of the *S40RTS* family (Ritsema et al., 2011) and of *LLNL-G3D-JPS* (Simmons et al., 2019), and resamples all outputs onto a regular geographic grid for analysis. The repository `README` doubles as a user guide, explaining the physical rationale for each step alongside practical instructions for running the pipeline. The version used in this thesis is the `mass-convert` branch, in which the workflow is orchestrated by a single driver script, `pipeline.sh`, that batch-processes archived simulation snapshots: for each snapshot it extracts the archive and runs the five processing stages in sequence, optionally restricted to a range of reconstruction ages.

Structure. The pipeline comprises five stages, summarised in Table A2. Each stage pairs a shell script with the Python script it executes; a shared helper, `_layer_mean.py`, computes relative velocity anomalies as deviations from the mean of each depth layer of the extruded mesh.

Table A2

Stages of the convection-to-seismic pipeline, orchestrated by ***`pipeline.sh`****.*

Stage	Files	Function
1	`01_convert.sh`, `convert_to_v.py`	Temperature → v_S, v_P conversion (G-DRIFT)
2	`02_srts_filter.sh`, `srts_filter.py`	*S12/S20/S40RTS* tomographic filtering (srts)
3	`03_llnl_filter.sh`, `llnl_filter.py`	*LLNL-G3D-JPS* tomographic filtering (llnltofi)
4	`04_interpolate.sh`	Resampling of all outputs to a regular grid (NetCDF; g-interp)
5	`05_rename.sh`, `rename.py`	Variable selection and renaming for analysis and cross-section plotting

Stage 1: velocity conversion. `convert_to_v.py` reads the parallel VTK (`.pvtu`) output written by G-ADOPT, dimensionalises the coordinates and the non-dimensional temperature field, and converts temperature to v_S and v_P at every mesh node using the *SLB* pyrolite thermodynamic look-up table (Stixrude & Lithgow-Bertelloni, 2024) via G-DRIFT. Two corrections, described in Chapter 2, Section 2.2 and implemented in G-DRIFT (Section 2.2), are applied during this stage: the gradient regularisation of the thermodynamic table, which removes phase-transition artefacts by linearising the conversion about the spherically averaged temperature profile extracted from the simulation itself, and the anelastic correction of Cammarano et al. (2003), which accounts for the velocity dispersion experienced by finite-frequency seismic waves. So that the effect of each modelling choice can be isolated downstream, the output retains three velocity variants—the raw table conversion, the regularised (elastic) conversion, and the regularised, anelastically corrected conversion—together with the relative anomaly ($d \ln v$) of each.

Stage 2: *S-RTS* filtering. `srts_filter.py` interpolates the unstructured mesh onto a regular 181×360 geographic grid at each depth layer by inverse-distance weighting, expands the velocity anomaly in spherical harmonics to degree $\ell_{\max} = 40$, projects the coefficients onto the 21-knot spline depth basis of the *S-RTS* models, applies the resolution operator of each of *S12RTS*, *S20RTS*, and *S40RTS* using srts, and synthesises the filtered fields back onto the simulation mesh. Alongside the filtered fields, the output retains the reparameterised but unfiltered field—v_S after the round trip through the spectral–spline basis—which is the appropriate unfiltered reference for filtered-versus-unfiltered comparisons.

Stage 3: *LLNL-G3D-JPS* filtering. `llnl_filter.py` projects v_S and v_P onto the irregular geographic grid of *LLNL-G3D-JPS*, forms slowness anomalies relative to a layer-mean one-dimensional reference, applies the explicit resolution matrix $\mathcal{R}$ via llnltofi, and back-projects the filtered velocities onto the simulation mesh. As in stage 2, the reparameterised unfiltered fields are retained alongside the filtered ones as the reference for comparison.

Stages 4–5: interpolation and renaming. The converted and filtered fields are resampled from the finite-element mesh onto a regular $360 \times 181 \times 129$ longitude–latitude–depth grid and written

as NetCDF files using g-interp (https://github.com/g-adopt/g-interp). The final stage subsets and renames the variables into a consistent analysis convention, reorders the dimensions, wraps and sorts the longitudes, and dimensionalises the radial coordinate, producing three NetCDF files per snapshot: the unfiltered conversion, the *S40RTS*-filtered model, and the *LLNL-G3D-JPS*-filtered model. These NetCDF files are the primary data products from which the figures and analyses of Chapter 2, Section 3 derive.

2.2 G-DRIFT: thermodynamic conversion, regularisation, and anelasticity

Repository. https://github.com/g-adopt/g-drift

Purpose. G-DRIFT (Geodynamics Data Reformatting and Integration Facilitation Toolkit) provides the mineral-physics machinery for converting geodynamic model output into seismic quantities. G-DRIFT is developed by S.G. within the G-ADOPT platform; I contributed to the validation and testing of the conversion routines, as well as the code to implement the anelastic corrections. The components of G-DRIFT used in this thesis are:

- `gdrift.mineralogy` — the `ThermodynamicModel` class wrapping the *SLB* look-up tables, and `regularise_thermodynamic_table`, which implements the gradient regularisation described in Chapter 2, Section 2.2. This function anchors the temperature-to-velocity conversion to the spherically averaged geotherm of the simulation, mapping temperature anomalies to velocity anomalies linearly about that reference and thereby eliminating the spurious velocity jumps that otherwise arise where the mean temperature crosses a phase boundary.
- `gdrift.anelasticity` — the `CammaranoAnelasticityModel` class and the `apply_anelastic_correction` function, which implement the anelastic velocity correction of Cammarano et al. (2003) using the Q_6 quality-factor profile, as applied in Chapter 2, Section 2.2.
- `gdrift.profile` — radial reference models (`PreliminaryRefEarthModel`) and spline-based radial profiles used to construct the geotherm for the regularisation.
- `gdrift.io` — automated download and caching of the required datasets, which are hosted remotely and fetched on first use.

A worked example of the anelastic correction is included in the repository under `examples/anelasticity_corrections/`, and the temperature-to-v_S conversion under `examples/temperature_to_vs/`; both are run as part of the package's automated test suite.

2.3 srts: the *S40RTS* resolution operator

Repository. https://github.com/g-adopt/srts

Purpose and provenance. srts applies the resolution operators of the *S12RTS*, *S20RTS*, and *S40RTS* tomographic models (Ritsema et al., 2011) to geodynamic model output, following the methodology of Ritsema et al. (2007). I developed and validated the original workflow for applying these operators, based on the Fortran codes distributed (on request to the authors) with the *S-RTS* models; S.G. subsequently refactored this work into the installable Python package described here, which is distributed on PyPI (`pip install srts`).

Structure.

- `srts/expansion.py` (`SphericalHarmonicExpansion`) — regularised least-squares expansion of gridded data into spherical harmonic coefficients, and the inverse synthesis.
- `srts/parameterization.py` and `srts/splines.py` (`DepthParameterization`) — projection of per-layer coefficients onto the 21-knot cubic spline depth basis of the *S-RTS* models, and evaluation of spline-basis models at arbitrary depths.
- `srts/tomographic_filter.py` and `srts/filtering.py` (*S12RTS*, *S20RTS*, *S40RTS*) — application of each model's resolution operator in the spectral–spline space.
- `srts/pipeline.py`, `srts/io.py`, `srts/model_data.py` — a convenience pipeline combining the above, file input/output, and automated retrieval of the resolution operator data files.

Validation. The package carries a comprehensive automated test suite, including `tests/test_fortran_validation.py`, which verifies the Python implementation against the originally distributed Fortran codes, ensuring that the refactored package reproduces the behaviour of the workflow developed for this thesis.

2.4 llnltofi: the *LLNL-G3D-JPS* resolution operator

Repository. https://github.com/g-adopt/llnltofi

Purpose and provenance. llnltofi applies the explicit resolution matrix $\mathcal{R}$ of the *LLNL-G3D-JPS* joint P- and S-wave tomographic model (Simmons et al., 2019) to a velocity model evaluated on the LLNL geographic grid, via a single sparse matrix–vector product. As with srts, I developed and validated the original workflow, modernising the LLNL_ToFi code of B. Schuberth published alongside Simmons et al. (2019); S.G. subsequently refactored it into the package described here.

Structure.

- `llnltofi/_resolution_matrix.py` and `llnltofi/_grid.py` — loading of the resolution matrix as a `scipy.sparse` CSR matrix and of the $\sim 10^6$-point LLNL grid geometry.
- `llnltofi/interpolation.py` (`project_onto_grid`, `project_from_grid`) — layer-aware inverse-distance-weighted projection of an arbitrary point cloud (such as a finite-element mesh) onto the LLNL grid and back.
- `llnltofi/convert.py` — one-off conversion of the original published text-file representation of $\mathcal{R}$ into the sparse binary format used by the package.

Validation. The test suite includes `tests/test_equivalence.py`, which cross-validates the bundled sparse matrix bit-for-bit against one assembled freshly from the original published text files. Notably, this validation work uncovered a previously unreported indexing bug in the original LLNL_ToFi implementation, in which matrix entries whose column index falls exactly on a layer boundary are silently read from the wrong depth layer, affecting approximately 0.1 % of output grid points. The refactored package avoids the issue by construction, delegating all index arithmetic to standard sparse linear algebra routines.

2.5 Availability and archived versions

All repositories are publicly available under open-source licences at the URLs given above. The exact versions used to produce the results in this thesis are pinned below: the three library packages by their PyPI release numbers, which are immutable and can be installed directly (e.g., `pip install srts==0.2.0`), and the remaining codes by git commit hash, which permanently identifies the exact state of the source:

- convection-to-seismic, branch `mass-convert`, commit `15fae75` (tagged `thesis`)
- gdrift v0.1.1 (PyPI)
- srts v0.2.0 (PyPI)
- llnltofi v0.2.0 (PyPI)
- ginterp, commit `b5043e4`

Together with the repository commit histories, which attribute each change to its author, these pinned versions provide a complete record of the software used in this thesis.

B | Supplement to Chapter 3

1 Additional figures

Figure B1

(a) The present-day tectonic setting of the Aegean anomaly. (b) G-ADOPT temperature perturbation from layer mean ΔT. (c), (d) G-ADOPT seismic velocity perturbation $d\ln v_{S,P}$ from layer mean, filtered by S40RTS and LLNL-G3D-JPS respectively. (e), (f) Seismic tomography in S40RTS and LLNL-G3D-JPS.

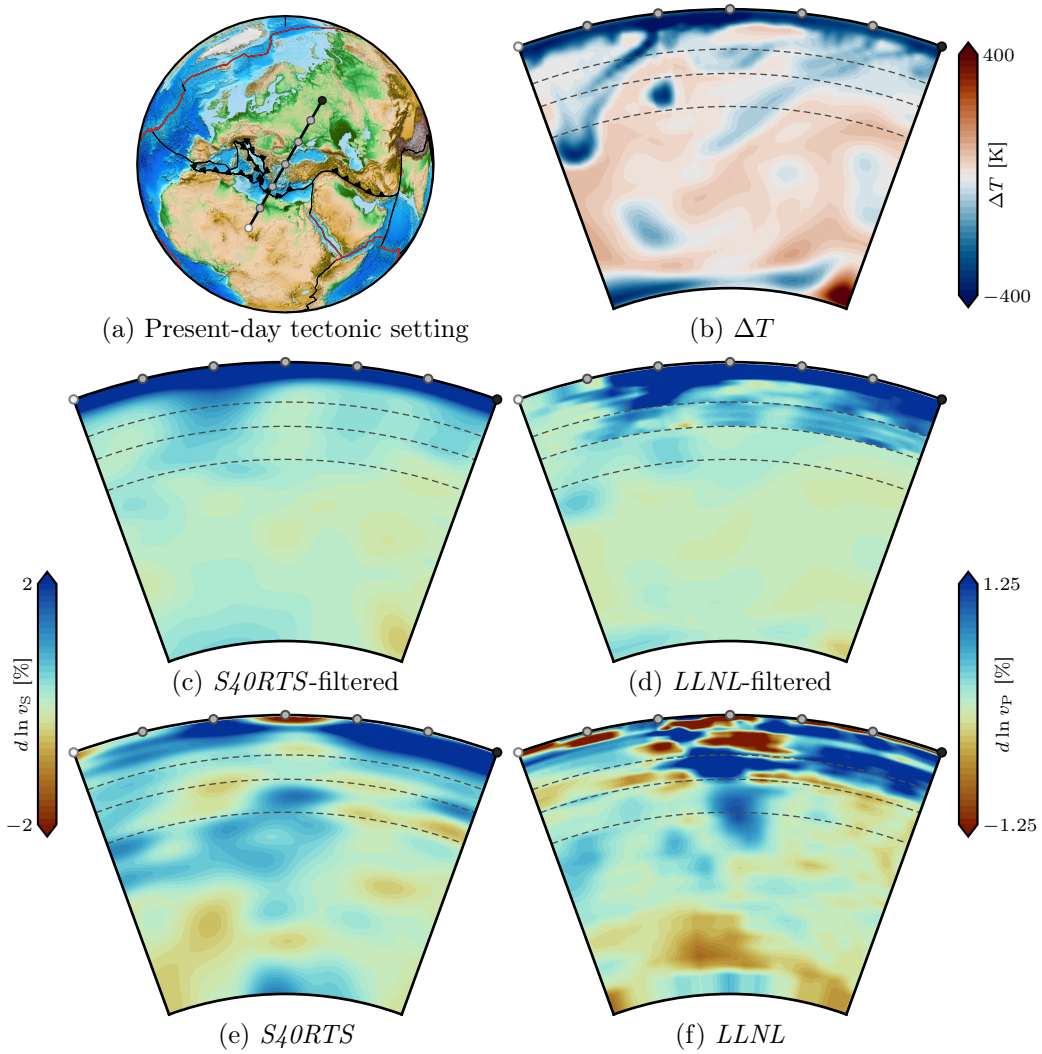

(a) Present-day tectonic setting
(b) ΔT
(c) *S40RTS*-filtered
(d) *LLNL*-filtered
(e) *S40RTS*
(f) *LLNL*

Figure B2

As in Figure B1 but for the Brasilia anomaly.

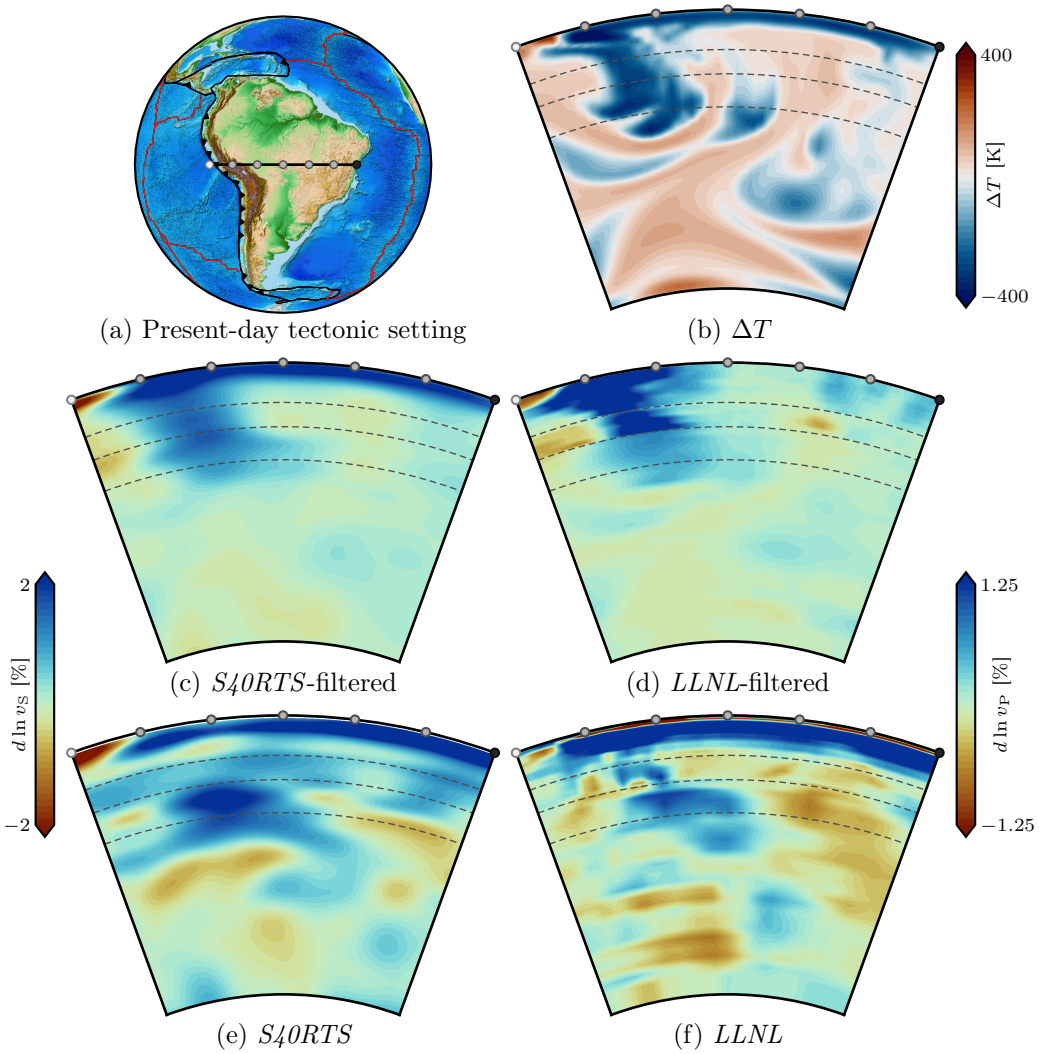

(a) Present-day tectonic setting (b) ΔT

(c) *S40RTS*-filtered (d) *LLNL*-filtered

(e) *S40RTS* (f) *LLNL*

Figure B3

Izu-Bonin anomaly history. (a) Palaeotrench locations. (b), (c), (d) G-ADOPT temperature perturbation structure ΔT at 35, 20 and 10 Ma, respectively.

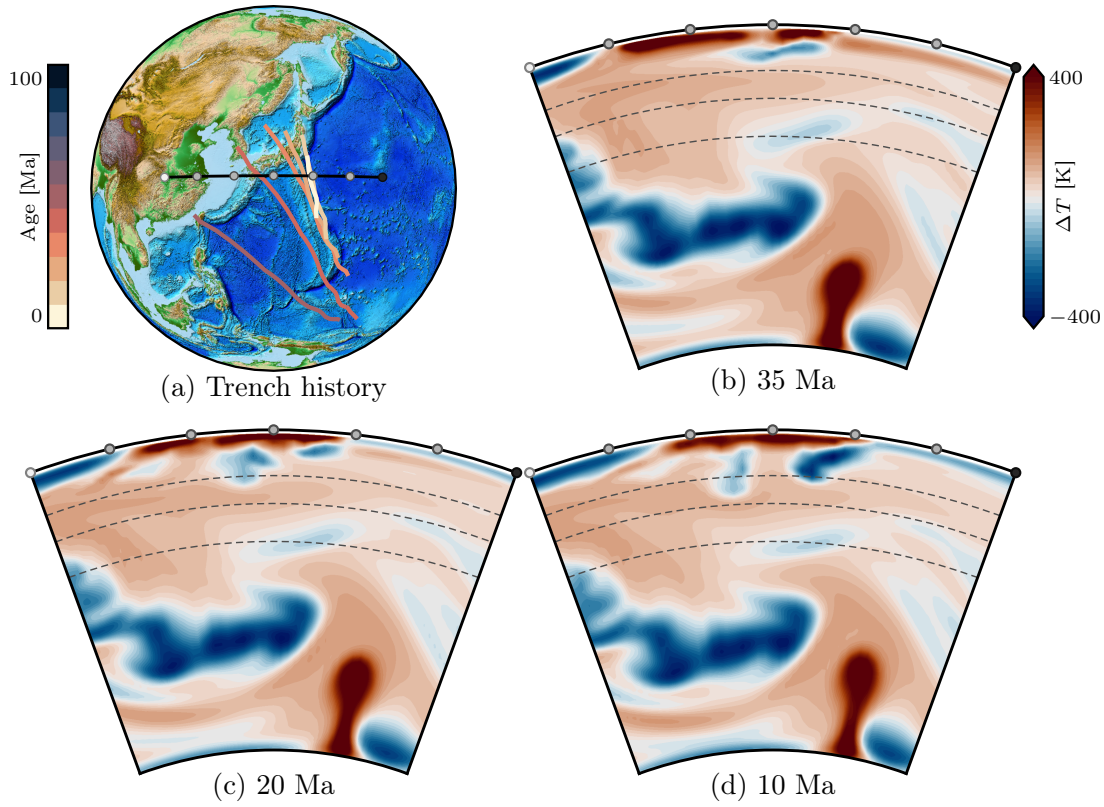

(a) Trench history (b) 35 Ma

(c) 20 Ma (d) 10 Ma

Figure B4

As in Figure B1 but for the Izu-Bonin anomaly.

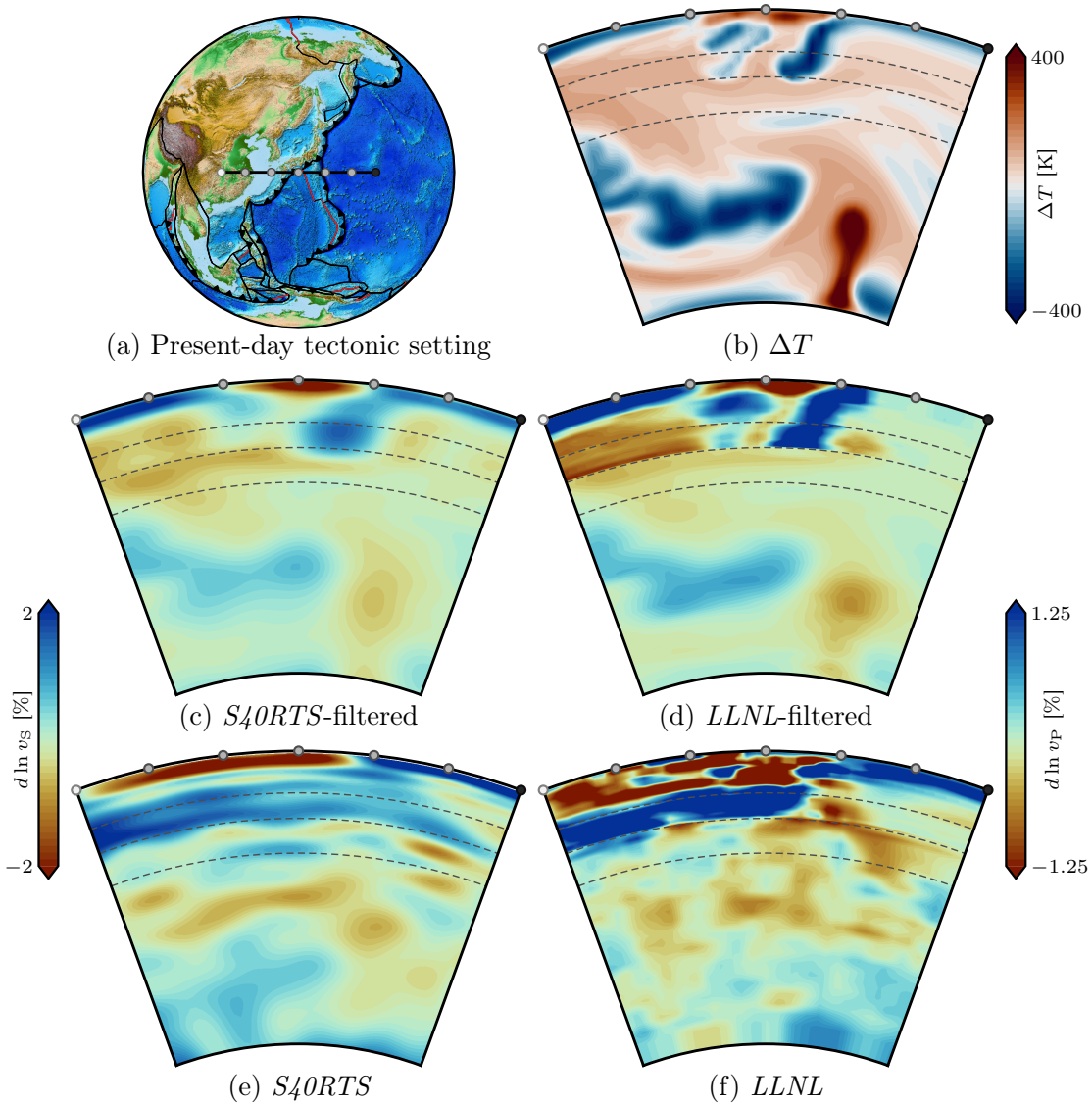

(a) Present-day tectonic setting (b) ΔT

(c) *S40RTS*-filtered (d) *LLNL*-filtered

(e) *S40RTS* (f) *LLNL*

Figure B5

Mariana anomaly history. (a) Palaeotrench locations. (b), (c), (d) G-ADOPT temperature perturbation structure ΔT at 35, 20 and 10 Ma, respectively.

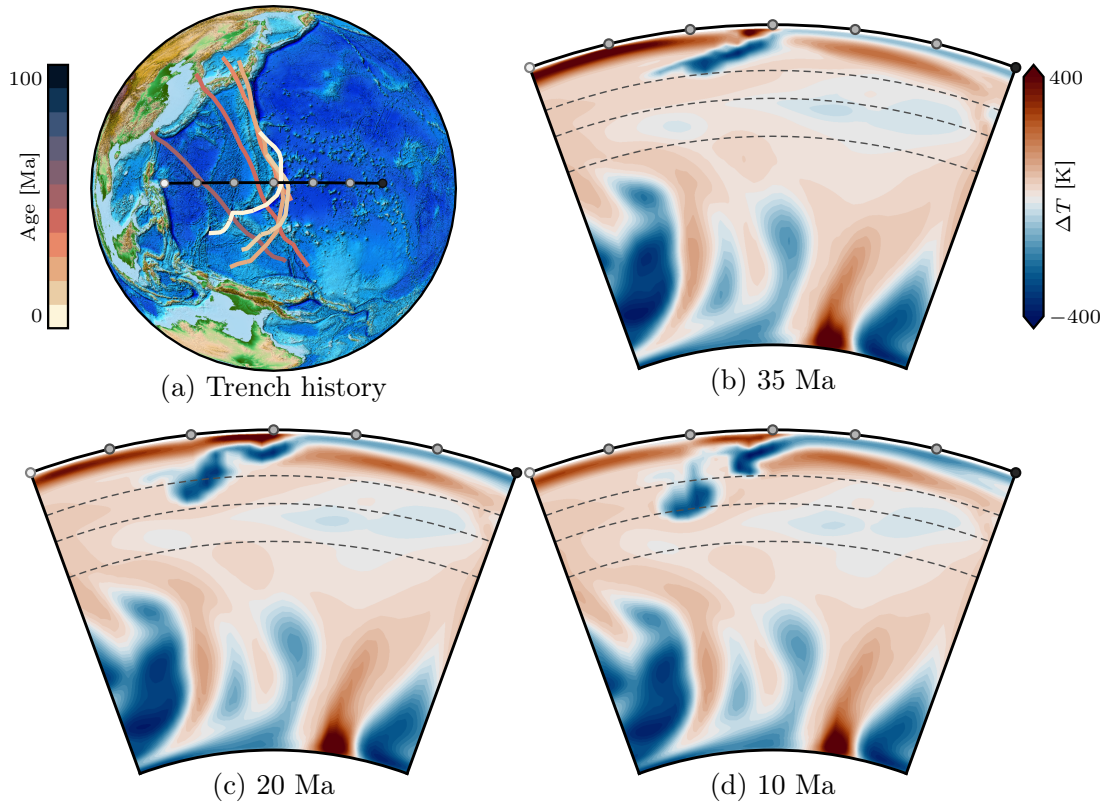

(a) Trench history (b) 35 Ma

(c) 20 Ma (d) 10 Ma

Figure B6

As in Figure B1 but for the Mariana anomaly.

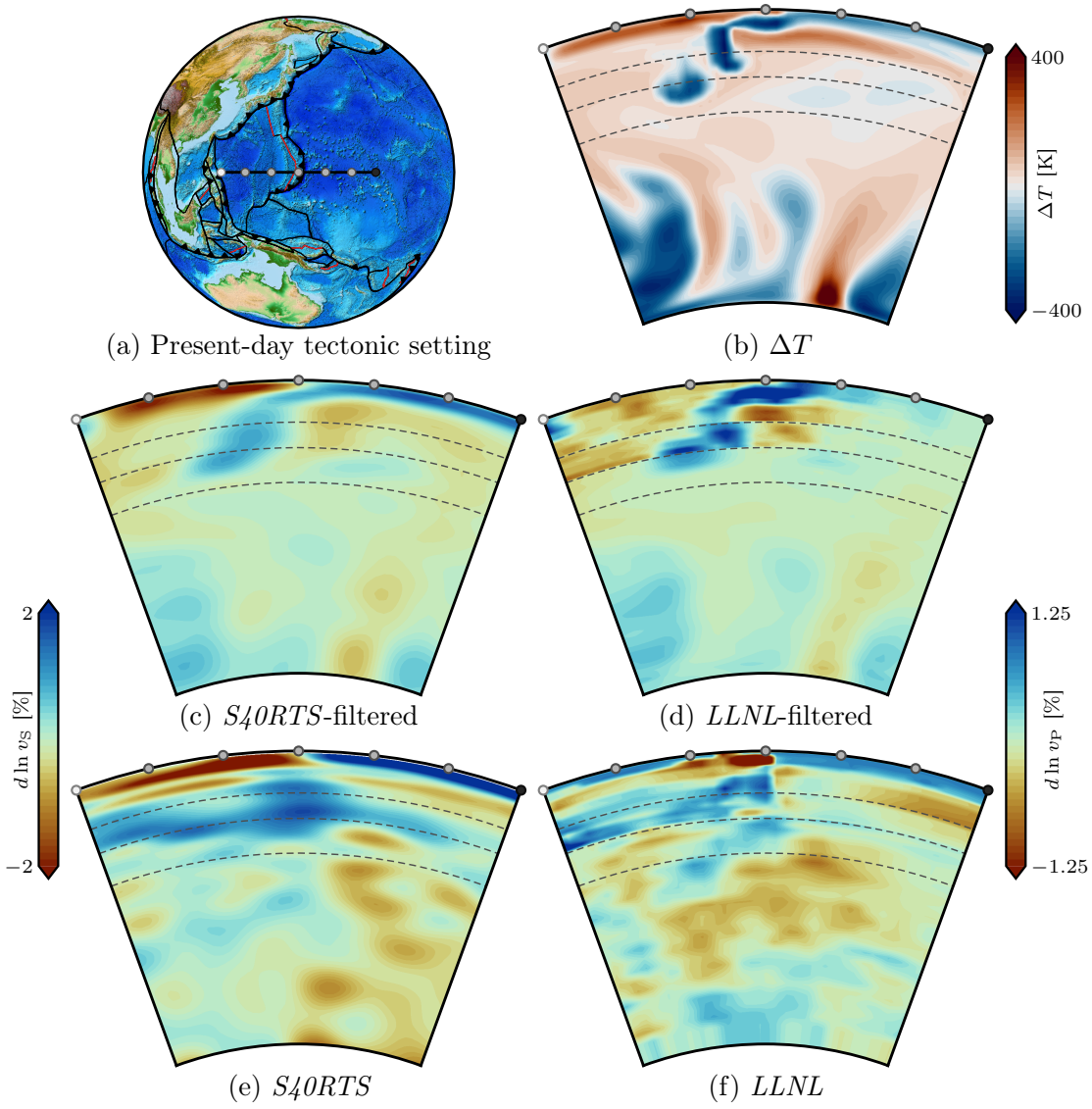

(a) Present-day tectonic setting (b) ΔT

(c) *S40RTS*-filtered (d) *LLNL*-filtered

(e) *S40RTS* (f) *LLNL*

Figure B7

Sunda anomaly history. (a) Palaeotrench locations. (b), (c), (d) G-ADOPT temperature perturbation structure ΔT at 70, 35 and 10 Ma, respectively.

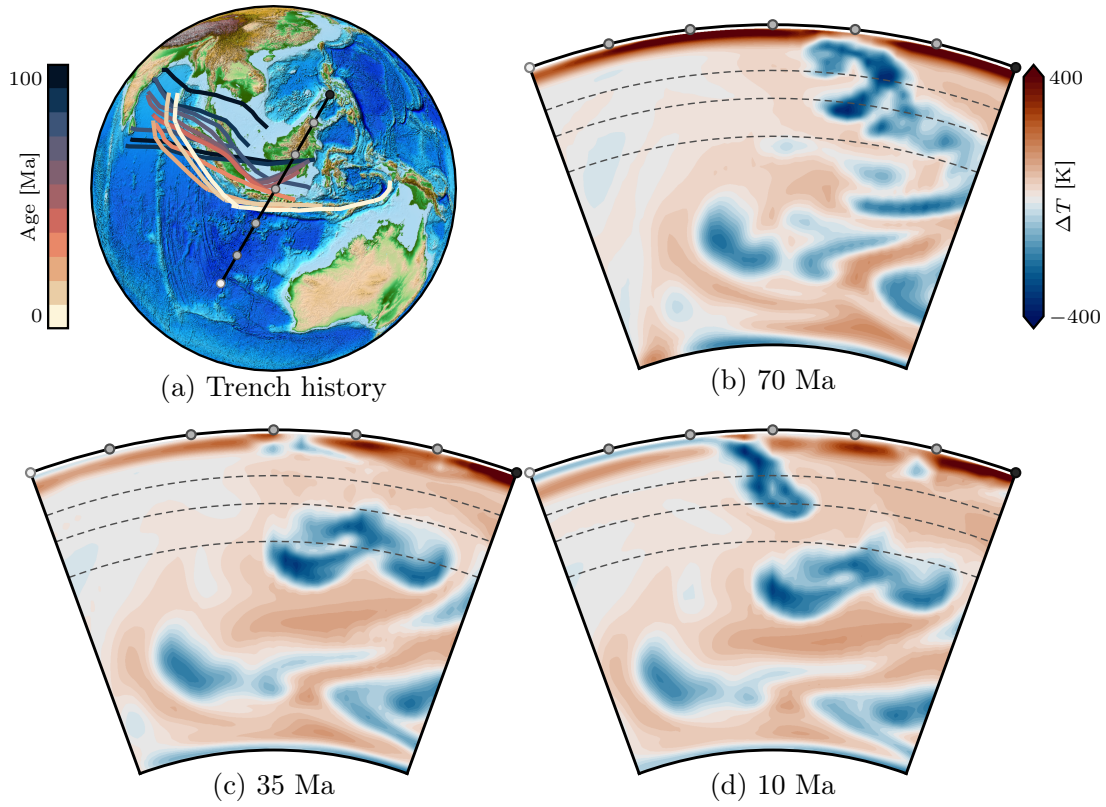

(a) Trench history (b) 70 Ma

(c) 35 Ma (d) 10 Ma

Figure B8

As in Figure B1 but for the Sunda anomaly.

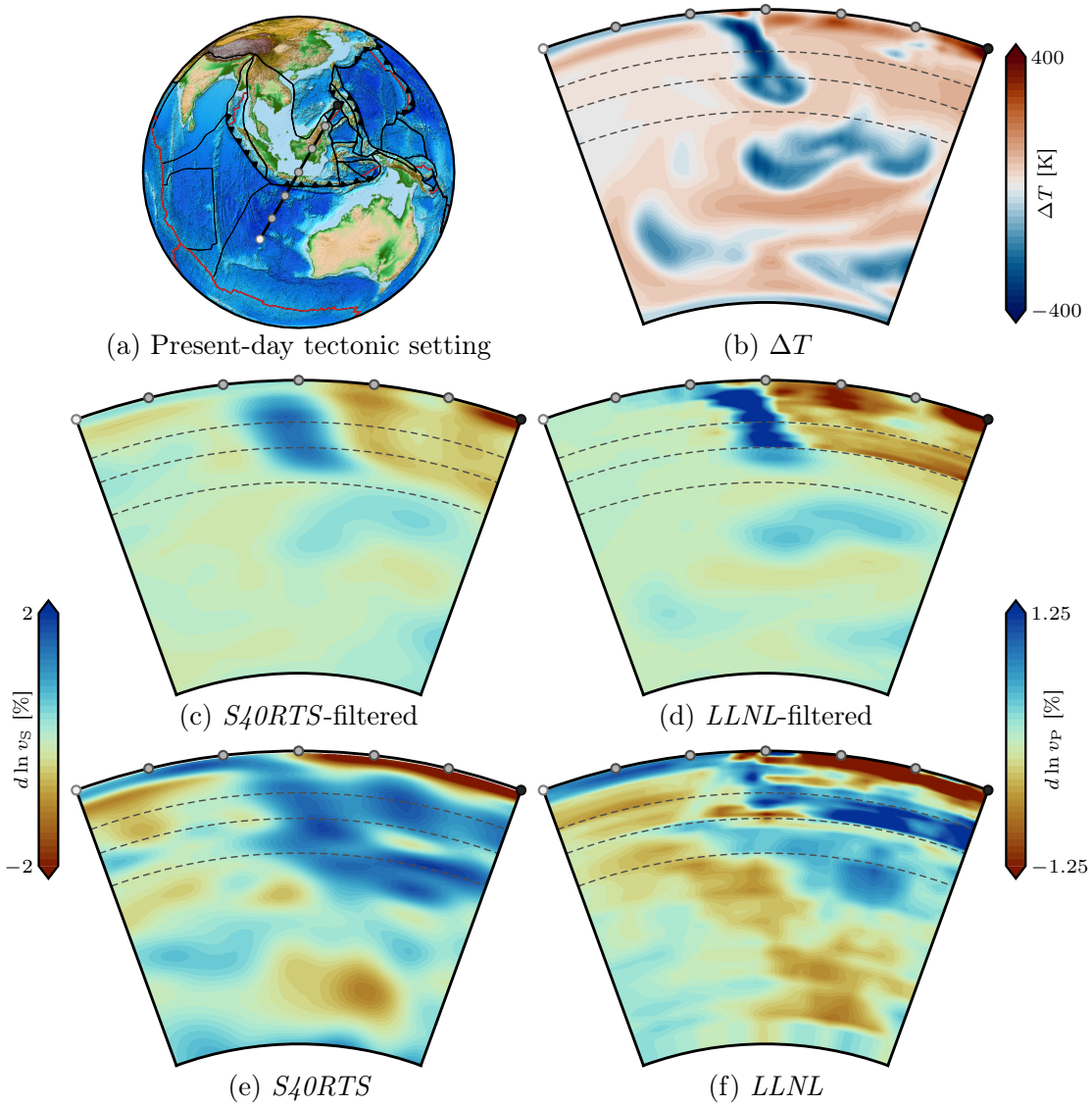

(a) Present-day tectonic setting (b) ΔT

(c) *S40RTS*-filtered (d) *LLNL*-filtered

(e) *S40RTS* (f) *LLNL*

Figure B9

Tonga–Kermadec–Hikurangi anomaly history. (a) Palaeotrench locations. (b), (c), (d) G-ADOPT *temperature perturbation structure* ΔT *at* 60, 35 *and* 10 Ma, *respectively.*

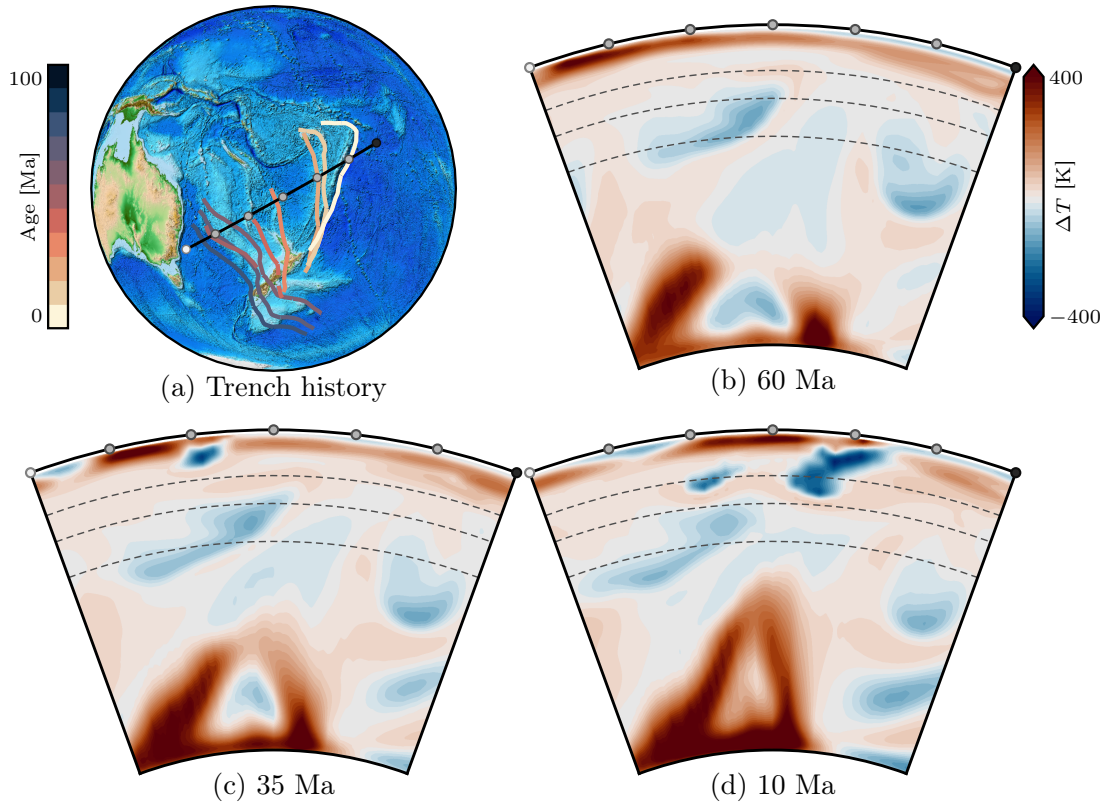

(a) Trench history (b) 60 Ma

(c) 35 Ma (d) 10 Ma

Figure B10

As in Figure B1 but for the Tonga–Kermadec–Hikurangi anomaly.

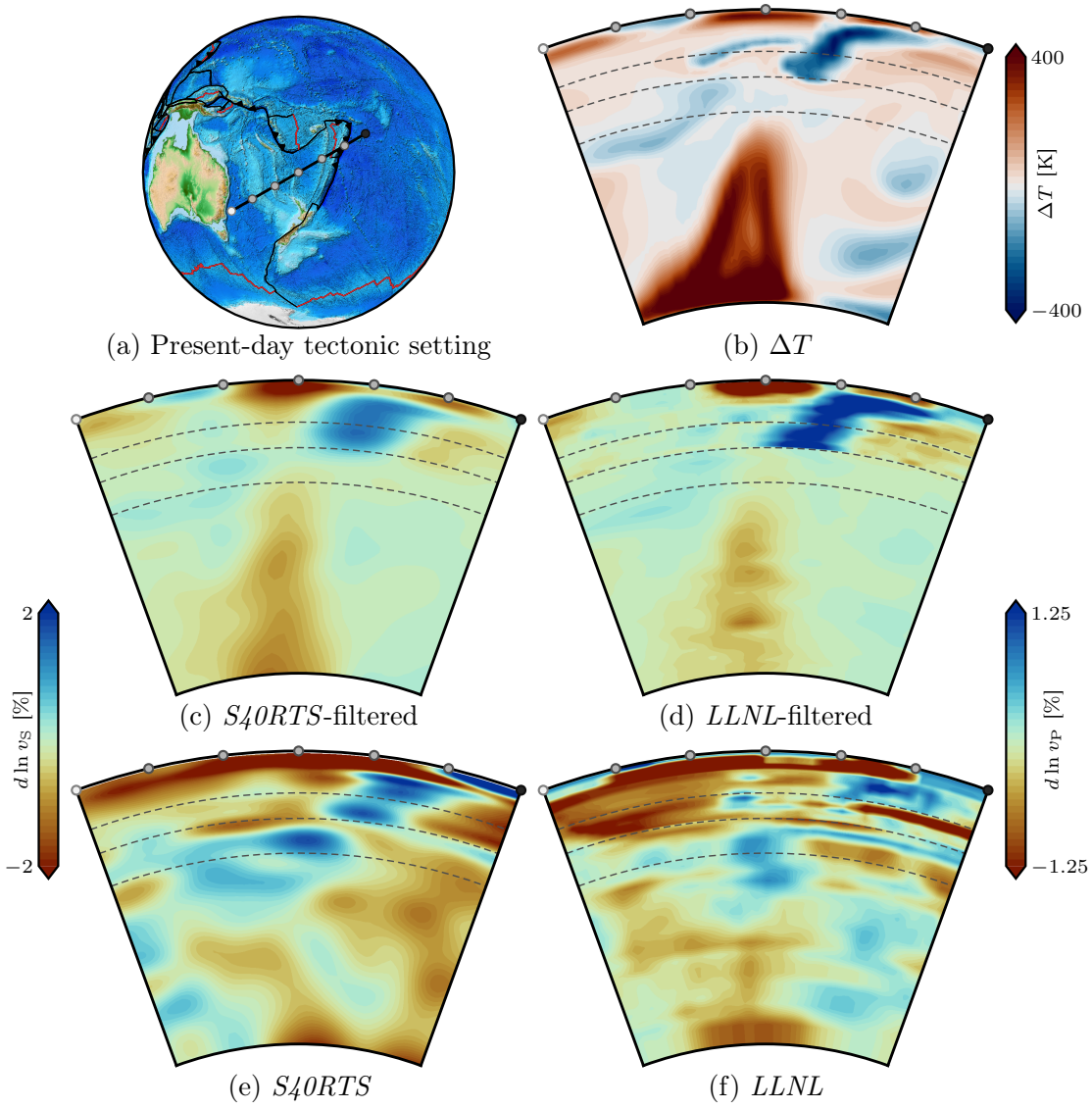

(a) Present-day tectonic setting (b) ΔT

(c) *S40RTS*-filtered (d) *LLNL*-filtered

(e) *S40RTS* (f) *LLNL*

C | Supplement to Chapter 4

1 Mantle circulation model details

We solve the Stokes and energy equations under the truncated anelastic liquid approximation in a spherical shell bounded by the core–mantle boundary (CMB) and Earth's surface. Radial reference properties (Figure C1) are derived using the open-source phase-equilibrium solver MMA-EoS (Chust et al., 2017), which minimises Gibbs free energy to determine stable mineral assemblages and thermodynamic parameters for a primitive pyrolitic mantle composition (CFMAS formulation of Workman & Hart, 2005). The adiabat is integrated downward from a surface temperature of 1600 K following $\frac{\partial T}{\partial z}=\frac{\alpha g}{C_p}\,T$, with the thermal expansion coefficient α, gravity g, and heat capacity C_p extracted from pre-computed MMA-EoS tables. Depths are converted to pressure assuming hydrostatic equilibrium, using the PREM density profile, allowing thermodynamic properties (ρ, α, C_v, C_p) to be sampled consistently with mantle conditions.

Viscosity is depth- and temperature-dependent, given by

$$\eta(T, r) = \eta_0(r) \exp[E\,(0.5 - T)]\,, \tag{C1}$$

where T is the non-dimensionalised mantle temperature, $\eta_0(r)$ a radially dependent prefactor, and E the non-dimensional activation energy (set to 10^5 in the upper-mantle [UM] and 10^4 in the lower-mantle [LM]) controlling thermal viscosity contrast. The resulting profile is compatible with independent geodetic and plate torque-balance constraints (e.g., Paulson & Richards, 2009; Iaffaldano & Lambeck, 2014; Stotz et al., 2018).

We employ a cubed sphere mesh with a nominal spacing of 70 km at the surface and 40 km at the CMB, with radial refinement toward both boundaries. For the Stokes system, we use Q2Q1 elements for velocity and pressure, respectively, with the linear system solved using a conjugate-gradient method, preconditioned with a geometric algebraic multigrid. Temperature is discretised with a second-order discontinuous Galerkin scheme, integrated in time using an implicit mid-point rule, and solved with the generalized minimal residual method and successive over-relaxation preconditioning. Higher-order polynomial discretisations for velocity and temperature ensure adequate resolution of flow and thermal fields.

2 Anelasticity model

Following Cammarano et al. (2003), the anelastic response is expressed as

$$Q_{\mathrm{S}}(\hat{r}, z) = B\omega^a \exp\left(\frac{agT_{\mathrm{m}}(z)}{T(\hat{r})}\right), \tag{C2}$$

Figure C1

Key material properties of mantle circulation model: (a) thermal expansivity α; (b) reference density $\bar{\rho}$; (c) reference temperature $\bar{T}$; and (d) viscosity η, showing mean (navy line) and range (shaded).

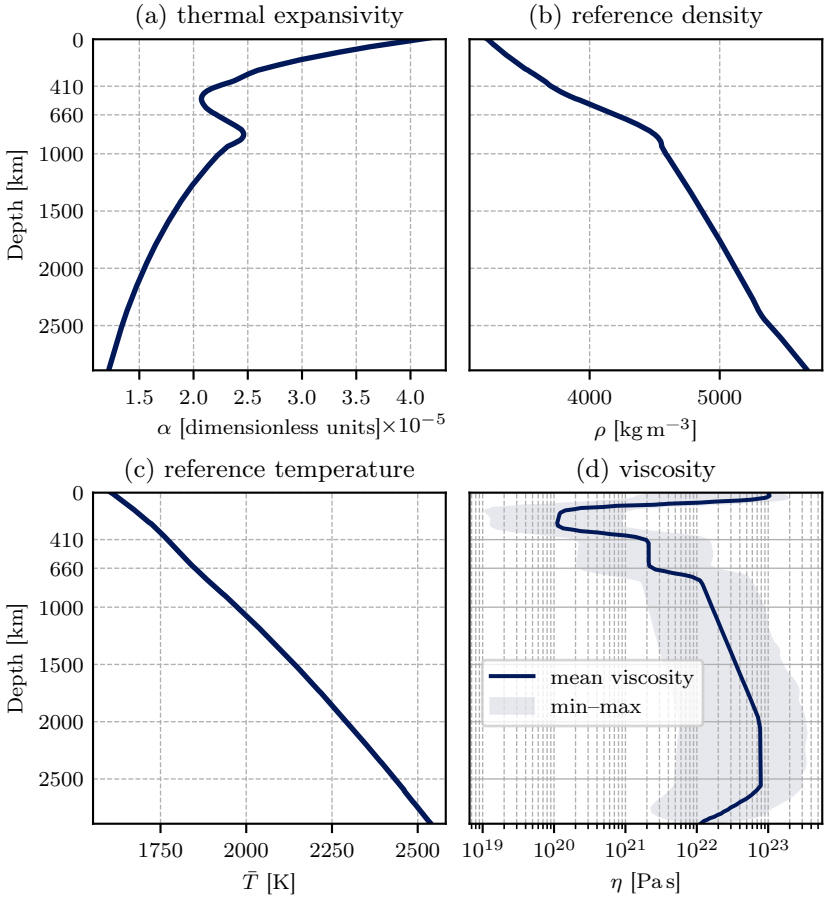

Table C1

Values for the anelasticity model parameters used in this study (Q6 from Cammarano et al., 2003).

Parameter	Upper-mantle	Lower-mantle
B	0.077	4.95
ω	1	
a	0.2	
g	30	15

where B is a normalisation factor, ω the seismic frequency, a the frequency dependence of attenuation, g a dimensionless scaling factor that reduces the pressure dependence to a dependence on temperature $T(\hat{r})$ at a given location in the model, and $T_{\mathrm{m}}(z)$ the solidus at depth z.

Figure C2

Relationship between temperature T and elastic (navy line) and anelastic (pink line) S-wave speed v_S at depths of (a) 300*, (b)* 600*, and (c)* 1750 km*, with temperature ranges in each spanning those found in our MCM at that depth. Panel (d) shows the effect of correcting for anelasticity throughout the whole mantle, given a change in temperature of* 100 K*, relative to the reference temperature shown in Figure C1.*

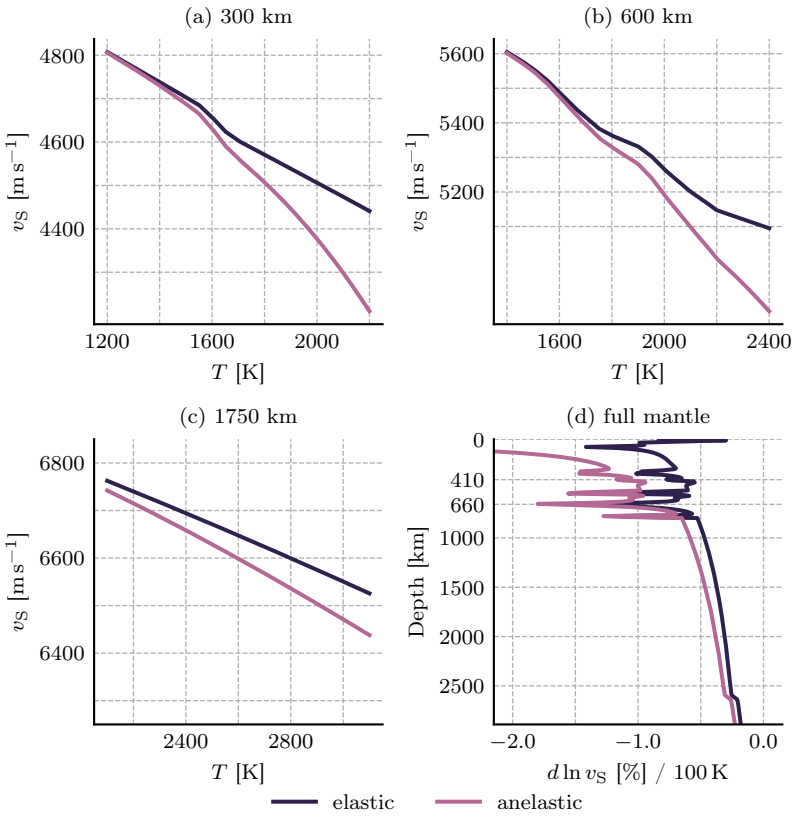

References

Arnould, M., Coltice, N., Flament, N., & Mallard, C. (2020). Plate tectonics and mantle controls on plume dynamics. *Earth and Planetary Science Letters*, *547*, 116439. https://doi.org/10.1016/j.epsl.2020.116439

Austermann, J., Pollard, D., Mitrovica, J. X., Moucha, R., Forte, A. M., DeConto, R. M., Rowley, D. B., & Raymo, M. E. (2015). The impact of dynamic topography change on Antarctic ice sheet stability during the mid-Pliocene warm period. *Geology*, *43*(10), 927–930. https://doi.org/10.1130/G36988.1

Baumgardner, J. R. (1985). Three-dimensional treatment of convective flow in the earth's mantle. *Journal of Statistical Physics*, *39*(5), 501–511. https://doi.org/10.1007/BF01008348

Bercovici, D. (2003). The generation of plate tectonics from mantle convection. *Earth and Planetary Science Letters*, *205*(3-4), 107–121. https://doi.org/10.1016/S0012-821X(02)01009-9

Biggin, A. J., Steinberger, B., Aubert, J., Suttie, N., Holme, R., Torsvik, T. H., van der Meer, D. G., & van Hinsbergen, D. J. J. (2012). Possible links between long-term geomagnetic variations and whole-mantle convection processes. *Nature Geoscience*, *5*(8), 526–533. https://doi.org/10.1038/ngeo1521

Bocher, M., Coltice, N., Fournier, A., & Tackley, P. (2016). A sequential data assimilation approach for the joint reconstruction of mantle convection and surface tectonics. *Geophysical Journal International*, *204*(1), 200–214. https://doi.org/10.1093/gji/ggv427

Bower, D. J., Gurnis, M., & Flament, N. (2015). Assimilating lithosphere and slab history in 4-D Earth models. *Physics of the Earth and Planetary Interiors*, *238*, 8–22. https://doi.org/10.1016/j.pepi.2014.10.013

Bradshaw, J. D. (1989). Cretaceous geotectonic patterns in the New Zealand Region. *Tectonics*, *8*(4), 803–820. https://doi.org/10.1029/TC008i004p00803

Bullard, E., Everett, J. E., & Gilbert Smith, A. (1965). The fit of the continents around the Atlantic. *Philosophical Transactions of the Royal Society of London, Series A: Mathematical and Physical Sciences*, *258*(1088), 41–51. https://doi.org/10.1098/rsta.1965.0020

Bunge, H.-P., Hagelberg, C. R., & Travis, B. J. (2003). Mantle circulation models with variational data assimilation: Inferring past mantle flow and structure from plate motion histories and seismic tomography. *Geophysical Journal International*, *152*(2), 280–301. https://doi.org/10.1046/j.1365-246X.2003.01823.x

Bunge, H.-P., Richards, M. A., & Baumgardner, J. R. (2002). Mantle-circulation models with sequential data assimilation: Inferring present-day mantle structure from plate-motion histories (J. H. Davies, J. P. Brodholt, & B. J. Wood, Eds.). *Philosophical Transactions of the Royal Society A: Mathematical, Physical and Engineering Sciences*, *360*(1800), 2545–2567. https://doi.org/10.1098/rsta.2002.1080

Bunge, H.-P., Richards, M. A., & Baumgardner, J. R. (1997). A sensitivity study of three-dimensional spherical mantle convection at 10^8 Rayleigh number: Effects of depth-dependent viscosity,

heating mode, and an endothermic phase change. *Journal of Geophysical Research: Solid Earth*, *102*(B6), 11991–12007. https://doi.org/10.1029/96JB03806

Butterworth, N. P., Talsma, A. S., Müller, R. D., Seton, M., Bunge, H.-P., Schuberth, B. S. A., Shephard, G. E., & Heine, C. (2014). Geological, tomographic, kinematic and geodynamic constraints on the dynamics of sinking slabs. *Journal of Geodynamics*, *73*, 1–13. https://doi.org/10.1016/j.jog.2013.10.006

Cammarano, F., Goes, S., Vacher, P., & Giardini, D. (2003). Inferring upper-mantle temperatures from seismic velocities. *Physics of the Earth and Planetary Interiors*, *138*(3), 197–222. https://doi.org/10.1016/S0031-9201(03)00156-0

Cao, W., Flament, N., Zahirovic, S., Williams, S., & Müller, R. D. (2019). The interplay of dynamic topography and eustasy on continental flooding in the late Paleozoic. *Tectonophysics*, *761*, 108–121. https://doi.org/10.1016/j.tecto.2019.04.018

Cawood, P. A., & Hawkesworth, C. J. (2014). Earth's middle age. *Geology*, *42*(6), 503–506. https://doi.org/10.1130/G35402.1

Chust, T. C., Steinle-Neumann, G., Dolejš, D., Schuberth, B. S. A., & Bunge, H.-P. (2017). MMA-EoS: A computational framework for mineralogical thermodynamics. *Journal of Geophysical Research: Solid Earth*, *122*(12), 9881–9920. https://doi.org/10.1002/2017JB014501

Clennett, E. J., Sigloch, K., Mihalynuk, M. G., Seton, M., Henderson, M. A., Hosseini, K., Mohammadzaheri, A., Johnston, S. T., & Müller, R. D. (2020). A Quantitative Tomotectonic Plate Reconstruction of Western North America and the Eastern Pacific Basin. *Geochemistry, Geophysics, Geosystems*, *21*(8). https://doi.org/10.1029/2020GC009117

Clevenger, T. C., & Heister, T. (2021). Comparison between algebraic and matrix-free geometric multigrid for a Stokes problem on adaptive meshes with variable viscosity. *Numerical Linear Algebra with Applications*, *28*(5), e2375. https://doi.org/10.1002/nla.2375

Cogné, J. P. (2003). PaleoMac: A Macintosh™ application for treating paleomagnetic data and making plate reconstructions. *Geochemistry, Geophysics, Geosystems*, *4*(1). https://doi.org/10.1029/2001GC000227

Cui, C., Lei, W., Liu, Q., Peter, D., Bozdağ, E., Tromp, J., Hill, J., Podhorszki, N., & Pugmire, D. (2024). GLAD-M35: A joint P and S global tomographic model with uncertainty quantification. *Geophysical Journal International*, *239*(1), 478–502. https://doi.org/10.1093/gji/ggae270

Dahlen, F. A., Hung, S.-H., & Nolet, G. (2000). Fréchet kernels for finite-frequency traveltimes—I. Theory. *Geophysical Journal International*, *141*(1), 157–174. https://doi.org/10.1046/j.1365-246X.2000.00070.x

Dannberg, J., Gassmöller, R., Thallner, D., LaCombe, F., & Sprain, C. (2024). Changes in core–mantle boundary heat flux patterns throughout the supercontinent cycle. *Geophysical Journal International*, *237*(3), 1251–1274. https://doi.org/10.1093/gji/ggae075

Davies, D. R., & Davies, J. H. (2009). Thermally-driven mantle plumes reconcile multiple hot-spot observations. *Earth and Planetary Science Letters*, *278*(1), 50–54. https://doi.org/10.1016/j.epsl.2008.11.027

Davies, D. R., Davies, J. H., Bollada, P. C., Hassan, O., Morgan, K., & Nithiarasu, P. (2013). A hierarchical mesh refinement technique for global 3-D spherical mantle convection modelling. *Geoscientific Model Development*, *6*(4), 1095–1107. https://doi.org/10.5194/gmd-6-1095-2013

Davies, D. R., Goes, S., Davies, J. H., Schuberth, B. S. A., Bunge, H.-P., & Ritsema, J. (2012). Reconciling dynamic and seismic models of Earth's lower mantle: The dominant role of

thermal heterogeneity. *Earth and Planetary Science Letters*, *353–354*, 253–269. https://doi.org/10.1016/j.epsl.2012.08.016

Davies, D. R., Kramer, S. C., Ghelichkhan, S., & Gibson, A. (2022). Towards automatic finite-element methods for geodynamics via Firedrake. *Geoscientific Model Development*, *15*(13), 5127–5166. https://doi.org/10.5194/gmd-15-5127-2022

Engebretson, D. C., Cox, A., & Gordon, R. G. (1985). Relative Motions Between Oceanic and Continental Plates in the Pacific Basin. In D. C. Engebretson, A. Cox, & R. G. Gordon (Eds.), *Relative Motions Between Oceanic and Continental Plates in the Pacific Basin* (Vol. 206). Geological Society of America. https://doi.org/10.1130/SPE206-p1

Faccenna, C., Glišović, P., Forte, A., Becker, T. W., Garzanti, E., Sembroni, A., & Gvirtzman, Z. (2019). Role of dynamic topography in sustaining the Nile River over 30 million years. *Nature Geoscience*, *12*(12), 1012–1017. https://doi.org/10.1038/s41561-019-0472-x

Fichtner, A. (2010). *Full seismic waveform modelling and inversion*. Springer.

Fichtner, A., Ritsema, J., & Thrastarson, S. (2025). A high-resolution discourse on seismic tomography. *Proceedings of the Royal Society A: Mathematical, Physical and Engineering Sciences*, *481*(2320), 20240955. https://doi.org/10.1098/rspa.2024.0955

Flament, N., Gurnis, M., & Müller, R. D. (2013). A review of observations and models of dynamic topography. *Lithosphere*, *5*(2), 189–210. https://doi.org/10.1130/L245.1

Flament, N., Gurnis, M., Müller, R. D., Bower, D. J., & Husson, L. (2015). Influence of subduction history on South American topography. *Earth and Planetary Science Letters*, *430*, 9–18. https://doi.org/10.1016/j.epsl.2015.08.006

Gassmöller, R., Dannberg, J., Bangerth, W., Heister, T., & Myhill, R. (2020). On formulations of compressible mantle convection. *Geophysical Journal International*, *221*(2), 1264–1280. https://doi.org/10.1093/gji/ggaa078

Gassmöller, R., Lokavarapu, H., Heien, E., Puckett, E. G., & Bangerth, W. (2018). Flexible and scalable particle-in-cell methods with adaptive mesh refinement for geodynamic computations. *Geochemistry, Geophysics, Geosystems*, *19*(9), 3596–3604. https://doi.org/10.1029/2018GC007508

Ghelichkhan, S., Bunge, H.-P., & Oeser, J. (2021). Global mantle flow retrodictions for the early Cenozoic using an adjoint method: Evolving dynamic topographies, deep mantle structures, flow trajectories and sublithospheric stresses. *Geophysical Journal International*, *226*(2), 1432–1460. https://doi.org/10.1093/gji/ggab108

Ghelichkhan, S., Gibson, A., Davies, D. R., Kramer, S. C., & Ham, D. A. (2024). Automatic adjoint-based inversion schemes for geodynamics: Reconstructing the evolution of Earth's mantle in space and time. *Geoscientific Model Development*, *17*(13), 5057–5086. https://doi.org/10.5194/gmd-17-5057-2024

Gibson, A., Davies, D. R., Kramer, S., Gelichkhan, S., Turner, R., Duvernay, T., & Scott, W. (2024, June). G-ADOPT. https://doi.org/10.5281/zenodo.5644391

Goes, S., Cammarano, F., & Hansen, U. (2004). Synthetic seismic signature of thermal mantle plumes. *Earth and Planetary Science Letters*, *218*(3), 403–419. https://doi.org/10.1016/S0012-821X(03)00680-0

Groves, D. I., & Bierlein, F. P. (2007). Geodynamic settings of mineral deposit systems. *Journal of the Geological Society*, *164*(1), 19–30. https://doi.org/10.1144/0016-76492006-065

Gürer, D., Granot, R., & van Hinsbergen, D. J. J. (2022). Plate tectonic chain reaction revealed by noise in the Cretaceous quiet zone. *Nature Geoscience*, *15*(3), 233–239. https://doi.org/10.1038/s41561-022-00893-7

Gurnis, M. (1988). Large-scale mantle convection and the aggregation and dispersal of supercontinents. *Nature*, *332*(6166), 695–699.

Gurnis, M., Turner, M., Zahirovic, S., DiCaprio, L., Spasojevic, S., Müller, R. D., Boyden, J., Seton, M., Manea, V. C., & Bower, D. J. (2012). Plate tectonic reconstructions with continuously closing plates. *Computers & Geosciences*, *38*(1), 35–42. https://doi.org/10.1016/j.cageo.2011.04.014

Gurnis, M., Yang, T., Cannon, J., Turner, M., Williams, S., Flament, N., & Müller, R. D. (2018). Global tectonic reconstructions with continuously deforming and evolving rigid plates. *Computers & Geosciences*, *116*, 32–41. https://doi.org/10.1016/j.cageo.2018.04.007

Gutenberg, B. (1959). *Physics of the Earth's Interior*. Academic Press.

Hager, B. H., Clayton, R. W., Richards, M. A., Comer, R. P., & Dziewonski, A. M. (1985). Lower mantle heterogeneity, dynamic topography and the geoid. *Nature*, *313*(6003), 541–545. https://doi.org/10.1038/313541a0

Hall, R. (2002). Cenozoic geological and plate tectonic evolution of SE Asia and the SW Pacific: Computer-based reconstructions, model and animations. *Journal of Asian Earth Sciences*, *20*(4), 353–431. https://doi.org/10.1016/S1367-9120(01)00069-4

Harrington, L., Zahirovic, S., Flament, N., & Müller, R. D. (2017). The role of deep Earth dynamics in driving the flooding and emergence of New Guinea since the Jurassic. *Earth and Planetary Science Letters*, *479*, 273–283. https://doi.org/10.1016/j.epsl.2017.09.039

Hasterok, D., Halpin, J. A., Collins, A. S., Hand, M., Kreemer, C., Gard, M. G., & Glorie, S. (2022). New Maps of Global Geological Provinces and Tectonic Plates. *Earth-Science Reviews*, *231*, 104069. https://doi.org/10.1016/j.earscirev.2022.104069

Heister, T., Dannberg, J., Gassmöller, R., & Bangerth, W. (2017). High accuracy mantle convection simulation through modern numerical methods — II: Realistic models and problems. *Geophysical Journal International*, *210*(2), 833–851. https://doi.org/10.1093/gji/ggx195

Hosseini, K., Matthews, K. J., Sigloch, K., Shephard, G. E., Domeier, M., & Tsekhmistrenko, M. (2018). SubMachine: Web-Based Tools for Exploring Seismic Tomography and Other Models of Earth's Deep Interior. *Geochemistry, Geophysics, Geosystems*, *19*(5), 1464–1483. https://doi.org/10.1029/2018GC007431

Hu, J., Gurnis, M., Rudi, J., Stadler, G., & Müller, R. D. (2022). Dynamics of the abrupt change in Pacific Plate motion around 50 million years ago. *Nature Geoscience*, *15*(1), 74–78. https://doi.org/10.1038/s41561-021-00862-6

Hu, J., Liu, L., Faccenda, M., Zhou, Q., Fischer, K. M., Marshak, S., & Lundstrom, C. (2018a). Modification of the Western Gondwana craton by plume–lithosphere interaction. *Nature Geoscience*, *11*(3), 203–210. https://doi.org/10.1038/s41561-018-0064-1

Hu, J., Liu, L., & Zhou, Q. (2018b). Reproducing past subduction and mantle flow using high-resolution global convection models. *Earth and Planetary Physics*, *2*(3), 189–207. https://doi.org/10.26464/epp2018019

Iaffaldano, G., & Lambeck, K. (2014). Pacific plate-motion change at the time of the Hawaiian–Emperor bend constrains the viscosity of Earth's asthenosphere. *Geophysical Research Letters*, *41*(10), 3398–3406. https://doi.org/10.1002/2014GL059763

Karato, S.-i. (1993). Importance of anelasticity in the interpretation of seismic tomography. *Geophysical Research Letters*, *20*(15), 1623–1626. https://doi.org/10.1029/93GL01767

Kreemer, C., Blewitt, G., & Klein, E. C. (2014). A geodetic plate motion and Global Strain Rate Model. *Geochemistry, Geophysics, Geosystems*, *15*(10), 3849–3889. https://doi.org/10.1002/2014GC005407

Kronbichler, M., Heister, T., & Bangerth, W. (2012). High accuracy mantle convection simulation through modern numerical methods. *Geophysical Journal International*, *191*(1), 12–29. https://doi.org/10.1111/j.1365-246X.2012.05609.x

Li, Y., Liu, L., Peng, D., Dong, H., & Li, S. (2023). Evaluating tomotectonic plate reconstructions using geodynamic models with data assimilation, the case for North America. *Earth-Science Reviews*, *244*, 104518. https://doi.org/10.1016/j.earscirev.2023.104518

Lin, Y.-A., Colli, L., & Wu, J. (2022). NW Pacific-Panthalassa Intra-Oceanic Subduction During Mesozoic Times From Mantle Convection and Geoid Models. *Geochemistry, Geophysics, Geosystems*, *23*(11), e2022GC010514. https://doi.org/10.1029/2022GC010514

Liu, L., & Gurnis, M. (2008). Simultaneous inversion of mantle properties and initial conditions using an adjoint of mantle convection. *Journal of Geophysical Research: Solid Earth*, *113*(B8). https://doi.org/10.1029/2008JB005594

Liu, L., Gurnis, M., Seton, M., Saleeby, J., Müller, R. D., & Jackson, J. M. (2010). The role of oceanic plateau subduction in the Laramide orogeny. *Nature Geoscience*, *3*(5), 353–357. https://doi.org/10.1038/ngeo829

Liu, L., & Stegman, D. R. (2011). Segmentation of the Farallon slab. *Earth and Planetary Science Letters*, *311*(1), 1–10. https://doi.org/10.1016/j.epsl.2011.09.027

Lu, C., Grand, S. P., Lai, H., & Garnero, E. J. (2019). TX2019slab: A new P and S tomography model incorporating subducting slabs. *Journal of Geophysical Research: Solid Earth*, *124*(11), 11549–11567. https://doi.org/10.1029/2019JB017448

Luyendyk, B. P. (1995). Hypothesis for Cretaceous rifting of east Gondwana caused by subducted slab capture. *Geology*, *23*(4), 373–376. https://doi.org/10.1130/0091-7613(1995)023<0373:HFCROE>2.3.CO;2

Mann, P., & Taira, A. (2004). Global tectonic significance of the Solomon Islands and Ontong Java Plateau convergent zone. *Tectonophysics*, *389*(3), 137–190. https://doi.org/10.1016/j.tecto.2003.10.024

Mao, W., & Zhong, S. (2018). Slab stagnation due to a reduced viscosity layer beneath the mantle transition zone. *Nature Geoscience*, *11*(11), 876–881. https://doi.org/10.1038/s41561-018-0225-2

Maruyama, S., Santosh, M., & Zhao, D. (2007). Superplume, supercontinent, and post-perovskite: Mantle dynamics and anti-plate tectonics on the Core–Mantle Boundary. *Gondwana Research*, *11*(1), 7–37. https://doi.org/10.1016/j.gr.2006.06.003

Mather, B. R., Müller, R. D., Zahirovic, S., Cannon, J., Chin, M., Ilano, L., Wright, N. M., Alfonso, C., Williams, S., Tetley, M., & Merdith, A. (2024). Deep time spatio-temporal data analysis using pyGPlates with PlateTectonicTools and GPlately. *Geoscience Data Journal*, *11*(1), 3–10. https://doi.org/10.1002/gdj3.185

Matthews, K. J., Seton, M., & Müller, R. D. (2012). A global-scale plate reorganization event at 105–100 Ma. *Earth and Planetary Science Letters*, *355–356*, 283–298. https://doi.org/10.1016/j.epsl.2012.08.023

McKenzie, D. P. (1969). Speculations on the consequences and causes of plate motions. *Geophysical Journal International*, *18*(1), 1–32. https://doi.org/10.1111/j.1365-246X.1969.tb00259.x

McKenzie, D. P., & Parker, R. L. (1967). The North Pacific: An Example of Tectonics on a Sphere. *Nature*, *216*(5122), 1276–1280. https://doi.org/10.1038/2161276a0

Miller, K. G., Kominz, M. A., Browning, J. V., Wright, J. D., Mountain, G. S., Katz, M. E., Sugarman, P. J., Cramer, B. S., Christie-Blick, N., & Pekar, S. F. (2005). The Phanerozoic record of global sea-level change. *Science*, *310*(5752), 1293–1298. https://doi.org/10.1126/science.1116412

Molnar, P., & Atwater, T. (1973). Relative Motion of Hot Spots in the Mantle. *Nature*, *246*(5431), 288–291. https://doi.org/10.1038/246288a0

Moresi, L., Quenette, S., Lemiale, V., Mériaux, C., Appelbe, B., & Mühlhaus, H. .-. (2007). Computational approaches to studying non-linear dynamics of the crust and mantle. *Physics of the Earth and Planetary Interiors*, *163*(1), 69–82. https://doi.org/10.1016/j.pepi.2007.06.009

Moresi, L.-N., & Solomatov, V. S. (1995). Numerical investigation of 2D convection with extremely large viscosity variations. *Physics of Fluids*, *7*(9), 2154–2162. https://doi.org/10.1063/1.868465

Morgan, W. J. (1968). Rises, trenches, great faults, and crustal blocks. *Journal of Geophysical Research (1896-1977)*, *73*(6), 1959–1982. https://doi.org/10.1029/JB073i006p01959

Morgan, W. J. (1971). Convection plumes in the lower mantle. *Nature*, *230*, 42–43.

Müller, R. D., Cannon, J., Qin, X., Watson, R. J., Gurnis, M., Williams, S., Pfaffelmoser, T., Seton, M., Russell, S. H. J., & Zahirovic, S. (2018). GPlates: Building a virtual Earth through deep time. *Geochemistry, Geophysics, Geosystems*, *19*(7), 2243–2261. https://doi.org/10.1029/2018GC007584

Müller, R. D., Flament, N., Cannon, J., Tetley, M. G., Williams, S. E., Cao, X., Bodur, Ö. F., Zahirovic, S., & Merdith, A. (2022a). A tectonic-rules-based mantle reference frame since 1 billion years ago—implications for supercontinent cycles and plate–mantle system evolution. *Solid Earth*, *13*(7), 1127–1159. https://doi.org/10.5194/se-13-1127-2022

Müller, R. D., Mather, B., Dutkiewicz, A., Keller, T., Merdith, A., Gonzalez, C. M., Gorczyk, W., & Zahirovic, S. (2022b). Evolution of Earth's tectonic carbon conveyor belt. *Nature*, *605*(7911), 629–639. https://doi.org/10.1038/s41586-022-04420-x

Müller, R. D., Seton, M., Zahirovic, S., Williams, S. E., Matthews, K. J., Wright, N. M., Shephard, G. E., Maloney, K. T., Barnett-Moore, N., Hosseinpour, M., Bower, D. J., & Cannon, J. (2016). Ocean basin evolution and global-scale plate reorganization events since Pangea breakup. *Annual Review of Earth and Planetary Sciences*, *44*(1), 107–138. https://doi.org/10.1146/annurev-earth-060115-012211

Müller, R. D., Zahirovic, S., Williams, S. E., Cannon, J., Seton, M., Bower, D. J., Tetley, M. G., Heine, C., Le Breton, E., Liu, S., Russell, S. H. J., Yang, T., Leonard, J., & Gurnis, M. (2019). A global plate model including lithospheric deformation along major rifts and orogens since the Triassic. *Tectonics*, *38*(6), 1884–1907. https://doi.org/10.1029/2018TC005462

Nerlich, R., Colli, L., Ghelichkhan, S., Schuberth, B., & Bunge, H.-P. (2016). Constraining central Neo-Tethys Ocean reconstructions with mantle convection models. *Geophysical Research Letters*, *43*(18), 9595–9603. https://doi.org/10.1002/2016GL070524

New, T., Ghelichkhan, S., Davies, D. R., Seton, M., Mather, B., & Müller, R. D. (2025a). Calibrating plate reconstructions with global mantle convection models. *Manuscript in revision, Geochemistry, Geophysics, Geosystems.*

New, T., Seton, M., Mather, B., Müller, R. D., Ghelichkhan, S., & Davies, D. R. (2025b). Coupled plate–mantle models support a 25 Ma Ontong–Java collision. *Prepared for submission to Earth and Planetary Science Letters.*

New, T., Seton, M., Müller, R. D., Davies, D. R., Ghelichkhan, S., & Mather, B. (2025c). Testing plate reconstructions with emergent slab geometry. *Prepared for submission to the Journal of Geodynamics.*

Obayashi, M., Yoshimitsu, J., Nolet, G., Fukao, Y., Shiobara, H., Sugioka, H., Miyamachi, H., & Gao, Y. (2013). Finite frequency whole mantle P wave tomography: Improvement of

subducted slab images. *Geophysical Research Letters*, *40*(21), 5652–5657. https://doi.org/10.1002/2013GL057401

Olierook, H. K. H., Jourdan, F., Whittaker, J. M., Merle, R. E., Jiang, Q., Pourteau, A., & Doucet, L. S. (2020). Timing and causes of the mid-Cretaceous global plate reorganization event. *Earth and Planetary Science Letters*, *534*, 116071. https://doi.org/10.1016/j.epsl.2020.116071

Paulson, A., & Richards, M. A. (2009). On the resolution of radial viscosity structure in modelling long-wavelength postglacial rebound data. *Geophysical Journal International*, *179*(3), 1516–1526. https://doi.org/10.1111/j.1365-246X.2009.04362.x

Peng, D., & Liu, L. (2022). Quantifying slab sinking rates using global geodynamic models with data-assimilation. *Earth-Science Reviews*, *230*, 104039. https://doi.org/10.1016/j.earscirev.2022.104039

Peng, D., Liu, L., Hu, J., Li, S., & Liu, Y. (2021a). Formation of east Asian stagnant slabs due to a pressure-driven Cenozoic mantle wind following mesozoic subduction. *Geophysical Research Letters*, *48*(18), e2021GL094638. https://doi.org/10.1029/2021GL094638

Peng, D., Liu, L., & Wang, Y. (2021b). A newly discovered late-Cretaceous east Asian flat slab explains its unique lithospheric structure and tectonics. *Journal of Geophysical Research: Solid Earth*, *126*(10), e2021JB022103. https://doi.org/10.1029/2021JB022103

Rathgeber, F., Ham, D. A., Mitchell, L., Lange, M., Luporini, F., Mcrae, A. T. T., Bercea, G.-T., Markall, G. R., & Kelly, P. H. J. (2016). Firedrake: Automating the finite element method by composing abstractions. *ACM Transactions on Mathematical Software*, *43*(3), 24:1–24:27. https://doi.org/10.1145/2998441

Raymo, M. E., & Ruddiman, W. F. (1992). Tectonic forcing of late Cenozoic climate. *Nature*, *359*(6391), 117–122. https://doi.org/10.1038/359117a0

Ringwood, A. E. (1991). Phase transformations and their bearing on the constitution and dynamics of the mantle. *Geochimica et Cosmochimica Acta*, *55*(8), 2083–2110. https://doi.org/10.1016/0016-7037(91)90090-R

Ritsema, J., Deuss, A., van Heijst, H. J., & Woodhouse, J. H. (2011). S40RTS: A degree-40 shear-velocity model for the mantle from new Rayleigh wave dispersion, teleseismic traveltime and normal-mode splitting function measurements. *Geophysical Journal International*, *184*(3), 1223–1236. https://doi.org/10.1111/j.1365-246X.2010.04884.x

Ritsema, J., McNamara, A. K., & Bull, A. L. (2007). Tomographic filtering of geodynamic models: Implications for model interpretation and large-scale mantle structure. *Journal of Geophysical Research: Solid Earth*, *112*(B1). https://doi.org/10.1029/2006JB004566

Romanowicz, B. (1991). Seismic Tomography of the Earth's Mantle. *Annual Review of Earth and Planetary Sciences*, *19*(Volume 19, 1991), 77–99. https://doi.org/10.1146/annurev.ea.19.050191.000453

Roy, P., Steinberger, B., Faccenda, M., & Pons, M. (2025). Lowermost mantle flow at thermochemical piles constrained by shear wave anisotropy: Insights from combined geodynamic and mantle fabric simulations at global scale. *Geochemistry, Geophysics, Geosystems*, *26*(10), e2025GC012510. https://doi.org/10.1029/2025GC012510

Schellart, W. P., Lister, G. S., & Toy, V. G. (2006). A late Cretaceous and Cenozoic reconstruction of the Southwest Pacific region: Tectonics controlled by subduction and slab rollback processes. *Earth-Science Reviews*, *76*(3), 191–233. https://doi.org/10.1016/j.earscirev.2006.01.002

Schettino, A. (1998). Computer-aided paleogeographic reconstructions. *Computers & Geosciences*, *24*(3), 259–267. https://doi.org/10.1016/S0098-3004(97)00128-3

Schuberth, B. S. A., Bunge, H.-P., Steinle-Neumann, G., Moder, C., & Oeser, J. (2009). Thermal versus elastic heterogeneity in high-resolution mantle circulation models with pyrolite composition: High plume excess temperatures in the lowermost mantle. *Geochemistry, Geophysics, Geosystems*, *10*(1). https://doi.org/10.1029/2008GC002235

Scotese, C. R. (2004). A Continental Drift Flipbook. *The Journal of Geology*, *112*(6), 729–741. https://doi.org/10.1086/424867

Scotese, C. R., Song, H., Mills, B. J. W., & van der Meer, D. G. (2021). Phanerozoic paleotemperatures: The Earth's changing climate during the last 540 million years. *Earth-Science Reviews*, *215*, 103503. https://doi.org/10.1016/j.earscirev.2021.103503

Seton, M., Müller, R. D., Zahirovic, S., Gaina, C., Torsvik, T., Shephard, G., Talsma, A., Gurnis, M., Turner, M., Maus, S., & Chandler, M. (2012). Global continental and ocean basin reconstructions since 200 Ma. *Earth-Science Reviews*, *113*(3), 212–270. https://doi.org/10.1016/j.earscirev.2012.03.002

Seton, M., Flament, N., Whittaker, J., Müller, R. D., Gurnis, M., & Bower, D. J. (2015). Ridge subduction sparked reorganization of the Pacific plate–mantle system 60–50 million years ago. *Geophysical Research Letters*, *42*(6), 1732–1740. https://doi.org/10.1002/2015GL063057

Seton, M., Williams, S. E., Domeier, M., Collins, A. S., & Sigloch, K. (2023). Deconstructing plate tectonic reconstructions. *Nature Reviews Earth & Environment*, *4*(3), 185–204. https://doi.org/10.1038/s43017-022-00384-8

Shephard, G. E., Bunge, H. .-., Schuberth, B. S. A., Müller, R. D., Talsma, A. S., Moder, C., & Landgrebe, T. C. W. (2012). Testing absolute plate reference frames and the implications for the generation of geodynamic mantle heterogeneity structure. *Earth and Planetary Science Letters*, *317–318*, 204–217. https://doi.org/10.1016/j.epsl.2011.11.027

Shephard, G. E., Matthews, K. J., Hosseini, K., & Domeier, M. (2017). On the consistency of seismically imaged lower mantle slabs. *Scientific Reports*, *7*(1), 10976. https://doi.org/10.1038/s41598-017-11039-w

Shephard, G. E., Müller, R. D., Liu, L., & Gurnis, M. (2010). Miocene drainage reversal of the Amazon River driven by plate–mantle interaction. *Nature Geoscience*, *3*(12), 870–875. https://doi.org/10.1038/ngeo1017

Sigloch, K., & Mihalynuk, M. G. (2013). Intra-oceanic subduction shaped the assembly of Cordilleran North America. *Nature*, *496*(7443), 50–56. https://doi.org/10.1038/nature12019

Simmons, N. A., Myers, S. C., Johannesson, G., Matzel, E., & Grand, S. P. (2015). Evidence for long-lived subduction of an ancient tectonic plate beneath the southern Indian Ocean. *Geophysical Research Letters*, *42*(21), 9270–9278. https://doi.org/10.1002/2015GL066237

Simmons, N. A., Schuberth, B. S. A., Myers, S. C., & Knapp, D. R. (2019). Resolution and covariance of the LLNL-G3D-JPS global seismic tomography model: Applications to travel time uncertainty and tomographic filtering of geodynamic models. *Geophysical Journal International*, *217*(3), 1543–1557. https://doi.org/10.1093/gji/ggz102

Steinberger, B., Torsvik, T. H., & Becker, T. W. (2012). Subduction to the lower mantle – A comparison between geodynamic and tomographic models. *Solid Earth*, *3*(2), 415–432. https://doi.org/10.5194/se-3-415-2012

Steinberger, B., & O'Connell, R. J. (1997). Changes of the Earth's rotation axis owing to advection of mantle density heterogeneities. *Nature*, *387*(6629), 169–173. https://doi.org/10.1038/387169a0

Stixrude, L., & Lithgow-Bertelloni, C. (2005). Thermodynamics of mantle minerals—I. Physical properties. *Geophysical Journal International*, *162*(2), 610–632. https://doi.org/10.1111/j.1365-246X.2005.02642.x

Stixrude, L., & Lithgow-Bertelloni, C. (2011). Thermodynamics of mantle minerals—II. Phase equilibria. *Geophysical Journal International*, *184*(3), 1180–1213. https://doi.org/10.1111/j.1365-246X.2010.04890.x

Stixrude, L., & Lithgow-Bertelloni, C. (2022). Thermal expansivity, heat capacity and bulk modulus of the mantle. *Geophysical Journal International*, *228*(2), 1119–1149. https://doi.org/10.1093/gji/ggab394

Stixrude, L., & Lithgow-Bertelloni, C. (2024). Thermodynamics of mantle minerals—III. The role of iron. *Geophysical Journal International*, *237*(3), 1699–1733. https://doi.org/10.1093/gji/ggae126

Stotz, I. L., Iaffaldano, G., & Davies, D. R. (2018). Pressure-driven Poiseuille flow: A major component of the torque-balance governing Pacific plate motion. *Geophysical Research Letters*, *45*(1), 117–125. https://doi.org/10.1002/2017GL075697

Styles, E., Goes, S., van Keken, P. E., Ritsema, J., & Smith, H. (2011). Synthetic images of dynamically predicted plumes and comparison with a global tomographic model. *Earth and Planetary Science Letters*, *311*(3), 351–363. https://doi.org/10.1016/j.epsl.2011.09.012

Su, J., Houser, C., Hernlund, J. W., & Deschamps, F. (2023). Tomographic filtering of shear and compressional wave models reveals uncorrelated variations in the lowermost mantle. *Geophysical Journal International*, *234*(3), 2114–2127. https://doi.org/10.1093/gji/ggad190

Taiwo, A., Bunge, H.-P., Schuberth, B. S. A., Colli, L., & Vilacis, B. (2023). Robust global mantle flow trajectories and their validation via dynamic topography histories. *Geophysical Journal International*, *234*(3), 2160–2179. https://doi.org/10.1093/gji/ggad188

Tarduno, J., Bunge, H.-P., Sleep, N., & Hansen, U. (2009). The Bent Hawaiian-Emperor Hotspot Track: Inheriting the Mantle Wind. *Science*, *324*(5923), 50–53. https://doi.org/10.1126/science.1161256

Tarduno, J. A., Duncan, R. A., Scholl, D. W., Cottrell, R. D., Steinberger, B., Thordarson, T., Kerr, B. C., Neal, C. R., Frey, F. A., Torii, M., & Carvallo, C. (2003). The Emperor Seamounts: Southward motion of the Hawaiian hotspot plume in earth's mantle. *Science*, *301*(5636), 1064–1069. https://doi.org/10.1126/science.1086442

Thrastarson, S., van Herwaarden, D.-P., Noe, S., Josef Schiller, C., & Fichtner, A. (2024). REVEAL: A global full-waveform inversion model. *Bulletin of the Seismological Society of America*, *114*(3), 1392–1406. https://doi.org/10.1785/0120230273

Torsvik, T. H., Doubrovine, P. V., Steinberger, B., Gaina, C., Spakman, W., & Domeier, M. (2017). Pacific plate motion change caused the Hawaiian-Emperor Bend. *Nature Communications*, *8*(1), 15660. https://doi.org/10.1038/ncomms15660

Torsvik, T. H., Müller, R. D., Van der Voo, R., Steinberger, B., & Gaina, C. (2008). Global plate motion frames: Toward a unified model. *Reviews of Geophysics*, *46*(3). https://doi.org/10.1029/2007RG000227

Torsvik, T. H., van der Voo, R., Doubrovine, P. V., Burke, K., Steinberger, B., Ashwal, L. D., Trønnes, R. G., Webb, S. J., & Bull, A. L. (2014). Deep mantle structure as a reference frame for movements in and on the Earth. *Proceedings of the National Academy of Sciences*, *111*(24), 8735–8740. https://doi.org/10.1073/pnas.1318135111

Torsvik, T. H., Van der Voo, R., Preeden, U., Mac Niocaill, C., Steinberger, B., Doubrovine, P. V., van Hinsbergen, D. J. J., Domeier, M., Gaina, C., Tohver, E., Meert, J. G., McCausland, P. J. A., & Cocks, L. R. M. (2012). Phanerozoic polar wander, palaeogeography and dynamics. *Earth-Science Reviews*, *114*(3), 325–368. https://doi.org/10.1016/j.earscirev.2012.06.007

Tuzo Wilson, J. (1963). A possible origin of the Hawaiian islands. *Canadian Journal of Physics*, *41*(6), 863–870. https://doi.org/10.1139/p63-094

van der Meer, D. G., van Hinsbergen, D. J. J., & Spakman, W. (2018). Atlas of the underworld: Slab remnants in the mantle, their sinking history, and a new outlook on lower mantle viscosity. *Tectonophysics*, *723*, 309–448. https://doi.org/10.1016/j.tecto.2017.10.004

Wolstencroft, M., Davies, J. H., & Davies, D. R. (2009). Nusselt–Rayleigh number scaling for spherical shell Earth mantle simulation up to a Rayleigh number of 10^9. *Physics of the Earth and Planetary Interiors*, *176*(1), 132–141. https://doi.org/10.1016/j.pepi.2009.05.002

Wolstencroft, M., & Davies, J. H. (2017). Breaking supercontinents; no need to choose between passive or active. *Solid Earth*, *8*(4), 817–825. https://doi.org/10.5194/se-8-817-2017

Woodhouse, J. H., & Dziewonski, A. M. (1984). Mapping the upper mantle: Three-dimensional modeling of earth structure by inversion of seismic waveforms. *Journal of Geophysical Research: Solid Earth*, *89*(B7), 5953–5986. https://doi.org/10.1029/JB089iB07p05953

Workman, R. K., & Hart, S. R. (2005). Major and trace element composition of the depleted MORB mantle (DMM). *Earth and Planetary Science Letters*, *231*(1), 53–72. https://doi.org/10.1016/j.epsl.2004.12.005

Young, A., Flament, N., Williams, S. E., Merdith, A., Cao, X., & Müller, R. D. (2022). Long-term Phanerozoic sea level change from solid Earth processes. *Earth and Planetary Science Letters*, *584*, 117451. https://doi.org/10.1016/j.epsl.2022.117451

Zahirovic, S., Eleish, A., Doss, S., Pall, J., Cannon, J., Pistone, M., Tetley, M. G., Young, A., & Fox, P. (2022). Subduction and carbonate platform interactions. *Geoscience Data Journal*, *9*(2), 371–383. https://doi.org/10.1002/gdj3.146

Zahirovic, S., Matthews, K. J., Flament, N., Müller, R. D., Hill, K. C., Seton, M., & Gurnis, M. (2016). Tectonic evolution and deep mantle structure of the eastern Tethys since the latest Jurassic. *Earth-Science Reviews*, *162*, 293–337. https://doi.org/10.1016/j.earscirev.2016.09.005

Zaroli, C., Koelemeijer, P., & Lambotte, S. (2017). Toward seeing the Earth's interior through unbiased tomographic lenses. *Geophysical Research Letters*, *44*(22). https://doi.org/10.1002/2017GL074996

Zhong, S., McNamara, A., Tan, E., Moresi, L., & Gurnis, M. (2008). A benchmark study on mantle convection in a 3-D spherical shell using CitcomS. *Geochemistry, Geophysics, Geosystems*, *9*(10). https://doi.org/10.1029/2008GC002048

Zhong, S., Zuber, M. T., Moresi, L., & Gurnis, M. (2000). Role of temperature-dependent viscosity and surface plates in spherical shell models of mantle convection. *Journal of Geophysical Research: Solid Earth*, *105*(B5), 11063–11082. https://doi.org/10.1029/2000JB900003